ISSN 2074-272X

науково-практичний журнал 2025/4

Електротехніка і Електромеханіка

Electrical Engineering & Electromechanics

Електротехнічні комплекси та системи
Промислова електроніка
Техніка сильних електричних та магнітних полів, інженерна електрофізика

Журнал включено до найвищої категорії «А» Переліку фахових видань України

З 2019 р. журнал індексується у Scopus

З 2015 р. журнал індексується у Web of Science Core Collection: Emerging Sources Citation Index

Electrical Engineering & Electromechanics

Scientific Journal was founded in 2002
Co-founders: National Technical University «Kharkiv Polytechnic Institute» (Kharkiv, Ukraine);
Anatolii Pidhornyi Institute of Power Machines and Systems of NAS of Ukraine (Kharkiv, Ukraine)

From no. 1 2019 Journal «Electrical Engineering & Electromechanics» is indexing in **Scopus**
and from no. 1 2005 Journal is indexing in **Web of Science Core Collection: Emerging Sources Citation Index (ESCI)**
Also included in DOAJ (Directory of Open Access Journals), in EBSCO's database, in ProQuest's databases – Advanced Technologies & Aerospace Database and Materials Science & Engineering Database, in Gale/Cengage Learning databases.

Editorial office address:
National Technical University «Kharkiv Polytechnic Institute», Kyrpychova Str., 2, Kharkiv, 61002, Ukraine
phone: +380 67 3594696, **e-mail:** a.m.grechko@gmail.com (**Grechko O.M.)**

ISSN (print) 2074-272X
ISSN (online) 2309-3404

Approved for printing on 30 June 2025. Format 60 × 90 ⅛. Paper – offset. Laser printing. Edition 50 copies.
Printed by Printing house «Madrid Ltd» (18, Gudanova Str., Kharkiv, 61024, Ukraine)

Electrical Engineering & Electromechanics
Scientific Journal

no. 4, 2025

Table of Contents

UDC 621.3 https://doi.org/10.20998/2074-272X.2025.4.01

M. L'Hadj Said, M. Ali Moussa, T. Bessaad

Control of an autonomous wind energy conversion system based on doubly fed induction generator supplying a non-linear load

Introduction. *Nowadays, many researches are being done on wind turbines providing electrical energy to a stable power grid by via a doubly fed induction generator (DFIG), but the studies on the autonomous networks are rare, due the difficulty of controlling powers often close to the nominal power of the generator.* ***Goal.*** *This paper presents a variable speed constant frequency (VSCF) autonomous control system to supply isolated loads (linear or non-linear). The main objective is the design of an effective strategy to reduce harmonic currents induced via the non-linear loads such as rectifier bridge with 6 diodes. The* ***novelty*** *of the work consists in study of system composed of a DFIG providing energy by his stator to a stand-alone grid. It uses a static converter connected to the rotor allowing operation in hypo and hyper synchronism. A permanent magnet synchronous machine (PMSM) connected to a wind turbine supplies this converter, that is sized proportionately to the variation range of the necessary rotational speed. In the case of linear loads there is no problem, all desired parameters are well controlled but in the non-linear loads case such as rectifier bridge with 6 diodes there is the harmonic problem. For this* ***purpose****, to reduce this harmonic, the proposed solution is the installation of a LC filter.* ***Methods.*** *The DFIG is controlled to provide a constant voltage in amplitude and frequency independently of the grid load or the drive turbine speed. This command is vector control in a reference related to the stator field. The stator flux is aligned along the d axis of this landmark allowing thus the decoupling of the active and reactive stator powers of DFIG. The DFIG is controlled by an internal control loop of rotor flux and an external control loop of output stator voltage. We present also the control of the PMSM and the DC bus of the converter. The PMSM is controlled by an internal control loop of the current and an external control loop of the continuous bus of the converter according to its nominal value. The control system of wind generator based on the maximum power point tracking and the control of bus continuous at output rectifier knowing that the non-linear loads introduce high harmonic currents and disrupt the proper functioning of the system. The installation of a LC filter between the stator and the network to be supplied reduce harmonics.* ***Results.*** *Simulation results carried out on MATLAB/Simulink show that this filter allows obtaining a quasi-sinusoidal network voltage and it also has the advantage of a simple structure, a good efficiency and a great performance. This proves the feasibility and efficiency of the proposed system for different loads (linear or non-linear).* ***Practical value.*** *This proposed system is very performing and useful compared to others because it ensures the permanent production of electricity at VSCF to feed isolated sites, whatever the load supplied (linear or non-linear), without polluting the environment so that the use of wind energy is very important to reduce the greenhouse effect.* References 34, figures 9.

Key words: **doubly fed induction generator, wind power, variable speed, autonomous operation, permanent magnet synchronous machine.**

Вступ*. В даний час проводиться багато досліджень вітряних турбін, що забезпечують електроенергією стабільну електромережу через асинхронний генератор з подвійним живленням (DFIG), але дослідження автономних мереж рідкісні через складність управління потужностями, часто близькими до номінальної потужності генератора.* ***Мета****. У статті представлена автономна система управління змінною швидкістю та постійною частотою (VSCF) для живлення ізольованих навантажень (лінійних чи нелінійних). Основною метою є розробка ефективної стратегії зниження гармонійних струмів, наведених через нелінійні навантаження, такі як випрямний міст із шістьма діодами.* ***Новизна*** *роботи полягає у вивченні системи, що складається з DFIG, що забезпечує енергією його статор в автономну мережу. Він використовує статичний перетворювач, підключений до ротора, що дозволяє працювати в гіпо-і гіперсинхронізмі. Синхронна машина з постійними магнітами (PMSM), підключена до вітряної турбіни, живить цей перетворювач, який має розмір, пропорційний діапазону зміни необхідної швидкості обертання. У разі лінійних навантажень проблем немає, всі бажані параметри добре контролюються, але у разі нелінійних навантажень, таких як випрямний міст із шістьма діодами, виникає проблема гармонік. Для цієї мети, щоб зменшити цю гармоніку, запропонованим рішенням є встановлення LC-фільтру.* ***Методи****. DFIG управляється для забезпечення постійної напруги за амплітудою та частотою незалежно від навантаження мережі або швидкості приводної турбіни. Ця команда є векторним управлінням в опорному сигналі, пов'язаному з полем статора. Потік статора вирівняний вздовж осі d цього орієнтиру, що дозволяє таким чином розв'язати активну та реактивну потужності статора DFIG. DFIG управляється внутрішнім контуром управління потоком ротора та зовнішнім контуром управління вихідною напругою статора. Представлено також управління PMSM та DC шиною перетворювача. PMSM управляється внутрішнім контуром керування струмом та зовнішнім контуром керування безперервною шиною перетворювача відповідно до його номінального значення. Система керування вітрогенератором базується на відстеженні точки максимальної потужності та безперервному керуванні шиною на вихідному випрямлячі, враховуючи, що нелінійні навантаження вводять струми високих гармонік та порушують належне функціонування системи. Встановлення LC-фільтра між статором і мережею живлення зменшує гармоніки.* ***Результати*** *моделювання, проведені в MATLAB/Simulink, показують, що цей фільтр дозволяє отримати квазісинусоїдальну напругу мережі, а також має перевагу щодо простоти структури, хорошої ефективності та значної продуктивності. Це доводить доцільність та ефективність запропонованої системи для різних навантажень (лінійних чи нелінійних).* ***Практична значимість****. Запропонована система дуже продуктивна і корисна в порівнянні з іншими, оскільки вона забезпечує постійне виробництво електроенергії на VSCF для живлення ізольованих ділянок, незалежно від навантаження, що подається (лінійне або нелінійне), не забруднюючи навколишнє середовище, тому що використовує енергію вітру, що є важливим для зниження парникового ефекту.* Бібл. 34, рис. 9.

Ключові слова: **асинхронний генератор з подвійним живленням, вітроенергетика, змінна швидкість, автономна робота, синхронна машина з постійними магнітами.**

Introduction. Electrical energy and electrical power systems frameworks play essential roles in the economic development of a country [1, 2].Sustainable development and renewable energies arouse the interest of several research teams. The use of wind energy and renewable sources is essential to reduce the greenhouse effect [3]. Thus, the development of wind turbines represents a great investment in technological research [4]. These systems which produce electrical energy from the wind can constitute a technological and economical alternative to the various exhaustible energy sources [5–7]. Wind turbines are believed to be a potential source of electrical energy in the near future [8, 9]. Wind turbines undergo both cycles, i.e. coercion and change in wind behavior [8–10].

A large part of the wind turbines use the asynchronous machines with double power. The utilization the doubly fed induction generator (DFIG) as a generation unit in the wind generation structures has been granted great concern during the past and present decades [11–14]. The superiority of the DFIG over other generation units comes from its ability to handle higher power ratings compared with the other units. Due to the physical construction of the DFIG, it has the ability to be controlled from both the grid and rotor sides [15]. The possibility of performing the control from the rotor side has enabled the utilization of low power inverters, which resulted in saving the cost [16, 17]. This generator allows the production of electricity at variable speed [18–23]. It gives the opportunity, then, to better control wind resources for different wind conditions [21–23].

Nowadays, many researches are being done on wind turbines providing electrical energy to a stable power grid by via a DFIG, but the studies on the autonomous networks are rare, due the difficulty of controlling powers often close to the nominal power of the generator.

The following work shows firstly, the control strategy of a DFIG, providing energy by the stator to an autonomous grid. It uses a static converter connected to the rotor allowing operation in hypo and hyper synchronism. A permanent magnet synchronous machine (PMSM) connected to a wind turbine feeds this converter (Fig. 1), that is sized proportionately to the variation range of the necessary rotational speed [24].

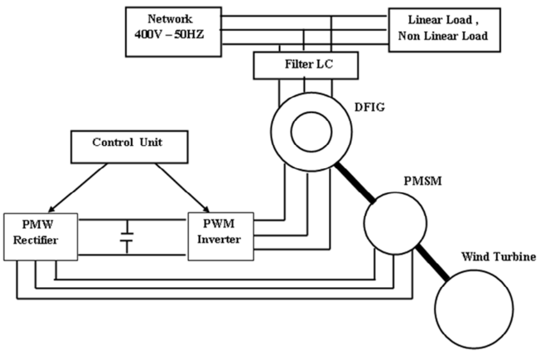

Fig 1. Global schema of the proposed system

The DFIG is controlled to provide a constant voltage in amplitude and frequency independently of the grid load or the drive turbine speed. This command is vector control in a reference related to the stator field. The stator flux is aligned along the d axis of this landmark allowing thus the decoupling of the active and reactive stator powers of DFIG [25–27].

The control strategy is carried out in two loops: an internal control loop of the rotor flux and an external control loop of the stator voltage. We have also; the PMSM is controlled by an internal control loop of the current and an external control loop of the continuous bus of the converter according to its nominal value [28].

The **aim** of this work is the improve the performance of this proposed system to feed isolated sites at variable speed constant frequency (VSCF), whatever the load desired to supply it, especially the non-linear loads. In the case of linear loads there is no problem, all desired parameters are well controlled but in the non-linear loads case such as the rectifier bridge with 6 diodes there is the harmonic problem.

These loads introduce high harmonic currents and disrupt the proper functioning of the system. The solution proposed to reduce harmonics is the installation of an LC filter between the stator and the network to be supplied. This filter allows obtaining a quasi-sinusoidal network voltage and it also has the advantage of a simple structure, a good efficiency and a great performance.

The control system of wind generator is based on the maximum power point tracking (MPPT) and the control of bus continuous at output rectifier. A power maximization algorithm determines the speed of the turbine that achieves maximum power generated, by estimating the speed of the wind corresponding to the optimal advance factor [29–31].

DFIG model. The equations of DFIG in d-q axis are [32]:

$$V_{sd} = R_s i_{sd} + \frac{\mathrm{d}\phi_{sd}}{\mathrm{d}t} - \omega_s \phi_{sq}; \qquad (1)$$

$$V_{sq} = R_s i_{sq} + \frac{\mathrm{d}\phi_{sq}}{\mathrm{d}t} - \omega_s \phi_{sd}; \qquad (2)$$

$$V_{rd} = R_r i_{rd} + \frac{\mathrm{d}\phi_{rd}}{\mathrm{d}t} - (\omega_s - \omega_r)\phi_{rq}; \qquad (3)$$

$$V_{rq} = R_r i_{rq} + \frac{\mathrm{d}\phi_{rq}}{\mathrm{d}t} - (\omega_s - \omega_r)\phi_{rd}; \qquad (4)$$

$$\phi_{sd} = L_s i_{sd} + M i_{rd}; \qquad (5)$$

$$\phi_{sq} = L_s i_{sq} + M i_{rq}; \qquad (6)$$

$$\phi_{rd} = L_r i_{rd} + M i_{sd}; \qquad (7)$$

$$\phi_{rq} = L_r i_{rq} + M i_{sq}, \qquad (8)$$

where V_s, V_r, R_s, R_r, i_s, i_r, ϕ_s, ϕ_r, L_s, L_r are the voltages, resistances, currents, fluxes and inductances of the stator and rotor, respectively; M is the mutual inductance; ω_s is the synchronous speed; ω_r is the rotor speed.

The reference related to the stator field is chosen. The stator flux is aligned with the axis d of this reference which corresponds to the following equations:

$$\phi_{sq} = 0, \quad \frac{\mathrm{d}\phi_{sq}}{\mathrm{d}t} = 0. \qquad (9)$$

In order to present the principles of this command, we neglect the resistances of stator and assume that the permanent state is reached. The voltage is therefore fixe in amplitude and frequency, we obtain the follow relation:

$$\begin{cases} V_{sd} \approx \dfrac{\mathrm{d}\phi_{sd}}{\mathrm{d}t} \approx 0; \\ V_{sq} \approx \omega_s \phi_{sd} \approx V_s. \end{cases} \qquad (10)$$

From (5), (6), (9), σ is the DFIG scattering coefficient, the constraint (11) corresponds to the good orientation of the landmark chosen:

$$i_{rq} = -\frac{L_s}{M} i_{sq} \Leftrightarrow \phi_{rq} = -\frac{\sigma L_s L_r}{M} i_{sq}. \qquad (11)$$

From (8), (10), (11), the new expression of active and reactive power became:

$$\begin{cases} P_s = \dfrac{(1-\sigma)}{\sigma M} V_s \phi_{rq}; \\ Q_s = \dfrac{(1-\sigma)}{\sigma M}\left(V_s \phi_{rd} - \dfrac{L_r}{M\omega_s} V_s^2\right). \end{cases} \quad (12)$$

Equation (12) shows the decoupling of the powers active via ϕ_{rq} and reactive via ϕ_{rd} when the permanent state is reached.

In generator mode, DFIG is represented by the state system with time varying following:

$$\left[\frac{\mathrm{d}\boldsymbol{\Phi}_r}{\mathrm{d}t}\right] = [\boldsymbol{A}][\boldsymbol{\Phi}_r] + [\boldsymbol{B}][\boldsymbol{V}_r] + [\boldsymbol{E}][\boldsymbol{I}_s]; \quad (13)$$

$$[\boldsymbol{V}_s] = [\boldsymbol{C}][\boldsymbol{\Phi}_r] + [\boldsymbol{D}][\boldsymbol{V}_r] + [\boldsymbol{F}][\boldsymbol{I}_s] + [\boldsymbol{G}]\left[\frac{\mathrm{d}\boldsymbol{I}_s}{\mathrm{d}t}\right]; \quad (14)$$

where:

$$[\boldsymbol{V}_s] = \begin{bmatrix} V_{sd} \\ V_{sq} \end{bmatrix}; \; [\boldsymbol{\Phi}_r] = \begin{bmatrix} \phi_{rd} \\ \phi_{rq} \end{bmatrix}; \; [\boldsymbol{V}_r] = \begin{bmatrix} V_{rd} \\ V_{rq} \end{bmatrix}; \; [\boldsymbol{I}_s] = \begin{bmatrix} I_{sd} \\ I_{sq} \end{bmatrix};$$

$$[\boldsymbol{A}] = \begin{bmatrix} -R_r/L_r & \omega_r \\ -\omega_r & -R_r/L_r \end{bmatrix}; \; [\boldsymbol{B}] = [\boldsymbol{I}_2]; \; [\boldsymbol{E}] = \frac{R_r M}{L_r}[\boldsymbol{I}_2];$$

$$[\boldsymbol{C}] = -\frac{M}{L_r}\begin{bmatrix} R_r/L_r & \omega_r \\ -\omega_r & R_r/L_r \end{bmatrix}; \; [\boldsymbol{D}] = \frac{M}{L_r}[\boldsymbol{I}_2]; \; [\boldsymbol{I}_2] = \begin{bmatrix} 1 & 0 \\ 0 & 1 \end{bmatrix};$$

$$[\boldsymbol{G}] = \sigma L_s [\boldsymbol{I}_2]; \; [\boldsymbol{F}] = \begin{bmatrix} R_s + \dfrac{M^2}{L_r^2} R_r & -\sigma L_s \omega_s \\ \sigma L_s \omega_s & R_s + \dfrac{M^2}{L_r^2} R_r \end{bmatrix};$$

where $[\boldsymbol{V}_r]$, $[\boldsymbol{V}_s]$, $[\boldsymbol{\Phi}_r]$ are respectively the input, output and system status vectors. The vector $[\boldsymbol{I}_s]$ depends on the load, it is considered as perturbation.

In the case of a DFIG operating as a generator, the difficulty comes from the derivative terms of the perturbation (14), which are difficult to simulate. There is also a direct link between the input and the output of the system.

The originality of this new method of control come of the choice of the rotor flux vector as a control vector, indeed the equation (13) shows that the rotor flux is the natural state vector of DFIG and it allows also a direct control on the voltage of the rotor. Compared to the regulation in the current, this method allows a minimization of harmonics introduced by non- linear loads.

Internal control loop of the rotor flux. From (13), we can deduct the following system, where E_d and E_q are coupling terms:

$$\frac{\mathrm{d}\phi_{rd}}{\mathrm{d}t} = V_{rd} - \frac{1}{T_r}\phi_{rd} + E_d; \quad (15)$$

$$\frac{\mathrm{d}\phi_{rq}}{\mathrm{d}t} = V_{rq} - \frac{1}{T_r}\phi_{rq} + E_q, \quad (16)$$

where $T_r = L_r / R_r$ is the DFIG rotor time constant:

$$\begin{cases} E_d = \dfrac{M}{T_r} i_{sd} + \omega_r \phi_{rq}; \\ E_q = \dfrac{M}{T_r} i_{sq} - \omega_r \phi_{rd}. \end{cases} \quad (17)$$

The transfer functions between the flux and tensions of the rotor depend only to the rotor time constant T_r. The regulation can be realized with simple PI correctors. It's also, the coupling terms can be compensated as shown in the block diagram (Fig. 2).

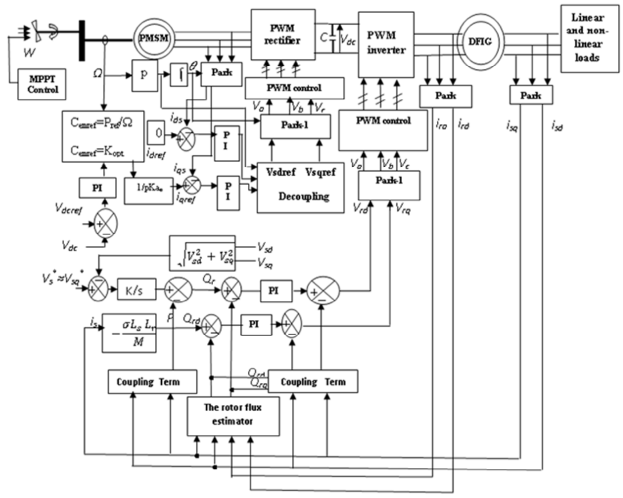

Fig. 2. Global block diagram of the control of the proposed wind power system

External control loop of the stator voltage. We have already seen that the constraint (11) correspond to the correct orientation of the reference chosen. The amplitude of the stator voltage is given by:

$$|V_s| = \sqrt{V_{sd}^2 + V_{sq}^2}. \quad (18)$$

This latter is controlled by an external loop (Fig. 2), because (14) shows that when the DFIG works as a generator on an autonomous grid, the stator voltage is the output vector of the system. The equations (10), (14) and (18) allow obtaining the following system, where A_d and A_q are terms of perturbation that we can compensate. The transfer functions between the stator voltages and the rotor flux are of simple gains, integrators will allow of cancel the static error between the measured and desired tension:

$$\begin{cases} |V_s| = V_{sq}; \quad V_{sd} = -\omega_s \dfrac{M}{L_r}(\phi_{rq} + A_d); \\ V_{sq} = \omega_s \dfrac{M}{L_r}(\phi_{rd} + A_q); \end{cases} \quad (19)$$

$$\begin{cases} A_d = \dfrac{L_r}{M}\left(-\dfrac{R_s}{\omega_s} i_{sd} + \sigma L_s i_{sq}\right); \\ A_q = \dfrac{L_r}{M}\left(-\dfrac{R_s}{\omega_s} i_{sq} + \sigma L_s i_{sd}\right). \end{cases} \quad (20)$$

Cascade rotor side. Figure 2 presents the system seen the rotor side of the DFIG. This configuration using a converter is very frequent for high power applications and the limited speed variation range. This method permits operation below and above at the synchronous speed. These are the limits of this speed variation range that secure the power of converter. Figure 2 also presents the control of the PMSM. The objective of this control is to keep the continuous bus voltage constant independently to the rotor power. This control will be realized by two control loops: internal control loop of the stator current of the PMSM and an external control loop of the continuous bus voltage to its nominal value.

Model of PMSM. The model of PMSM is given by the system (21) using Park method in a reference frame linked to its rotating field:

$$\begin{cases} V_d = R_{ms} I_d + L_d \dfrac{\mathrm{d}I_d}{\mathrm{d}t} - E_{md}; \\ V_q = R_{ms} I_q + L_q \dfrac{\mathrm{d}I_q}{\mathrm{d}t} - E_{mq}; \end{cases} \tag{21}$$

$$\begin{cases} E_{md} = -\omega L_q I_q; \\ E_{mq} = -\omega L_d I_d - \omega \Phi_a, \end{cases} \tag{22}$$

where E_{md}, E_{mq} are the coupling terms; R_{ms} is the stator resistance; L_d, L_q are the direct and quadrature inductances; V_d, V_q, I_d, I_q are the components *d-q* stator voltages and currents; Φ_a is the flux of the permanent magnet; $\omega = p\Omega$ is the voltage pulsation; Ω is the speed of rotation; p is the number of pairs of poles.

The voltages being input variables, we can express the output variables (current) as follows:

$$\begin{cases} \dfrac{\mathrm{d}I_d}{\mathrm{d}t} = \dfrac{1}{L_d}\left(V_d - R_{ms} I_d + \omega L_q I_q\right); \\ \dfrac{\mathrm{d}I_q}{\mathrm{d}t} = \dfrac{1}{L_d}\left(V_q - R_{ms} I_q - \omega L_d I_d - \omega \Phi_a\right). \end{cases} \tag{23}$$

Knowing that in our case $L_d = L_q = L$.

Control of wind generator. The block control of wind generator diagram is shown in Fig. 2. The control system based on two functions: MPPT and the control of bus continuous at output rectifier.

Power maximization strategy. The equations of electric and mechanical powers of the system in permanent regime allow to new the formulation of the new objective. However, the function of mechanical power, a simpler form is used. To reduce the degrees of freedom of the system, wind speed, only uncontrollable variable of the system, is out of the mathematical formulation by the use of an optimal form [33, 34].

The equation of the wind power P_w corresponding to a wind speed V_v is given as:

$$P_w = C_p(\lambda) \frac{\rho S V_v^3}{2}, \tag{24}$$

where C_p is the power coefficient; λ is the tip-speed ratio; ρ is the air density; S is the blade surface.

If the tip-speed ratio λ is maintained at its optimal λ_{opt} value, the power coefficient is always at its maximum value $C_{p\max} = C_p(\lambda_{opt})$.

Therefore, the power of wind is also at its maximum value:

$$P_w^{opt} = C_{p\max} \frac{\rho S V_v^3}{2}. \tag{25}$$

On the other hand, if the equation of assumed tip-speed ratio maintained at the optimal value, we isolate the wind speed (26) for replacing in the equation of the maximum mechanical power (25), we obtain the (27):

$$\lambda^{opt} = \frac{\Omega R}{V_v} \Rightarrow V_v = \frac{\Omega R}{\lambda^{opt}}; \tag{26}$$

$$P_w^{opt} = \frac{1}{2} C_{p\max} \rho S \left(\frac{R}{\lambda^{opt}}\right)^3 \Omega^3. \tag{27}$$

We obtain an analytical form of the maximum mechanical power of the wind turbine depending to its speed of rotation Ω only. Considering that the conditions are optimal (at optimum power) then the (27) allows the calculation of the value of the optimum torque:

$$T_w^{opt} = \frac{1}{2} C_{p\max} \rho S \left(\frac{R}{\lambda^{opt}}\right)^3 \Omega^2. \tag{28}$$

Regulation of the stator current of the PMSM. The transfer functions between the voltages and currents of the PMSM are first order and are regulated by PI correctors as shown in the block diagram on Fig. 3. The transfer function of the machine being of the form:

$$H(s) = \frac{I_{dq}(s)}{V_{dq}(s) + E_{mdq}(s)}; \tag{29}$$

$$H(s) = \frac{1}{E_{ms} + L_{dq}(s)} = \frac{1/R_{ms}}{1 + \dfrac{L_{dq}}{R_{ms}} s}. \tag{30}$$

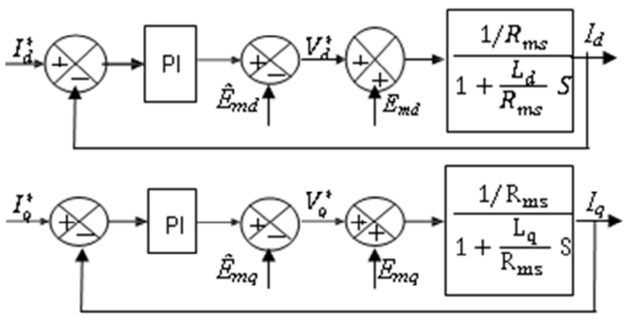

Fig. 3. Regulation loop of current of the PMSM

In permanent regime and neglecting the stator resistance, the equations (21), (22) give the following system:

$$\begin{cases} V_d = -\omega L_q I_q; \\ V_q = \omega L_d I_d + \omega \Phi_a \end{cases}. \tag{31}$$

Furthermore, neglecting the losses introduced by the converter, we can write:

$$P_{dc} = V_d I_d + V_q I_q = V_{dc} I_{dc}, \tag{32}$$

where P_{dc} is the active power; V_{dc} is the continuous bus voltage; I_{dc} is the output current of the rectifier.

With the help of (31), (32) we obtain:

$$I_q^* = P_{dc} / \omega \Phi_a, \tag{33}$$

$$V_d = P_{dc} L_q / \Phi_a. \tag{34}$$

The relations (33), (34) show that the components of the direct voltage and the quadrature current depend to the desired rotor power. A conventional method controlling of the motor starting asynchronous power (MSAP) seeking to obtain maximum power for a minimum of current. However if I_{dref}=0 the stator voltage is given by (35). This voltage is acceptable as long as it is below the limit voltage V_{lim} fixed by the continuous bus voltage (36):

$$|V| = \sqrt{\left(\frac{P L_q}{\Phi_a}\right)^2 + \left(\omega \Phi_a\right)^2}; \tag{35}$$

$$|V| < V_{\lim}. \tag{36}$$

Control loop of the continuous voltage V_{dc} According to (32), (33) the equation of the power is:

$$P_{dc} = \omega \Phi_a I_q = V_{dc} I_{dc} \Rightarrow I_q = \frac{V_{dc}}{\omega \Phi_a} I_{dc} . \quad (37)$$

Figure 3 allows us to write:

$$I_{dc} = I_c + I_L . \quad (38)$$

Supposing that the losses are null

$$C \frac{\mathrm{d}V_{dc}}{\mathrm{d}t} = I_{dc} - I_L . \quad (39)$$

The block diagram of this loop is shown in Fig. 4. The regulation is done with PI correctors after setting the damping factor and the natural frequency desired.

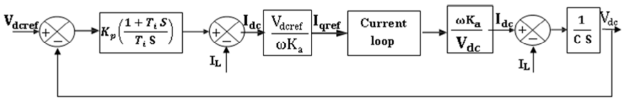

Fig. 4. Regulation of the continuous bus voltage

Simulation results. Linear load case. The proposed system has been tested in MATLAB / Simulink using the electrical parameters of the DFIG and PMSM, the reference voltage at the rectifier output being taken equal to 150 V, it is assumed that this DFIG and MSAP are driven by a wind turbine, wind speed is variable in time to feed a load RL. Load whose power consumption is expected to vary according to the following time table: 0 kVA at time $t = 0$ s, 12 kVA at $t = 0.5$ s and 9 kVA at time $t = 2$ s with 0.8 power factor. The obtained simulation results (Fig. 5) prove the feasibility of the proposed system for the maximum load variable power in the time. The values also show that the stator voltage V_s and the continuous voltage V_{dc} are entirely controlled during the variation of the load and wind speed. This therefore proves the feasibility of the system in hypo and hyper synchronism.

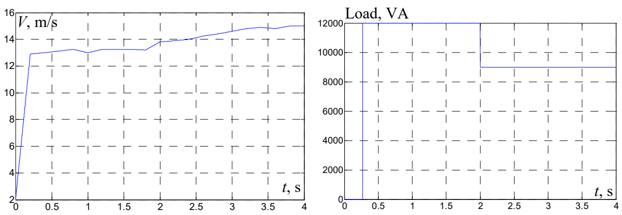

a) wind speed *b*) load

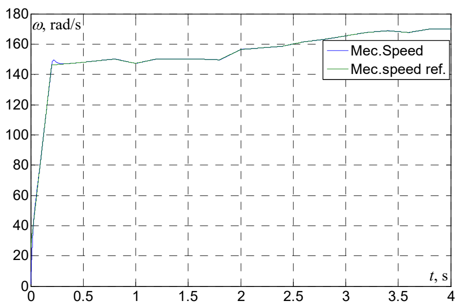

c) mechanical speed

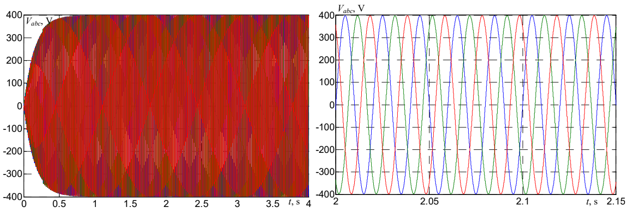

d) stator voltage generated by the DFIG with zoom

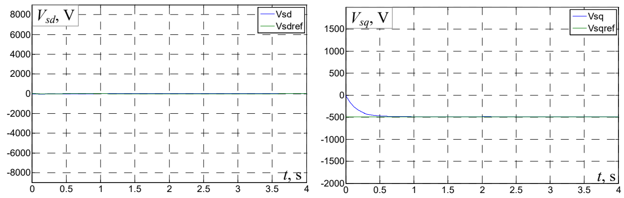

e) DFIG stator voltages in the axis *d-q*

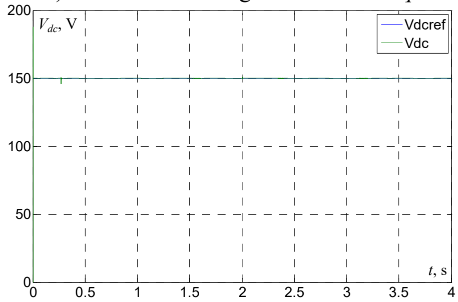

f) continuous bus voltage V_{dc}

Fig. 5. Simulation results of the proposed system for linear load

Non-linear load case. After having studied the functioning of the DFIG on linear load, we will study the performance of the latter on a non-linear load made up of a converter (rectifier bridges with 6 diodes) which supplies an inductive load (see Fig. 6):

$$I_d = U_d / (L_s + R) . \quad (40)$$

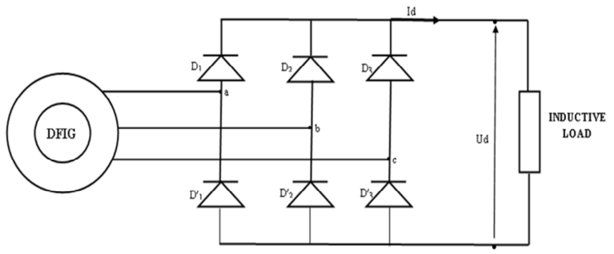

Fig. 6. Structure of a 6-pulse diode rectifier

The rectified voltage is obtained by:

$$U_d = V_{js\,\max} - V_{js\,\min} . \quad (41)$$

Inserting a 6-diode rectifier bridge into the system does not change the test procedure; the only difference is the introduction of non-linear loads instead of linear RL loads. Indeed, this type of converter induces a large number of current harmonics:

$$\begin{cases} I_{sf} = \sqrt{3} I_d / \pi ; \quad I_{sh} = I_{sf} / h ; \\ h = 6n \pm 1; \quad THD_{Is} = \sqrt{\sum I_{sh}^2} / I_{sf} , \end{cases} \quad (42)$$

where I_{sf} is the amplitude of the fundamental current; I_{sh} is the harmonic current of order h; I_d is the continue current flowing through the load; THD_{Is} is the total harmonic distortion of the load current.

The simulation results clearly show the deterioration of the stator voltage due to the induced harmonic currents caused by the load currents. The more the load increases the load current becomes more and more distorting. The active and reactive powers are also deteriorated by this non-linear load due to the harmonics induced by the 6-diode rectifier bridge. These harmonics increase the losses in the DFIG and promote excessive heating of the latter. The simulation results are shown in Fig. 7.

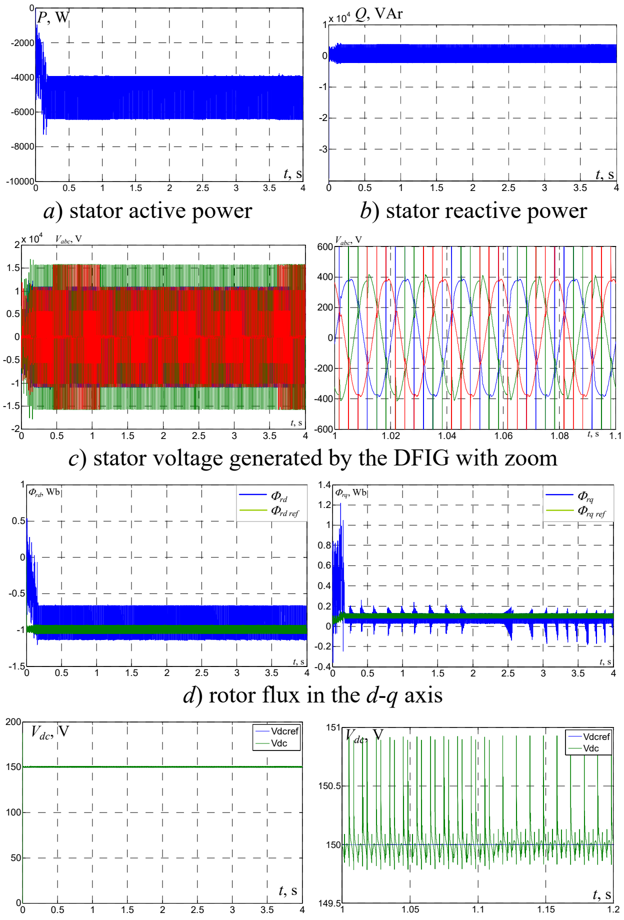

a) stator active power *b*) stator reactive power

c) stator voltage generated by the DFIG with zoom

d) rotor flux in the *d*-*q* axis

e) continuous bus voltage V_{dc} with zoom

Fig. 7. Simulation results of the proposed system for non-linear load

Filtering characteristics. LC filter is placed on the stator side of the DFIG to eliminate voltage harmonics from the on-board network. The single-phase equivalent model of the filter is given in Fig. 8.

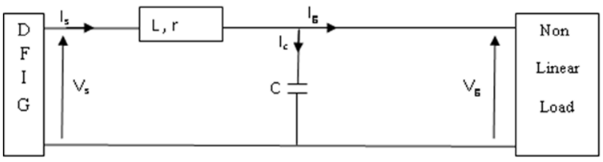

Fig 8. Single-phase equivalent diagram of the LC filter

This filter can be represented by the following equation of state:

$$\frac{\mathrm{d}}{\mathrm{d}t}\begin{bmatrix} I_s \\ V_g \end{bmatrix} = \begin{bmatrix} -\dfrac{r}{L} & -\dfrac{1}{L} \\ \dfrac{1}{C} & 0 \end{bmatrix}\begin{bmatrix} I_s \\ V_g \end{bmatrix} + \begin{bmatrix} 0 & \dfrac{1}{L} \\ -\dfrac{1}{C} & 0 \end{bmatrix}\begin{bmatrix} I_g \\ V_s \end{bmatrix}, \quad (43)$$

where L, r are the filter inductance and its internal resistance; C is the filter capacitance; V_s, I_s, I_g, V_g are respectively the stator voltage and current of the DFIG, and the current and voltage of the non-linear load. V_s can be considered as the filter input variable, I_g – the disturbance variable and V_g – the filter output variable. From (43), we can write 4 transfer functions to describe the operation of the filter:

$$\begin{bmatrix} I_s(s) \\ V_g(s) \end{bmatrix} = \frac{\omega_0^2}{s^2 + 2m\omega_0 s + \omega_0^2}\begin{bmatrix} 1 & Cs \\ Ls + r & 1 \end{bmatrix}\begin{bmatrix} I_g(s) \\ V_s(s) \end{bmatrix}, \quad (44)$$

where $\omega_0 = 1/\sqrt{LC}$ is the resonance frequency; m is the damping coefficient.

This presentation shows that the load current harmonics due to the 6-diode rectifier bridge deteriorate the stator current as well as the load voltage vector. The filter parameters must therefore be chosen so as to reduce the harmonic distortion rate of the mains voltage to a value less than 5 %. We can derive from (44) the transfer function between $I_g(s)$ and $V_g(s)$:

$$\frac{V_g(s)}{I_g(s)} = \frac{(Ls + r)\omega_0^2}{s^2 + 2m\omega_0 s + w_0^2}. \quad (45)$$

Design procedure. The filter inductance is typically sized equal to a fraction of the rated motor impedance, so voltage drop is reduced across the filter inductance. In this case, we will choose:

$$L = 0.7 \cdot L_s. \quad (46)$$

The resistance in this case corresponds to the internal resistance of the inductance and thus is proportional to the internal Joule losses of the inductance. This resistance creates losses at the level of the filter. In this case, the Joule losses are defined to be less than 1 % of the total power, so the maximum acceptable internal resistance $r_{\max}$ can be calculated as:

$$r_{\max} = \frac{0.01 P_{s-nom}}{3 I_{s-nom}^2}. \quad (47)$$

The attenuation provided by the filter depends on the damping coefficient m. The cutoff frequency should be low enough to give the desired attenuation and the damping coefficient large enough to increase that attenuation. On the other hand, (44) shows that a low cutoff frequency may result in large components value and size. In addition, a very large damping coefficient would result in an internal resistance value more important than $r_{\max}$. It is therefore necessary to find a compromise between the dimensions of the filter and the desired THD.

From the components of the harmonic current described by (42), the amplitude-frequency characteristics given by (45) and knowing that the amplitude of the voltage of the fundamental is 400 V, we can calculate the relationship between the filter cutoff frequency and the THD of the mains voltage after filtering.

Finally, knowing w_0 and L, we can deduce the capacity of the filter:

$$C = 1/L\omega_0^2. \quad (48)$$

The introduction of an *LC* filter with a cutoff frequency of 816.5 rad/s with a damping coefficient m=0.734 to reduce current harmonics is simulated in the same way as before.

The simulation results (Fig. 9) show that the load voltage is almost sinusoidal for a non-linear load. Compared to the signal obtained without a filter, the oscillations on the active and reactive power are greatly reduced by the introduction of the filter. These simulations carried out on MATLAB/Simlink prove the efficiency of the proposed system in the event of non-linear loads.

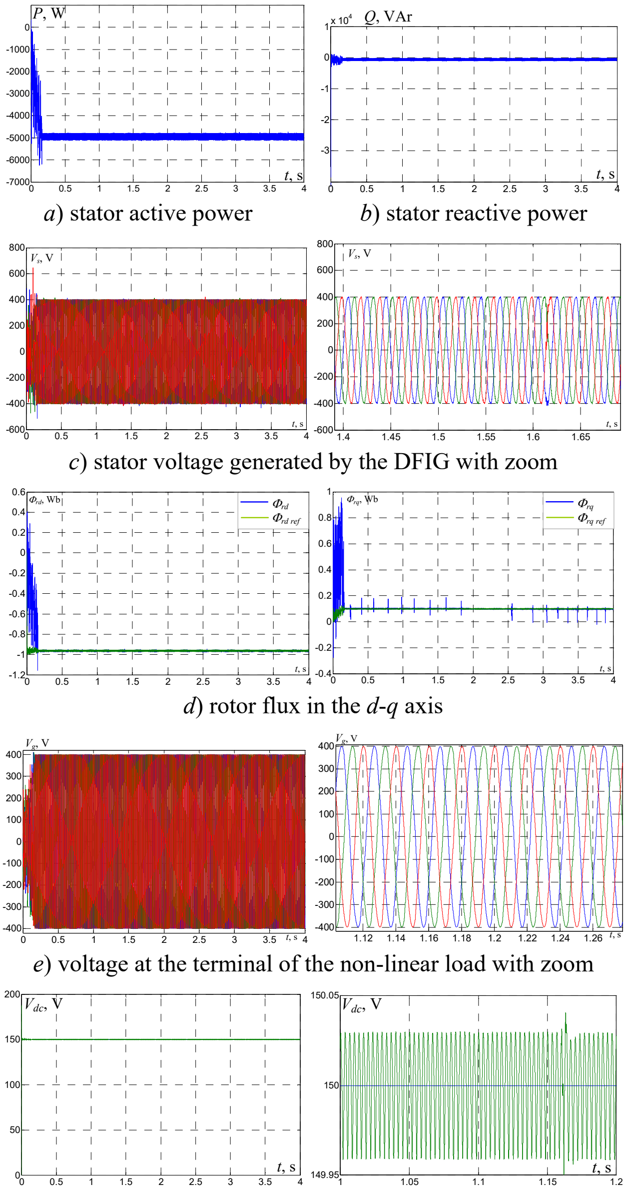

a) stator active power *b*) stator reactive power

c) stator voltage generated by the DFIG with zoom

d) rotor flux in the *d*-*q* axis

e) voltage at the terminal of the non-linear load with zoom

e) continuous bus voltage V_{dc} with zoom

Fig 9. Simulation results of the proposed system for non-linear load after the introduction of LC filter

Conclusions.

This paper has enabled us to study an autonomous electrical generation system working at variable speed and fixed frequency to supply isolated loads. The principles of vector control of DFIG and PMSM have been presented. The simulation results carried out on MATLAB/Simulink show that this method makes it possible to obtain a voltage at fixed frequency and amplitude under a wide range of variation of the turbine drive speed. The addition of non-linear loads, such as diode rectifier bridges, introduces harmonics which deteriorate the voltages of the network. The introduction of an LC filter on the stator side of the DFIG allows these harmonics to be reduced to an acceptable level. This proves the efficiency of the proposed system for different loads (linear and non-linear loads).

Conflict of interest. The authors declare that they have no conflicts of interest.

REFERENCES

1. Strielkowski W., Civín L., Tarkhanova E., Tvaronavičienė M., Petrenko Y. Renewable Energy in the Sustainable Development of Electrical Power Sector: A Review. *Energies*, 2021, vol. 14, no. 24, art. no. 8240. doi: https://doi.org/10.3390/en14248240.

2. Duong M., Leva S., Mussetta M., Le K. A Comparative Study on Controllers for Improving Transient Stability of DFIG Wind Turbines During Large Disturbances. *Energies*, 2018, vol. 11, no. 3, art. no. 480. doi: https://doi.org/10.3390/en11030480.

3. Benbouhenni H., Lemdani S. Combining synergetic control and super twisting algorithm to reduce the active power undulations of doubly fed induction generator for dual-rotor wind turbine system. *Electrical Engineering & Electromechanics*, 2021, no. 3, pp. 8-17. doi: https://doi.org/10.20998/2074-272X.2021.3.02.

4. Ouerghi F.H., Omri M., Menaem A.A., Taloba A.I., Abd El-Aziz R.M. Feasibility evaluation of wind energy as a sustainable energy resource. *Alexandria Engineering Journal*, 2024, vol. 106, pp. 227-239. doi: https://doi.org/10.1016/j.aej.2024.06.055.

5. Shanu S., Barath Raj R.K., Thampatty K.C.S. Wind Resource Assesment and Techno-economic Analysis using WaSP software – A Case Study. *2023 IEEE Technology & Engineering Management Conference - Asia Pacific (TEMSCON-ASPAC)*, 2023, pp. 1-7. doi: https://doi.org/10.1109/TEMSCON-ASPAC59527.2023.10531485.

6. Evans L.E., Dolšak N., Prakash A. Do windy areas have more wind turbines: An empirical analysis of wind installed capacity in Native tribal nations. *PLOS ONE*, 2022, vol. 17, no. 2, art. no. e0261752. doi: https://doi.org/10.1371/journal.pone.0261752.

7. Muthukaruppasamy S., Dharmaprakash R., Sendilkumar S., Parimalasundar E. Enhancing off-grid wind energy systems with controlled inverter integration for improved power quality. *Electrical Engineering & Electromechanics*, 2024, no. 5, pp. 41-47. doi: https://doi.org/10.20998/2074-272X.2024.5.06.

8. Nejad A.R., Keller J., Guo Y. et al. Wind turbine drivetrains: state-of-the-art technologies and future development trends. *Wind Energy Science*, 2022, vol. 7, no. 1, pp. 387-411. doi: https://doi.org/10.5194/wes-7-387-2022.

9. Ahmed S.D., Al-Ismail F.S.M., Shafiullah M., Al-Sulaiman F.A., El-Amin I.M. Grid Integration Challenges of Wind Energy: A Review. *IEEE Access*, 2020, vol. 8, pp. 10857-10878. doi: https://doi.org/10.1109/ACCESS.2020.2964896.

10. Berhanu Tuka M., Leidhold R., Mamo M. Modeling and control of a Doubly Fed Induction Generator using a back-to-back converters in grid tied wind power system. *2017 IEEE PES PowerAfrica*, 2017, pp. 75-80. doi: https://doi.org/10.1109/PowerAfrica.2017.7991202.

11. El Moudden A., Hmidat A., Aarib A. Comparison of the active and reactive powers of the asynchronous cage machine and the doubly fed induction generator used in wind turbine energy in the case of decentralized production on an isolated site. *International Journal on Electrical Engineering and Informatics*, 2023, vol. 15, no. 1, pp. 50-63. doi: https://doi.org/10.15676/ijeei.2023.15.1.4.

12. Abdeen M., Li H., Kamel S., Khaled A., El-Dabah M., Kharrich M., Sindi H.F. A Recent Analytical Approach for Analysis of Sub-Synchronous Resonance in Doubly-Fed Induction Generator-Based Wind Farm. *IEEE Access*, 2021, vol. 9, pp. 68888-68897. doi: https://doi.org/10.1109/ACCESS.2021.3075965.

13. Chhipa A.A., Chakrabarti P., Bolshev V., Chakrabarti T., Samarin G., Vasilyev A.N., Ghosh S., Kudryavtsev A. Modeling and Control Strategy of Wind Energy Conversion System with Grid-Connected Doubly-Fed Induction Generator. *Energies*, 2022, vol. 15, no. 18, art. no. 6694. doi: https://doi.org/10.3390/en15186694.

14. Marques G.D., Iacchetti M.F. DFIG Topologies for DC Networks: A Review on Control and Design Features. *IEEE Transactions on Power Electronics*, 2019, vol. 34, no. 2, pp. 1299-1316. doi: https://doi.org/10.1109/TPEL.2018.2829546.

15. Mossa M.A., Duc Do T., Saad Al-Sumaiti A., Quynh N.V., Diab A.A.Z. Effective Model Predictive Voltage Control for a Sensorless Doubly Fed Induction Generator. *IEEE Canadian Journal of Electrical and Computer Engineering*, 2021, vol. 44, no. 1, pp. 50-64. doi: https://doi.org/10.1109/ICJECE.2020.3018495.
16. Wei X., Cheng M., Wang W., Han P., Luo R. Direct Voltage Control of Dual-Stator Brushless Doubly Fed Induction Generator for Stand-Alone Wind Energy Conversion Systems. *IEEE Transactions on Magnetics*, 2016, vol. 52, no. 7, pp. 1-4. doi: https://doi.org/10.1109/TMAG.2016.2526049.
17. Bebars A.D., Eladl A.A., Abdulsalam G.M., Badran E.A. Internal electrical fault detection techniques in DFIG-based wind turbines: a review. *Protection and Control of Modern Power Systems*, 2022, vol. 7, no. 1, art. no. 18. doi: https://doi.org/10.1186/s41601-022-00236-z.
18. Zhang Y., Jiang T. Robust Predictive Stator Current Control Based on Prediction Error Compensation for a Doubly Fed Induction Generator Under Nonideal Grids. *IEEE Transactions on Industrial Electronics*, 2022, vol. 69, no. 5, pp. 4398-4408. doi: https://doi.org/10.1109/TIE.2021.3080200.
19. Din Z., Zhang J., Xu Z., Zhang Y., Zhao J. Low voltage and high voltage ride-through technologies for doubly fed induction generator system: Comprehensive review and future trends. *IET Renewable Power Generation*, 2021, vol. 15, no. 3, pp. 614-630. doi: https://doi.org/10.1049/rpg2.12047.
20. Metwally M.M., Ratib M.K., Aly M.M., Abdel-Rahim A.M. Effect of Grid Faults on Dominant Wind Generators for Electric Power System Integration: A Comparison and Assessment. *Energy Systems Research*, 2021, vol. 3, no. 15, pp. 70-78. doi: https://doi.org/10.38028/esr.2021.03.0007.
21. Beniss M.A., El Moussaoui H., Lamhamdi T., El Markhi H. Performance analysis and enhancement of direct power control of DFIG based wind system. *International Journal of Power Electronics and Drive Systems (IJPEDS)*, 2021, vol. 12, no. 2, pp. 1034-1044. doi: https://doi.org/10.11591/ijpeds.v12.i2.pp1034-1044.
22. Dannier A., Fedele E., Spina I., Brando G. Doubly-Fed Induction Generator (DFIG) in Connected or Weak Grids for Turbine-Based Wind Energy Conversion System. *Energies*, 2022, vol. 15, no. 17, art. no. 6402. doi: https://doi.org/10.3390/en15176402.
23. Ansari A.A., Dyanamina G. Fault Ride-Through Operation Analysis of Doubly Fed Induction Generator-Based Wind Energy Conversion Systems: A Comparative Review. *Energies*, 2022, vol. 15, no. 21, art. no. 8026. doi: https://doi.org/10.3390/en15218026.
24. Cardenas R., Pena R., Alepuz S., Asher G. Overview of Control Systems for the Operation of DFIGs in Wind Energy Applications. *IEEE Transactions on Industrial Electronics*, 2013, vol. 60, no. 7, pp. 2776-2798. doi: https://doi.org/10.1109/TIE.2013.2243372.
25. Xiao H., Zhao Z., Zhou K., Guo J., Lai C.S., Lei Lai L. Voltage-Source Control of DFIG in Standalone Wind Power-Based Microgrids. *2020 IEEE 1st China International Youth Conference on Electrical Engineering (CIYCEE)*, 2020, pp. 1-7. doi: https://doi.org/10.1109/CIYCEE49808.2020.9332674.
26. Hamid B., Hussain I., Iqbal S.J., Singh B., Das S., Kumar N. Optimal MPPT and BES Control for Grid-Tied DFIG-Based Wind Energy Conversion System. *IEEE Transactions on Industry Applications*, 2022, vol. 58, no. 6, pp. 7966-7977. doi: https://doi.org/10.1109/TIA.2022.3202757.
27. Smai Y., Touaiti B., Jemli M., Ben Azza H. Experimental implementation of voltage and frequency regulation in DFIG connected to a DC-link for marine current energy conversion system. *Electrical Engineering*, 2022, vol. 104, no. 4, pp. 2355-2367. doi: https://doi.org/10.1007/s00202-021-01485-1.
28. Said M.L., Moulahoum S., Bounekhla M., Kabache N., Houassine H. Autonomous operation of a doubly fed induction generator driven by a wind turbine. *2015 20th International Conference on Methods and Models in Automation and Robotics (MMAR)*, 2015, pp. 1050-1055. doi: https://doi.org/10.1109/MMAR.2015.7284024.
29. Shutari H., Ibrahim T., Mohd Nor N.B., Saad N., Tajuddin M.F.N., Abdulrab H.Q.A. Development of a Novel Efficient Maximum Power Extraction Technique for Grid-Tied VSWT System. *IEEE Access*, 2022, vol. 10, pp. 101922-101935. doi: https://doi.org/10.1109/ACCESS.2022.3208583.
30. Hammoudi B.A., Serhoud H. The wind turbine's direct power control of the doubly-fed induction generator. *International Journal of Power Electronics and Drive Systems (IJPEDS)*, 2024, vol. 15, no. 2, pp. 1201-1210. doi: https://doi.org/10.11591/ijpeds.v15.i2.pp1201-1210.
31. Mahgoun M.S., Badoud A.E. New design and comparative study via two techniques for wind energy conversion system. *Electrical Engineering & Electromechanics*, 2021, no. 3, pp. 18-24. doi: https://doi.org/10.20998/2074-272X.2021.3.03.
32. Forchetti D., Garcia G., Valla M.I. Vector control strategy for a doubly-fed stand-alone induction generator. *IEEE 2002 28th Annual Conference of the Industrial Electronics Society. IECON 02*, 2002, vol. 2, pp. 991-995. doi: https://doi.org/10.1109/IECON.2002.1185407.
33. Mirecki A., Roboam X., Richardeau F. Architecture Complexity and Energy Efficiency of Small Wind Turbines. *IEEE Transactions on Industrial Electronics*, 2007, vol. 54, no. 1, pp. 660-670. doi: https://doi.org/10.1109/TIE.2006.885456.
34. Knight A.M., Peters G.E. Simple Wind Energy Controller for an Expanded Operating Range. *IEEE Transactions on Energy Conversion*, 2005, vol. 20, no. 2, pp. 459-466. doi: https://doi.org/10.1109/TEC.2005.847995.

Received 14.12.2024
Accepted 27.01.2025
Published 02.07.2025

M. L'Hadj Said[1], *Doctoral Student,*
M. Ali Moussa[1], *Associate Professor,*
T. Bessaad[1], *Associate Professor,*
Laboratory LGEER, Department of Electrotechnic,
University of Hassiba BenBouali, Chlef, Algeria,
e-mail: m.lhadjsaid@univ-chlef.dz (Corresponding Author);
m.alimoussa@univ-chlef.dz; t.bessaad@univ-chlef.dz

How to cite this article:
L'Hadj Said M., Ali Moussa M., Bessaad T. Control of an autonomous wind energy conversion system based on doubly fed induction generator supplying a non-linear load. *Electrical Engineering & Electromechanics*, 2025, no. 4, pp. 3-10. doi: https://doi.org/10.20998/2074-272X.2025.4.01

UDC 621.3.013 https://doi.org/10.20998/2074-272X.2025.4.02

V.Yu. Rozov, D.Ye. Pelevin, S.Yu. Reutskiy, K.D. Kundius, A.O. Vorushylo

The complex influence of external and internal electricity networks on the magnetic field level in residential premises of buildings

*The **problem** of determining the complex influence of a group of electricity networks (external electricity networks, built-in transformer substations, cable electric heating systems, etc.) on the magnitude of the summary magnetic field (MF) in a residential premise of a building has not been sufficiently researched. This results in an overestimation of the assess the magnitude of the summary MF, generated by the group of electricity networks, as well as to the use of technical measures to reduce this MF, which have excessive efficiency and are accompanied by excessive expenses. The **goal** of the work is to investigate of the complex influence of external and internal electricity networks on the MF level in residential premises of buildings and definition of conditions, which provide the minimum necessary limitations on the MF flux density of individual electricity networks, at which the summary level of MF in residential premises, does not exceed the normative level of 0.5 μT. The **methodology** of determining the complex influence of the group of electricity networks on the level of MF in residential premises is based on the Biot-Savart's law and the principle of superposition and allows determining the functional dependence between the instantaneous values of currents in electricity networks, their geometrical and physical parameters, and the summary effective value of MF flux density in the premise. **Scientific novelty**. For the first time, the methodology for determining the complex influence of the group of external and internal electricity networks on the level of MF in residential premises is proposed. **Practical significance.** The implementation of the proposed methodology will allow to reduce the calculated coefficient of normalization of the MF of individual electricity networks by 25–50 %, which, in turn, will contribute to the reduction of economic costs for engineering means of normalizing the summary MF in residential premises, caused by the influence of the group of electricity networks.* References 56, tables 4, figures 8.
Key words: **magnetic field of a group of electricity networks, residential premises, high-voltage overhead power line, built-in transformer substations, cable electric heating system of the floors**.

***Проблема** визначення комплексного впливу групи електромереж (зовнішніх електромереж, вбудованих трансформаторних підстанцій, систем кабельного електрообігріву тощо) на величину сумарного магнітного поля (МП) в житловому приміщенні будинку не достатньо досліджена. Це призводить до завищеної оцінки величини сумарного МП, що створюється группою електромереж, а також до застосування технічних заходів зі зменшення цього МП, які мають надмірну ефективність і супроводжуються зайвими витратами. **Метою** роботи є дослідження комплексного впливу зовнішніх та внутрішніх електромереж на рівень МП в житлових приміщеннях будинків, та визначення умов, які забезпечують мінімально необхідні обмеження індукції МП окремих електромереж, за яких сумарний рівень МП в житлових приміщеннях не перевищує нормативний рівень 0,5 мкТл. **Методика** визначення комплексного впливу групи електромереж на рівень МП в житлових приміщеннях базується на законі Біо-Савара та принципі суперпозиції і дозволяє визначити функціональну залежність між миттєвими значеннями струмів в електромережах, їх геометричними і фізичними параметрами, та сумарним діючим значенням індукції МП в приміщенні. **Наукова новизна**. Вперше запропоновано методологію визначення комплексного впливу групи зовнішніх і внутрішніх електромереж на рівень МП в житлових приміщеннях. **Практична значимість**. Впровадження запропонованої методології дозволить зменшити розрахунковий коефіцієнт нормалізації МП окремих електромереж на 25–50 %, що, у свою чергу, сприятиме зменшенню економічних витрат на інженерні засоби нормалізації сумарного МП у житлових приміщеннях, зумовленого впливом групи електромереж.* Бібл. 56, табл. 4, рис. 8.
Ключові слова: **магнітне поле групи електромереж, житлові приміщення, високовольтні повітряні лінії електропередачі, вбудовані трансформаторні підстанції, кабельні системи електрообігріву підлог.**

Abbreviations

PL	power line	IPS	internal power supply system
TS	transformer substation	LVB	low-voltage busbar
CEHS	cable electric heating system	EN	electricity networks
MF	magnetic field		

Introduction. Reducing the MF of the industrial frequency of in residential buildings to a safe level is an important problem of protecting people's health from man-made electromagnetic impact [1–5]. The main sources of this impact are EN located near residential premises. As shown by the authors [6], unlike the electric field, the MF of EN penetrates through the walls in residential buildings with almost no attenuation.

In Ukraine, the maximum permissible level of power frequency MF flux density in residential premises is regulated by normative documents [7, 8]. According to them, the effective value of MF flux density should not exceed of 0.5 μT inside the premises and of 3 μT at a distance of 0.5 m from their walls. Therefore, when designing new or modernizing existing EN, technical measures are applied [9, 10], are aimed at limiting the MF flux density inside residential premises to the normative level of 0.5 μT. Now the measures are aimed at individually reducing the MF flux density of each EN to the normative level (0.5 μT).

The greatest impact on residential buildings according to MF is exerted by EN located closer than 100 m from them (Fig. 1). These high-voltage overhead PL of 0.4–330 kV [11], LVB of built-in TS of 6/(10)0.4 kV [12], CEHS of the floors [13], and IPS of residential premises [14, 15].

Many scientific researches have been devoted to the creation of effective methods for modeling, calculating and normalizing the MF of EN [10, 16–52]. However, still remains insufficiently researched the distribution of MF in residential premises of buildings under the condition of simultaneous the complex influence of several (n) different EN (Fig. 1).

Even if the influence of each of these EN will be limited by flux density $\widetilde{B}_{norm}$ = 0.5 μT (normalized), then with their complex influence, the summary MF flux density can significantly exceed the normative level of 0.5 μT. Since the level $\widetilde{B}_{\Sigma}$ depends on numerous parameters of the EN, its magnitude can vary within $\widetilde{B}_{\Sigma} \in \left(\widetilde{B}_{norm}(1 \ldots n)\right)$ and will approach the maximum boundary value $n\widetilde{B}_{norm}$.

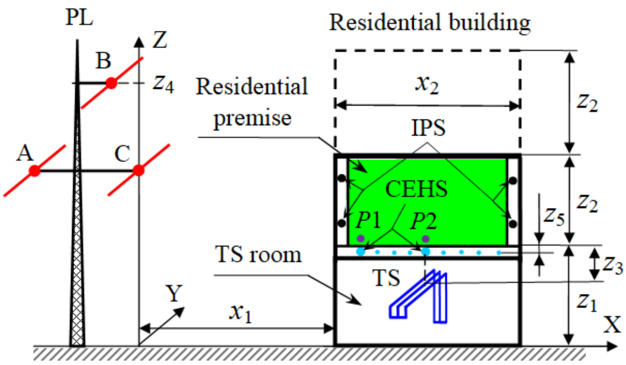

Fig. 1. The residential building with the built-in transformer substation (TS), which is an element of the electrical complex consisting of the external (PL) and internal (TS, CEHS, IPS) electricity networks

There is no possibility to determine the real level of the summary MF $\widetilde{B}_{\Sigma}$ forces us to take into account its maximum limit value $n\widetilde{B}_{norm}$. This leads to its excessive reduction ($\widetilde{B}_{\Sigma}$<0.5 μT), as well as to the unjustified increase in the cost of engineering means of the MF normalizing.

Therefore, it is relevant to study the complex influence of a group of EN at the MF level in residential premises in order to determine cost-effective limitation of the MF flux density for individual EN, at which the summary value of the MF in residential premises corresponds to the normative level $\widetilde{B}_{norm}$ = 0.5 μT.

The goal of the work is to investigate the complex influence of external and internal electricity networks on the MF level in residential premises of buildings and definition of conditions, which provide the minimum necessary limitations on the MF flux density of individual electricity networks, at which the summary level of MF in residential premises, does not exceed the normative level of 0.5 μT.

Assumptions adopted during the analysis.

1) The effective value of the MF flux density and its spatial components are investigated.

2) The supply voltages of the EN are synchronized, have a frequency of 50 Hz, and cosφ = 1.

3) The current conductors of all EN are oriented parallel to the coordinate axes.

4) The currents in EN are sinusoidal, symmetrical, and modeled by current filaments with different directions of power transfer.

5) There are no ferromagnetic and electrically conductive elements and the additional sources of MF in the studied area.

6) The MF flux density of each of the n EN is independent on the MF of other EN and depends linearly on its current.

7) The PL MF is three-phase two-dimensional, the TS MF is three-phase three-dimensional and is modeled by its LVB, the CEHS MF characterized by the vertical z component and is modeled by straight sections of two-wire heating cables, powered by a voltage of 220 V.

8) The IPS is powered by a voltage of 220 V, modeled by standard two-wire cables with a current of up to 30 A, which are mounted in the walls of a residential premises.

The adopted assumptions do not introduce a significant error in the analysis and allow us to take into account the worst cases when the impact of EN on magnetic field of premise is maximized.

Determination of the complex influence of the EN group. The complex influence of n different EN (PL, TS, CEHS, IPS) on the MF flux density distribution in a residential premise can be determined by summing the instantaneous values of spatial components $b_x(t)$, $b_y(t)$, $b_z(t)$ of MF flux density of each of these EN according to relations:

$$b_{\Sigma i,\lambda,x}(P,t)=\sum_{i=1}^{n}\beta^i b_{\lambda,x}(P,t); \quad (1)$$

$$b_{\Sigma i,\lambda,y}(P,t)=\sum_{i=1}^{n}\beta^i b_{\lambda,y}(P,t); \quad (2)$$

$$b_{\Sigma i,\lambda,z}(P,t)=\sum_{i=1}^{n}\beta^i b_{\lambda,z}(P,t). \quad (3)$$

In this case, the parameters of the studied EN are determined by the relations:

$$\beta^i \in (-1,+1),\ \omega = 2pf,\ f = 50\ \text{Hz}; \quad (4)$$

$$\lambda = A,B,C;\ i = 1 \equiv \text{PL},\ i = 2 \equiv \text{TS},\ i = 3 \equiv \text{CEHS}, \quad (5)$$

$$A^i \sim \sin(\omega t - \varphi_i), \quad (6)$$

$$B^i \sim \sin(\omega t + 2\pi/3 - \varphi_i), \quad (7)$$

$$C^i \sim \sin(\omega t - 2\pi/3 - \varphi_i), \quad (8)$$

where A, B, C are the phases of EN; i, n are the number and quantity of EN; β^i is the current direction coefficient; φ_i is the current shift angle respectively to voltage; x, y, z are the coordinate axes; P is the observation point.

We also take into account additional conditions caused by the above assumptions:

$$\varphi_{PL} = 0;\ \varphi_{TS} = 0;\ \varphi_{CEHS} = p/6, \quad (9)$$

$$b_{PL\ y}(P) = b_{CEHS\ x}(P) = b_{CEHS\ y}(P) = 0. \quad (10)$$

The magnitude of the influence of the EN group on the population through the MF is determined by calculating the effective value of the MF flux density, which is subject to sanitary regulation [7, 8] and physical measurements. The MF flux density effective values are defined as [17, 49]:

$$\widetilde{B}_i(P)=\sqrt{\frac{1}{T}\int_0^T [b_i(P,t)]^2 \,\mathrm{d}t}\ ,\ T=2\pi/\omega\,. \qquad (11)$$

Then, using (1–3) and (11), we get:

$$\widetilde{B}_{\sum i,\lambda,x}(P,t)=\sqrt{\frac{1}{T}\int_0^T \left(b_{\sum i,\lambda,x}(P,t)\right)^2 \mathrm{d}t}\ , \qquad (12)$$

$$\widetilde{B}_{\sum i,\lambda,y}(P,t)=\sqrt{\frac{1}{T}\int_0^T \left(b_{\sum i,\lambda,y}(P,t)\right)^2 \mathrm{d}t}\ , \qquad (13)$$

$$\widetilde{B}_{\sum i,\lambda,z}(P,t)=\sqrt{\frac{1}{T}\int_0^T \left(b_{\sum i,\lambda,z}(P,t)\right)^2 \mathrm{d}t}\ . \qquad (14)$$

The integration operation in the ratios (12–14) according to (11) can be carried out by numerical methods, based on specialized computer programs, or analytically.

The searched effective value of the MF flux density module for n the group of EN $\widetilde{B}_{\sum}(P)$ is defined as rms sum of effective values of the spatial components x, y, z of (12–14):

$$\widetilde{B}_{\sum}(P)=\sqrt{\left[\widetilde{B}_{\sum i,\lambda,x}(P)\right]^2+\left[\widetilde{B}_{\sum i,\lambda,y}(P)\right]^2+\left[\widetilde{B}_{\sum i,\lambda,z}(P)\right]^2}\ . \qquad (15)$$

In accordance with current normative [7, 8], effective value of the MF flux density $\widetilde{B}_{\sum}(P)$, given by (15), should not exceed the normative $\widetilde{B}_{norm}$ = 0.5 μT value inside the residential premise.

Research of the impact of individual EN. Based on the obtained relations of (1–15), we will determine the individual influence of the PL, TS, and CEHS on the MF level in a residential premise (Fig. 1). To do this, we will determine the instantaneous values of the spatial components x, y, z the MF flux density of the individual EN under consideration.

For overhead power line the instantaneous values of the spatial components, their MF flux density are determined according to the results obtained by the authors in [12, 22, 25] relations:

$$b_{A,x}(P)=\frac{\mu_0 I_A}{2\pi}\cdot\frac{z-z_A}{r_A^2}\sin(\omega t-\varphi), \qquad (16)$$

$$b_{A,z}(P)=\frac{\mu_0 I_A}{2\pi}\cdot\frac{x-x_A}{r_A^2}\sin(\omega t-\varphi), \qquad (17)$$

$$b_{B,x}(P)=\frac{\mu_0 I_B}{2\pi}\cdot\frac{z-z_B}{r_B^2}\sin\left(\omega t+\frac{2\pi}{3}-\varphi\right), \qquad (18)$$

$$b_{B,z}(P)=\frac{\mu_0 I_B}{2\pi}\cdot\frac{x-x_B}{r_B^2}\sin\left(\omega t+\frac{2\pi}{3}-\varphi\right), \qquad (19)$$

$$b_{C,x}(P)=\frac{\mu_0 I_C}{2\pi}\cdot\frac{z-z_C}{r_C^2}\sin\left(\omega t-\frac{2\pi}{3}-\varphi\right), \qquad (20)$$

$$b_{C,z}(P)=\frac{\mu_0 I_C}{2\pi}\cdot\frac{x-x_C}{r_C^2}\sin\left(\omega t-\frac{2\pi}{3}-\varphi\right), \qquad (21)$$

$$r_A^2=(x-x_A)^2+(z-z_A)^2\,,$$
$$r_B^2=(x-x_B)^2+(z-z_B)^2\,,$$
$$r_C^2=(x-x_C)^2+(z-z_C)^2\,. \qquad (22)$$

For the built-in TS, the instantaneous values of the spatial components are determined according to [13] based on the Biot-Savart's law and the superposition principle [53, 54]. They are obtained by summing the components of the MF flux density, which is created by each of the straight-line sections $L1$–$L5$ (Fig. 2) of LVB TS. For example, the components of the MF flux density for the A phase are defined as [13]:

$$b_{A,x}(P)=\sum_n^N b_{zx}\left(I_{A,z,n},x_{0,n},y_{0,n},z_{1,2,n}\right)\sin(\omega t+\varphi)+$$
$$+\sum_k^K b_{yx}\left(I_{A,x,k},x_{0,k},y_{1,2,k},z_{0,k}\right)\sin(\omega t+\varphi), \qquad (23)$$

$$b_{A,y}(P)=\sum_n^N b_{zy}\left(I_{A,z,n},x_{0,n},y_{0,n},z_{1,2,n}\right)\sin(\omega t+\varphi)+$$
$$+\sum_v^V b_{xy}\left(I_{A,x,v},x_{1,2,v},y_{0,v},z_{0,v}\right)\sin(\omega t+\varphi), \qquad (24)$$

$$b_{A,z}(P)=\sum_v^V b_{xz}\left(I_{C,x,v},x_{1,2,v},y_{0,v},z_{0,v}\right)\sin(\omega t+\varphi)+$$
$$+\sum_k^K b_{yz}\left(I_{C,y,k},x_{0,k},y_{1,2,k},z_{0,k}\right)\sin(\omega t+\varphi), \qquad (25)$$

where $I_{A,z,n}$, $x_{0,n}$, $y_{0,n}$, $z_{1,2,n}$ are the current and coordinates of the ends of the n-th straight-line section of the parallel Z-axis; $I_{A,y,k}$, $x_{0,k}$, $y_{1,2,k}$, $z_{0,k}$ are the current and coordinates of the ends of the k-th straight-line section of the parallel Y-axis; $I_{C,x,v}$, $x_{1,2,v}$, $y_{0,v}$, $z_{0,v}$ are the current and coordinates of the ends of the v-th straight-line section of the parallel X-axis; N, K, V are the number of straight-line sections parallel to the axis Z, Y, X respectively.

For the phases B and C of the busbar, the MF flux density components are determined similarly [13].

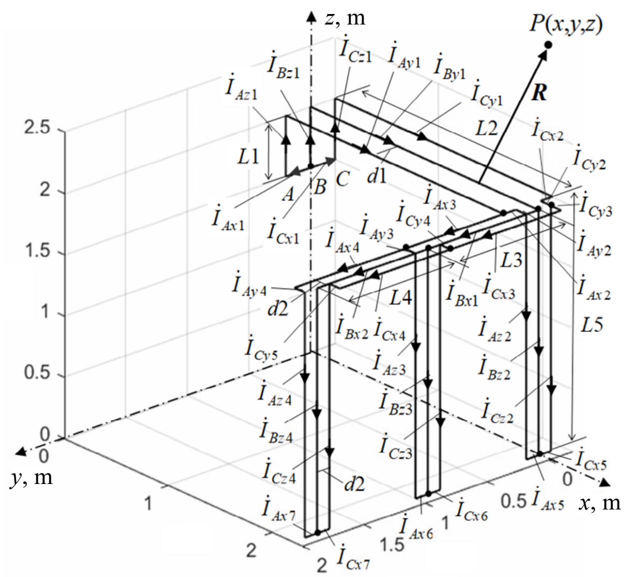

Fig. 2. The investigated low-voltage busbar TS 100 kVA 6(10)/0.4 kV

The cable electric heating system. In order to simplify the analysis and consider the worst case with maximum of the MF [10]. The CEHS is replaced by two straight sections of two-core heating cables (Fig. 1), laid under the floor of the premise, which are parallel to the *y*-axis: the first section is located at a distance of 0.5 m from the wall (point *P*1), and the *x* coordinate of the second segment axis (point *P*2) coincides with the *x* coordinate of the middle phase of the LVB TS (Fig. 2). If the CEHS is made of a two-wire heating cable with current I_{CEHS} then instantaneous maximum value of the CEHS MF flux density is determined by its spatial component *z* [12].

When powered from a single-phase EN of 220 V, this flux density will be:

$$b_{A,z}(r,P) = \frac{\mu_0}{2\pi} \frac{\sqrt{2} \cdot I_{\mathrm{CEHS}} \cdot d}{\left[r^2 + (0{,}5d)^2\right]} \sin(\omega t - \varphi), \quad (26)$$

where $\mu_0 = 4\pi \cdot 10^{-7}$ H/m; *d* is the distance between the axes of the cable cores; *r* is the distance from the cable axis to the observation point *P*, $\varphi = \pi/6$ is the phase shift between the linear current of phase A of the PL (TS) and the corresponding phase current of the CEHS.

The internal EN IPS has the current of up to 30 A and powered by one of the 220 V phase of the EN of building. The IPS is executed from standard two-wire cables laid in the walls with a distance between the cores of no more than 4 mm. At the same time, according to (26), the maximum value of the MF flux density generated by the cable at the current of 30 A at the distance of 0.5 m from the wall of the dwelling will not exceed of 0.1 μT. Therefore, in further analysis, the influence of IPS can be neglected due to the insignificant level of flux density of their MF.

Investigation on the complex influence of EN. The above analysis and obtained relations of (1–21) allow us to investigate the distribution of the effective value of the MF of PL, TS, CEHS in residential premise (Fig. 1). When studying, the complex influence of MF from the group of *n* EN, the most likely is the occurrence of this influence from the pair PL+CEHS EN. Less likely is the influence of the combination TS+PL or TS+CEHS, as well as from three EN PL+TS+CEHS. However, from the point of view of ensuring the safety of the population's health, it is expedient to study all the mentioned variants of complex influence.

Parameters of the investigated EN. As an external EN, we consider the typical overhead of the 110 kV PL, 250 A with a triangular suspension of phase wires oriented parallel to the *y*-axis (Fig. 1). The wires coordinates are: A (–6.3 m; 7 m), B (–2.1 m; 13 m), C (0 m; 7 m), $x1 = 20$ m.

We consider the TS with the 100 kVA power as, an example of the built-in TS (Fig. 1), which is modeled by the LVB (Fig. 2) in accordance with [10]. The LVB parameters: $d1 = 0.16$ m, $d2 = 0.05$ m, $L1 = 0.5$ m, $L2 = 2.2$ m, $L3 = L4 = 0.9$ m, $L5 = 2$ m, the nominal current of $I = 150$ A, the currents of straight-line sections of the busbar ($L1 - L5$): $I1 = I2 = I$, $I3 = I \cdot 2/3$, $I4 = I5 = I/3$.

The CEHS is executed from standard two-wire heating cables oriented parallel to the *y*-axis with the distance between the wires 2.2 mm, has a nominal current of 10 A, $z5 = 0.05$ m, powered by the phase voltage of one of the phases (a, b, c) of the apartment EN of 220 V. The CEHS cables is represented as straight-line segments oriented parallel to the y-axis that according to [10] allows modeling the maximum CEHS MF in the place of laying the cable. The observation points *P*1, *P*2 (Fig. 1) are located between current conductors PL and busbar TS, CEHS. The residential building (Fig. 1) has the TS room located on the 1st floor, and the residential premise on the 2nd floor above the TS, $z1 = 3.5$ m, $z2 = 2.5$ m, $z3 = 2.5$ m, $z4 = 13$ m. When calculating the summary MF it is taken into account that the observation points *P*1, *P*2 (Fig. 1) are located between current conductor PL and busbars TS.

Complex influence investigate methodology. The investigation of the complex influence is carried out by the relations (1–26) applying computer modeling in the MATLAB software environment [55].

1. We set the initial values of the currents (I_{in}) of PL, TS, CEHS, at which each of these EN separately creates the MF in the premises (Fig. 3), flux density which is equal to the normative level of 0.5 μT:

$$\widetilde{B}_{PL} = \widetilde{B}_{TS} = \widetilde{B}_{\mathrm{CEHS}} = \widetilde{B}_{norm}. \quad (27)$$

At the same time, the control point for the PL is the closest point to it *P*1 (Fig. 1), and for the TS and CEHS this is a point *P*2 (Fig. 1), the x coordinate which coincides with the x coordinate middle phase of the busbar *L*2 of TS (Fig. 2). At these points the summary MF flux density will be maximum.

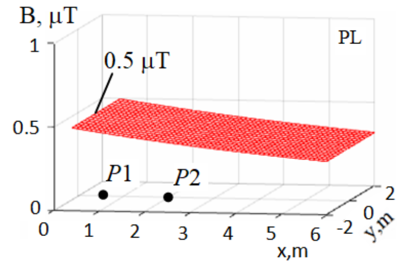

a

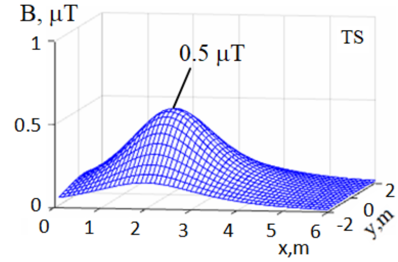

b

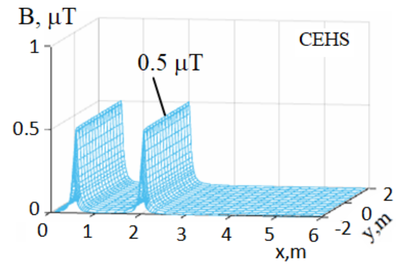

c

Fig. 3. Distribution of the MF flux density in the residential building under the individual influence of different EN, the flux density of which corresponds to the normative level (a – PL, b – TS, c – CEHS)

2. Calculate the summary MF $\widetilde{B}_{\Sigma}$, created by the PL, TS, CEHS when the condition (27) are fulfilled. The results obtained for different combinations of EN parameters are included in Table 1.

3. We reduce the current proportionally I_{in}, of each EN according to point 1 of the methodology to the level, when their summary value $\widetilde{B}_{\Sigma 1}$ decreases to the level $\widetilde{B}_{norm} = 0.5$ μT for each item in Table 1. At the same time, the MF flux density each of the EN $\widetilde{B}_{\Sigma norm}$ is the same in accordance with (27):

$$\widetilde{B}_{\Sigma norm} = \widetilde{B}_{PL} = \widetilde{B}_{TS} = \widetilde{B}_{CEHS}. \quad (28)$$

Next, we determine and enter into Table 1 the MF flux density value $\widetilde{B}_{\Sigma}$ subject to (27) and $\widetilde{B}_{\Sigma norm}$ each of the EN. Also we determine and fixate in Table 1 the values of the normalization coefficient K_m

$$K_m = \widetilde{B}_{\Sigma} / \widetilde{B}_{norm},\ K_m \in (1 \div n),\ \widetilde{B}_{\Sigma norm} = \widetilde{B}_{norm} / K_m. \quad (29)$$

It defines the necessary amount of reduction of the summary MF flux density $\widetilde{B}_{\Sigma}$ to achieve the normative level. Also we define the normalized summary MF flux density $\widetilde{B}_{\Sigma norm}$ of each of the EN, when reaching which their summary level is reduced to 0.5 μT.

4. Similar actions under p. 1–3 are carried out when studying the complex influence of two different EN in combination PL–TS, PL–CEHS, TS–CEHS. The calculation results are entered in Tables 2–4.

The most characteristic investigate results are presented in the form of graphs in Fig. 5–8.

Analysis of result. For the TS–PL pair (Table 2, Fig. 5) the maximum value $\widetilde{B}_{\Sigma}$ reaches 0.85 μT with opposite signs of currents EN and requires reduction of the MF flux density each of these sources to 1.7 times (from 0.5 μT to 0.29 μT), and the minimum value $\widetilde{B}_{\Sigma}$ is 0.7 μT occurs when the direction of the TS and PL. For the TS–CEHS pair (Table 3, Fig. 6) the maximum value $\widetilde{B}_{\Sigma}$ reaches 0.86 μT at supply of CEHS from phase +A (+B) and minimal (0.57 μT) at supply of CEHS from phase +C (–B). For the PL–CEHS pair (Table 4, Fig. 7) the maximum value $\widetilde{B}_{\Sigma}$ is 0.89 μT at supply of CEHS from phase +A (–A) and minimal (0.59 μT) at supply of CEHS from phase –C. Thus, for groups of two considered EN, the maximum value $\widetilde{B}_{\Sigma}$ is 0.89 μT, and minimal is 0.57 μT. At the same time, for the normalization of MF of these EN, the necessary normalization coefficient K_m will be from 1.06 to 1.96 units and at $n = 2$ approaches the limit values – 1 or 2 units.

For the group of TS, PL, CEHS (Table 1, Fig. 8) maximum value $\widetilde{B}_{\Sigma}$ is 1.32 μT and occurs with opposite currents of TS and PL and supply of CEHS from the –C phase, and the minimum value is 0.66 μT at the direction of the currents coincides of TS and PL and supply of CEHS from the +B phase. At the same time, for the normalization MF these three *(n* = 3) EN, the necessary normalization coefficient K_m consists of 1.32 to 2.64 units. Changing the order of phase alternation does not significantly affect the MF level.

Additional studies also show that changing the geometry of the 110 kV PL wire suspension from triangular (Fig. 1) to horizontal or vertical does not fundamentally affect the value $\widetilde{B}_{\Sigma}$.

For all groups of EN, the values and K_m significantly depend on the CEHS supply parameters (current sign and supply phase), which creates conditions for minimizing the MF value in the premise by the consumer.

The results of modeling using the developed methodology of (1–29) were confirmed by experimental tests (Fig. 4), carried out at the magnetic measuring stand Anatolii Pidhornyi Institute of Power Machines and Systems of NAS of Ukraine (IEMS of NAS of Ukraine) [56]. The deviation between the results of modeling and experiment did not exceed 10 %.

Thus, to normalize the complex influence of two normalized MF EN, it is necessary to reduce the MF flux density of each of them from 1.06 to 1.96 times, and for three normalized EN – reduction from 1.32 to 2.64 times. The implementation of the proposed methodology will reduce normalization coefficient K_m their MF from maximum values of 3 (2) units to minimum values of 1.32 (1.06) units, what provides reduction of this coefficient by 25–50 % and accordingly reduces economic losses on the MF normalization.

Peculiarities of normalization of the complex influence of the EN group on MF. To normalize the complex influence of the group of *n* already pre-normalized EN, the MF which does not exceed 0.5 μT, the use the above research methodology. For this, such well-known engineering methods of reducing the MF of EN can be introduced [9, 10]. They include: protection by distance, active and passive shielding, constructive-technological measures.

The choice of these methods is based of the technical and economic analysis.

Obviously, the smaller normalization coefficient K_m, the lower the economic costs of practical implementation of the normalization will be needed.

Therefore, the minimization of the K_m is the important task of MF normalization, which, first of all, it is advisable to implement by means of the proposed methodology based on the determination of all actual parameters of the group of EN given in Tables 1–4. Significant reduction K_m also possible through the implementation of an optimal power supply regime CEHS.

More difficult will be the normalization of the complex influence for the EN group, the each of which have not yet been normalized and have an excess of the MF above the normative level of 0.5 μT. In this case, the required initial normalization coefficient of the MF $K_{m,n,i} = \widetilde{B}_i / \widetilde{B}_{norm}$ for the each *i*-th EN is first determined. At the second stage, the final normalization coefficient $K_{m,i}$ is calculated:

$$K_{m,i} = K_{m,n,i} K_m. \quad (30)$$

a b

Fig. 4. Laboratory installation for the study of the complex effect of PL+TS, created on the magnetic measuring stand of the IEMS NAS of Ukraine (a – physical model of a low-voltage busbar of the TS, 150 A; b – physical model of the PL 150 A)

Table 1

The effective value of flux density of the summary MF TS+PL+CEHS $\tilde{B}_{\Sigma}$, value $\tilde{B}_{\Sigma norm}$ and coefficient K_m when changing the currents signs, the order of phase alternation (ABC–ACB) and the power supply phases of CEHS

№	TS β^n, ABC	PL β^n, ABC	CEHS β^n, phase	$\tilde{B}_{\Sigma}$ μT	$\tilde{B}_{\Sigma norm}$ μT	K_m
1	+	+	+, a	0.84	0.3	1.68
2	+	+	–, a	0.84	0.3	1.68
3	+	–	+, a	1.14	0.22	2.28
4	+	–	– , a	0.97	0.26	1.94
5	+	+	+ , b	0.66	0.38	1.32
6	+	+	– , b	0.69	0.36	1.38
7	+	–	+ , b	1.22	0.2	2.44
8	+	–	– , b	0.94	0.27	1.88
9	+	+	+ , c	0.93	0.27	1.86
10	+	+	– , c	0.79	0.32	1.58
11	+	–	+ , c	0.91	0.28	1.82
12	+	–	– , c	1.32	0.19	2.64
13	+	+	+ , a	1.09	0.23	2.18
14	+	+	–, a	0.91	0.28	1.82
15	+	–	+, a	1.12	0.22	2.24
16	+	–	– , a	0.79	0.32	1.58
17	+	+	+ , b	0.77	0.33	1.54
18	+	+	– , b	1.09	0.23	2.18
19	+	–	+ , b	0.87	0.29	1.74
20	+	–	– , b	0.87	0.29	1.74
21	+	+	+ , c	0.96	0.26	1.92
22	+	+	– , c	0.81	0.31	1.62
23	+	–	+ , c	0.74	0.34	1.48
24	+	–	– , c	1.11	0.23	2.22

Thus, proposed by the authors the methodology for determining the complex influence of the EN group on the level of MF in residential premises is based on (1–30) and includes analytical methods, calculation and assessment of the impact of external and internal EN (PL, TS, CEHS). It allows to identify and implement conditions for economically feasible limitation of the MF flux density of individual EN, at which the summary level of MF in residential premises does not exceed the normative level of 0.5 μT.

Table 2

The effective value of flux density of the summary MF TS+PL $\tilde{B}_{\Sigma}$, value $\tilde{B}_{\Sigma norm}$ and coefficient K_m at changing the order of phase alternation and current signs

№	TS β^n	PL β^n	$\tilde{B}_{\Sigma}$, μT	$\tilde{B}_{\Sigma norm}$ μT	K_m
1	+ ABC	+ ABC	0.53	0.47	1.06
2	+ ABC	–ABC	0.85	0.29	1.7
3	+ ABC	+ ACB	0.7	0.36	1.4
4	+ABC	– ACB	0.7	0.36	1.4

Table 3

The effective value of flux density of the summary MF TS+CEHS $\tilde{B}_{\Sigma}$, value $\tilde{B}_{\Sigma norm}$ and coefficient K_m at changing current sign and power supply phase CEHS

№	TS β^n, ABC	CEHS β^n, phase	$\tilde{B}_{\Sigma}$, μT	$\tilde{B}_{\Sigma norm}$ μT	K_m
1	+	+ , a	0.87	0.29	1.74
2	+	– , a	0.56	0.45	1.12
3	+	+ , b	0.86	0.29	1.72
4	+	– , b	0.57	0.44	1.14
5	+	+ , c	0.57	0.44	1.14
6	+	– , c	0.98	0.26	1.96

Table 4

The effective value of flux density of the summary MF PL+CEHS $\tilde{B}_{\Sigma}$, value $\tilde{B}_{\Sigma norm}$ and coefficient K_m at chan ging current sign and power supply phase CEHS

№	PL β^n, ABC	CEHS β^n, phase	$\tilde{B}_{\Sigma}$, μT	$\tilde{B}_{\Sigma norm}$ μT	K_m
1	+	+ , a	0.77	0.33	1.54
2	+	– , a	0.79	0.32	1.58
3	+	+ , b	0.64	0.39	1.28
4	+	– , b	0.9	0.28	1.8
5	+	+ . c	0.89	0.28	1.78
6	+	– , c	0.59	0.42	1.18

Taking into account the importance of the practical implementation of the proposed methodology to reduce the complex influence of external and internal EN on the MF level in residential premises of buildings, it is necessary to consider the draft amendments to the regulatory documents of the Ministry of Energy [7, 8, 22], and State Building Standards [15].

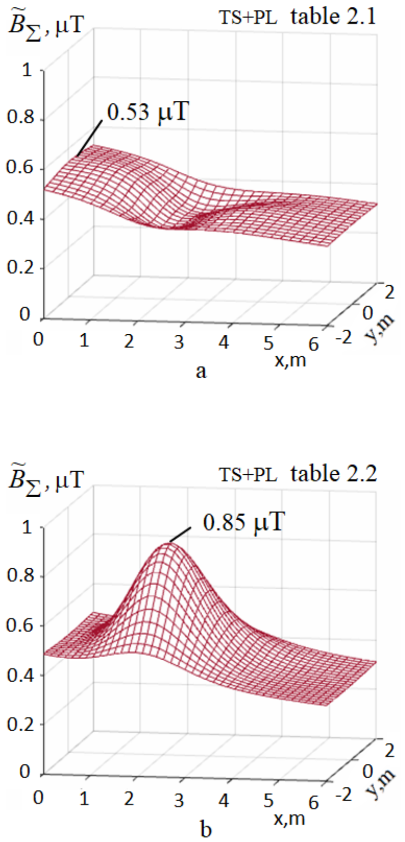

Fig. 5. Total minimum (a) and maximum (b) influences of the PL+TS to the level $\tilde{B}_\Sigma$

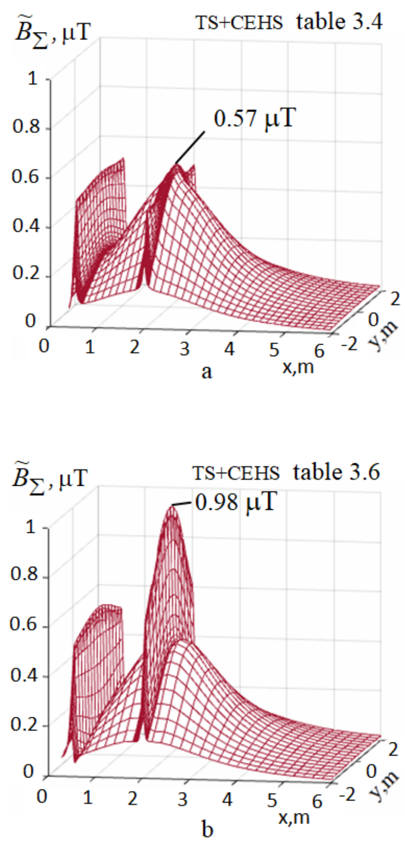

Fig. 6. Total minimum (a) and maximum (b) influences of the TS + CEHS to the level $\tilde{B}_\Sigma$

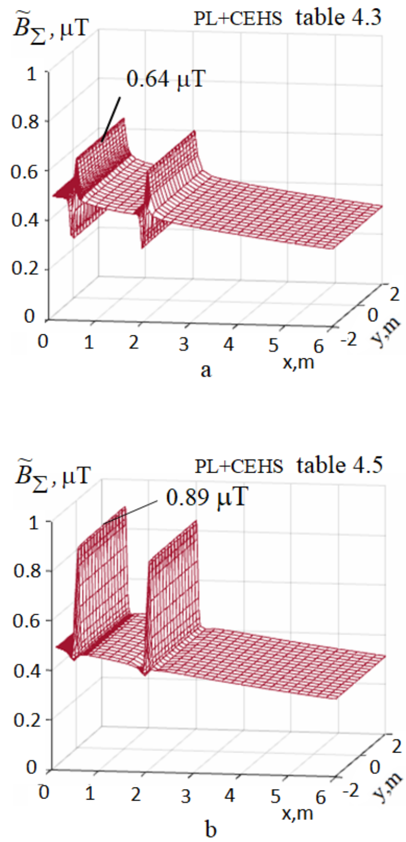

Fig. 7. Total minimum (a) and maximum (b) influences of the PL + CEHS to the level $\tilde{B}_\Sigma$

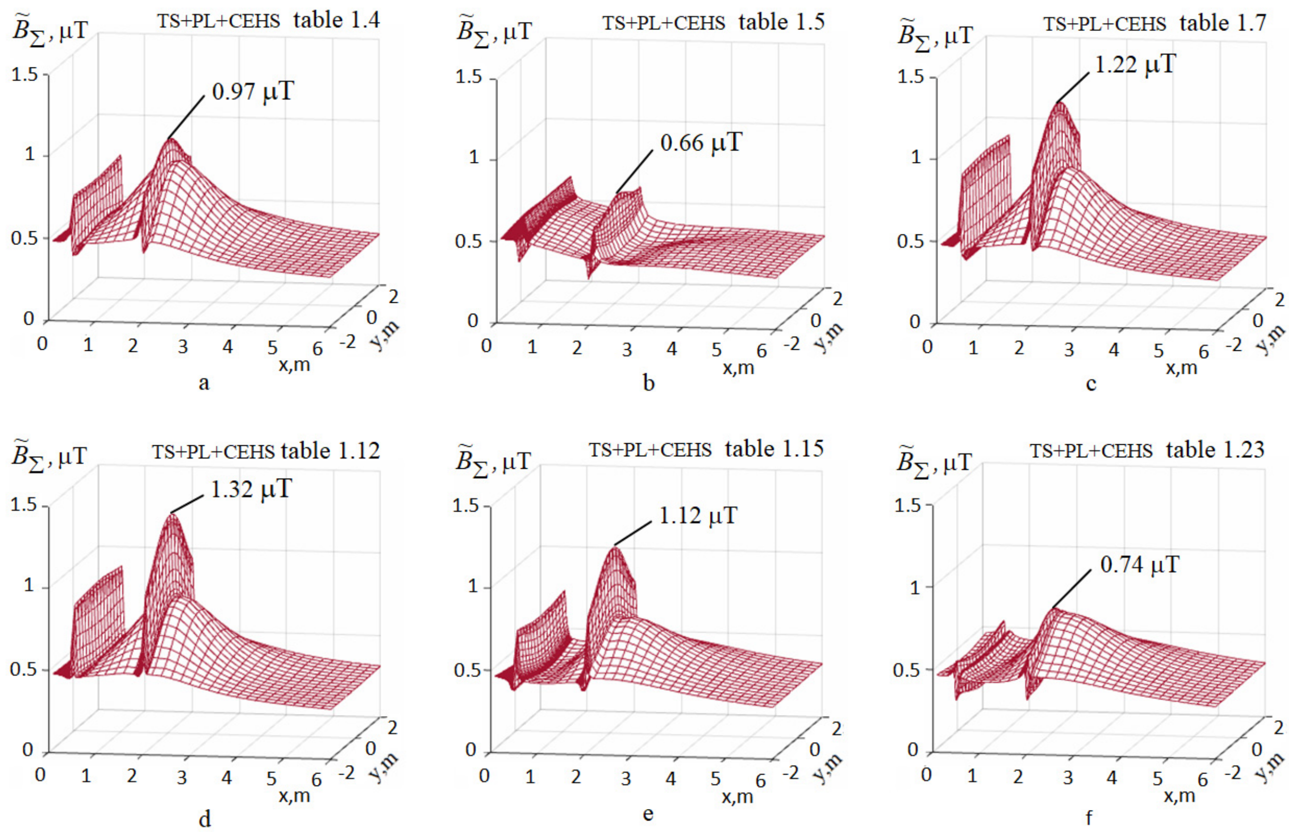

Fig. 8. Characteristic total influences of the PL + TS + CEHS on the level $\tilde{B}_\Sigma$

Conclusions.

1. Uncertainty of the processes of complex influence of the magnetic field of the group with n electricity networks on the level of the magnetic field in residential premises may lead to the usage of methods to reduce the induction of their magnetic field with overefficiency, and cause irrational economic losses.

2. The methodology for determining the complex influence of the group of electricity networks on the level of the magnetic field in residential premises is proposed. This approach is based on Biot-Savart's law and the principle of superposition. At the same time, the functional dependence between the instantaneous values of currents in electricity networks, their geometric and physical parameters, as well as the total effective value of the magnetic field flux density in the premise is taken into account. The technique makes it possible to establish the minimum necessary limits of the magnetic field flux density for individual electricity networks to normalize the summary magnetic field in the premise.

3. The method for normalizing the summary magnetic field is proposed, which is formed by the group of electricity networks in the residential premise, based on the above methodology. This method allows you to determine the actual level of the summary magnetic field in the premise and, on this basis, develop cost-effective measures to normalize the magnetic field in the premise.

4. It is theoretically substantiated and experimentally confirmed that the implementation of the proposed methodology for determining the complex influence of real electricity networks (overhead PL of 110 kV, built-in TS of 6/10 kV, cable electric heating system of 2.2 kW) allows reduction of the normalization coefficient K_m of magnetic field of individual electricity networks on 25 – 50 %, which allows to reduce the economic costs of normalizing the magnetic field in the premise accordingly.

5. Taking into account the importance of the practical implementation of the proposed methodology for cost-effective reduction of the impact of the group of electricity networks on the magnetic field level in residential premises to values that are safe for the population, it is planned to prepare draft amendments to the regulatory documents of the Ministry of Energy and the State Construction Standards.

Conflict of interest. The authors declare that they have no conflicts of interest.

REFERENCES

1. *Non-Ionizing Radiation, Part 1: Static and Extremely Low-Frequency (ELF) Electric and Magnetic Fields*. IARC Monographs on the Evaluation of Carcinogenic Risks to Humans, 2002, no. 80, p. 395.

2. Kheifets L., Ahlbom A., Crespi C.M., Draper G., Hagihara J., Lowenthal R.M., Mezei G., Oksuzyan S., Schьz J., Swanson J., Tittarelli A., Vinceti M., Wunsch Filho V. Pooled analysis of recent studies on magnetic fields and childhood leukaemia. *British Journal of Cancer*, 2010, vol. 103, no. 7, pp. 1128-1135. doi: https://doi.org/10.1038/sj.bjc.6605838.

3. *Standard of Building Biology Testing Methods: SBM−2015*. Germany: Institut fer Baubiologie + Ekologie IBN, 2015, 5 p. Available at: https://buildingbiology.com/site/downloads/SBM-2015-eng.zip (Accessed 07 April 2025).

4. Tognola G., Chiaramello E., Bonato M., Magne I., Souques M., Fiocchi S., Parazzini M., Ravazzani P. Cluster Analysis of Residential Personal Exposure to ELF Magnetic Field in Children: Effect of Environmental Variables. *International Journal of Environmental Research and Public Health*, 2019, vol. 16, no. 22, art. no. 4363. doi: https://doi.org/10.3390/ijerph16224363.

5. Malagoli C., Malavolti M., Wise L. A., et al. Residential exposure to magnetic fields from high-voltage power lines and risk of childhood leukemia. *Environmental Research*, 2023, vol. 232, art. no. 116320. doi: https://doi.org/10.1016/j.envres.2023.116320.

6. Rozov V.Yu., Grinchenko V.S., Pelevin D.Ye., Chunikhin K.V. Simulation of electromagnetic field in residential buildings located near overhead lines. *Technical Electrodynamics*, 2016, no. 3, pp. 6-8. (Rus). doi: https://doi.org/10.15407/techned2016.03.006.

7. *Electrical installation regulations*. Kharkiv, Fort Publ., 2017, 760 p. (Ukr).

8. *SOU-N MEV 40.1-37471933-49:2011 Design of cable lines up to 330 kV. Guideline (in the edition of the order of the Minenergvugillya dated Jan. 26, 2017 no. 82)*. Kyiv, Minenergvugillya Ukraine Publ., 2017. 168 p. (Ukr).

9. Rozov V.Yu., Reutskyi S.Yu., Pelevin D.Ye., Pyliugina O.Yu. The magnetic field of power transmission lines and the methods of its mitigation to a safe level. *Technical Electrodynamics*, 2013, no. 2, pp. 3-9. (Rus).

10. Rozov V. Y., Pelevin D. Y., Pielievina K. D. External magnetic field of urban transformer substations and methods of its normalization. *Electrical Engineering & Electromechanics*, 2017, no 5, pp. 60-66. doi: https://doi.org/10.20998/2074-272X.2017.5.10. (Rus).

11. Rozov V.Y., Reutskyi S.Y., Pelevin D.Y., Yakovenko V.N. The research of magnetic field of high-voltage AC transmissions lines. *Technical Electrodynamics*, 2012, no. 1, pp. 3-9. (Rus).

12. Pelevin D. Y. Calculation of the magnetic field of a low-voltage busbars of a built-in transformer substation. *Bulletin of the National Technical University "KhPI". Series: Energy: Reliability and Energy Efficiency*, 2024. no. 2(9). pp. 63-71. (Ukr). doi: https://doi.org/10.20998/EREE.2024.2(9).310498.

13. Rozov V.Y., Reutskiy S.Yu., Pelevin D.Y., Kundius K.D. Magnetic field of electrical heating cable systems of the floors for residential premises. *Electrical Engineering & Electromechanics*, 2024, no. 5, pp. 48-57. doi: https://doi.org/10.20998/2074-272X.2024.5.07.

14. Pelevin D.Y. Magnetic field of two-wire electric cables of residential premises. *Energy saving. Power engineering. Energy audit*, 2024. no. 7 (197). pp. 8-15. (Ukr). doi: https://doi.org/10.20998/2313-8890.2024.07.01.

15. *DBN V.2.5-23:2010 Engineering equipment of buildings and structures. Design of electrical equipment of civil facilities.* Kyiv Minrehionbud Ukrainy, 2010. 165 p. (Ukr). Available at: https://e-construction.gov.ua/laws_detail/3084989669637621022?doc_type=2 (Accessed 07 April 2025).

16. Moriyama K., Yoshitomi K. Apartment electrical wiring: a cause of ELF magnetic field exposure in residential areas. *Bioelectromagnetics*, 2005, vol. 26, no. 3, pp. 238-241 doi: https://doi.org/10.1002/bem.20099.

17. Balanis C.A. *Advanced Engineering Electromagnetics*. John Wiley & Sons, 1989. 985 p.

18. Thuroczy G., Janossy G., Nagy N., Bakos J., Szabo J., Mezei G. Exposure to 50 Hz magnetic field in apartment buildings with built-in transformer stations in Hungary. *Radiation Protection Dosimetry*, 2008, vol. 131, no. 4, pp. 469-473. doi: https://doi.org/10.1093/rpd/ncn199.

19. Moro F., Turri R. Accurate calculation of the right-of-way width for power line magnetic field impact assessment. *Progress in Electromagnetics Research B*, 2012, vol. 37, pp. 343-364. doi: https://doi.org/10.2528/PIERB11112206.

20. Okokon E.O., Roivainen P., Kheifets L., Mezei G., Juutilainen J. Indoor transformer stations and ELF magnetic field exposure: use of transformer structural characteristics to improve exposure assessment. *Journal of Exposure Science & Environmental Epidemiology*, 2014, vol. 4, no. 1, pp. 100-104. doi: https://doi.org/10.1038/jes.2013.54.

21. Barsali S., Giglioli R., Poli D. Active shielding of overhead line magnetic field: Design and applications. *Electric Power Systems Research*, 2014, vol. 110, pp. 55-63. doi: https://doi.org/10.1016/j.epsr.2014.01.005.

22. *SOU-N EE 20.179:2008 Calculation of electric and magnetic fields of power lines. Methodology (with changes) (in the edition of the order of the Minenergvugillya dated July 1, 2016, no. 423)*. Kyiv, Minenergvugillya Ukraine Publ., 2016. 37 p. (Ukr).

23. Grbic M., Canova A., Giaccone L. Magnetic field in an apartment located above 10/0.4 kV substation: levels and mitigation techniques. *CIRED – Open Access Proceedings Journal*, 2017, no. 1, pp. 752-756. doi: https://doi.org/10.1049/oap-cired.2017.1230.

24. Navarro-Camba E.A., Segura-Garcнa J., Gomez-Perretta C. Exposure to 50 Hz Magnetic Fields in Homes and Areas Surrounding Urban Transformer Stations in Silla (Spain): Environmental Impact Assessment. *Sustainability,* 2018, vol. 10, no. 8, art. no. 2641. doi: https://doi.org/10.3390/su10082641.

25. *Development of a verified methodology for calculating the magnetic field induction of three-phase power transmission lines (code Metod-M) report NDR/ State Institution "Institute Technical Problems Magnetism of the National Academy of Sciences of Ukraine", № DR 0113U001980*, Kharkiv, 2015. 105 p. (Ukr).

26. Medved D., Pavlik M., Zbojovsky J. Computer modeling of electromagnetic field around the 22 kV high voltage overhead lines. *2018 International IEEE Conference and Workshop in Óbuda on*

Electrical and Power Engineering (CANDO-EPE), 2018, pp. 289-294. doi: https://doi.org/10.1109/CANDO-EPE.2018.8601179.
27. Acosta J.S, Tavares M. C. Multi-objective optimization of overhead transmission lines including the phase sequence optimization. *International Journal of Electrical Power & Energy Systems*. 2020, vol. 115, art. no. 105495. doi: https://doi.org/10.1016/j.ijepes.2019.105495.
28. Krasnozhon A.V., Buinyi R.O., Dihtyaruk I.V., Kvytsynskyi A.O. The investigation of distribution of the magnetic flux density of operating two-circuit power line 110 kV «ChTPP-Chernihiv-330» in the residential area and methods of its decreasing to a safe level. *Electrical Engineering & Electromechanics*, 2020, no. 6, pp. 55-62. doi: https://doi.org/10.20998/2074-272X.2020.6.08.
29. Zhuang Y., Xu C., Song C., Chen A., Lee W., Huang Y., Zhou J. Improving Current Transformer-Based Energy Extraction From AC Power Lines by Manipulating Magnetic Field. *IEEE Transactions on Industrial Electronics*, 2020, vol. 67, no. 11, pp. 9471-9479. doi: https://doi.org/10.1109/TIE.2019.2952795.
30. Canova A., Giaccone L., Quercio M. A proposal for performance evaluation of low frequency shielding efficiency. *IET Conference Proceedings*, vol. 2021, no. 6, pp. 935-939. doi: https://doi.org/10.1049/icp.2021.1634.
31. Damatopoulou T., Angelopoulos S., Christodoulou C., Gonos I., Hristoforou E., Kladas A. On the Power Lines -Electromagnetic Shielding Using Magnetic Steel Laminates. *Energies*, 2021, vol. 14, no. 21, art. no. 7215. doi: https://doi.org/10.3390/en14217215.
32. Zeng X., Yang Z., Wu P., Cao L., Luo Y., Power Source Based on Electric Field Energy Harvesting for Monitoring Devices of High-Voltage Transmission Line. *IEEE Transactions on Industrial Electronics*, 2021, vol. 68, no. 8, pp. 7083-7092. doi: https://doi.org/10.1109/TIE.2020.3003551.
33. Hasan G.T., Mutlaq A.H., Ali K.J. The Influence of the Mixed Electric Line Poles on the Distribution of Magnetic Field. *Indonesian Journal of Electrical Engineering and Informatics*, 2022, vol. 10, no. 2, pp. 292-301. doi: https://doi.org/10.52549/ijeei.v10i2.3572.
34. Fikry A, Lim S.C., Ab Kadir M.Z.A. EMI radiation of power transmission lines in Malaysia. *F1000Research*, 2022, vol. 10, art. no. 1136. doi: https://doi.org/10.12688/f1000research.73067.2.
35. Rozov V.Y., Reutskyi S.Y., Pelevin D.Y., Kundius K.D. Approximate method for calculating the magnetic field of 330-750 kV high-voltage power line in maintenance area under voltage. *Electrical Engineering & Electromechanics*, 2022, no. 5. pp. 71-77. doi: https://doi.org/10.20998/2074-272X.2022.5.12.
36. Nikitina T.B., Bovdui I.V., Voloshko O.V., Kolomiets V.V., Kobilyanskiy B.B. Method of adjustment of three circuit system of active shielding of magnetic field in multi-storey buildings from overhead power lines with wires triangular arrangement. *Electrical Engineering & Electromechanics*, 2022, no. 1, pp. 21-28. doi: https://doi.org/10.20998/2074-272X.2022.1.03.
37. Rozov V.Y., Pelevin D.Y., Kundius K.D. Simulation of the magnetic field in residential buildings with built-in substations based on a two-phase multi-dipole model of a three-phase current conductor. *Electrical Engineering & Electromechanics*, 2023, no. 5, pp. 87-93. doi: https://doi.org/10.20998/2074-272X.2023.5.13.
38. Kuznetsov B.I., Nikitina T.B., Bovdui I.V., Voloshko O.V., Kolomiets V.V., Kobylianskyi B.B. Optimization ofspatial arrangement of magnetic field sensors of closed loop system ofoverhead power lines magnetic field active silencing. *Electrical Engineering & Electromechanics*, 2023, no. 4, pp. 26-34. doi: https://doi.org/10.20998/2074-272X.2023.4.04.
39. Quercio M., Barlassina L., Canova A. Characterization of the shielding properties of a power transformer enclosure. *IEEE EUROCON 2023 - 20th International Conference on Smart Technologies*, Torino, Italy, 2023, pp. 349-353. doi: https://doi.org/10.1109/EUROCON56442.2023.10198995.
40. Grbić M. Levels of electromagnetic fields in the vicinity of transmission power lines and facilities and mitigation techniques. *Tesla Innovation Days (2024, Belgrade) - Zbornik Radova*, 2024, pp. 46-49. doi: https://doi.org/10.5937/TID24046G.
41. Meng Q., Wang Z., Lin Q., Ju D., Liang X., Xian D. Theoretical Analysis of a Magnetic Shielding System Combining Active and Passive Modes. *Nanomaterials*, 2024, vol. 14, no. 6, art. no. 538. doi: https://doi.org/10.3390/nano14060538.
42. Kuznetsov B.I., Kutsenko A.S., Nikitina T.B., Bovdui I.V, Chunikhin K.V., Voloshko O.V. Reducing the Magnetic Field Level of Single-Circuit Overhead Power Lines in Multi-Storey Buildings by Means of Active and Passive Shielding. *Problems of the Regional Energetics*, 2024, no. 3(63), pp. 1-13. (Rus). doi: https://doi.org/10.52254/1857-0070.2024.3-63.01.
43. Kuznetsov B.I., Kutsenko A.S., Nikitina T.B., Bovdui I.V., Kolomiets V.V., Kobylianskyi B.B. Method for design of two-level system of active shielding of power frequency magnetic field based on a quasi-static model. *Electrical Engineering & Electromechanics*, 2024, no. 2, pp. 31-39. doi: https://doi.org/10.20998/2074-272X.2024.2.05.
44. Kuznetsov B., Nikitina T., Bovdui I., Voloshko O., Kolomiets V., Kobylianskyi B. Synthesis of the Spatial Arrangement of Magnetic Field Sensors for Active Magnetic Field Shielding Systems of Overhead Power Lines. *Problems of the Regional Energetics*, 2024, no. 1(61), pp. 1-16. (Rus). doi: https://doi.org/10.52254/1857-0070.2024.1-61.01.
45. Bendík J., Cenký M., Eleschová Ž. The Influence of Harmonic Content on the RMS Value of Electromagnetic Fields Emitted by Overhead Power Lines. *Modelling*, 2024, vol. 5, no. 4, pp. 1519-1531. doi: https://doi.org/10.3390/modelling5040079.
46. Ahsan M., Baharom M.N.R., Zainal Z., Khalil I.U. Measuring and simulation of magnetic field generated by high voltage overhead transmission lines. *Results in Engineering*, 2024, vol. 23, art. no. 102688, p. 14. doi: https://doi.org/10.1016/j.rineng.2024.102688.
47. Deprez K., Van de Steene T., Verloock L., Tanghe E., Gommé L., Verlaek M., Goethals M., van Campenhout K., Plets D., Joseph W. 50 Hz Temporal Magnetic Field Monitoring from High-Voltage Power Lines: Sensor Design and Experimental Validation. *Sensors*, 2024, vol. 24, no. 16, art. no. 5325. doi: https://doi.org/10.3390/s24165325.
48. Rozov V.Y., Reutskyi S.Y., Kundius K.D. Protection of workers against the magnetic field of 330-750 kV overhead power lines when performing work without removing the voltage under load. *Electrical Engineering & Electromechanics*, 2024, no. 4, pp. 70-78. doi: https://doi.org/10.20998/2074-272X.2024.4.09.
49. Grbic M., Canova A., Giaccone L., Pavlovic A., Grasso S. Mitigation of Low Frequency Magnetic Field Emitted by 10/0.4 kV Substation in the School. *International Journal of Numerical Modelling: Electronic Networks Devices and Fields*, 2025, vol. 38, no. 2, art. no. e70015. doi: https://doi.org/10.1002/jnm.70015.
50. Shcherba A.A., Podoltsev A.D., Kucheriava I.M. The reduction of magnetic field of underground cable line in essential areas by means of finite-length composite magnetic shields. *Technical Electrodynamics*, 2022, no. 1, pp. 17-24. (Ukr). doi: https://doi.org/10.15407/techned2022.01.017.
51. Bolyukh V.F. Electromechanical processes during the start of induction-type magnetic levitation. *Electrical Engineering & Electromechanics*, 2025, no. 3, pp. 3-10. doi: https://doi.org/10.20998/2074-272X.2025.3.01.
52. Bezprozvannych G.V., Grynyshyna M.V., Kyessayev A.G., Grechko O.M. Providing technical parameters of resistive cables of the heating floor system with preservation of thermal resistance of insulation. *Electrical Engineering & Electromechanics*, 2020, no. 3, pp. 43-47. doi: https://doi.org/10.20998/2074-272X.2020.3.07.
53. Nesterenko A.D. *Introduction to Theoretical Electrical Engineering*. Kyiv, Naukova Dumka Publ., 1969. 351 p. (Rus).
54. Shimoni K. *Theoretical Electrical Engineering (translation from German)*. Moscow, Mir Publ., 1964. 774 p. (Rus).
55. Lypez C.P. *MATLAB Optimization Techniques*. Apress Berkeley, CA, 2014. 292 p.
56. Baranov M.I., Rozov V.Yu., Sokol E.I. To the 100th anniversary of the National Academy of Sciences of Ukraine – the cradle of domestic science and technology. *Electrical Engineering & Electromechanics*, 2018, no. 5, pp. 3-11. (Ukr). doi: https://doi.org/10.20998/2074-272X.2018.5.01.

Received 23.11.2024
Accepted 25.01.2025
Published 02.07.2025

V.Yu. Rozov[1], *Doctor of Technical Science, Professor, Corresponding member of NAS of Ukraine,*
D.Ye. Pelevin[1], *PhD, Senior Research Scientist,*
S.Yu. Reutskiy[1], *PhD, Senior Research Scientist,*
K.D. Kundius[1], *PhD,*
A.O. Vorushylo[2], *PhD Student,*
[1] Anatolii Pidhornyi Institute of Power Machines and Systems of the National Academy of Sciences of Ukraine,
2/10, Komunalnykiv Str., Kharkiv, 61046, Ukraine,
e-mail: vyurozov@gmail.com;
pelevindmitro@ukr.net; sergiyreutskiy@gmail.com;
kundiuckateryna@ukr.net (Corresponding Author).
[2] General Energy Institute of NAS of Ukraine,
172, Antonovycha Str., Kyiv, 03150, Ukraine,
e-mail: Anton2320@gmail.com

How to cite this article:
Rozov V.Yu., Pelevin D.Ye., Reutskiy S.Yu., Kundius K.D., Vorushylo A.O. The complex influence of external and internal electricity networks on the magnetic field level in residential premises of buildings. *Electrical Engineering & Electromechanics*, 2025, no. 4, pp. 11-19. doi: https://doi.org/10.20998/2074-272X.2025.4.02

UDC 621.3 https://doi.org/10.20998/2074-272X.2025.4.03

D. Zehar, K. Behih, A. Cherif

Robust control of single input multi outputs systems

Introduction. *Most of mechanical systems are nonlinear and complex, the complexity of these latter lies on highly nonlinear characteristics, or on dynamics that stimulate the development or change of the process through an applied force in a disturbed environment. Single input multi outputs (SIMO) systems, which are structured into subsystems, are considered as complex systems. The task to control their degrees of freedom is more complicated, and it is not easily reachable, due to the fact that nonlinear laws are not directly applicable to those systems, which requires to trait them in a particular way.* ***Problem****. First order sliding mode control (FOSMC) has already been applied in several previous works to this kind of systems, and due to its robustness property, this control gave good results in term of stabilization and tracking, but the chattering phenomenon remains a big problem, which affects the control structure and the actuators.* ***Purpose.*** *In order to address the problem of chattering encountered when applying the FOSMC to a category of second order subsystems, a second order sliding mode control (SOSMC) is designed.* ***Methods.*** *This work consists of developing an appropriate second order system structure, which can go with the sliding control expansion, and then studying the SOSMC for this chosen system. The hierarchical structure of the sliding surface which is made using a linear combination between subsurfaces, according to the system structure, allows the only control input to affect subsystems in graded manner from the last one to the first one.* ***Results.*** *We have applied the constructed control law to a SIMO system for two cases with and without disturbances. Simulation results of the application have shown the effectiveness and the robustness of the designed controller*. References 30, figures 10.

Key words: **nonlinear system, single input multi outputs system, stability, robustness, sliding mode control.**

Вступ*. Більшість механічних систем нелінійні та складні, що полягає у значно нелінійних характеристиках або в динаміці, яка стимулює розвиток або зміну процесу за допомогою прикладеної сили у збудженому середовищі. Системи з одним входом та кількома виходами (SIMO), які структуровані у підсистеми, розглядаються як складні системи. Завдання управління їх ступенями свободи складніше, і воно складно досяжне через те, що нелінійні закони не застосовуються безпосередньо до цих систем, що вимагає характеризувати їх певним чином.* ***Проблема****. Управління ковзним режимом першого порядку (FOSMC) вже застосовувалося в кількох попередніх роботах до цього типу систем, і завдяки своїй надійності дане управління показало хороші результати з точки зору стабілізації та відстеження, але явище вібрації залишається великою проблемою, яка впливає на структуру управління та приводи.* ***Мета****. Для вирішення проблеми вібрації, що виникає при застосуванні FOSMC до категорії підсистем другого порядку, розроблено керування ковзним режимом другого порядку (SOSMC).* ***Методи****. Ця робота складається з розробки відповідної структури системи другого порядку, яка може йти з розширенням ковзного керування, а потім вивчення SOSMC для цієї обраної системи. Ієрархічна структура ковзної поверхні, яка зроблена з використанням лінійної комбінації між підповерхнями, відповідно до структури системи, дозволяє єдиному вхідному сигналу управління впливати на підсистеми градуйованим чином від останньої до першої.* ***Результати****. Застосовано побудований закон управління до системи SIMO для двох випадків із збудженням та без нього. Результати моделювання показали ефективність та надійність розробленого контролера.* Бібл. 30, рис. 10.

Ключові слова: **нелінійна система, система з одним входом та кількома виходами, стійкість, надійність, керування ковзним режимом.**

Introduction. The control of single input multi outputs (SIMO) systems has been constantly evolving for several years. The complexity of these systems (nonlinearity, single input of control and decomposition), makes the task of designing and developing a control more difficult, and performed more slowly.

A structured system with subsystems is nonlinear system, which has a minimum number of control inputs compared to what it needs. This property limits the application of conventional and classical theories of control, which has been established for nonlinear systems. The use of the control with variable structure, such as the sliding mode control (SMC), it has been adopted and applied to control SIMO systems, using their new structure, but unfortunately this control has the drawback of chattering.

Mainly, applications in robotics, automotive and automation are essential sources that motivate the analysis and control of this category of systems. Generally, researchers rely on benchmarks set up in laboratories, which are the subject of in-depth studies and a source of knowledge that makes it possible to develop more and more control techniques. For this raison this category of subsystems is of great importance.

Among the most effectiveness robust control, we find the SMC, this later has been widely applied for different type of systems linear, nonlinear, complex, uncertain systems, as in [1–5], it also has been applied for power converter as in [6, 7] and for photovoltaic systems as in [8]. Many works based on SMC has been developed for SIMO systems. A stable sliding mode controller has been designed in [9] for a class of second-order mechanical systems, an SMC of double-pendulum crane systems has been designed in [10]. More recently, sliding mode controller has been developed, as an effective strategy against uncertainties, in such important applications as self-balancing robots, mobile robots [11, 12] and submarines as in [13]. Using incremental SMC system method, in [14] was proposed a robust controller for a class of mechanical systems for the trajectory tracking. An adaptive multiple-surface sliding controller based on function approximation techniques for a nonlinear system with disturbances and mismatched uncertainties, has been proposed in [15].

An approach to design an SMC for a specific structured mechanical system in cascade form has been presented in [9]. In this approach, the system has been decoupled using a systematic approach to transform a class of mechanical systems into a subsystems form. In this work, we have adopted this approach to develop our controller. SMC achieves robust control by adding a discontinuous control signal across the sliding surface, satisfying the sliding condition. Nevertheless, this type of control has an essential disadvantage, which is the chattering phenomenon caused by the discontinuous control action. To treat these difficulties, several modifications to the original SMC law have been proposed, the most popular being the boundary layer approach [16]. The chattering phenomenon can have a detrimental effect on the actuators and manifests itself on the controlled quantities. This difficulty can be solved using the second order sliding mode control (SOSMC), several works have adopted this strategy of control as in [17, 18]. This technique consists of moving the discontinuity of the control law on the higher order derivatives of the sliding variable [19]. The conventional SMC technique implies that the control input appears after the first differentiation of the sliding manifold, in other words, the relative degree of the sliding manifold is equal to one. For nonlinear systems where the relative degree is greater than one, higher-order sliding mode methods have been developed, which have attracted considerable research interest in the last three decades [20]. SOSMC controller is a special case of higher order SMC which preserve the desirable properties, particularly invariance and order reduction but they achieve better accuracy and guarantee finite-time stabilization of relative degree two systems [21]. A number of different algorithms based on high order SMC, have been developed to achieve finite-time stability in a variety of system, but twisting (TA) and super-twisting algorithms (STA) are two of the best-known SOSMC methods [22].

To resolve the problem of chattering, encountered in SMC while applying it on SIMO systems, we have proposed to use the SOSMC, where we have used STA taking into account the sliding surfaces combination of subsystems.

Model development of the second order mechanical system. Mechanical systems are nonlinear, and have specific properties, which make the control more difficult, these properties come from several reasons, either the dynamics are not completely actuated which belong to SIMO systems (by conception in order to reduce the cost and the weight, and maybe for security reason when one of the controller fails), or the system is non affine in control. The variety and the complexity of those systems lead to classify them in several classes and study them case by case. In this work we focus on second order mechanical systems, which have the following Lagrangian [23, 24]:

$$L(q,\dot{q}) = K - V = \frac{1}{2}\dot{q}^T H(q)\dot{q} - V(q), \quad (1)$$

where $V(q)$, $K(q)$ are respectively the potential and kinetic energies; $q = (q_1, q_2)^T$ is the configuration vector; and $H = \begin{pmatrix} h_{11}(q_2) & h_{12}(q_2) \\ h_{21}(q_2) & h_{22}(q_2) \end{pmatrix}$ – is the inertia matrix.

From some mathematical development, using Euler-Lagrange equation, we can obtain the following matrix representation:

$$\begin{pmatrix} h_{11}(q_2) & h_{12}(q_2) \\ h_{21}(q_2) & h_{22}(q_2) \end{pmatrix}\begin{pmatrix} \ddot{q}_1 \\ \ddot{q}_2 \end{pmatrix} + \begin{pmatrix} G_1(q,\dot{q}) \\ G_2(q,\dot{q}) \end{pmatrix} = \begin{pmatrix} U \\ 0 \end{pmatrix}, \quad (2)$$

where $G_i (i = 1, 2)$ is the vector which represents centrifugal, Coriolis and gravity term, where:

$$G_1(q,\dot{q}) = \frac{dh_{11}(q_2)}{dq_2}\dot{q}_2\dot{q}_1 + \frac{dh_{12}(q_2)}{dq_2}\dot{q}_2^2 + b_1(q); \quad (3)$$

$$G_2(q,\dot{q}) = \frac{dh_{21}(q_2)}{dq_2}\dot{q}_1\dot{q}_2 + \frac{dh_{22}(q_2)}{dq_2}\dot{q}_2^2 + b_2(q), \quad (4)$$

where $b_1(q) = \frac{\partial V(q)}{\partial q_1}$ and $b_2(q) = \frac{\partial V(q)}{\partial q_2}$.

Thus, the system can be presented as the following state representation [19]:

$$\begin{cases} \dot{x}_1 = x_2; \\ \dot{x}_2 = f_1(x) + g_1(x)U + d(t); \\ \dot{x}_3 = x_4; \\ \dot{x}_4 = f_2(x) + g_2(x)U + d(t), \end{cases} \quad (5)$$

where $d(t)$ is the vector of extern disturbances; $f_1(x)$, $g_1(x)$, $f_2(x)$, $g_2(x)$ are the nonlinear functions.

We suppose that system in (5) is bounded input bounded output and all state variables signals are measurable.

First order sliding mode control procedure (FOSMC). SMC strategy is a very powerful nonlinear tool that has been widely employed by researchers [25, 26]. It has been also applied for nonlinear and complex mechanical systems.

In this work, we will apply this controller to the mechanical system presented in (5), the objective is to construct a control law which simultaneously leads errors e_1 and e_2 converge to zero, such that: $e_1 = x_1 - x_{1d}$, $e_3 = x_3 - x_{3d}$, x_{1d}, x_{3d} are desired values [9, 17].

The first sliding surface is chosen as:

$$s_1 = \sigma_1 e_1 + e_2. \quad (6)$$

The second sliding surface is chosen as:

$$s_2 = \sigma_2 e_3 + s_1. \quad (7)$$

The third and the last sliding surface is given by:

$$s_3 = \sigma_3 e_4 + s_2. \quad (8)$$

Lyapunov functions $V_1 - V_3$ are defined as:

$$V_1 = \frac{1}{2}s_1^2 = \frac{1}{2}\sigma_1^2 e_1^2 + \sigma_1 e_1 e_2 + \frac{1}{2}e_2^2, \quad (9)$$

for V_1 to be greater than 0, it must be $\sigma_1 e_1 e_2 > 0$.

$$V_2 = \frac{1}{2}s_2^2 = \frac{1}{2}\sigma_2^2 e_3^2 + \sigma_2 e_3 s_1 + \frac{1}{2}s_1^2, \quad (10)$$

for V_2 to be greater than 0, it must be $\sigma_2 e_3 s_1 > 0$, so we have:

$$\frac{1}{2}s_1^2 < \frac{1}{2}s_2^2 \Rightarrow 0 \le V_1 \le V_2;$$

$$V_3 = \frac{1}{2}s_3^2 = \frac{1}{2}\sigma_3^2 e_4^2 + \sigma_3 e_4 s_2 + \frac{1}{2}s_2^2, \quad (11)$$

for V_2 to be greater than 0, it must be $\sigma_3 e_4 s_2 > 0$, so:

$$\frac{1}{2}s_2^2 < \frac{1}{2}s_3^2 \Rightarrow 0 \le V_1 \le V_2 \le V_3.$$

where σ_i, $i = \{1, 2, 3\}$ are the positive constants chosen such that: $\sigma_1 e_1 e_2 > 0$, $\sigma_2 e_3 s_1 > 0$, $\sigma_3 e_4 s_2 > 0$.

From the derivative of (11) we can get the control law of the whole system as follows:

$$U = U_{eq} + U_{sw} - \\ - \frac{\sigma_1 x_2 + \sigma_2 x_4 + \sigma_3 f_2 + f_1 - \sigma_1 \dot{x}_{1d} - \ddot{x}_{1d}}{\sigma_3 g_2 + g_1} + \\ + \frac{\sigma_2 \dot{x}_{3d} + \sigma_3 \ddot{x}_{3d} - k\,\mathrm{sign}(s_3)}{\sigma_3 g_2 + g_1}, \quad (12)$$

where U_{eq} is the equivalent control; U_{sw} is the switching control; k is a positive constant.

Stability analysis for the FOSMC procedure. The Lyapunov expression is given by (11), we calculate its derivative as follows:

$$\dot{V}_3 = s_3\dot{s}_3 = s_3(\sigma_3\dot{e}_4 + \dot{s}_2); \quad (13)$$

$$\dot{V}_3 = s_3(\sigma_3 f_2 + \sigma_3 b_2 U + \sigma_2 x_4 + \sigma_1 x_2 + f_1 + b_1 U) - \\ - \sigma_2\dot{x}_{3d} - \sigma_1\dot{x}_{1d} - \ddot{x}_{1d} - \sigma_3\ddot{x}_{1d} + (\sigma_3 + 1)d. \quad (14)$$

Substituting the control law (12) in (14), we can get:

$$\dot{V}_3 = -k\,\mathrm{sign}(s_3). \quad (15)$$

So:

$$\dot{V}_3 \le 0. \quad (16)$$

From (16), we can conclude that the system is stable.

SOSMC procedure. A basic approach to avoid chattering problem is to augment the controlled system dynamics, by adding integrators at the input side, so as to obtain a higher-order system in which the actual control signal and its derivatives explicitly appear. If the discontinuous signal coincides with the highest derivative of the actual plant control, the latter results are continuous with a smoothness degree depending on the considered derivative order. This procedure refers to higher order SMC, as mentioned in [27].

Among the most algorithms which are used in SOSMC we find the TA and the STA. In this work we have chosen to use the STA, because of its simplicity and durability, and in this algorithm the convergence of state variables is faster and more precise, than other techniques. This method has been applied in several fields [28]. In the STA, the system trajectory rotates around the phase plan origin, approaching it in typical way (Fig. 1).

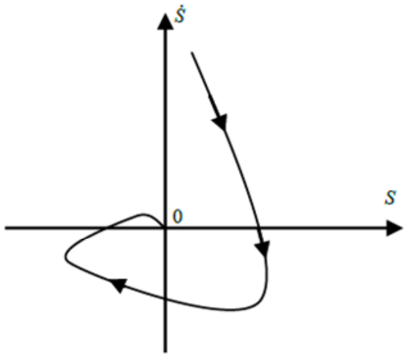

Fig. 1. Super twisting controller trajectory in the phase plane

The control objective is to establish a second order sliding regime with respect to s_3, such as: $s_3 = \dot{s}_3 = 0$. The continuous control law is composed of two terms, the first one is defined by a continuous function of the sliding variable and the second is defined by its discontinuous time derivative.

Since our system is of relative degree equal to 1 with respect to S, which means $\frac{\partial s}{\partial U} \neq 0$, then we have:

$$\dot{s} = \alpha(x,t) + \beta(x,t)U, \quad (18)$$

where α and β are the bounded functions:

$$\alpha(x,t) = f_1 + \sigma_1\dot{e}_1 - \ddot{x}_{1d} + \sigma_3 f_2 + \sigma_2\dot{e}_3 - \sigma_3\ddot{x}_{3d}; \quad (19)$$

$$\beta(x,t) = g + \sigma_3 g_2. \quad (20)$$

To state a rigorous control problem, (reach ability of the sliding surface and boundedness of $\ddot{s}$), the following conditions are assumed [29, 30]:

1) Control values are part of the set $\upsilon = \{U : |U| \le U_M\}$, where U_M > 1 is a real constant, moreover the solution of the system is well defined for all t, provided that $U(t)$ is continuous, and $\forall t, U(t) \in \upsilon$.

2) There exists $U_1(t) \in (0, 1)$, such that for any continuous function $U(t)$, $|U(t)| > U_1$, there is t_1, such that $s(t)U(t)>0$ for any $t > t_1$. However the control $U(t) = -U_M\,\mathrm{sign}(s(t_0))$, where t_0 is the initial value of time, allows to reach the variety $s = 0$ in finite time.

3) Let $\dot{s}(x,t,U)$, the derivative with respect to time of the sliding surface $s(x, t)$, there are positive constants $s_0, U_0 < 1, \Gamma_m; \Gamma_M$, such that if $|s(x,t)| < s_0$, so: $0 < \Gamma_m \le \frac{\partial}{\partial U}\dot{s}(x,t,U) \le \Gamma_M, \forall U \in \upsilon, x \in X$, and the inequality $|U| > U_0$ leads $sU > 0$.

4) There exists a positive constant ϕ such that in the region $|s(x,t)| < s_0$, the following inequality is satisfied:

$$\left| \frac{\partial}{\partial t}\dot{s}(x,t,U) + \frac{\partial}{\partial x}\dot{s}(x,t,U)\dot{x} \right| \le \phi.$$

The control law of our system is given by:

$$U = U_{eq} + U_{st}, \quad (21)$$

such that:

$$U_{eq} = \frac{-(\sigma_1 x_2 + \sigma_2 x_4 + \sigma_3 f_2 + f_1 - \sigma_1\dot{x}_{1d})}{\sigma_3 g_2 + g_1} - \\ - \frac{(\sigma_3\ddot{x}_{3d} - \ddot{x}_{1d} + \sigma_2\dot{x}_{3d})}{\sigma_3 g_2 + g_1}; \quad (22)$$

$$U_{st} = -c_1|s_3|^{\rho}\,\mathrm{sign}(s_3) - c_2 s_3 + \omega, \quad (23)$$

and

$$\dot{\omega} = -c_3\mathrm{sign}(\omega) - \varepsilon s_3, \quad (24)$$

where U_{eq} is the equivalent control; U_{st} is the super twisting control; $c_1 - c_3$ are the positive constants.

Stability analysis for STA. The Lyapunov function candidate is given by:

$$V = \frac{1}{2}s_3^2 + \frac{1}{2\varepsilon}\omega^2; \quad (25)$$

$$\dot{V} = s_3\dot{s}_3 + \frac{1}{\varepsilon}\omega\dot{\omega}; \quad (26)$$

$$\dot{V} = s_3\left(-c_1|s_3|^{\rho}\,\mathrm{sign}(s_3) - c_2 s_3 + \omega\right) + \\ + \frac{1}{\varepsilon}\omega(-c_3\mathrm{sign}(\omega) - \varepsilon s_3); \quad (27)$$

$$\dot{V} = -c_1|s_3|^{\rho+1} - c_2 s_3^2 - \frac{c_3}{\varepsilon}|\omega|, \quad (28)$$

such that $-1 < \rho < 0.5$ and $\varepsilon > 0$, therefore $\dot{V} \le 0$, which guarantees the stability of the system.

Simulation results. The studied controller is applied to a cart-pendulum system as presented in Fig. 2. The objective of the control is the stabilization of this system in its equilibrium points $(x, \theta) = (x, 0)$, which are the linear position of the cart and the upright position of the pendulum. The dynamical model of this system is given by (5) [19], where:

$$f_1(x)=\frac{-\sin\theta\left(mgl\cos\theta-ml^2\dot{\theta}^2\right)}{l\left(M+m\sin^2\theta\right)};$$

$$f_2(x)=\frac{\left((M+m)g-mgl\cos\theta\,\dot{\theta}^2\right)\sin\theta}{l\left(M+m\sin^2\theta\right)};$$

$$g_1(x)=\frac{l}{l\left(M+m\sin^2\theta\right)};$$

$$g_2(x)=\frac{-\cos\theta}{l\left(M+m\sin^2\theta\right)},$$

where M, m are respectively the masses of the cart and the pendulum; l is the length of the pendulum; U is the controller signal; y is the output vector.

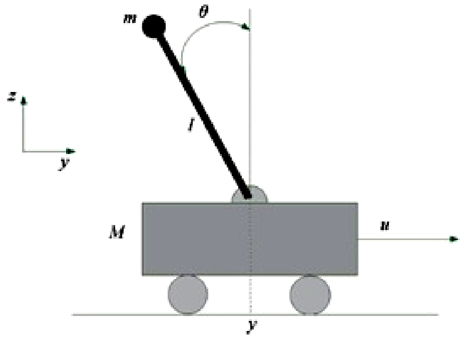

Fig. 2. The cart-pendulum system

Case 1 (without disturbances). Parameters of the system are: l = 0.25 m, M = 2 kg, m = 0.1 kg. The initial conditions of the system are:

$$(x,\dot{x})=(0.2{,}0),\ (\theta,\dot{\theta})=\left(-\frac{\pi}{6},0\right),$$

and the desired position is chosen as:

$$(x_d,\dot{x}_d)=(0{,}0)=(\theta_d,\dot{\theta}_d)=(0{,}0).$$

From the development, we refer x by x_1, and θ by x_3. From Fig. 3, 4 we can see that the system could follow the reference trajectory when using the two controllers – FOSMC and SOSMC. We can also see in Fig. 5 that the sliding surface is stable and converge to 0. Figure 6 shows the control signal; this latter is very smooth when using SOSMC, which presents the advantage of the second controller in reducing or even eliminating the chattering phenomenon.

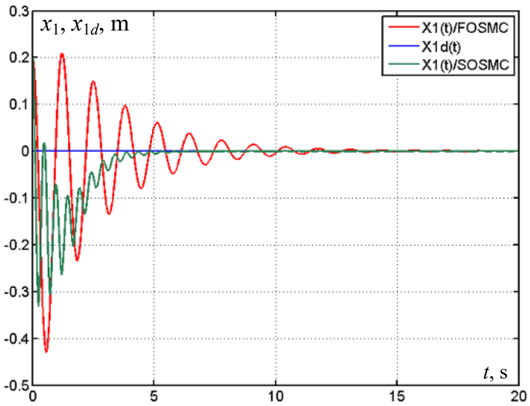

Fig. 3. The output $x_1(t)$ for case 1

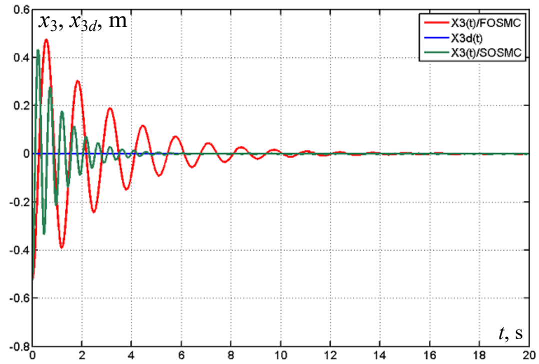

Fig. 4. The output $x_3(t)$ for case 1

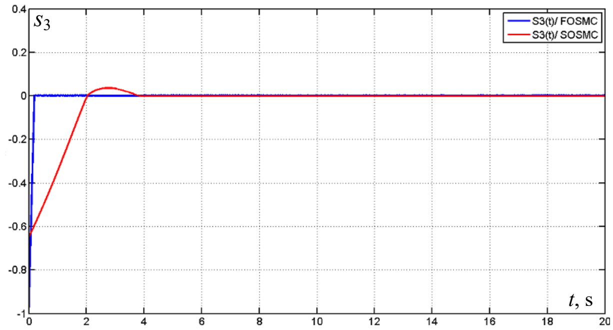

Fig. 5. The sliding surface $s_3(t)$ for case 1

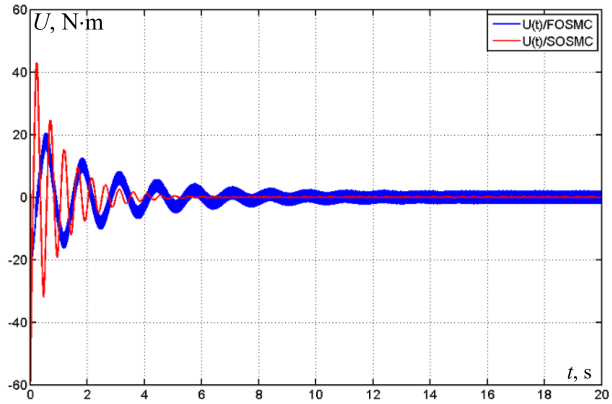

Fig. 6. The control signal $U(t)$ for case 1

Case 2 (with disturbances). In this section, we assume that the system undergoes structured external perturbation, and parameter uncertainties. The parameter uncertainty of the pendulum's mass is Δm = ±0.1 kg, and the perturbation is $d(t)$ = 0.05·randn(1, tf), where $d(t)$ is a Gaussian white noise function of 1 row and tf columns.

The initial conditions of the system are:

$$(x,\dot{x})=(0.1{,}0),\ (\theta,\dot{\theta})=\left(\frac{\pi}{8},0\right),$$

and the desired position is chosen as:

$$(x_d,\dot{x}_d)=(2{,}0)=(\theta_d,\dot{\theta}_d)=(0{,}0).$$

Figure 7 shows the sliding surface, so we can see that it is stable. Figure 8 shows the control signal, it is clear that using SOSMC this signal is smooth than using FOSMC. We see that despite the existence of disturbances and uncertainties, the system was able to follow its reference, but the response of the system is slower when using SOSMC, which is shown in Fig. 9, 10.

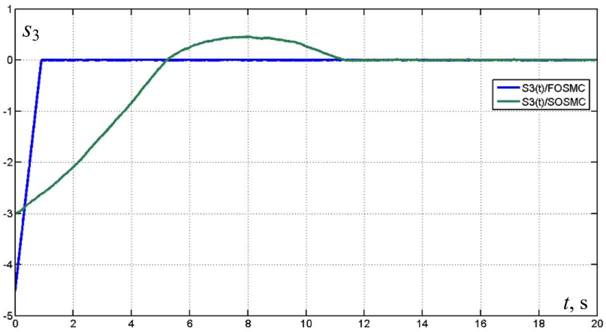

Fig. 7. The sliding surface $s_3(t)$ for case 2

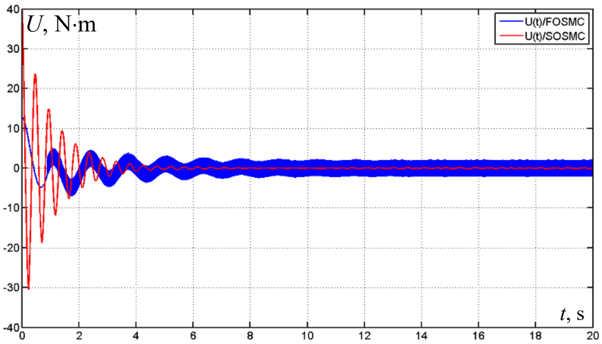

Fig. 8. The control signal $U(t)$ for case 2

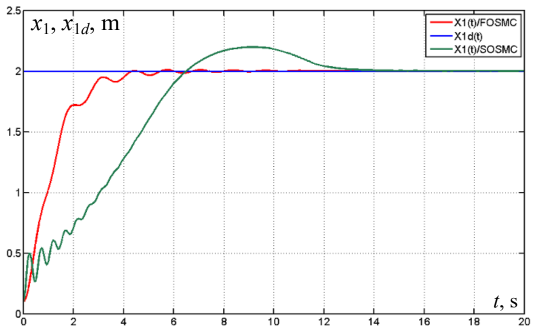

Fig. 9. The output $x_1(t)$ for case 2

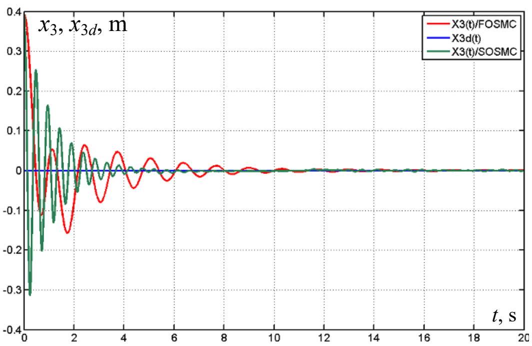

Fig. 10. The output $x_3(t)$ for case 2

Conclusions. In this paper, a SOSMC has been given to stabilize a category of second order SIMO systems which are structured into subsystems.

SOSMC is an extension of the first order SMC, and can preserve the robustness property of this latter. In this work, we had presented the mathematical development of the two controllers, and then we applied them to the system.

The proposed SOSMC controller is effective, it guarantees robustness with good performances, namely the stability and the good precision, which is shown in simulation results, and resolve the problem of chattering encountered in FOSMC that affects the actuators, by shifting the control law discontinuity, to the higher order derivatives of the sliding variable.

As perspectives, we can propose to enhance the performances of the system (such as the response time and the precision) by developing an integral SOSMC controller for this category of systems. Also, it will be more significant, if we resolve the problem considering unstructured uncertainties and perturbations.

Conflict of interest. The authors declare that they have no conflicts of interest.

REFERENCES

1. Krzysztofik I., Koruba Z. Sliding Mode Control for a Gyroscope System. *Problems of Mechatronics Armament Aviation Safety Engineering*, 2017, vol. 8, no. 4, pp. 47-60. doi: https://doi.org/10.5604/01.3001.0010.7317.

2. Prabhakar Rao B., Sunil K. G. Sliding mode controller design for spacecraft attitude stabilization. *International Journal of Advanced Engineering Sciences and Technologies*, 2011, vol. 11, no. 1, pp. 183-189.

3. Wang X., Hou B. Sliding mode control of a 2-DOF manipulator with random base vibration based on modified exponential reaching law. *Vibroengineering Procedia*, 2016, vol. 10, pp. 247-252.

4. Glaoui H., Harrouz A. Sliding mode control of the dfig used in wind energy system. *Electrical Engineering & Electromechanics*, 2018, no. 3, pp. 61-67. doi: https://doi.org/10.20998/2074-272X.2018.3.08.

5. Gulshan Z.A., Ali M.Z.H., Shah M.S., Nouman D., Anwar M., Ullah M.F. A robust control design approach for altitude control and trajectory tracking of a quadrotor. *Electrical Engineering & Electromechanics*, 2021, no. 5, pp. 17-23. doi: https://doi.org/10.20998/2074-272X.2021.5.03.

6. Hamdi R., Hadri Hamida A., Bennis O. On modeling and real-time simulation of a robust adaptive controller applied to a multicellular power converter. *Electrical Engineering & Electromechanics*, 2022, no. 6, pp. 48-52. doi: https://doi.org/10.20998/2074-272X.2022.6.08.

7. Oualah O., Kerdoun D., Boumassata A. Comparative study between sliding mode control and the vector control of a brushless doubly fed reluctance generator based on wind energy conversion systems. *Electrical Engineering & Electromechanics*, 2022, no. 1, pp. 51-58. doi: https://doi.org/10.20998/2074-272X.2022.1.07.

8. Nebti K., Lebied R. Fuzzy maximum power point tracking compared to sliding mode technique for photovoltaic systems based on DC-DC boost converter. *Electrical Engineering & Electromechanics*, 2021, no. 1, pp. 67-73. doi: https://doi.org/10.20998/2074-272X.2021.1.10.

9. Yinxing Hao, Jianqiang Yi, Dongbin Zhao, Dianwei Qian. Design of a new incremental sliding mode controller. *2008 7th World Congress on Intelligent Control and Automation*, 2008, pp. 3407-3412. doi: https://doi.org/10.1109/WCICA.2008.4593467.

10. Tuan L.A., Lee S.-G. Sliding mode controls of double-pendulum crane systems. *Journal of Mechanical Science and Technology*, 2013, vol. 27, no. 6, pp. 1863-1873. doi: https://doi.org/10.1007/s12206-013-0437-8.

11. Bessas A., Benalia A., Boudjema F. Integral Sliding Mode Control for Trajectory Tracking of Wheeled Mobile Robot in Presence of Uncertainties. *Journal of Control Science and Engineering*, 2016, vol. 2016, pp. 1-10. doi: https://doi.org/10.1155/2016/7915375.

12. Toujeni N., Mnasri C., Gasmi M. Repetitive Control based on Integral Sliding Mode Control of Matched Uncertain Systems. *International Journal of Advanced Computer Science and Applications*, 2018, vol. 9, no. 12, pp. 446-455 doi: https://doi.org/10.14569/IJACSA.2018.091263.

13. Zeghlache S., Saigaa D., Kara K., Harrag A., Bouguerra A. Fuzzy based sliding mode control strategy for an UAV type-

quadrotor. *The Mediterranean Journal of Measurement and Control*, 2012, vol. 8, no. 3, pp. 436-445.
14. Hong G.B., Nguyen H.T., Nguyen M.T., Le T.T.H., Nguyen V.D.H. Trajectory tracking for futura pendulum by incremental sliding mode control. *Robotica & Management*, 2019, vol. 24, no. 1, pp. 4-7.
15. Chen P.C., Huang A.C. Adaptive multiple-surface sliding control of hydraulic active suspension systems based on the function approximation technique. *Journal of Vibration and Control*, 2005, vol. 11, no. 5, pp. 685-706. doi: https://doi.org/10.1177/1077546305052788.
16. Benkahla M., Taleb R., Boudjema Z. A new robust control using adaptive fuzzy sliding mode control for a DFIG supplied by a 19-level inverter with less number of switches. *Electrical Engineering & Electromechanics*, 2018, no. 4, pp. 11-19. doi: https://doi.org/10.20998/2074-272X.2018.4.02.
17. Guezi A., Bendaikha A., Dendouga A. Direct torque control based on second order sliding mode controller for three-level inverter-fed permanent magnet synchronous motor: comparative study. *Electrical Engineering & Electromechanics*, 2022, no. 5, pp. 10-13. doi: https://doi.org/10.20998/2074-272X.2022.5.02.
18. Hinda A., Khiat M., Boudjema Z. Fuzzy second order sliding mode control of a unified power flow controller. *Electrical Engineering & Electromechanics*, 2019, no. 6, pp. 55-61. doi: https://doi.org/10.20998/2074-272X.2019.6.08.
19. Mishra S.K., Chandra D. Stabilization and tracking control of inverted pendulum using fractional order PID controllers. *Journal of Engineering*, 2014, vol. 2014, pp. 1-9. doi: https://doi.org/10.1155/2014/752918.
20. Shah M.S., Mahmood T., Ullah M.F. Power quality improvement using ultra capacitor based dynamic voltage restorer with real twisting sliding mode control. *Electrical Engineering & Electromechanics*, 2022, no. 1, pp. 59-63. doi: https://doi.org/10.20998/2074-272X.2022.1.08.
21. Parvat B.J., Ratnaparkhi S.D. A Second Order Sliding Mode Controller Applications in Industrial Process. *International Journal of Engineering Trends and Technology*, 2015, vol. 19, no. 4, pp. 217-222. doi: https://doi.org/10.14445/22315381/IJETT-V19P238.
22. Chawengkrittayanont P., Pukdeboon C., Kuntanapreeda S., Moore E.J. Smooth second-order sliding mode controller for multivariable mechanical systems. *SN Applied Sciences*, 2021, vol. 3, no. 10, art. no. 816. doi: https://doi.org/10.1007/s42452-021-04800-4.
23. Bloch A.M., Leonard N.E., Marsden J.E. Stabilization of mechanical systems using controlled Lagrangians. *Proceedings of the 36th IEEE Conference on Decision and Control*, 1997, vol. 3, pp. 2356-2361. doi: https://doi.org/10.1109/CDC.1997.657135.
24. Bullo F., Lewis A.D. *Geometric Control of Mechanical Systems. Modeling, Analysis, and Design for Simple Mechanical Control Systems*. Springer, New York, 2005. 727 p. doi: https://doi.org/10.1007/978-1-4899-7276-7.
25. Bouraghda S., Sebaa K., Bechouat M., Sedraoui M. An improved sliding mode control for reduction of harmonic currents in grid system connected with a wind turbine equipped by a doubly-fed induction generator. *Electrical Engineering & Electromechanics*, 2022, no. 2, pp. 47-55. doi: https://doi.org/10.20998/2074-272X.2022.2.08.
26. Chih-Min Lin, Yi-Jen Mon. Decoupling control by hierarchical fuzzy sliding-mode controller. *IEEE Transactions on Control Systems Technology*, 2005, vol. 13, no. 4, pp. 593-598. doi: https://doi.org/10.1109/TCST.2004.843130.
27. Behnamgol V., Vali A.R., Mohammadzaman I. Second order sliding mode control with finite time convergence. *AUT Journal of Modeling and Simulation*, 2013, vol. 45, no. 2, pp. 41-52. doi: https://doi.org/10.22060/miscj.2015.528.
28. Benbouhenni H., Lemdani S. Combining synergetic control and super twisting algorithm to reduce the active power undulations of doubly fed induction generator for dual-rotor wind turbine system. *Electrical Engineering & Electromechanics*, 2021, no. 3, pp. 8-17. doi: https://doi.org/10.20998/2074-272X.2021.3.02.
29. Bartolini G., Pisano A., Punta E., Usai E. A survey of applications of second-order sliding mode control to mechanical systems. *International Journal of Control*, 2003, vol. 76, no. 9–10, pp. 875-892. doi: https://doi.org/10.1080/0020717031000099010.
30. Karam E.H., Jadoo E.H. Design modified second order sliding mode controller based on st algorithm for blood glucose regulation systems. *Applied Computer Science*, 2020, vol. 16, no. 2, pp. 18-31. doi: https://doi.org/10.23743/acs-2020-10.

Received 16.12.2024
Accepted 07.02.2025
Published 02.07.2025

D. Zehar[1,2], *Doctor of Sciences, Lecturer,*
K. Behih[2,3], *PhD, Associate Professor,*
A. Cherif[1], *Doctor of Sciences, Professor,*
[1] MIER Laboratory, Department of Electromechanical Engineering, University Mohamed El Bachir El Ibrahimi of Bordj Bou Arreridj, Algeria,
e-mail: djamila.zehar@univ-bba.dz (Corresponding Author); aida.cherif@univ-bba.dz
[2] LSI Laboratory, Department of Electrical Engineering, Ferhat Abbas University of Setif 1, Setif, Algeria,
e-mail: khalissabehih@univ-setif.dz
[3] QUERE Laboratory, Department of Electrical Engineering, Ferhat Abbas University of Setif 1, Setif, Algeria

How to cite this article:
Zehar D., Behih K., Cherif A. Robust control of single input multi outputs systems. *Electrical Engineering & Electromechanics*, 2025, no. 4, pp. 20-25. doi: https://doi.org/10.20998/2074-272X.2025.4.03

UDC 621.319 https://doi.org/10.20998/2074-272X.2025.4.04

M. Benboukous, H. Bahri, M. Talea, M. Bour, K. Abdouni

Comparative analysis of principal modulation techniques for modular multilevel converter and a modified reduced switching frequency algorithm for nearest level pulse width modulation

Introduction. *The Modular Multilevel Converter (MMC) is an advanced topology widely used in medium and high-power applications, offering significant advantages over other multilevel converters, including high efficiency and superior output waveform quality.* ***Problem.*** *The modulation techniques and submodule capacitor voltage balancing significantly affect the performance of the MMC, influencing output voltage and current quality, capacitor voltage balancing, and power losses.* ***Goal.*** *This study presents a comparative analysis of 3 modulation techniques for a 3-phase MMC: Level-Shifted Pulse Width Modulation (LS-PWM), Nearest Level Control (NLC), and hybrid Nearest Level Pulse Width Modulation (NL-PWM). In addition, this study proposes a modification to the Reduced Switching Frequency (RSF) capacitor voltage balancing algorithm to adapt it for use with the NL-PWM technique.* ***Methodology.*** *The performance of each modulation technique is evaluated through simulations using MATLAB/Simulink software, in terms of output signal quality, capacitor voltage balancing, converter losses, and behavior under a line-to-ground fault.* ***Results.*** *The results show that both LS-PWM and NL-PWM generate lower harmonic content compared to NLC. However, the NLC technique presents the lowest switching losses, followed by NL-PWM and LS-PWM. The NL-PWM technique shows intermediate performance, making it more appropriate for medium-voltage applications. The results also confirm the proposed modifications to the RSF capacitor voltage balancing algorithm. Additionally, the LS-PWM technique shows greater robustness under fault conditions compared to the other techniques.* ***Originality****. For the first time, a comparative analysis of 3 modulation techniques for the MMC, LS-PWM, NLC, and NL-PWM has been conducted, highlighting their performance under different operating conditions. The study also proposes a modified RSF capacitor voltage balancing algorithm specifically for NL-PWM, which has not been previously explored in the literature.* ***Practical value.*** *The results of this study contribute to the selection of the most suitable modulation technique for MMC for specific applications.* References 34, table 5, figures 17.

Key words: **modular multilevel converter, level-shifted pulse width modulation, nearest level control, nearest level pulse width modulation, capacitor voltage balancing, reduced switching frequency.**

Вступ*. Модульний багаторівневий перетворювач (ММС) – це вдосконалена топологія, що широко використовується в системах середньої та високої потужності, пропонуючи значні переваги над іншими багаторівневими перетворювачами, включаючи високу ефективність та якість вихідної форми сигналу.* ***Проблема****. Методи модуляції та балансування напруги на конденсаторах підмодулів суттєво впливають на продуктивність ММС, впливаючи на якість вихідної напруги та струму, балансування напруги на конденсаторах та втрати потужності.* ***Мета****. Це дослідження представляє порівняльний аналіз трьох методів модуляції для трифазного ММС: імпульсна широтна модуляція зі зсувом рівнів (LS-PWM), керування найближчим рівнем (NLC) та гібридна імпульсна широтна модуляція найближчим рівнем (NL-PWM). Крім того, це дослідження пропонує модифікацію алгоритму балансування напруги на конденсаторах зі зниженою частотою перемикання (RSF) для адаптації його для використання з методом NL-PWM.* ***Методологія****. Продуктивність кожного методу модуляції оцінюється за допомогою моделювання з використанням програмного забезпечення MATLAB/Simulink з точки зору якості вихідного сигналу, балансування напруги на конденсаторах, втрат перетворювача та поведінки при замиканні між лінією та землею.* ***Результати*** *показують, що як LS-PWM, так і NL-PWM генерують нижчий вміст гармонік порівняно з NLC. Однак, метод NLC має найнижчі втрати на перемикання, за ним йдуть NL-PWM та LS-PWM. Метод NL-PWM демонструє проміжні характеристики, що робить його більш придатним для застосувань середньої напруги. Результати також підтверджують запропоновані модифікації алгоритму балансування напруги конденсаторів RSF. Крім того, метод LS-PWM демонструє більшу стійкість в умовах несправності порівняно з іншими методами.* ***Оригінальність****. Вперше було проведено порівняльний аналіз трьох методів модуляції для ММС, LS-PWM, NLC та NL-PWM, що підкреслює їхню ефективність за різних умов експлуатації. У дослідженні також пропонується модифікований алгоритм балансування напруги конденсаторів RSF спеціально для NL-PWM, який раніше не досліджувався в літературі.* ***Практична значимість****. Результати цього дослідження сприяють вибору найбільш підходящого методу модуляції для ММС для конкретних застосувань.* Бібл. 34, табл. 5, рис. 17.

Ключові слова: **модульний багаторівневий перетворювач, широтно-імпульсна модуляція зі зміщенням рівня, керування найближчим рівнем, широтно-імпульсна модуляція найближчим рівнем, балансування напруги конденсатора, знижена частота комутації.**

Introduction. The modular multilevel converter (MMC), initially proposed in the early 2000s by Lesnicar and Marquardt, has become a widely adopted solution for high-power and high-voltage applications, owing to its features, including modularity, scalability, high efficiency, capacitor-less DC link, and transformer-less operation [1, 2]. The MMC is capable of generating high-quality voltages at elevated levels with low-rated power devices and with reduced energy losses [3, 4]. The MMC is currently employed in various projects, including HVDC electric power transmission system [5], wind energy systems [6], photovoltaic energy systems [7], energy storage systems [8], and static compensators (STATCOM) for reactive power [9].

The MMC necessitates a complex control structure to ensure optimal performance across of control dynamics, circulating current, capacitor voltage, harmonic content, and energy losses. In recent years, the MMC has engendered substantial interest among academic researchers, resulting in numerous research publications focusing on various aspects, including control strategies [3], circulating current suppression [10, 11], modulation methods [12–14], and balancing capacitor voltages [1, 15].

The modulation techniques significantly influence various aspects of MMC performance, including harmonic content, capacitor voltage balancing, and switching losses [12, 16]. These techniques can be classified into 3 categories according to their switching frequency [17]. Techniques that utilize high switching frequencies include space vector pulse width modulation (PWM) [18], selective harmonic elimination PWM [19], and multicarrier PWM. The multicarrier PWM techniques are commonly employed in low-level MMC for their simplicity, although they result in high switching losses [10, 13]. Furthermore, the number of carrier signals rises proportionally with the increase in the number of submodules (SMs) within the MMC, thereby complicating the implementation of carrier-based PWM methods [20, 21]. The multicarrier PWM techniques can be divided into 2 principal based on the position of the carrier, either level-shifted (LS-PWM) [20] or phase-shifted (PS-PWM) [22]. A comparison between these 2 types of multicarrier PWM modulation was conducted in [23]. The PS-PWM technique allows for a uniform distribution of power and balanced use of switches. Conversely, the LS-PWM technique provides lower harmonic distortion for low-level MMC but results in an uneven power distribution [24]. In contrast, low-frequency modulation methods such as selective harmonic elimination [25] and nearest level control (NLC) [26], operate at the fundamental switching frequency, thereby minimizing switching losses. The NLC method is simpler than the selective harmonic elimination method, which necessitates more complex calculations. However, the NLC method produces lower-quality waveforms in low-level MMC, including low-order harmonics, which consequently leads to a high total harmonic distortion (THD). However, by employing a greater number of SMs, the NLC method can improves the voltage output quality and the reduction of THD, making such an approach more suitable for high-level MMC in HV applications [27]. Furthermore, there are different hybrid modulation methods in the literature. In [28] was presented a hybrid technique, combining both PS-PWM and LS-PWM methods to exploit the advantages of each. In [29] was proposed a hybrid method that combines low and high frequency modulation schemes, applying one technique to half of the SMs in each arm and the other technique to the remaining SMs. Moreover, this method incorporates an additional rotation strategy aimed at ensuring an even distribution of power among all the SMs. In [12] was proposed a hybrid nearest level pulse width modulation (NL-PWM) method, which integrates NLC control with PWM method, to take advantage of the reduced switching frequency (RSF) offered by the NLC technique and the low harmonic distortion achieved by the PWM technique. Therefore, the NL-PWM technique is considered better suited for medium voltage applications.

One of the challenges in controlling the MMC is maintaining the SM capacitor voltages at their nominal values. Imbalance in capacitor voltages results in lower order harmonics in the output voltages, thereby decreasing their quality [1]. Existing methods for balancing capacitor voltages are based on a sorting algorithm, where the capacitor voltages are sorted in each control cycle and the SMs to be inserted are selected based on the capacitor charge state [30]. However, this sorting method results in a higher and variable switching frequency, increasing switching losses and threatening the reliability of semiconductor devices (IGBT/GTO) [15]. To address this problem, several methods have been proposed in the literature, including the RSF voltage balancing algorithm, which eliminates certain unnecessary switching operations to lower the switching frequency and associated losses [15, 31].

The goal of the paper. This research aims to provide a comparative analysis of 3 modulation techniques from different categories for the MMC, namely LS-PWM, NLC, and NL-PWM. The study will evaluate the impact of these techniques on output voltage and current quality, capacitor voltage balancing, switching losses, and their robustness under short-circuit fault conditions. This analysis aims to facilitate the selection of the most suitable modulation technique for specific applications. Furthermore, the capacitor voltage balancing of the SMs in this study was performed using the RSF algorithm. Additionally, to the best of the author's knowledge, the NL-PWM technique cannot be directly applied with the RSF algorithm. To address this limitation, the paper proposes a modification to the RSF algorithm, enabling its compatibility with the NL-PWM method and opening new perspectives for enhancing MMC performance.

MMC topology and operation principle. The MMC topology utilized in this study is a 3-phase, 9-level configuration (Fig. 1,*a*). It comprises 6 arms, each of which consists of an inductance (L_{arm}) and 8 SMs connected in series. The inductances serve to limit the circulating current in the arms to protect the system in the event of a short circuit [32].

A variety of SM types are available, with the full-bridge SM and the half-bridge SM being the most common [33]. In this study, we have used the half-bridge SM (Fig. 1,*b*).

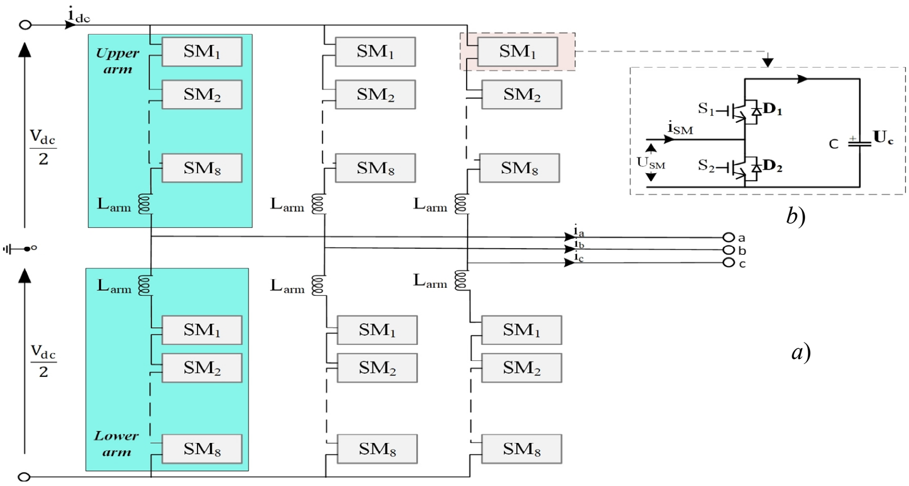

Fig. 1. Topology of the 3-phase 9-level MMC (*a*); half-bridge submodule (*b*)

This SM is composed of a pair of switches and a capacitor (C), with each switch comprising an IGBT or MOSFET and an antiparallel diode. The half-bridge SM is widely utilized in HV applications, particularly in HVDC systems, due to its high efficiency, reduced number of components and low energy losses [20, 32]. The SMs operate according to 2 normal operating states: the active state and the bypass state. In the active state, the lower switch (S_2) is OFF while the upper switch (S_1) is ON. In this mode, the output voltage of the SM (U_{SM}) equals the voltage across the capacitor (U_C), and the capacitor charges or discharges based on the direction of the arm current flow (Fig. 2). Conversely, in the bypass state, switch S_1 is deactivated while S_2 is activated. The voltage across the SM remains at zero, and the arm current does not flow through the capacitor. Table 1 summarizes the operation of the SM based on the switching state and the direction of the current in the arms.

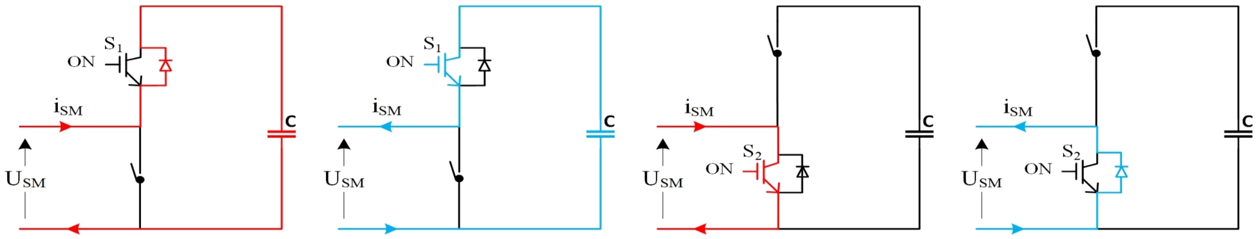

Fig. 2. Operating modes of the half-bridge submodule

Table 1
Switching state of sub-module

Mode	S_1	S_2	i_{SM}	U_{SM}	Capacitor state	S^k
1	1	0	> 0	U_C	Charging	1
2	1	0	< 0	U_C	Discharging	1
3	0	1	> 0	0	Bypass	0
4	0	1	< 0	0	Bypass	0

The output voltage of the SM is expressed as a function of the SM insertion index (S^k) as follows:

$$U^k_{SMji} = S^k_{ji} \cdot U^k_{cji}\,, \tag{1}$$

where j is the indices of the upper (u) or lower (l) arms, respectively; $i = a, b, c$ corresponds to the phase indices; k is the index of the k-th SM; U^k_{cji} is the SM capacitor voltage, which can be calculated as:

$$U_c = V_{dc} / N. \tag{2}$$

The voltage of each arm is the sum of the output voltages of the inserted SMs and is expressed as:

$$U_{ji} = \sum_{k=1}^{N} S^k_{ji} \cdot U^k_{cji}\,. \tag{3}$$

The MMC equivalent circuit models the SM capacitors as a voltage source shown in Fig. 3, where u_{ui}, u_{li} are the upper and lower arm voltages, respectively; i_i is the line current, which is expressed as:

$$i_i = i_{ui} - i_{li}, \tag{4}$$

where i_{ui}, i_{li} are the circulating currents in the upper and lower arm, respectively.

According to the Kirchhoff's voltage law, the arm voltages are expressed as:

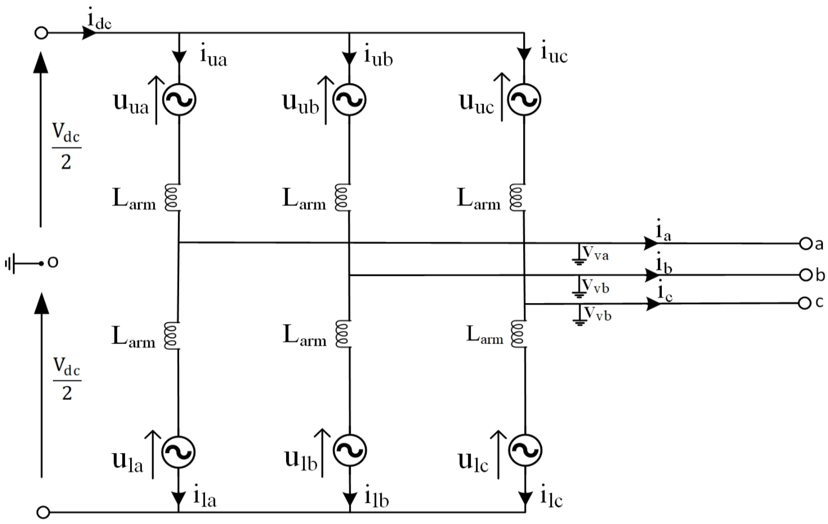

Fig. 3. Equivalent circuit of the MMC

$$u_{ui} = \frac{V_{dc}}{2} - L_{arm}\frac{\mathrm{d}i_{ui}}{\mathrm{d}t} - V_{vi}\,; \tag{5}$$

$$u_{li} = \frac{V_{dc}}{2} - L_{arm}\frac{\mathrm{d}i_{li}}{\mathrm{d}t} + V_{vi}\,, \tag{6}$$

where V_{vi} is the internal AC voltage of the MMC, which can be defined by the following equation:

$$V_{vi} = \frac{u_{li} - u_{ui}}{2} = \frac{1}{2}V_{dc}M\sin(2\pi f_0 t), \tag{7}$$

where M is the modulation index of the voltage; f_0 is the fundamental frequency.

Ideally, neglecting the voltage of the inductance and according to (5), (6), the DC bus voltage can be expressed as:

$$V_{dc} = u_{ui} + u_{li}. \tag{8}$$

MMC modulation methods. The modulation technique influences the behavior and performance of the MMC, particularly in terms of output voltage quality and energy losses. This work presents 3 modulation techniques for MMC: LS-PWM, NLC and NL-PWM. Each technique offers specific advantages and limitations. An analysis of their characteristics will guide the selection of the most appropriate technique for specific projects.

Level-shifted PWM techniques are widely employed in various applications and are categorized into 3 main types: phase disposition (PD), phase opposition disposition, and alternate phase opposition disposition. This study employs the PD-PWM technique, the principles of which are illustrated in Fig. 4. For an (N+1)-level converter, each arm requires N carrier waveforms, where the carriers are amplitude-shifted, have the same amplitude (V_{dc}/N) and frequency [14]. This method can produce a (2N+1)-level waveform by introducing a phase shift of π between the lower and upper arm carriers.

The PD-PWM technique operates by comparing the arm voltage reference with N carrier signals. When the reference signal exceeds a carrier signal, a pulse of 1 is generated; otherwise, the pulse is set to 0. These comparisons are performed in real-time, and the resulting pulses are summed to determine the total number of SMs to activate in the arm (N_{on}), as depicted in Fig. 4,*b*.

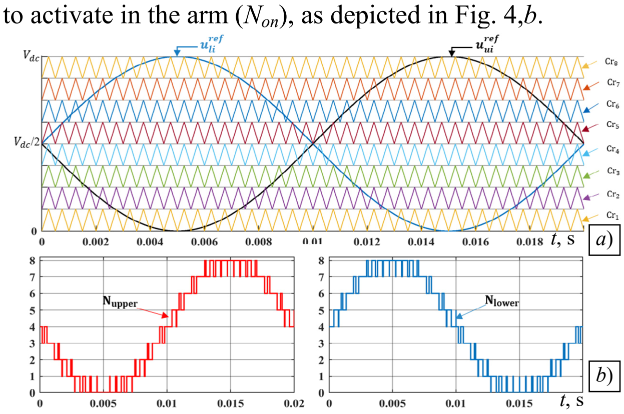

Fig. 4. Principle of PD-PWM:
references and carriers waves (*a*); number of inserted SMs (*b*)

Nearest level control. The NLC technique offers several advantages, including reduced switching losses, excellent harmonic characteristics in high-level MMC, and simplified implementation. The principle of this method is illustrated in Fig. 5, where the reference signal is divided by the capacitor voltage and then rounded to the nearest value to determine the number of SMs to be inserted in the arm. The output signal generated by the NLC method is discrete and can approximate a sinusoidal shape when a large number of SMs are used.

The arm reference voltages are:

$$u_{ui}^{*} = N_{ui} \cdot U_c ; \tag{9}$$

$$u_{li}^{*} = N_{li} \cdot U_c , \tag{10}$$

where N_{ui}, N_{li} are the number of SMs activated in the upper and lower arms, respectively.

The arm voltages generated by the NLC technique are expressed as:

$$u_{ui} = \text{round}\left(\frac{u_{ui}^{*}}{U_c}\right) \cdot U_c ; \tag{11}$$

$$u_{li} = \text{round}\left(\frac{u_{li}^{*}}{U_c}\right) \cdot U_c ; \tag{12}$$

where «round» is the function that rounds a number to the nearest integer. If the decimal part is 0.5 or higher, the number is rounded up; if it is less than 0.5, it is rounded down.

According to (2) and (9)–(12), the number of SMs to be inserted into the upper and lower arms can be calculated as:

$$N_{ui} = N \cdot \text{round}\left(\frac{u_{ui}^{*}}{V_{dc}}\right); \tag{13}$$

$$N_{li} = N \cdot \text{round}\left(\frac{u_{li}^{*}}{V_{dc}}\right). \tag{14}$$

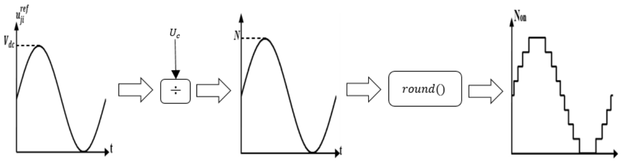

Fig. 5. Principle of the NLC technique

Nearest level PWM. The NL-PWM modulation technique combines the 2 previous modulation approaches, offering an effective solution to 2 major challenges encountered in power converters: high-frequency switching in PWM techniques and the low-order harmonic issue found in the NLC in low-level MMC [12].

The strategy of this technique is illustrated in Fig. 6. In this technique, each arm of the MMC has an SM operating in PWM mode to reduce harmonic distortion, with the capacitor voltage balancing algorithm determining which SM operates in PWM mode. The reference signal is quantified by the «floor» function to determine the number of SMs operating in the active state (Fig. 7,*a*). The remainder of the signal is then used to generate the reference signal for the SM operating in PWM mode (Fig. 7,*b*). Additionally, the converter can generate (2*N*+1)-level by using opposing carriers in both arms [12].

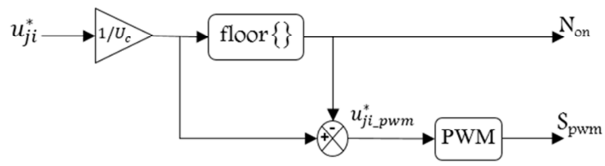

Fig. 6. Strategy of the NL-PWM technique

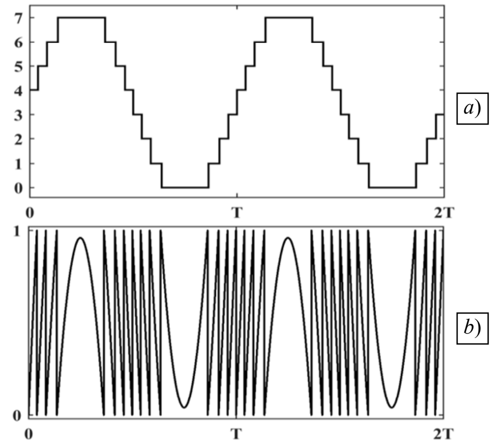

Fig. 7. NL-PWM technique: number of SMs to be inserted (*a*); reference wave of the PWM module (*b*)

The number of SMs in active mode is calculated as:

$$N_{ui} = \text{floor}\left(\frac{u_{ui}^{*}}{U_c}\right); \tag{15}$$

$$N_{li} = \text{floor}\left(\frac{u_{li}^{*}}{U_c}\right), \tag{16}$$

where «floor» represents the mathematical function that rounds a number down to the nearest integer.

The reference voltages for the SMs in PWM mode are expressed as:

$$u_{ui\_pwm}^{*} = \frac{u_{ui}^{*}}{U_c} - \text{floor}\left(\frac{u_{ui}^{*}}{U_c}\right); \tag{17}$$

$$u_{li\_pwm}^{*} = \frac{u_{li}^{*}}{U_c} - \text{floor}\left(\frac{u_{li}^{*}}{U_c}\right). \tag{18}$$

Capacitor voltage balancing algorithm. Balancing the capacitor voltages of the SMs is essential for ensuring the stability of the MMC converter. In this study, the RSF voltage balancing algorithm is employed, and a modified version is proposed to adapt it to the NL-PWM technique.

RSF capacitor voltage balancing algorithm. The RSF algorithm is based on the classical principle of capacitor voltage balancing, which aims to discharge overcharged capacitors and charge undercharged capacitors. Accordingly, when the arm current is positive, the SMs with the lowest voltage are inserted. Conversely, when the arm current is negative, the SMs with the highest voltage are inserted [14]. In addition, the RSF algorithm includes specific operations to avoid sorting when the number of SMs inserted or bypassed in an arm remains constant, thereby reducing both switching losses and energy losses in the MMC [15].

The principle of the RSF balancing algorithm (Fig. 8) involves inserting or bypassing specific SMs based on the variation in the number of SMs activated during each control cycle (Δ*N*). |Δ*N*| indicates the additional number of SMs to insert or bypass during the current control cycle. N_{on} is the number of SMs to activate, while N_{on_prev} is the number of SMs activated in the previous cycle. The RSF voltage balancing algorithm operates as follows:

- When ΔN is positive, $|\Delta N|$ SMs must be inserted. These SMs are selected from those in a bypass state, with no switching applied to those already in an active state.
- If ΔN is negative, certain active SMs must be switched to a bypass state, with no SMs currently in a bypass state being activated.
- If ΔN is zero, no changes are made.

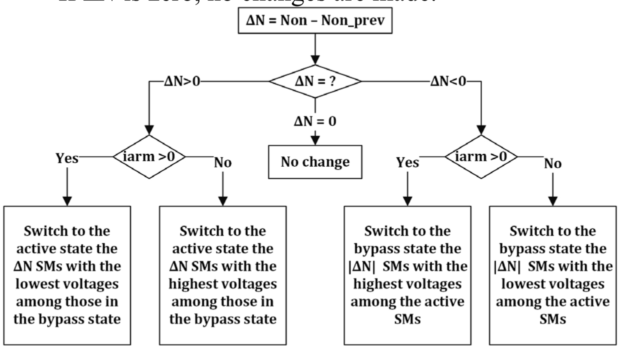

Fig. 8. Flowchart of the RSF voltage balancing algorithm

Modified RSF voltage balancing algorithm. The NL-PWM technique cannot be used with the RSF balancing algorithm, as the latter requires adjustments for selecting the SM that should be activated in PWM mode. The SM operates in PWM mode alternates between the active and bypass states, resulting in a reduction in the discharging or charging currents of its capacitor compared to other SMs operating in the active state. This work proposes modifications to the RSF algorithm to adapt it for compatibility with the NL-PWM technique (Fig. 9).

The principles of the modified RSF algorithm are explained below:

- When ΔN is positive, the last SM selected in PWM mode is switched to the bypass state. Then, among the SMs in the bypass state, ΔN SMs are switched to the active state, and one SM is activated in PWM mode. These SMs are selected based on the direction of current flow.
- When ΔN is negative, the last SM activated in PWM mode is switched to the active state, while $|\Delta N|$ others SMs are switched to the bypass state, and one SM among those in the active state is selected in PWM mode.

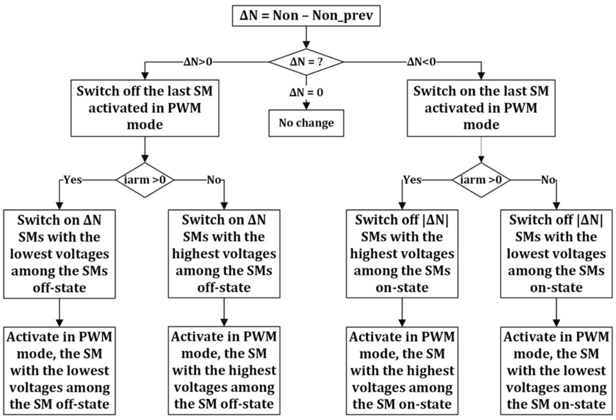

Fig. 9. Modified RSF voltage balancing algorithm

Simulation results. The LS-PWM, NLC and NL-PWM modulation techniques, along with the modified voltage balancing algorithm presented in this paper, were evaluated by simulation using MATLAB/Simulink software. The simulated system consists of a 3-phase MMC with an R-L load. Table 2 presents the system parameters.

Table 2

Parameters of the MMC system

Parameter	Values
DC-side voltage V_{dc}, kV	11
Number of SMs per arm N	8
SM capacitor C, mF	25
Load resistance R, Ω	10
Load inductance L, mH	15
Arm inductance L_{arm}, mH	0.1
Rated frequency f_s, Hz	50
Carrier frequency of LS-PWM, kHz	3
Carrier frequency of NL-PWM, kHz	1
Voltage modulation index	0.95

Output and capacitor voltage analysis. The 3 modulation techniques studied were evaluated in terms of line current quality, phase voltage, and capacitor voltage balancing. The results are presented in Fig. 10–13. Figure 10 shows the line current, while Fig. 11 presents its THD. Similarly, Fig. 12, 13 illustrate the output voltages and their corresponding THD, respectively.

Figure 11 shows that the THD of the line current is less than 5% for the 3 techniques studied, with the NLC technique providing the lowest quality. For the output voltage (Fig. 12, 13), the MMC generates the lowest THD (6.86%) using the LS-PWM technique due to the absence of lower-order harmonics. The THD obtained with the NL-PWM technique (7.05%) is close to that of LS-PWM. In contrast, the NLC technique has the highest THD (9.33%).

These results are summarized in Table 3.

Table 3

Analysis of line current and phase voltage

	Current		Voltage	
	Fundamental, A	THD, %	Fundamental, V	THD, %
LS-PWM	494.6	0.28	5475	6.86
NLC	500.5	1.28	5548	9.33
NL-PWM	492.4	0.56	5412	7.05

However, the NL-PWM and LS-PWM techniques are well-suited for low-level converters due to their low THD. In contrast, the THD decreases with an increasing number of SMs when using the NLC technique, making it more suitable for high-level converters.

Figure 14 shows the capacitor voltages in the upper arm of phase A. When the RSF balancing method is used with the LS-PWM technique, the capacitor voltages converge to the nominal value. The NLC method shows more pronounced oscillations due to a lower switching frequency, indicating a greater need for higher capacitance capacitors in low-frequency modulation techniques.

In contrast, the NL-PWM technique shows less oscillations compared to the NLC technique, with capacitor voltages varying around the nominal value of 1375 V. These results confirm that the RSF algorithm is suitable for use with the NL-PWM technique, validating the proposed adjustments to the RSF algorithm.

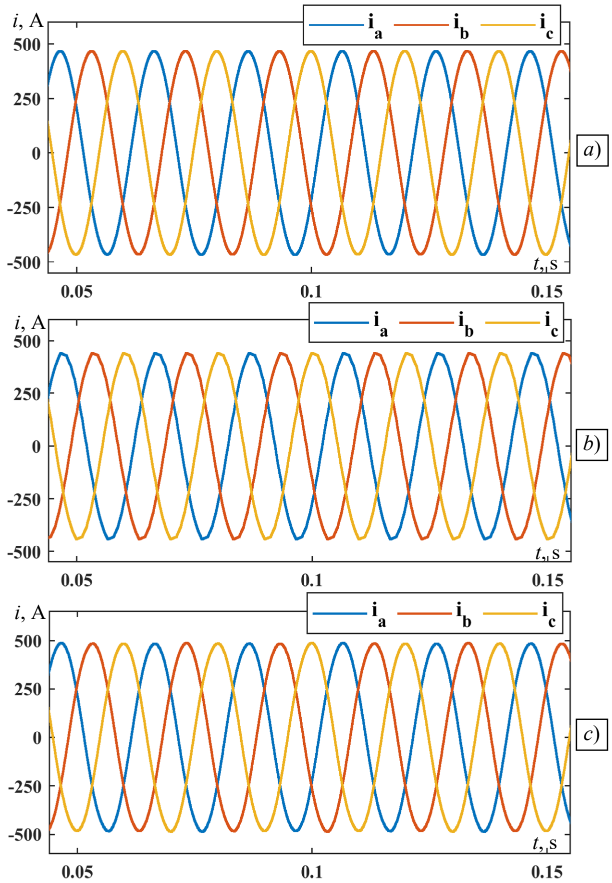

Fig. 10. Line currents: LS-PWM (*a*); NLC (*b*); NL-PWM (*c*)

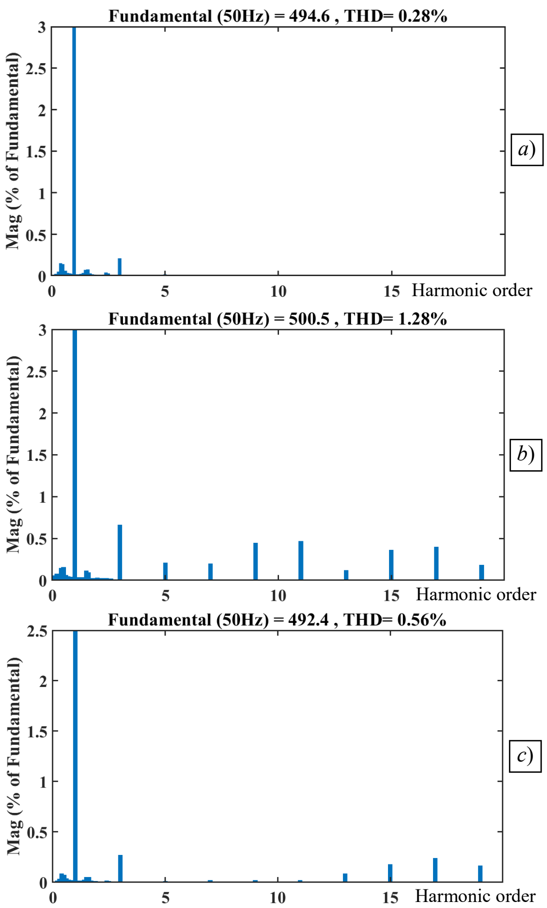

Fig. 11. THD analysis of output currents: LS-PWM (*a*); NLC (*b*); NL-PWM (*c*)

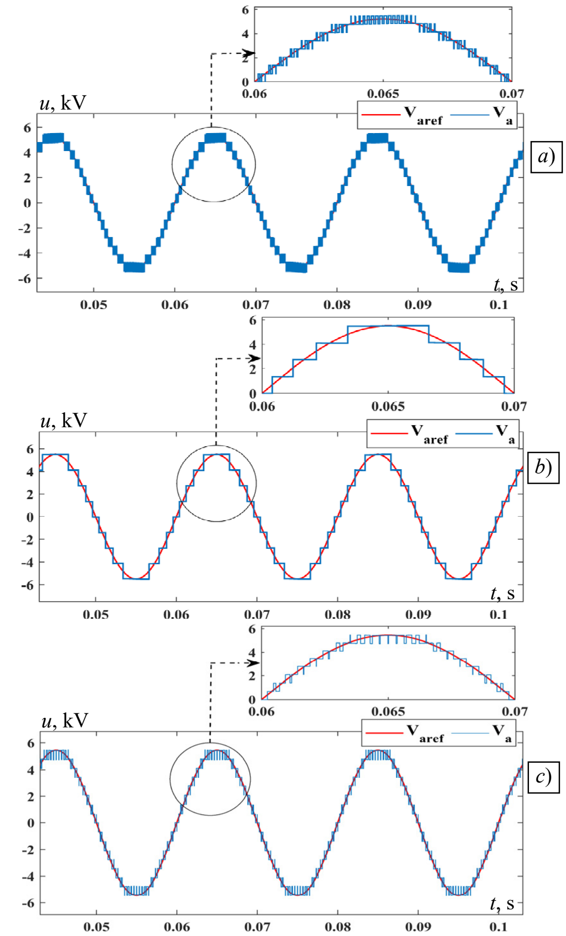

Fig. 12. Output voltages: LS-PWM (*a*); NLC (*b*); NL-PWM (*c*)

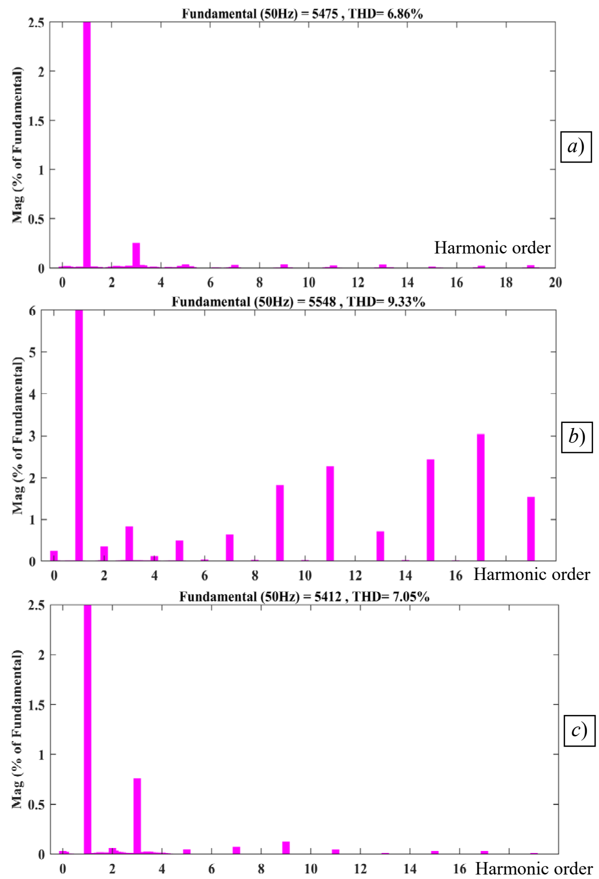

Fig. 13. THD analysis of output voltages: LS-PWM (*a*); NLC (*b*); NL-PWM (*c*)

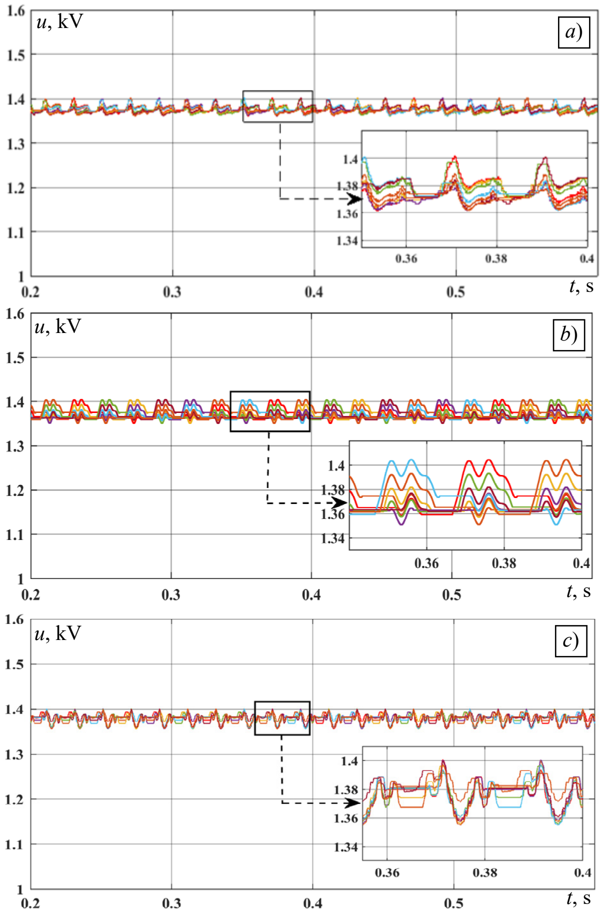

Fig. 14. Capacitor voltages in the upper arm of phase A: LS-PWM (*a*); NLC (*b*); NL-PWM (*c*)

Power loss analysis. Power losses in the MMC include those associated with both diodes and IGBTs. The total losses for the IGBTs can be expressed as:

$$P_{loss\_IGBT} = P_{c\_IGBT} + P_{sw\_IGBT}, \qquad (19)$$

where $P_{c\text{-}IGBT}$ is the conduction losses; $P_{sw\text{-}IGBT}$ is the switching losses. Switching losses occur during transitions between the on and off states, resulting from the energy dissipated during the switching period.

For diodes the total losses are given by:

$$P_{loss\_diode} = P_{c\_diode} + P_{rec\_diode}, \qquad (20)$$

where $P_{c\text{-}diode}$ is the conduction losses; $P_{rec\text{-}diode}$ is the reverse recovery losses, generated during the transition from the conducting to the blocking state.

In this study, the FZ3600R17HP4 IGBT/diode module was used, and its characteristics are presented in Table 4. The power losses were calculated according to the methods described in [34].

Table 4

Parameters of IGBT module FZ3600R17HP4

IGBT	V_{CES}, V	1700
	$I_{C\text{-}nom}$, A	3600
	V_{CE}, V	2.25
	E_{on}, mJ	800
	E_{off}, mJ	1500
Diode	V_{RRM}, V	1700
	I_F, A	3600
	V_F, V	1.9
	E_{rec}, mJ	1100

Figure 15 illustrates the switching pulses for the 4 SMs in the upper arm of phase A. Table 5 shows the total power losses and efficiency associated with each modulation technique. The results show that conduction losses are relatively similar among the 3 techniques, which is explained by their independence from the modulation method. In contrast, the switching losses vary considerably. The NLC technique has the lowest switching losses, characterized by a single switch per period, while the LS-PWM technique results in the highest losses.

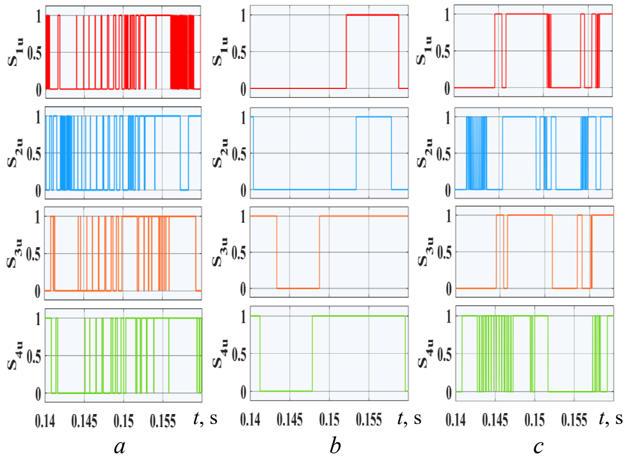

Fig. 15. Gate signals of 4 SMs in the upper arms of phase A: LS-PWM(*a*); NLC (*b*); NL-PWM (*c*)

Table 5

Power losses and efficiency of the MMC

Power losses	LS-PWM	NLC	NL-PWM
IGBT conduction losses, kW	18.575	18.846	18.729
IGBT switching losses, kW	54.084	24.472	31.634
Diode conduction losses, kW	1.992	1.973	1.912
Diode reverse recovery losses, kW	0.569	1.829	1.073
Total power loss, kW	75.22	47.12	53.35
Efficiency, %	97.98	98.75	98.39

Analysis under fault condition. To evaluate the robustness of the modulation techniques under fault conditions, a line-to-ground (L-G) short circuit was simulated. This type of fault is one of the most common in power transmission systems. The fault was applied between phase *A* and the ground at t = 1.4 s, with a duration of 50 ms. The impact of this fault on the RMS value of the voltage and on the capacitor voltages is illustrated in Fig. 16, 17, respectively. The performance of the each modulation techniques was compared in terms of their ability to maintain stability and balance the capacitor voltages after the fault is eliminated.

At the time of the L-G fault (t = 1.4 s), as depicted in Fig. 16, an immediate drop in the RMS voltage is observed for all the techniques studied. The NLC technique exhibits the most significant disturbance, followed by NL-PWM, while the LS-PWM technique shows the least voltage decrease. During the fault period, the LS-PWM technique maintains the most stable RMS voltage, with minimal oscillations. After the fault, LS-PWM is characterized by a rapid and stable return to the nominal value, in contrast to the NLC and NL-PWM, which show significant overshoot before stabilizing.

Moreover, as shown in Fig. 17, the fault significantly affects the balancing of the capacitor voltages.

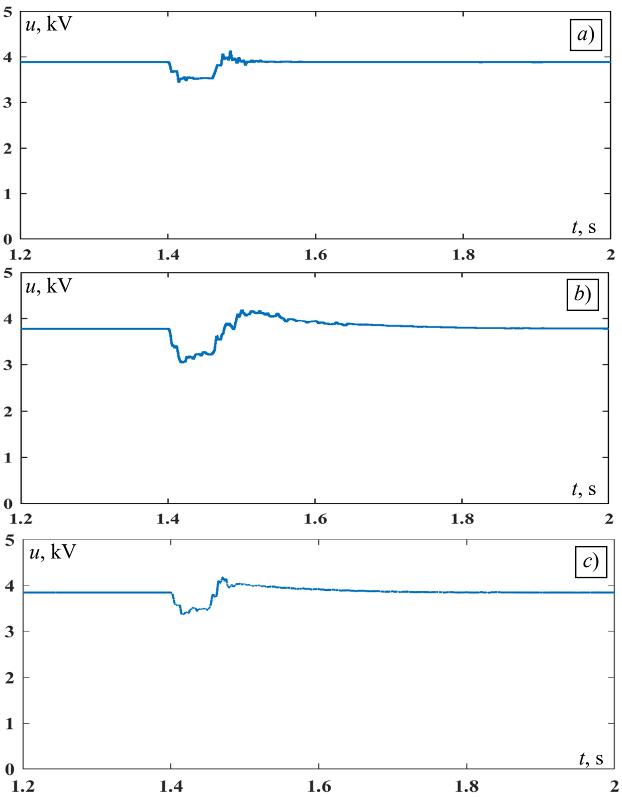

Fig. 16. RMS voltage of phase *A* under L-G fault:
LS-PWM (*a*); NLC (*b*); NL-PWM (*c*)

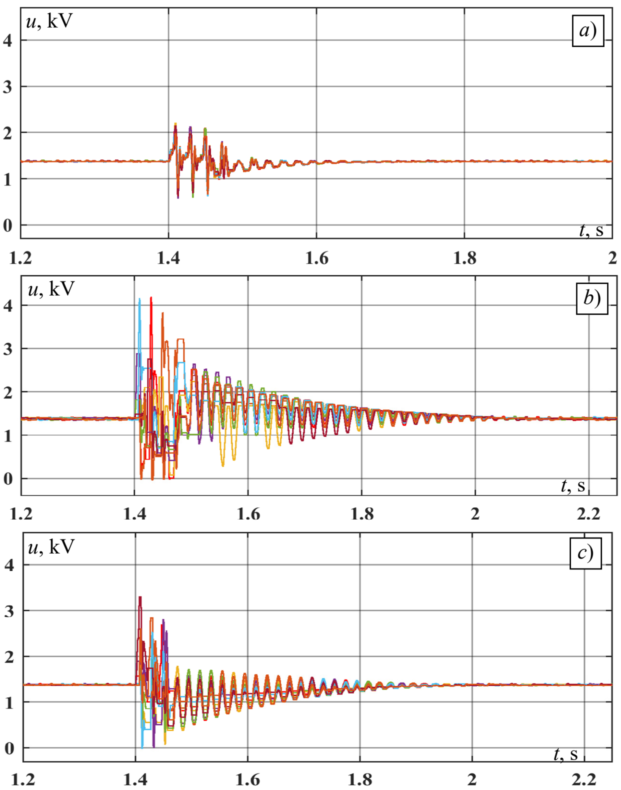

Fig. 17. Capacitor voltage in the upper arm of phase A
under L-G fault: LS-PWM (*a*); NLC (*b*); NL-PWM (*c*)

The LS-PWM technique exhibits the most subdued oscillations and the fastest return to equilibrium. In contrast, with the NLC technique, the capacitor voltage increases up to 3 times its nominal value at the start of the fault, causing significant oscillations and a longer stabilization time. The NL-PWM technique shows intermediate performance, offering more effective balancing than the NLC technique, but less effective than the LS-PWM.

Conclusions. This article presents a comparative analysis of the performance of 3 modulation techniques for the MMC: LS-PWM, NLC and NL-PWM. The analysis focused on key criteria, including the harmonic content of the output signals, power losses, behavior under short-circuit conditions, and the impact on capacitor voltage balancing. The study was conducted on a 9-level 3-phase MMC connected to an R-L load. LS-PWM and NLC modulation techniques were used with the RSF capacitor voltage balancing algorithm, while the NL-PWM technique was used with the modified RSF algorithm proposed in this study.

Simulation results show that the LS-PWM and NL-PWM techniques generate output signals with similar total harmonic distortion, which is lower than that obtained with the NLC technique. Furthermore, capacitor voltage balancing was effectively achieved with the NL-PWM technique, validating the modification of the RSF algorithm proposed. In addition, the NLC technique exhibited more pronounced oscillations in the capacitor voltages compared to the other techniques, indicating that low-frequency modulation techniques require capacitors with higher capacity.

In terms of power losses, the NLC technique is characterized by lower switching losses than the others, with an efficiency of 98.75 %. Furthermore, regarding fault robustness, the LS-PWM technique shows the best performance, with a rapid and stable return to equilibrium after a short circuit.

The results of the study demonstrate that the LS-PWM and NL-PWM techniques are particularly suited for low-level MMC used in low or medium-voltage applications, while the NLC technique is more suitable for high-level MMC, intended for high-voltage applications such as HVDC systems.

Acknowledgments. This work was supported by the Centre National de la Recherche Scientifique et Technique (CNRST) as part of the «PhD-Associate Scholarship – PASS» program.

Conflict of interest. The authors declare that they have no conflicts of interest.

REFERENCES

1. Bashir S.B., Beig A.R. An improved voltage balancing algorithm for grid connected MMC for medium voltage energy conversion. *International Journal of Electrical Power & Energy Systems*, 2018, vol. 95, pp. 550-560. doi: https://doi.org/10.1016/j.ijepes.2017.09.002.

2. Sun P., Li K., Li Y., Zhang L. DC voltage control for MMC-based railway power supply integrated with renewable generation. *IET Renewable Power Generation*, 2020, vol. 14, no. 18, pp. 3679-3689. doi: https://doi.org/10.1049/iet-rpg.2020.0132.

3. Li J., Konstantinou G., Wickramasinghe H.R., Pou J. Operation and Control Methods of Modular Multilevel Converters in Unbalanced AC Grids: A Review. *IEEE Journal of Emerging and Selected Topics in Power Electronics*, 2019, vol. 7, no. 2, pp. 1258-1271. doi: https://doi.org/10.1109/JESTPE.2018.2856505.

4. Parimalasundar E., Muthukaruppasamy S., Dharmaprakash R., Suresh K. Performance investigations of five-level reduced switches count H-bridge multilevel inverter. *Electrical Engineering & Electromechanics*, 2023, no. 6, pp. 58-62. doi: https://doi.org/10.20998/2074-272X.2023.6.10.

5. Ayari M., Bichiou S., Belhaouane M.M., Benhadj Braiek N. An Advanced Anti-Windup Control Strategy for MMC-HVDC System. *IETE Journal of Research*, 2022, vol. 68, no. 3, pp. 1831-1846. doi: https://doi.org/10.1080/03772063.2019.1676663.

6. Rachananjali K., Srinu Naik R., Bala Krishna K., Srinivasa Rao Y. Efficient modeling and simulation of grid connected MMC for sustainable photovoltaic and wind conversion system. *Sustainable*

Computing: Informatics and Systems, 2020, vol. 28, art. no. 100402. doi: https://doi.org/10.1016/j.suscom.2020.100402.
7. Barcellona S., Barresi M., Piegari L. MMC-Based PV Single-Phase System with Distributed MPPT. *Energies*, 2020, vol. 13, no. 15, art. no. 3964. doi: https://doi.org/10.3390/en13153964.
8. Cai W., Hu P., Jiang D., Liang Y. An MMC Based Hybrid Energy Storage System: Concept, Topology, and Control. *2020 IEEE 3rd Student Conference on Electrical Machines and Systems (SCEMS)*, 2020, pp. 680-685. doi: https://doi.org/10.1109/SCEMS48876.2020.9352256.
9. Hahn F., Camurca L., Liserre M. Investigation of Modular Multilevel Converters for E-STATCOM Applications. *2020 IEEE 29th International Symposium on Industrial Electronics (ISIE)*, 2020, pp. 1028-1032. doi: https://doi.org/10.1109/ISIE45063.2020.9152265.
10. Zhang G., Song J., Li C., Gu X. A Circulating Current Suppression Strategy for MMC Based on the 2N+1 PWM Approach. *World Electric Vehicle Journal*, 2023, vol. 14, no. 4, art. no. 106. doi: https://doi.org/10.3390/wevj14040106.
11. Hafeez K., Khan S.A., Van den Bossche A., Ul Hasan Q. Circulating current reduction in MMC-HVDC system using average model. *Applied Sciences*, 2019, vol. 9, no. 7, art. no. 1383. doi: https://doi.org/10.3390/app9071383.
12. Wang Y., Hu C., Ding R., Xu L., Fu C., Yang E. A Nearest Level PWM Method for the MMC in DC Distribution Grids. *IEEE Transactions on Power Electronics*, 2018, vol. 33, no. 11, pp. 9209-9218. doi: https://doi.org/10.1109/TPEL.2018.2792148.
13. Ronanki D., Williamson S.S. A Novel 2N+1 Carrier-Based Pulse Width Modulation Scheme for Modular Multilevel Converters With Reduced Control Complexity. *IEEE Transactions on Industry Applications*, 2020, vol. 56, no. 5, pp. 5593-5602. doi: https://doi.org/10.1109/TIA.2020.3009078.
14. Ronanki D., Williamson S.S. New modulation scheme and voltage balancing control of modular multilevel converters for modern electric ships. *IET Power Electronics*, 2019, vol. 12, no. 13, pp. 3403-3410. doi: https://doi.org/10.1049/iet-pel.2018.6362.
15. Luo Y., Jia Z., Xu L., Li Q., Song Y. A reduced switching frequency capacitor voltage balancing control for modular multilevel converters. *International Journal of Electrical Power & Energy Systems*, 2022, vol. 142, art. no. 108272. doi: https://doi.org/10.1016/j.ijepes.2022.108272.
16. Saidi F., Djahbar A., Bounadja E., Kacemi W.M., Fettah K. Novel modular multilevel matrix converter topology for efficient high-voltage AC-AC power conversion. *Electrical Engineering & Electromechanics*, 2024, no. 6, pp. 49-56. doi: https://doi.org/10.20998/2074-272X.2024.6.07.
17. Sujatha M.S., Sreelakshmi S., Parimalasundar E., Suresh K. Mitigation of harmonics for five level multilevel inverter with fuzzy logic controller. *Electrical Engineering & Electromechanics*, 2023, no. 4, pp. 52-56. doi: https://doi.org/10.20998/2074-272X.2023.4.08.
18. Ronanki D., Williamson S.S. A Simplified Space Vector Pulse Width Modulation Implementation in Modular Multilevel Converters for Electric Ship Propulsion Systems. *IEEE Transactions on Transportation Electrification*, 2019, vol. 5, no. 1, pp. 335-342. doi: https://doi.org/10.1109/TTE.2018.2884610.
19. Perez-Basante A., Ceballos S., Konstantinou G., Pou J., Sanchez-Ruiz A., Lopez I., De Alegria I.M. Circulating Current Control for Modular Multilevel Converters with (N+1) Selective Harmonic Elimination – PWM. *IEEE Transactions on Power Electronics*, 2020, vol. 35, no. 8, pp. 8712-8725. doi: https://doi.org/10.1109/TPEL.2020.2964522.
20. Zhou F., Xiang X., Ma F., Wang Y., Zhou F., Peng P. An Improved Phase-Disposition Pulse Width Modulation Method for Hybrid Modular Multilevel Converter. *Energies*, 2023, vol. 16, no. 3, art. no. 1192. doi: https://doi.org/10.3390/en16031192.
21. Priyanka G., Surya Kumari J., Lenine D., Srinivasa Varma P., Sneha Madhuri S., Chandu V. MATLAB-Simulink environment based power quality improvement in photovoltaic system using multilevel inverter. *Electrical Engineering & Electromechanics*, 2023, no. 2, pp. 43-48. doi: https://doi.org/10.20998/2074-272X.2023.2.07.
22. Zhou D., Yang S., Tang Y. Model-Predictive Current Control of Modular Multilevel Converters With Phase-Shifted Pulsewidth Modulation. *IEEE Transactions on Industrial Electronics*, 2019, vol. 66, no. 6, pp. 4368-4378. doi: https://doi.org/10.1109/TIE.2018.2863181.
23. Uddin W., Zeb K., Khan M.A., Ishfaq M., Busarello T.D.C., Kim H.J. Effect of Modulation Techniques on Capacitor Voltage of Modular Multilevel Converter. *2020 IEEE 23rd International Multitopic Conference (INMIC)*, 2020, pp. 1-6. doi: https://doi.org/10.1109/INMIC50486.2020.9318121.
24. Ronanki D., Williamson S.S. Modified Phase-disposition PWM Technique for Modular Multilevel Converters. *2018 IEEE Transportation Electrification Conference and Expo (ITEC)*, 2018, pp. 26-31. doi: https://doi.org/10.1109/ITEC.2018.8450084.
25. Jin Y., Wang S., Xiao Q., Liu Y., Mu Y., Ji Y., Chaudhary S.K., Teodorescu R. A Novel Harmonic Control Method for MMC Combining Improved Nearest Level Control and Selective Harmonic Elimination method. *2019 IEEE Energy Conversion Congress and Exposition (ECCE)*, 2019, pp. 6368-6375. doi: https://doi.org/10.1109/ECCE.2019.8912529.
26. Nguyen M.H., Kwak S. Nearest-Level Control Method With Improved Output Quality for Modular Multilevel Converters. *IEEE Access*, 2020, vol. 8, pp. 110237-110250. doi: https://doi.org/10.1109/ACCESS.2020.3001587.
27. Lin L., Lin Y., He Z., Chen Y., Hu J., Li W. Improved Nearest-Level Modulation for a Modular Multilevel Converter With a Lower Submodule Number. *IEEE Transactions on Power Electronics*, 2016, vol. 31, no. 8, pp. 5369-5377. doi: https://doi.org/10.1109/TPEL.2016.2521059.
28. Ronanki D., Azeez N.A., Patnaik L., Williamson S.S. Hybrid multi-carrier PWM technique with computationally efficient voltage balancing algorithm for modular multilevel converter. *2018 IEEE International Conference on Industrial Electronics for Sustainable Energy Systems (IESES)*, 2018, pp. 224-229. doi: https://doi.org/10.1109/IESES.2018.8349878.
29. Kim S.-M., Jeong M.-G., Kim J., Lee K.-B. Hybrid Modulation Scheme for Switching Loss Reduction in a Modular Multilevel High-Voltage Direct Current Converter. *IEEE Transactions on Power Electronics*, 2019, vol. 34, no. 4, pp. 3178-3191. doi: https://doi.org/10.1109/TPEL.2018.2848620.
30. Hu P., Teodorescu R., Wang S., Li S., Guerrero J.M. A Currentless Sorting and Selection-Based Capacitor-Voltage-Balancing Method for Modular Multilevel Converters. *IEEE Transactions on Power Electronics*, 2019, vol. 34, no. 2, pp. 1022-1025. doi: https://doi.org/10.1109/TPEL.2018.2850360.
31. Samajdar D., Bhattacharya T., Dey S. A Reduced Switching Frequency Sorting Algorithm for Modular Multilevel Converter With Circulating Current Suppression Feature. *IEEE Transactions on Power Electronics*, 2019, vol. 34, no. 11, pp. 10480-10491. doi: https://doi.org/10.1109/TPEL.2019.2896932.
32. Dekka A., Wu B., Fuentes R.L., Perez M., Zargari N.R. Evolution of Topologies, Modeling, Control Schemes, and Applications of Modular Multilevel Converters. *IEEE Journal of Emerging and Selected Topics in Power Electronics*, 2017, vol. 5, no. 4, pp. 1631-1656. doi: https://doi.org/10.1109/JESTPE.2017.2742938.
33. Ali S., Bogarra S., Khan M.M., Taha A., Phyo P.P., Byun Y.-C. Prospective Submodule Topologies for MMC-BESS and Its Control Analysis with HBSM. *Electronics*, 2022, vol. 12, no. 1, art. no. 20. doi: https://doi.org/10.3390/electronics12010020.
34. Hafezi H., Faranda R. A New Approach for Power Losses Evaluation of IGBT/Diode Module. *Electronics*, 2021, vol. 10, no. 3, art. no. 280. doi: https://doi.org/10.3390/electronics10030280.

Received 16.12.2024
Accepted 28.01.2025
Published 02.07.2025

M. Benboukous[1], *PhD Student,*
H. Bahri[1], *Associate Professor,*
M. Talea[1], *Professor,*
M. Bour[1], *Professor,*
K. Abdouni[1], *PhD Student,*
[1] Laboratory of Information Processing,
Department of Physics, Faculty of Science Ben M'Sick,
University of Hassan II, Casablanca, Morocco,
e-mail: benboukous5@gmail.com (Corresponding Author);
hbahri.inf@gmail.com; taleamohamed@yahoo.fr;
med11bour@gmail.com; abdounikhadija8@gmail.com

How to cite this article:
Benboukous M., Bahri H., Talea M., Bour M., Abdouni K. Comparative analysis of principal modulation techniques for modular multilevel converter and a modified reduced switching frequency algorithm for nearest level pulse width modulation. *Electrical Engineering & Electromechanics*, 2025, no. 4, pp. 26-34. doi: https://doi.org/10.20998/2074-272X.2025.4.04

UDC 621.3 https://doi.org/10.20998/2074-272X.2025.4.05

Z. Khammassi, H. Khaterchi, A. Zaafouri

Experimental analysis of the effects of potential-induced degradation on photovoltaic module performance parameters

Introduction. *Photovoltaic (PV) power plants are subject to various forms of degradation that can impair their performance and lead to significant faults within PV systems. Among these, Potential-Induced Degradation (PID) stands out as one of the most severe, impacting the efficiency and output of PV generators while shortening their lifespan.* ***Problem****. This phenomenon is the result of a decrease in the shunt resistance of the cells encapsulated within the PV module, directly associated with a reduction in its insulation resistance. Although extensive research has been conducted in this area, our understanding of the factors contributing to PID, as well as its detection and effects on PV systems, remains incomplete. The* ***goal*** *of this work is to investigate the variations in insulation resistance at the module's glass and frame, and to map the changes in shunt resistance at the module level to identify the most vulnerable areas, characterized by lower insulation resistance values and significantly affected by PID.* ***Methodology.*** *This study utilizes a comparative experimental method to investigate the behavior of two identical PV modules under similar climatic conditions, where one module is exposed to voltage stress while the other remains unstressed. A high-voltage insulation resistance tester was employed to apply voltage stress between the terminals of the stressed module and its metal frame, with insulation resistance systematically measured at various points to analyze changes in electrical properties. The* ***originality*** *of this study lies in the estimation of the shunt resistance based on the operating voltage of the PV string, which depends on the types of grounding, climatic conditions such as temperature and humidity, as well as the position of the cell within the PV module. This estimation is correlated with the I-V characteristic curves of two PV modules, one of which is subjected to operating voltages under well-controlled environmental conditions. The* ***results*** *reveal that an increase in the test voltage leads to a reduction in insulation resistance, a phenomenon that becomes more pronounced in humid environments. This highlights the vulnerability of PV modules to PID, which can significantly affect their lifespan and performance, particularly through the reduction of shunt resistance and the distortion of the characteristic curve of the stressed module affected by this phenomenon, thereby causing increased difficulty in extracting its maximum power.* References 30, table 3, figures 17.

Key words: **potential-induced degradation, insulation resistance, maximum power point tracking, solar photovoltaic system.**

Вступ*. Фотоелектричні (PV) електростанції схильні до різних форм деградації, які можуть погіршити їхню продуктивність і призвести до значних несправностей у PV системах. Серед них потенціально-індукована деградація (PID), виділяється як одна з найсерйозніших, впливаючи на ефективність та вихідну потужність PV генераторів, одночасно скорочуючи термін їхньої служби.* ***Проблема****. Це явище є результатом зниження опору шунтуючого з'єднання елементів, вбудованих у PV модулі, що безпосередньо пов'язано зі зниженням опору його ізоляції. Хоча в цій галузі було проведено широкі дослідження, наше розуміння факторів, що сприяють PID, а також його виявлення та впливу на PV системи, залишається неповним.* ***Метою*** *роботи є дослідження змін опору ізоляції на склі та каркасі модуля, а також картографування змін опору шунтуючого з'єднання на рівні модуля для виявлення найбільш вразливих зон, що характеризуються нижчими значеннями опору ізоляції та значно зазнають впливу PID.* ***Методологія****. У цьому дослідженні використовується порівняльний експериментальний метод для дослідження поведінки двох ідентичних PV модулів за подібних кліматичних умов, де один модуль піддається впливу напруги, а інший залишається ненапруженим. Для застосування напруги між клемами напруженого модуля та його металевим каркасом було використано високовольтний тестер опору ізоляції, при цьому опір ізоляції систематично вимірювався в різних точках для аналізу змін електричних властивостей.* ***Оригінальність*** *дослідження полягає в оцінці опору шунту на основі робочої напруги PV кола, яка залежить від типів заземлення, кліматичних умов, таких як температура та вологість, а також положення елемента всередині PV модуля. Ця оцінка корелює з ВАХ двох PV модулів, один з яких піддається робочій напрузі в добре контрольованих умовах навколишнього середовища.* ***Результати*** *показують, що збільшення випробувальної напруги призводить до зниження опору ізоляції, явище, яке стає більш вираженим у вологому середовищі. Це підкреслює вразливість PV модулів до PID, що може суттєво вплинути на їхній термін служби та продуктивність, зокрема через зменшення опору шунту та спотворення характеристик модуля, що піддається впливу цього явища, що призводить до збільшення труднощів в отриманні його максимальної потужності.* Бібл. 30, табл. 3, рис. 17.

Ключові слова: **потенціально-індукована деградація, опір ізоляції, відстеження точки максимальної потужності, сонячна фотоелектрична система.**

Introduction. The contemporary energy and environmental landscape is defined by a significant demand for primary energy sources. Despite the growth of renewable energy, fossil fuels continue to dominate the global energy mix [1, 2]. The International Energy Agency estimates that global energy demand could rise by 45 % by 2030 due to population growth and industrialization in developing nations. This increase would lead to higher carbon dioxide (CO_2) emissions, the primary greenhouse gas produced by fossil fuel combustion, which significantly contributes to global warming and climate change, impacting agriculture and water resources [3–5]. To address these challenges, humanity must explore sustainable, renewable, and cost-effective energy alternatives. Renewable energy systems such as solar, photovoltaic (PV), wind, hydropower, biomass and geothermal energy represent promising options. Among these, PV energy stands out as a sustainable and economically viable technology. Over the past decade, global PV installations have surged from 229 GW in 2015 to 1,177 GW by the end of 2022. That year alone, 239 GW of solar capacity was added, marking a 45 % increase compared to 2021. If this trend persists, global PV capacity could reach 800 GW by 2027 and 1 TW by 2030 [6]. The work [7] analyzes the effects of aging on PV modules, showing an annual power loss of 1 % and a resistance increase of 12.8 % over 20 years, impacting large-scale systems. The article [8] examined the effect of aging PV modules on the electrical performance of grid-connected systems, revealing a 1 % annual reduction in maximum power and a 12.8 % increase in resistance over 20 years. Projections indicate a cumulative capacity of approximately 4.7 TW, accounting for 16 % of the global electricity mix by 2050. This rapid expansion has enhanced attention on PV technology reliability, considering factors such as system configurations, module size, technology, climatic zones, and degradation mechanisms like microcracks, discoloration, hot spots, glass breakage, corrosion, and specific forms of degradation such as ultraviolet light-induced degradation, light-induced degradation, moisture-induced degradation, and Potential-Induced Degradation (PID) [9–12]. The reliability of PV modules is affected by degradation mechanisms such as PID, which significantly reduces power output, especially in rooftop installations and hot climates, and although difficult to detect through annual production data, it was clearly identified by infrared imaging and linked to a linear decrease in the performance of a 314 kWp plant [13]. Diagnostic advancements include real-time thermoelectrical models linking degradation to environmental factors [14], modified Maximum Power Point Tracking (MPPT) techniques for defect detection [15], and artificial intelligence tools enabling rapid and accurate fault diagnosis in under 9 s [16]. Studies highlight PID's substantial impact on mono- and multi-crystalline modules, with power losses of up to 18.7 % after 96 hours of stress [17], and explore its mechanisms, evaluation methods, mitigation strategies, and recovery under environmental influences [18]. The works [19–21] examine common defects in PV modules, including cell cracks and hot spots. These insights aid in improving module durability and performance monitoring. Among these, PID has been observed in all PV technologies and in almost all operating climates. It does not occur so frequently, but if it does it effect can lead to a severe performance loss within a short period PID identified as a major contributor to higher degradation rates, particularly in younger modules. With the accelerated deployment of large-scale PV plants, designers aim to boost profits while keeping investment and operational costs low. To achieve this, they increase the voltage across PV strings by connecting more modules in series. This approach reduces ohmic losses in wiring and lowers installation and operational costs by decreasing the number of cables, connectors, junction boxes, and inverters required. Consequently, PV module voltage levels have evolved from 600 V in 1990 to 1 kV in 2010, with the current industry standard being 1.5 kV. Research is ongoing to explore even higher voltage levels. Discovered in 2010, PID has been extensively studied to understand its underlying mechanisms and develop mitigation strategies. Its significance has grown in recent years due to its potential to cause severe module failures under certain conditions [22, 23]. The paper [24] studied the recombination behavior of solar modules affected by PID, and based on the findings, analyzed the relative mismatch losses of these PID-affected modules. The mismatch effect, resulting from partial shading, is highlighted in [25]. The phenomenon generated impacts the maximum power extraction technique mentioned in [26]. PID results from a high potential difference between PV cells and the module frame, particularly at the ends of PV strings in grid-connected systems. This potential difference can cause leakage currents, leading to performance degradation [27]. The trend toward higher system voltages (up to 1.5 kV) exacerbates this issue. PV systems, which consist primarily of PV strings and inverters, are characterized by electrical parameters such as open-circuit voltage (V_{oc}), short-circuit current (I_{sc}), DC voltage connecting each string to the MPPT input of the inverter, and AC voltage output from the inverter. The work [28] presents an innovative IoT-based system for fault detection in hybrid PV installations, aimed at improving reliability, grid stability, and fault management through advanced algorithms. The paper [29] proposes an optimized sensor placement model, validated through simulations, enabling precise fault detection and enhancing system reliability and maintenance. Finally, the work [30] develops a fuzzy logic-based algorithm to detect and classify 12 types of faults in PV systems, ensuring optimal energy production and improved reliability.

The goal of this work is to investigate the variations in insulation resistance at the module's glass and frame, and to map the changes in shunt resistance at the module level to identify the most vulnerable areas, characterized by lower insulation resistance values and significantly affected by PID.

This study focuses on a comparative experimental analysis conducted on two identical PV modules exposed to the same climatic conditions. A high-voltage insulation resistance tester was employed to apply a voltage stress between the terminals of one module and its metal frame while measuring the insulation resistance at various points. Subsequently, the *I-V* curves of both modules were plotted under similar climatic conditions. The objective is to examine the variation in insulation resistance at the module's glass and frame, identified as a critical factor contributing to PID.

Methods. Modeling of PV string elements. In a grid-connected PV system, inverters are designed to accommodate various input voltage ranges, typically up to 600 V, 1 kV, or even 1.5 kV, depending on standards and design specifications. This flexibility enables the maximization of power generated by PV modules. To meet these operational requirements, multiple modules are connected in series to form a PV string, ensuring that the voltage at its terminals aligns with the inverter's input range.

PV cell is the smallest component of a PV string, designed to capture irradiation and convert it into electricity through the PV effect. It serves as the core element of the PV conversion process and can be likened to a current source. When exposed to light, a PV cell generates a high current (typically ranging from 6 A to 8 A) compared to its relatively low voltage (0.4 V to 0.6 V), which results in a limited power output. Therefore, it is essential to connect multiple cells in series or parallel configurations to produce a usable power level.

We adopted a five-parameter model of PV cell. It consists of a photocurrent source (I_{ph}) generated by irradiation, placed in parallel with a diode D and a parallel resistance R_{sh}, which represents the path for leakage current at the edge of the cell, caused by impurities, electron-hole recombination, irregularities in the N-P junction thickness, and the presence of cracks in the cell. Additionally, a series resistance R_s is connected in series with these components, representing ohmic losses in the collectors, fingers, the contact resistance between the metal and semiconductor, as well as the interconnections between PV cells (Fig. 1). The photocurrent I_{ph} generated by a single PV cell is directly proportional to the incident irradiance (G, W/m²) and dependent on the temperature (T, K).

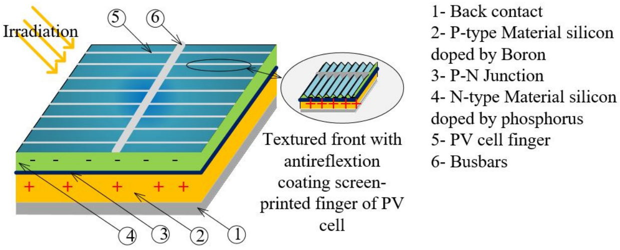

Fig. 1. PV cell

In accordance with the equivalent scheme of a PV cell (Fig. 2), and applying Kirchhoff's law, the current-voltage characteristic equation of a PV cell is:

$$I = I_{ph} - I_d - I_{sh}, \tag{1}$$

where I is the output current; I_{ph} is the photocurrent. Equations (2), (3) also define the diode current I_d and the shunt resistor current I_{sh}

$$I_d = I_{sd}\left[\exp\left(\frac{V + R_s I}{AV_t}\right) - 1\right]; \tag{2}$$

$$I_{sh} = \frac{V + R_s I}{R_{sh}}; \tag{3}$$

$$V_t = kT/q; \tag{4}$$

$$I = I_{ph} - I_{sd}\left[\exp\left(\frac{V + R_s I}{AV_t}\right) - 1\right] - \frac{V + R_s I}{R_{sh}}, \tag{5}$$

where R_s is the series resistance; A is the diode ideality factor (typically ranging from 1 to 2); R_{sh} is the shunt resistance; V_t is the thermal voltage of the diode; k is the Boltzmann constant; q is the electron charge; T is the cell temperature.

The saturation current I_{sd} is influenced by temperature, the surface area of the diode (and thus the PV cell), and the properties of the junction. It varies exponentially with temperature and can be represented as:

$$I_{sd} = I_{sc}\left(\frac{T_{op}}{T_{ref}}\right)^3 \exp\left(\frac{qE_g}{Ak}\left(\frac{1}{T_{ref}} - \frac{1}{T_{op}}\right)\right); \tag{6}$$

$$I_{ph} = I_{sc} + k_i\left(T_{op} - T_{ref}\right)\frac{G}{G_0}, \tag{7}$$

where I_{sc} is the short-circuit current of the PV cell; T_{op} is the operating temperature of the PV cell; T_{ref} is the reference temperature of the PV cell; E_g is the optical band gap of the material; k_i is the temperature coefficient at short-circuit; G_0 is the irradiance under standard test conditions; G is the irradiance under the operating conditions.

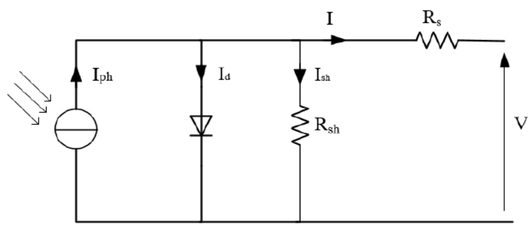

Fig. 2. Equivalent scheme of a PV cell

PV module is a device designed to capture sunlight and convert it into electricity through the PV effect. It is an essential component in PV systems. The module is made up of several identical PV cells connected in series or parallel to achieve specific required characteristics such as voltage, current, and fill factor. To obtain a usable voltage across the terminals of a PV module, the cells that constitute it must be connected in series to increase the voltage at the terminals and reduce ohmic losses. However, with this configuration of cells, in the case of partial or total shading of a cell, the current generated by that cell will decrease, leading to a reverse voltage across its terminals. This causes a local temperature increase and generates the phenomenon of hot spots, which can result in cell failures and module malfunction. Therefore, adding bypass diodes is crucial to limit this effect also to minimize the effect of shading on PV modules and reduce ohmic losses, a half-cell technology has been developed and commercialized. This technology is based on the parallel connection of identical half-cell groups, which are connected in series. PV cells are only a part of the overall laminated structure. This structure also includes components such as the module packaging (protective glass, encapsulant, backsheet), internal circuitry (electrodes, interconnections), bypass diodes, junction boxes, frame, cables, and connectors. Each of these elements can affect the reliability of the PV module (Table 1).

Table 1

Example of characteristics of a PV module

Characteristics	Value
Maximum power P_{max}, W	165
Open-circuit voltage V_{oc}, V	23.45
Short-circuit current I_{sc}, A	8.8
Voltage at maximum power V_{mpp}, V	19.4
Current at maximum power I_{mpp}, A	8.51
Maximum system voltage, V	1000
Temperature coefficient for P_{max}, %	–0.45
Number of cells connected in series N_s	36
Type of cell	polycrystalline
Number of bypass diodes in the junction box	2
Diode quality factor	1.3
Series resistance R_s, Ω	0.15
Parallel resistance R_{sh}, Ω	120
Optical band gap of the material E_g, eV	1.1

PID in PV systems. Connecting multiple PV modules in series to achieve the required voltage range for the inverter results in high voltage within the PV string. The selection and proper grounding of the DC side are crucial for ensuring the stable operation of the electrical PV system. Furthermore, to guarantee safety, the metal frames of the PV modules must be grounded (Fig. 3).

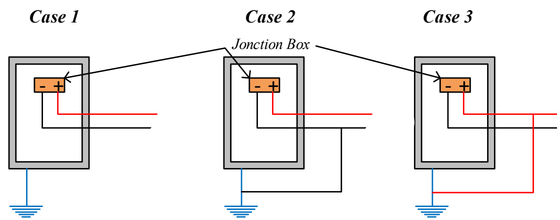

Fig. 3. Types of grounding for PV module frames

Depending on the type of inverter (with or without a transformer) and the selected grounding configuration, a significant voltage may develop between the module frames and the PV cells. This can lead to PID, which shortens the system's lifespan and may cause operational failures. The following sections outline the various inverter configurations based on grounding topologies that are adapted for PV Generator.

A floating ground. Transformerless inverters do not offer galvanic isolation between the DC and AC sides, which may lead to specific potential differences within the system. When these inverters are used, a floating ground topology is often employed, as it is the most commonly used configuration, particularly in humid areas. This approach reduces the need for complex isolation systems and lowers the installation cost. The negative voltage generated across the PV string gradually induces the PID effect through the progressive accumulation of charges. This voltage draws electrical charges toward the surface of the PV cells, disrupting their operation and leading to a loss of efficiency. Over time, the PID effect degrades the performance of PV cells, reducing their electricity production capacity.

The maximum voltage responsible for this effect, as shown in Fig. 4, is given as:

$$V_{PID} = -\frac{1}{2} n_s V_{op} , \tag{8}$$

where n_s is the number of modules in a PV string; V_{op} is the operating voltage of a PV module; V_{PID} is the PID voltage.

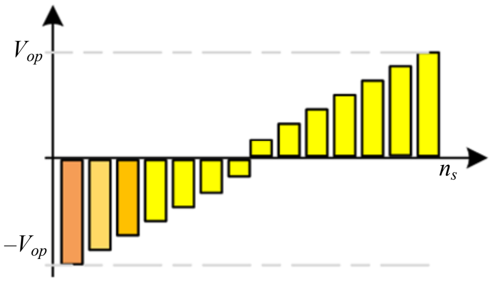

Fig. 4. Conversion with a transformerless inverter

Positive pole grounding. This topology is implemented with a transformer-based inverter that provides galvanic isolation between the DC and the AC sides. It is rarely used because it leads to a significant PID effect. This phenomenon results from the high negative voltage applied to the modules at the end of the string, this increases their susceptibility to PID, as illustrated by the negative voltage generated along the entire string, shown in Fig. 5,*a*, and represented as

$$V_{PID} = -n_s V_{op} . \tag{9}$$

Negative pole grounding. Installations located in dry or moderately humid environments favor this configuration (Fig. 5,*b*) due to the relatively low risk of corrosion compared to coastal or highly humid regions. This topology is implemented with a transformer-based inverter, providing galvanic isolation between the DC and the AC sides (Fig. 6). It ensures a positive voltage between the PV cells and the module frame, thus reducing the risk of degradation caused by PID. Furthermore, this configuration is particularly suitable for large-scale installations, as it helps extend the lifespan of the modules, although it may increase their vulnerability to corrosion.

The main cause of PID is the high voltage between the solar cells and the glass surface at the front of the module, as illustrated in the following figures.

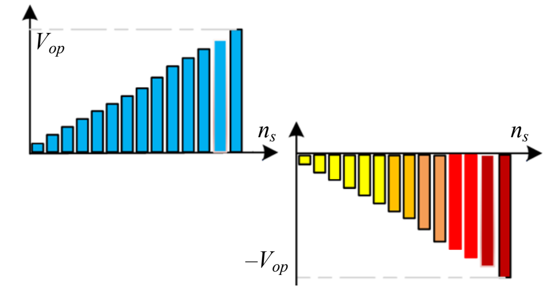

a) grounding the negative pole *b*) grounding the positive pole

Fig. 5. Conversion with transformer-based inverter

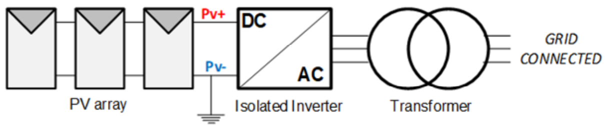

Fig. 6. Grounding topology for the negative pole of the PV string

PID affects the PV cell by increasing the leakage current. Leakage current refers to the current flowing from the base to the emitter without passing through the load (Fig. 7). This current can be categorized into 4 distinct types. First, the current may leak through the sodalime glass and the water molecules present on the surface (I_1). Second, current can leak due to electrons or ions on the upper surface of the cell (I_2). Third, leakage can occur through the ethylene-vinyl acetate (EVA) encapsulation layer (I_3). Finally, current can leak through the rear contact, thus completing the circuit (I_4).

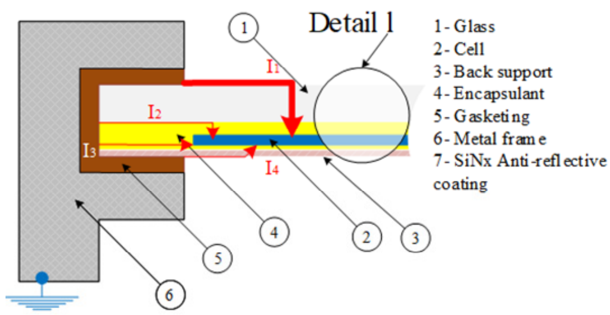

Fig. 7. Leakage current caused by the PID effect

To clearly explain PID at the cell and module levels, a voltage divider circuit is used. It is hypothesized that the intensity of the electric field in the SiNx layer plays a key role in the development of PID (Fig. 8,*a*). Three resistances, representing each layer, are connected in series to model the main path of the leakage current (glass, encapsulation sheet, and SiNx anti-reflection coating on the solar cell).

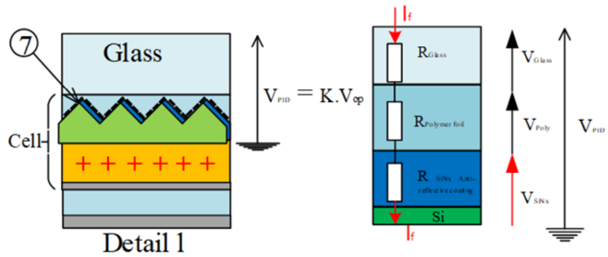

a *b*

Fig. 8. Cross-sectional modeling of a PV module

The voltage across the SiNx layer can be estimated using the model shown in Fig. 8,*b*

$$V_{SiNx} = \frac{R_{SiNx}}{R_{SiNx} + R_{Poly} + R_{Glass}} V_{PID}, \quad (10)$$

where V_{PID} is the voltage between the front glass of the module and the surface of the encapsulated silicon cells; V_{SiNx} is the voltage between layer SiNx; R_{SiNx}, R_{Poly}, R_{Glass} are respectively the resistances of SiNx layer, EVA layer and glass.

The glass or polymer layers have high resistivity, while the silicon nitride (SiNx) layers are highly conductive. This combination helps resist PID by reducing the voltage across the SiNx film. The encapsulation material surrounding the PV cells provides thermal stability, protection against moisture, UV degradation resistance, and electrical insulation for the module components. A higher overall resistivity leads to a lower leakage current for a given potential difference, which reduces the accumulation of voltage on the surface of the solar cells, thus mitigating the effects of PID. The variation in resistance between the PV cell and the module frame is a critical indicator of PID in a PV system. This measurement helps assess the module's integrity and identify anomalies related to insulation.

PID modeling. Researchers have studied how PID affects PV modules at different voltages (750 V, 500 V, 250 V) under constant conditions of 70 °C temperature and 100 g/m³ humidity. They found that the degradation over time follows an exponential pattern. At first, the degradation happens quickly, but the rate slows down over time. Eventually, the PID degradation rate becomes very small or almost zero. This behavior can be described as:

$$PID(t) = PID_{\infty}[1 - e^{-t/\tau}], \quad (11)$$

where $PID_{\infty} = \lim_{t \to \infty} PID$ is the maximum degradation level of a PV module caused by PID at infinite time; t is the PID stress duration; τ is the time constant.

PID_{∞} increases as the applied voltage rises, for instance, at 250 V, 500 V and 750 V. The value of τ indicates the rate at which PID reaches its limit. It depends on the PID resistance properties of the PV module materials and the environmental conditions. PV module with high PID resistance will have a higher τ, requiring more time to reach PID_{∞}. Conversely, a PV module with low PID resistance will have a lower τ, reaching PID_{∞} in a shorter time. Therefore, we can define:

$$R_{sh,\deg}(t) = R_{sh0} e^{(-t/\tau)}, \quad (12)$$

where $R_{sh,\deg}(t)$ is the degraded shunt resistance value corresponding to PID_{∞}

Through extensive experiments and testing, a model was developed to understand the impact of various parameters on PID. It was observed that the leakage current increases proportionally to the square of the operating voltage (panel-to-ground voltage). Similarly, the leakage current is also proportional to the square of the panel's lifespan and the square of the relative humidity. Additionally, the leakage current follows an Arrhenius relationship, with activation energy of 0.94 eV. The shunt resistance in the equivalent circuit of the PV cell models the leakage current. Its variation is fitted to the following [14]:

$$R_{sh,\deg}(t) = \frac{1}{7 \cdot 10^{-6} V_{op}^2 R_H^2 \exp\left(-\frac{90700}{RT_{avg}}\right) t^2}, \quad (13)$$

where V_{op} is the operating voltage of the panel (panel-to-ground voltage); R_H is the relative humidity; R is the gas constant; T_{avg} is the average temperature; t is the time.

The degraded shunt resistance also depends on the position of the PV cell relative to the metal frame of the PV module. When the cell is closer to the frame, the degradation rate caused by PID becomes more severe. Similarly, cells located in the corners experience an even higher intensity of degradation. To do this, a factor that characterizes this condition is added to (7), as shown in Fig. 9.

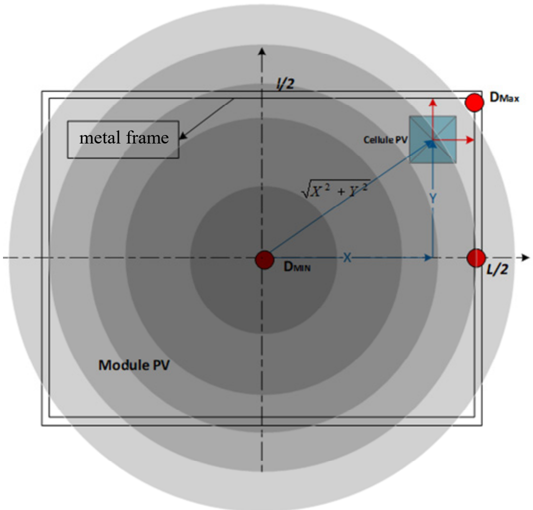

Fig. 9.The distribution of the parallel resistance of a PV cell based on its position within the PV module

At the corner of the PV module, degradation by the PID process is maximal, while at the center of the PV module, degradation is minimal. We can define a function whose lowest value is at the center of the panel and the highest value is near the edges. Therefore, the following equation determines a normalization coefficient which represents the position of PV cell encapsulated in the PV module relative to its center

$$r_{(n,m)} = \frac{\sqrt{X^2 + Y^2}}{\sqrt{(L/2)^2 + (l/2)^2}}; \quad (14)$$

$$R_{sh,\deg(n,m)} = R_{sh,\deg} \cdot r_{(n,m)}, \quad (15)$$

where $R_{sh,\deg(n,m)}$ is the degraded shunt resistance in relation to their position within the encapsulation; $r_{(n,m)}$ is the normalization coefficient; X, Y are the horizontal and vertical positions of the center of the PV module, respectively; L, l are the length and width of the PV module, respectively.

Experiments. All measurements are carried out under stable weather conditions, with uniform illumination, consistent temperature, and identical tilt angles for both modules. This method ensures measurement reliability by reducing the impact of environmental variables. The experimental parameters, such as irradiation, humidity (both high and low), air temperature and panel temperature were carefully controlled throughout the tests. The average irradiance was estimated at 800 W/m^2, and the ambient temperature was approximately 32 °C during the tests, which were conducted around noon from September 25th to 30th, a period characterized by hot and sunny days. Regarding humidity, module 1 was exposed to both dry and humid environments, with a relative humidity exceeding 85 %. This exposure was essential to analyze and compare the behavior of the two PV modules subjected to outdoor rooftop conditions for 5 years without being operational. Both modules experienced similar climatic and environmental conditions during this period. These field testing conditions differ significantly from laboratory tests conducted in accordance with the IEC 62804 standard.

We examined two identical PV modules (Module 1 and Module 2) from the same brand, exposed to the same climatic conditions (Fig. 10). For this reason, under both dry and humid conditions, we used an insulation tester Megger 5 kV to practically demonstrate how the voltage of a PV string (V_{op}) affects the insulation resistance and triggers the PID degradation process in a PV module. Initially, both modules exhibited similar *I-V* behavior under both dry and humid conditions. We applied a DC voltage of up to 1 kV between the positive terminal and carefully selected points on the metal frame and glass surface of the front of the PV module to measure the corresponding insulation resistance. This test helps determine whether the PV module maintains adequate insulation or shows signs of degradation that could impact its long-term performance. Moreover, while ensuring similar climatic conditions, we conducted voltage and current measurements at several operating points of both Module 1 and Module 2. This allowed us to plot their *I-V* characteristic curves, providing an overview of their performance. It also illustrated how the voltage in a PV string affects insulation resistance and triggers the PID process.

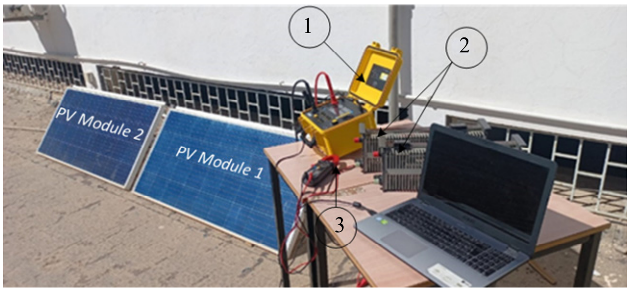

Fig. 10. An experimental test bench with two PV modules:
1 – insulation tester; 2 – two variable resistors, each rated at 10 A;
3 – ammeters and voltmeters

Measurements and results. The insulation resistance of a PV module is significantly influenced by the applied test voltage. For this reason, under dry or humid conditions, we applied different levels of DC voltage between the positive terminal of the PV module and its metal frame, while accurately measuring the corresponding insulation resistance for each voltage level, as shown in Fig. 11, 12. The purpose of this test is to simulate the module's real operating conditions by subjecting it to voltages generated by the Megger, similar to those it encounters during its actual operation in a PV string.

The insulation resistance of the module (Table 2) indicates that an increase in the test voltage leads to a decrease in the insulation resistance. Furthermore, a humid environment also causes a significant reduction in this insulation resistance compared to the value measured in a dry environment.

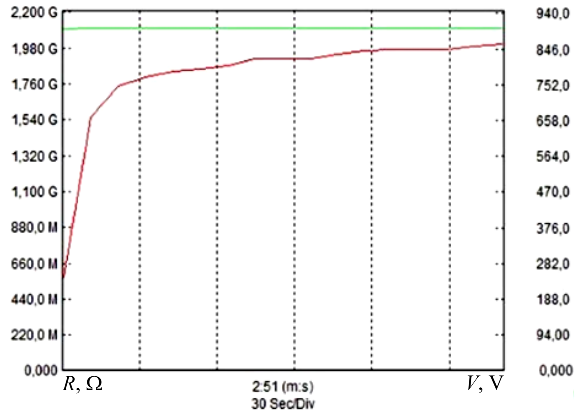

Fig. 11. Insulation resistance of the module under of 1 kV DC in a damp environment

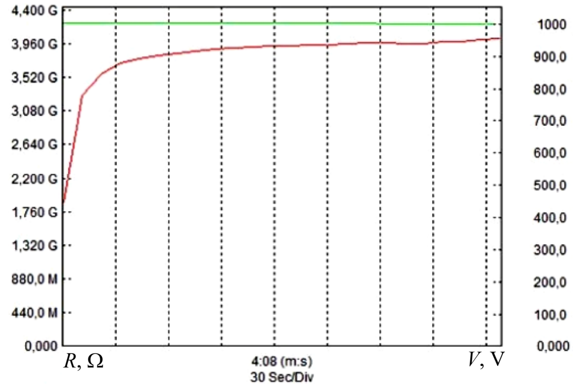

Fig. 12. Insulation resistance of the module under of 1 kV DC in a dry environment

Table 2

Isolation resistance values for dry and damp conditions

	Insulation resistance, GΩ	
Applied voltage, V	Dry environment	Damp environment
500	4.24	2.47
700	4.17	2.19
900	4.13	1.98
1000	3.96	1.76

The degradation rate D is:

$$D = \left(1 - \frac{P_{M1\max}}{P_{M2\max}}\right) \cdot 100\% \,, \qquad (14)$$

where $P_{M1\max}$, $P_{M2\max}$ are the maximum power generated by Module 1 and Module 2, respectively.

The theoretical maximum power of the module shows degradation, dropping from 142 W before testing to 123 W after dry condition tests, representing a decrease of 11 W or a degradation rate of 7.7 %. Conversely, after wet condition tests, the power reaches 123 W, reflecting a drop of 19 W, equivalent to a degradation rate of 13 %. This reduction in theoretical maximum power is attributed to the decrease in short-circuit current (I_{sc}), as shown in Table 3.

Table 3

Values of V_{oc} and I_{sc} before and after dry and wet testing

	Not stressed module	Dry env. stressed module	Humid env. stressed module
V_{oc}, V	20.1	19.93	20.91
I_{sc}, A	7.07	6.58	5.91
$P_{\max}$, W	142.107	131.139	123.578

The increase in open-circuit voltage (V_{oc}) under wet conditions is due to the reduction in module temperature caused by these testing conditions. It can be concluded in this section that the reduction in insulation resistance may increase the electric field within the SiNx layer, potentially causing polarization of this layer. Such polarization can interfere with current generation, leading to a loss of efficiency in the PV module due to PID.

The procedure for the insulation resistance test involves selecting specific measurement points on the module. Three points (no. 2, no. 3, no. 4) are chosen diagonally on the front glass surface, with a lengthwise spacing of 25.4 cm and a widthwise spacing of 11 cm (Fig. 13). Additionally, two points are identified on the aluminum frame: point no. 1 is located at the top-right corner of the frame, while point no. 5 is positioned at the center of the right vertical rail. Once these points are established, the resistance between the module's positive terminal and each of these points is measured. The measurements are conducted under a dry environment and a wet environment.

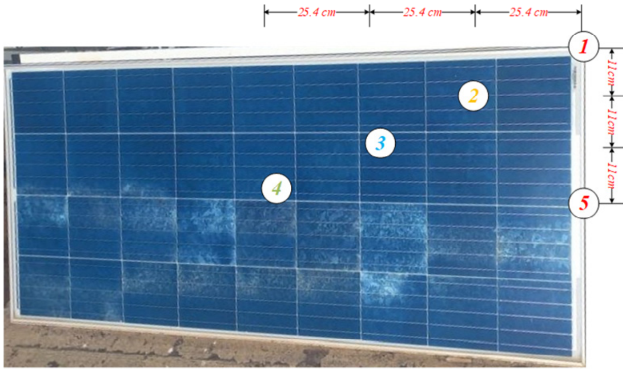

Fig. 13. Measurement points for insulation resistance test

The insulation resistance of the module, measured at different points on the glass and the frame, reveals that the resistance at the selected points on the frame is lower compared to that measured on the glass. The insulation resistance at the corner of the frame (point 1) is lower than at point 2, located in the middle of the frame's vertical rail. This indicates increased susceptibility to PID at this location. As one moves toward the center of the module, away from the frame, the insulation resistance increases, providing better protection against PID. It can be concluded that PV cells located at the corners of the module's frame are the most stressed and the first to experience the effects of PID.

Characteristics of the two modules and comparison of results. At this stage, Module 2 was chosen as the reference module, as it had not been exposed to the high voltages previously applied to Module 1. To determine the operating points of the PV module, a variable resistor was utilized. Under the same weather conditions, similar measurements were conducted simultaneously on Module 1.

By identification, R_{sh} represents the slope of the characteristic *I-V* curve of the module to the left of the maximum power point

$$I \approx I_{sc} - (V/R_{sh})\,. \quad (15)$$

In our case, R_{sh} refers to the specific value ($R_{sh} \approx 120\ \Omega$) that reflects the rate of change in current with respect to voltage before reaching the maximum power point (Fig. 14, 15).

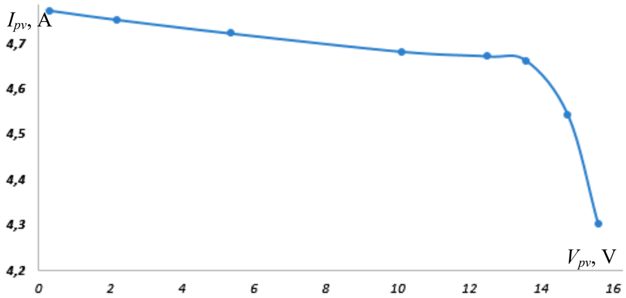

Fig. 14. *I-V* characteristics for a reference PV module

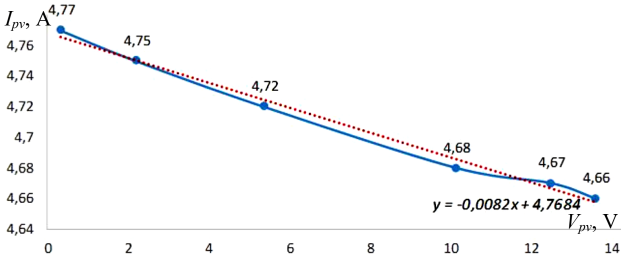

Fig. 15. R_{sh} represented by the inverse of the slope of the dashed line (unstressed module)

As shown in Fig. 16, 17, it is observed that the shunt resistance R_{sh} of the stressed Module 1 has been evaluated $R_{sh} \approx 90\ \Omega$ is lower than that of the reference Module 2. Since R_{sh} represents the resistance of the parallel paths through which current can leak when a voltage is applied, we can conclude that the R_{sh} parameter of Module 1 has been degraded due to the voltage levels applied during the tests. Additionally, our module, equipped with two bypass diodes (a 32-cell module), shows bends in the *I-V* curve, even under uniform lighting conditions. These irregularities point to the effect of PID on the module's behavior. The bypass diodes are designed to protect the cells from overloads and shading; however, the presence of these bends suggests that, despite uniform lighting, certain cells experience performance losses. This could be due to increased resistance at connection points or variations in conductivity caused by PID. This phenomenon highlights the importance of monitoring and assessing the integrity of PV modules, even when lighting conditions appear to be ideal.

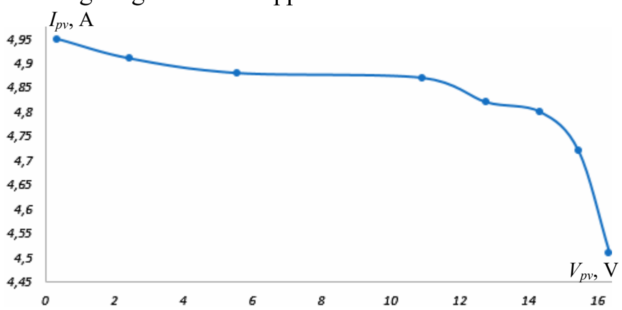

Fig. 16. *I-V* characteristics of PV stressed module

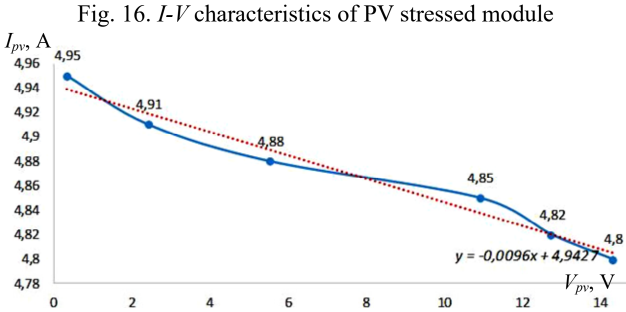

Fig. 17. R_{sh} represented by the inverse of the slope of the dashed line (stressed module)

Discussion. The test results conducted on the PV modules reveal several key aspects related to their performance and lifespan. The anomalies observed in the *I-V* characteristic curves, even under uniform illumination, suggest that PID negatively impacts the functioning of the cells. This implies that certain cells may be less efficient, leading to a reduction in the current generated. By comparing the values of R_{sh} between the reference module (Module 2) and the stressed module (Module 1), it is evident that R_{sh} in Module 1 is lower. This indicates that the parallel paths through which current can flow are compromised, which can impair the efficiency and reliability of the module. This degradation appears to be correlated with the voltages applied during the tests, emphasizing the importance of careful voltage management to maintain the performance of PV modules. The bypass diodes integrated into the module are designed to protect the cells from overheating and shading. However, the anomalies in the *I-V* curve could suggest that these diodes activate at certain times to compensate for current losses caused by PID. This raises questions about the potential for optimizing module design to better address these challenges. The results indicate that PID can have long-lasting effects on the reliability and efficiency of PV modules. Therefore, it is essential to regularly monitor their performance, with a particular focus on shunt resistance and *I-V* characteristics, in order to anticipate and address degradation issues. To reduce the impact of PID, it is recommended to choose high-quality materials, design optimized circuits, and install monitoring systems for early detection of anomalies. Additionally, a thorough evaluation of operating conditions, including voltage levels, is crucial to ensure optimal performance of PV modules.

Conclusions. This study offers a comprehensive evaluation of the performance of two identical PV modules under strictly controlled conditions, including irradiation, humidity (both high and low), air temperature, and panel temperature. The tests were conducted with an average irradiance of 800 W/m^2 and an ambient temperature of approximately 32 °C, around noon between September 25th and 30th, during hot and sunny days. By maintaining uniform illumination and stable temperature, we were able to isolate the effects of the applied voltage on the insulation resistance and electrical performance of the modules. The results indicate that an increase in test voltage leads to a decrease in insulation resistance, with a more pronounced reduction in a humid environment. Also significant decrease in the shunt resistance of the stressed module, from 120 Ω to 90 Ω, compared to the identical non-stressed module. This highlights the modules' susceptibility to potential-induced degradation, which could have significant implications for their longevity and efficiency. The analysis of the various measurement points on the modules revealed that the areas located at the corners of the frame are the most vulnerable, exhibiting lower insulation resistance values. This suggests that special attention should be given to these areas during the design and installation of PV modules. Regarding the *I-V* characteristics, the comparison between the reference module and the module subjected to high voltages showed clear signs of degradation, particularly in terms of shunt resistance. The irregularities in the *I-V* curve of the stressed module emphasize potential performance losses, even under uniform illumination. In conclusion, this study highlights the importance of regular monitoring of PV installations and continuous performance evaluation. To ensure long-term efficiency of PV systems, it is essential to explore solutions to mitigate the effects of potential-induced degradation and establish preventive maintenance protocols. Future research could focus on innovations in design and materials to minimize the vulnerability of modules to voltage-related degradation.

Conflict of interest. The authors declare that they have no conflicts of interest.

REFERENCES

1. *World Energy Outlook 2024*. International Energy Agency Publ., 2024, 398 p. Available at: https://iea.blob.core.windows.net/assets/140a0470-5b90-4922-a0e9-838b3ac6918c/WorldEnergyOutlook2024.pdf (Accessed: 30 August 2024).

2. Wiatros-Motyka M., Jones D., Fulghum N. *Global Electricity Review 2024*. Ember Publ., 2024, 191 p. Available at: https://ember-energy.org/app/uploads/2024/05/Report-Global-Electricity-Review-2024.pdf (Accessed: 30 August 2024).

3. Lyu L., Fang L. A Study on E-C Translation of BP Statistical Review of World Energy 2022 from the Perspective of Schema Theory. *Journal of Linguistics and Communication Studies*, 2023, vol. 2, no. 1, pp. 10-14. doi: https://doi.org/10.56397/JLCS.2023.03.02.

4. Fawzy S., Osman A.I., Doran J., Rooney D.W. Strategies for mitigation of climate change: a review. *Environmental Chemistry Letters*, 2020, vol. 18, no. 6, pp. 2069-2094. doi: https://doi.org/10.1007/s10311-020-01059-w.

5. Crippa M., Guizzardi D., Muntean M., Schaaf E., Solazzo E., Monforti-Ferrario F., Olivier J.G.J., Vignati E. *Fossil CO_2 emissions of all world countries - 2020 report*. Publ. Office of the EU, Luxembourg, 2020. 244 p. doi: https://doi.org/10.2760/143674.

6. Rossi R., Schmela M. *Global market outlook for solar power 2019–2023*. Solar Power Europe, Brussels, Belgium, Tech. Rep., 2019. Available at: https://www.solarpowereurope.org/insights/webinars/eu-market-outlook-solar-power-2019-2023 (Accessed: 30 August 2024).

7. Azizi A., Logerais P.-O., Omeiri A., Amiar A., Charki A., Riou O., Delaleux F., Durastanti J.-F. Impact of the aging of a photovoltaic module on the performance of a grid-connected system. *Solar Energy*, 2018, vol. 174, pp. 445-454. doi: https://doi.org/10.1016/j.solener.2018.09.022.

8. Bouaichi A., Alami Merrouni A., Hajjaj C., Messaoudi C., Ghennioui A., Benlarabi A., Ikken B., El Amrani A., Zitouni H. In-situ evaluation of the early PV module degradation of various technologies under harsh climatic conditions: The case of Morocco. *Renewable Energy*, 2019, vol. 143, pp. 1500-1518. doi: https://doi.org/10.1016/j.renene.2019.05.091.

9. Kim J., Rabelo M., Padi S.P., Yousuf H., Cho E.-C., Yi J. A Review of the Degradation of Photovoltaic Modules for Life Expectancy. *Energies*, 2021, vol. 14, no. 14, art. no. 4278. doi: https://doi.org/10.3390/en14144278.

10. Jordan D.C., Kurtz S.R. Photovoltaic Degradation Rates – an Analytical Review. *Progress in Photovoltaics: Research and Applications*, 2013, vol. 21, no. 1, pp. 12-29. doi: https://doi.org/10.1002/pip.1182.

11. Peshek T.J., Fada J.S., Martin I.T. Degradation processes in photovoltaic cells. *Durability and Reliability of Polymers and Other Materials in Photovoltaic Modules*, 2019, pp. 97-118. doi: https://doi.org/10.1016/B978-0-12-811545-9.00004-5.

12. Golive Y.R., Zachariah S., Dubey R., Chattopadhyay S., Bhaduri S., Singh H.K., Bora B., Kumar S., Tripathi A.K.,

Kottantharayil A., Vasi J., Shiradkar N. Analysis of Field Degradation Rates Observed in All-India Survey of Photovoltaic Module Reliability 2018. *IEEE Journal of Photovoltaics*, 2020, vol. 10, no. 2, pp. 560-567. doi: https://doi.org/10.1109/JPHOTOV.2019.2954777.
13. Buerhop C., Pickel T., Patel T., Fecher F.W., Zetzmann C., Camus C., Hauch J., Brabec C.J. Analysis of inhomogeneous local distribution of potential induced degradation at a rooftop photovoltaic installation. *IET Renewable Power Generation*, 2017, vol. 11, no. 10, pp. 1253-1260. doi: https://doi.org/10.1049/iet-rpg.2017.0105.
14. Nehme B.F., Akiki T.K., Naamane A., M'Sirdi N.K. Real-Time Thermoelectrical Model of PV Panels for Degradation Assessment. *IEEE Journal of Photovoltaics*, 2017, vol. 7, no. 5, pp. 1362-1375. doi: https://doi.org/10.1109/JPHOTOV.2017.2711430.
15. Ahmad J., Ciocia A., Fichera S., Murtaza A.F., Spertino F. Detection of Typical Defects in Silicon Photovoltaic Modules and Application for Plants with Distributed MPPT Configuration. *Energies*, 2019, vol. 12, no. 23, art. no. 4547. doi: https://doi.org/10.3390/en12234547.
16. Haque A., Bharath K.V.S., Khan M.A., Khan I., Jaffery Z.A. Fault diagnosis of Photovoltaic Modules. *Energy Science & Engineering*, 2019, vol. 7, no. 3, pp. 622-644. doi: https://doi.org/10.1002/ese3.255.
17. Kwembur I.M., Crozier McCleland J.L., Van Dyk E.E., Vorster F.J. Detection of Potential Induced Degradation in mono and multi-crystalline silicon photovoltaic modules. *Physica B: Condensed Matter*, 2020, vol. 581, art. no. 411938. doi: https://doi.org/10.1016/j.physb.2019.411938.
18. Luo W., Khoo Y.S., Hacke P., Naumann V., Lausch D., Harvey S.P., Singh J.P., Chai J., Wang Y., Aberle A.G., Ramakrishna S. Potential-induced degradation in photovoltaic modules: a critical review. *Energy & Environmental Science*, 2017, vol. 10, no. 1, pp. 43-68. doi: https://doi.org/10.1039/C6EE02271E.
19. Rahman M.M., Khan I., Alameh K. Potential measurement techniques for photovoltaic module failure diagnosis: A review. *Renewable and Sustainable Energy Reviews*, 2021, vol. 151, art. no. 111532. doi: https://doi.org/10.1016/j.rser.2021.111532.
20. Lee S., Bae S., Park S.J., Gwak J., Yun J., Kang Y., Kim D., Eo Y.-J., Lee H.-S. Characterization of Potential-Induced Degradation and Recovery in CIGS Solar Cells. *Energies*, 2021, vol. 14, no. 15, art. no. 4628. doi: https://doi.org/10.3390/en14154628.
21. Roy S., Kumar S., Gupta R. Investigation and analysis of finger breakages in commercial crystalline silicon photovoltaic modules under standard thermal cycling test. *Engineering Failure Analysis*, 2019, vol. 101, pp. 309-319. doi: https://doi.org/10.1016/j.engfailanal.2019.03.031.
22. Dhimish M., Badran G. Recovery of Photovoltaic Potential-Induced Degradation Utilizing Automatic Indirect Voltage Source. *IEEE Transactions on Instrumentation and Measurement*, 2022, vol. 71, pp. 1-9. doi: https://doi.org/10.1109/TIM.2021.3134328.
23. Carolus J., Tsanakas J.A., van der Heide A., Voroshazi E., De Ceuninck W., Daenen M. Physics of potential-induced degradation in bifacial p-PERC solar cells. *Solar Energy Materials and Solar Cells*, 2019, vol. 200, art. no. 109950. doi: https://doi.org/10.1016/j.solmat.2019.109950.
24. Wang H., Cheng X., Yang H., He W., Chen Z., Xu L., Song D. Potential-induced degradation: Recombination behavior, temperature coefficients and mismatch losses in crystalline silicon photovoltaic power plant. *Solar Energy*, 2019, vol. 188, pp. 258-264. doi: https://doi.org/10.1016/j.solener.2019.06.023.
25. Srinivasan A., Devakirubakaran S., Meenakshi Sundaram B. Mitigation of mismatch losses in solar PV system – Two-step reconfiguration approach. *Solar Energy*, 2020, vol. 206, pp. 640-654. doi: https://doi.org/10.1016/j.solener.2020.06.004.
26. Zied K., Hechmi K., Hedi M.M., Abderrahmen Z. Efficiency of different control algorithms for a PV panel. *2022 IEEE International Conference on Electrical Sciences and Technologies in Maghreb (CISTEM)*, 2022, pp. 1-6. doi: https://doi.org/10.1109/CISTEM55808.2022.10043961.
27. Khammassi Z., Chrouta J., Moulehi M.H., Zaafouri A. Comparative study of different types of PV plant grounding on the Potential Induced Degradation. *2023 9th International Conference on Control, Decision and Information Technologies (CoDIT)*, 2023, pp. 2677-2682. doi: https://doi.org/10.1109/CoDIT58514.2023.10284498.
28. Shweta R., Sivagnanam S., Kumar K.A. Fault detection and monitoring of solar photovoltaic panels using internet of things technology with fuzzy logic controller. *Electrical Engineering & Electromechanics*, 2022, no. 6, pp. 67-74. doi: https://doi.org/10.20998/2074-272X.2022.6.10.
29. Latreche S., Khenfer A., Khemliche M. Sensors placement for the faults detection and isolation based on bridge linked configuration of photovoltaic array. *Electrical Engineering & Electromechanics*, 2022, no. 5, pp. 41-46. doi: https://doi.org/10.20998/2074-272X.2022.5.07.
30. Lahiouel Y., Latreche S., Khemliche M., Boulemzaoud L. Photovoltaic fault diagnosis algorithm using fuzzy logic controller based on calculating distortion ratio of values. *Electrical Engineering & Electromechanics*, 2023, no. 4, pp. 40-46. doi: https://doi.org/10.20998/2074-272X.2023.4.06.

Received 01.12.2024
Accepted 25.01.2025
Published 02.07.2025

Z. Khammassi [1], *PhD,*
H. Khaterchi [1], *PhD,*
A. Zaafouri [1], *Professor of Electrical Engineering,*
[1] University of Tunis,
Higher National Engineering School of Tunis,
Industrial Systems Engineering and Renewable Energies Research Laboratory, Tunisia,
e-mail: ziedkhammassi@yahoo.fr (Corresponding Author);
hechmi.khaterchi@uvt.tn; rhaiem.zaafouri@ensit.rnu.tn

How to cite this article:
Khammassi Z., Khaterchi H., Zaafouri A. Experimental analysis of the effects of potential-induced degradation on photovoltaic module performance parameters. *Electrical Engineering & Electromechanics*, 2025, no. 4, pp. 35-43. doi: https://doi.org/10.20998/2074-272X.2025.4.05

UDC 621.319 https://doi.org/10.20998/2074-272X.2025.4.06

I. Kovacova, D. Kovac

Designing the optimal number of active branches in a multi-branch buck-boost converter

Introduction. *Multi-branch buck-boost converters, widely used in energy conversion from alternative sources, offer significant advantages over single-branch configurations. Critical, however, is the question of the appropriate number of branches for optimal efficiency and the given output power of the converter.* ***The novelty*** *of the proposed work consists in the development of a precise method for determining the optimal number of branches in a multi-branch buck-boost converter for a specified output power. Additionally, the findings enable the development of adaptive control strategies that dynamically adjust the number of active branches based on the converter's instantaneous power. This approach enhances the overall efficiency of the converter.* ***Goal.*** *The study aims to analyze the efficiency of multi-branch buck-boost converters, focusing on the optimal number of branches and the required output power.* ***Methods.*** *The problem was addressed through a theoretical analysis of the converter's electrical equivalent circuit. The theoretical results were validated through practical measurements conducted on a prototype converter.* ***Results.*** *A detailed equivalent circuit for the converter was developed and analyzed for various operational modes. Based on this analysis, the converter's losses were quantified, and a relationship was derived to determine the optimal number of parallel branches, taking into account the desired output power.* ***Practical value.*** *The findings provide guidelines for selecting the optimal number of branches in a multi-branch buck-boost converter based on the desired output power. Furthermore, they enable the implementation of adaptive switching strategies to maximize the converter's efficiency.* References 22, table 2, figures 20.

Key words: **multi-branch buck-boost converter, power losses, efficiency.**

Вступ. *Багатогілкові понижувально-підвищувальні перетворювачі, що широко використовуються в перетворенні енергії з альтернативних джерел, пропонують значні переваги порівняно з одногілковими конфігураціями. Однак критичним є питання відповідної кількості гілок для оптимальної ефективності та заданої вихідної потужності перетворювача.* ***Новизна*** *запропонованої роботи полягає в розробці точного методу визначення оптимальної кількості гілок у багатогілковому понижувально-підвищувальному перетворювачі для заданої вихідної потужності. Крім того, отримані результати дозволяють розробляти адаптивні стратегії керування, які динамічно регулюють кількість активних гілок на основі миттєвої потужності перетворювача. Такий підхід підвищує загальну ефективність перетворювача.* ***Метою*** *дослідження є аналіз ефективності багатогілкових понижувально-підвищувальних перетворювачів, зосереджуючись на оптимальній кількості гілок та необхідній вихідній потужності.* ***Методи.*** *Проблему вирішено за допомогою теоретичного аналізу електричної еквівалентної схеми перетворювача. Теоретичні результати перевірені за допомогою практичних вимірювань, проведених на прототипі перетворювача.* ***Результати.*** *Була розроблена та проаналізована детальна еквівалентна схема перетворювача для різних режимів роботи. На основі цього аналізу було кількісно визначено втрати перетворювача та виведено співвідношення для визначення оптимальної кількості паралельних гілок з урахуванням бажаної вихідної потужності.* ***Практична значимість.*** *Отримані результати надають рекомендації щодо вибору оптимальної кількості гілок у багатогілковому понижувально-підвищувальному перетворювачі на основі бажаної вихідної потужності. Крім того, вони дозволяють реалізувати адаптивні стратегії перемикання для максимізації ефективності перетворювача.* Бібл. 22, табл. 2, рис. 20.

Ключові слова: **багатогілковий понижувально-підвищувальний перетворювач, втрати потужності, ефективність.**

Introduction. Multi-branch DC/DC converters offer several advantages over their single-branch counterparts. Key benefits include significantly reduced output current ripple at the same switching frequency [1–4], a narrower range of operation in discontinuous current modes [5–8], and increased energy conversion efficiency from input to output [9–11]. This is achieved by eliminating operational intervals where energy is merely stored within the converter without being transferred to the output.

However, the optimal number of active branches in these multi-branch configurations remains an open question [12, 13]. The study **aims** to analyze the efficiency of multi-branch buck-boost converters, focusing on the optimal number of branches and the required output power. Addressing this issue requires an analysis focused on maximizing the converter's efficiency. Therefore, the subsequent sections provide a detailed analysis of the calculation for the optimal number of active branches, considering both buck and boost operating modes. The topology of such a converter is illustrated in Fig. 1.

Analysis of buck-boost converter operation in buck mode and associated losses. The configuration of the analyzed converter operating in step-down (buck) mode with n branches is shown in Fig. 2 [14–16]. In this case, the second transistor for the n-th branch is not considered.

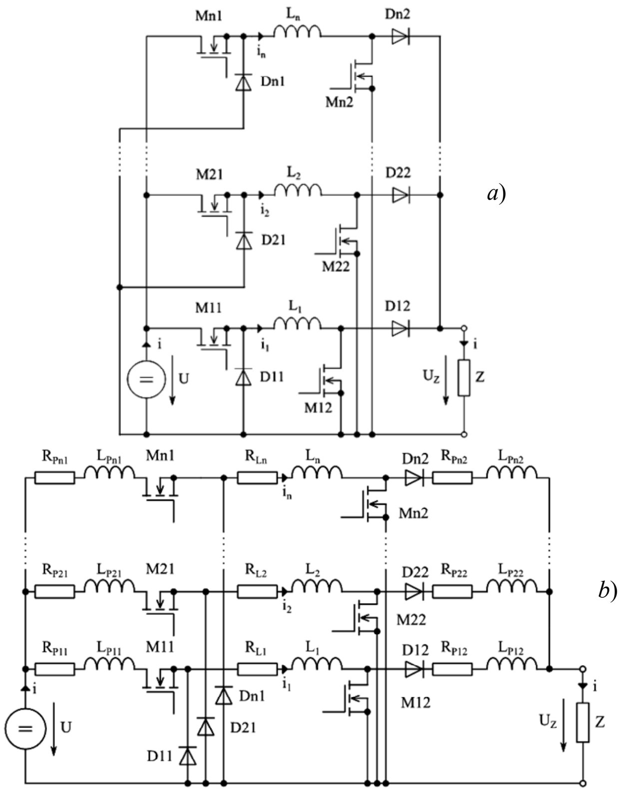

Fig. 1. Circuit diagram of the n-branch buck-boost converter
a) principle design; *b*) including parasitic elements

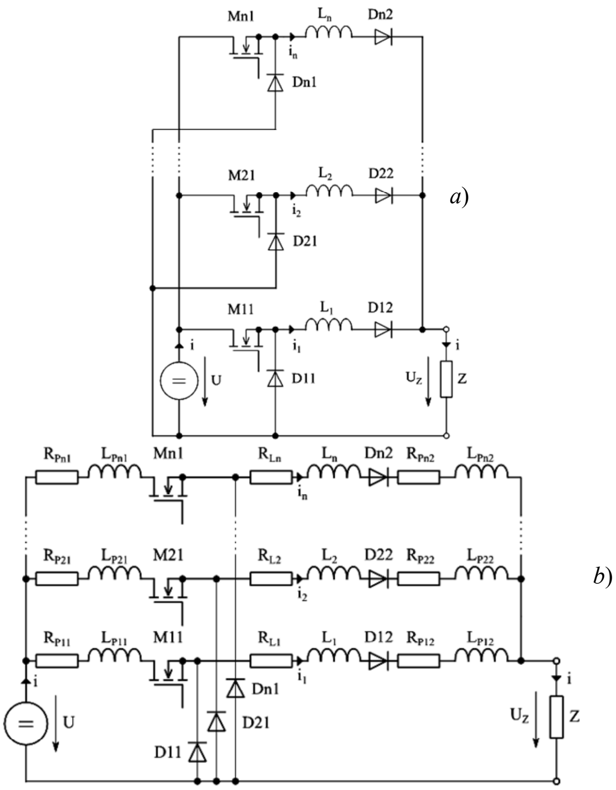

Fig. 2. Configuration of the n-branch buck-boost converter in buck mode:
a) fundamental design; *b*) including parasitic elements

All components in the circuit diagram marked with the index p represent the parasitic elements of the circuit. According to the 1st Kirchhoff's law (KCL), the currents in the circuit satisfy the equation (1):

$$i = \sum_{j=1}^{n} i_j \, . \tag{1}$$

Each branch of the converter operates with identical switching behavior, but the control signals for individual branches are time-shifted relative to each other by an interval of T/n, where T is the switching period and n is the number of branches in the converter [17–19]. Fundamentally, the operation of each branch can be divided into two primary intervals.

1st Interval. During this phase of operation, the transistor in the branch is switched on, allowing energy to accumulate in the circuit's main inductance, which is supplied by the input voltage source with a value of U. This scenario is illustrated in Fig. 3.

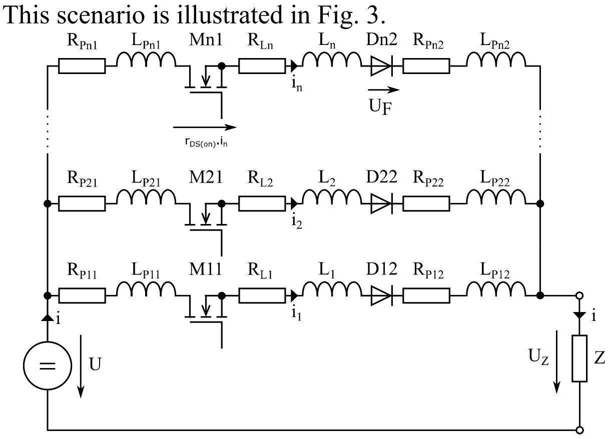

Fig. 3. Equivalent circuit for the first operational interval of the converter

For the n-th conductive loop of the converter, the equation can be written according to Kirchhoff's voltage law (KVL):

$$\begin{aligned} &-U + R_{Pn1} i_n + L_{Pn1}\frac{\mathrm{d}i_n}{\mathrm{d}t} + r_{DS(on)n} i_n + R_{Ln} i_n + \\ &+ L_n \frac{\mathrm{d}i_n}{\mathrm{d}t} + U_F + R_{Pn2} i_n + L_{Pn2}\frac{\mathrm{d}i_n}{\mathrm{d}t} + U_Z = 0, \end{aligned} \tag{2}$$

where U is the input voltage; R_{Pn1} is the resistance of the supply conductor; L_{Pn1} is the parasitic inductance of the supply conductor; $r_{\mathrm{DS(on)}}$ is the resistance of the MOSFET transistor in the on-state; R_{Ln} is the resistance of the main inductor; L_{n} is the inductance of the main inductor; U_{F} is the voltage drop across the diode; R_{Pn2} is the resistance of the conductor leading to the load; U_{Z} is the voltage across the load.

Since the described circuit contains only an ohmic-inductive load, the current waveform will take the form depicted in Fig. 4.

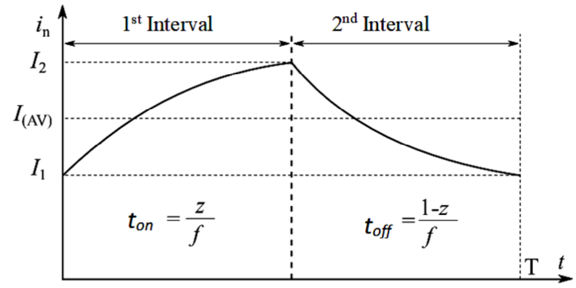

Fig. 4. Current waveform in the n-th branch

The n-th loop of the converter, shown in Fig. 3, can be simplified by concentrating the parameters:

$$U_Z = Z \cdot i = Z \cdot \sum_{i=1}^{n} i_i = Z \cdot n \cdot i_n \, ; \tag{3}$$

$$U_F = U_{TO} + r_F i_n \, ; \tag{4}$$

$$R_{n1} = R_{Pn1} + r_{DS(on)} + R_{Ln} + R_{Pn2} + r_F \, ; \tag{5}$$

$$L_{n1} = L_{Pn1} + L_n + L_{Pn2} \, , \tag{6}$$

where U_{TO} is the threshold voltage across the diode; Z is the magnitude of the load impedance; R_{n1} is the resistance of the n-th branch during the first interval; r_{F} is the forward resistance of the diode; L_{n1} is the inductance of the n-th branch during the first interval.

By considering (3) through (6), the initial equation (2) takes the following form:

$$U_{TO} - U + Z \cdot n \cdot i_n + R_{n1} i_n + L_{n1}\frac{\mathrm{d}i_n}{\mathrm{d}t} = 0 \, . \tag{7}$$

The solution to this equation, expressing the current i_n, is obtained as follows:

$$i_n = \frac{U - U_{TO}}{(R_{n1} + nZ)}\left(1 - e^{-\frac{(R_{n1}+nZ)}{L_{n1}}t}\right) + I_1 e^{-\frac{(R_{n1}+nZ)}{L_{n1}}t} \, . \tag{8}$$

If, in this temporal expression of current, the time t is substituted with $t = t_{on} = z/f$, then at this specific moment, the current i_n, as shown in Fig. 4, assumes the value I_2:

$$I_2 = \frac{U - U_{TO}}{(R_{n1} + nZ)}\left(1 - e^{-\frac{(R_{n1}+nZ)}{L_{n1}}\cdot\frac{z}{f}}\right) + I_1 e^{-\frac{(R_{n1}+nZ)}{L_{n1}}\cdot\frac{z}{f}} \, , \tag{9}$$

where z is the pulse width (duty cycle) of the converter's control; f denotes its switching frequency.

2[nd] Interval. During the 2[nd] operational interval of the converter, the transistor is switched off, allowing the energy stored in the inductance L_n to be transferred to the load through diodes D_{n1} and D_{n2} (Fig. 5).

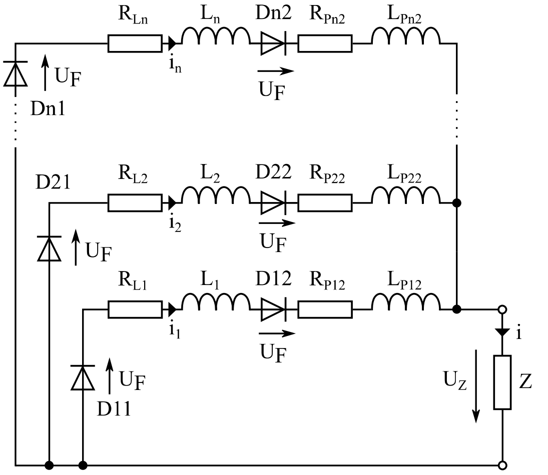

Fig. 5. Equivalent circuit diagram for the second operational interval of the converter

For the n-th conductive loop of the converter, the equation can be formulated based on KVL as follows:

$$U_Z + U_F + R_{Ln} i_n + L_n \frac{\mathrm{d}i_n}{\mathrm{d}t} + U_F + R_{Pn2} i_n + L_{Pn2} \frac{\mathrm{d}i_n}{\mathrm{d}t} = 0, \quad (10)$$

where equation (3) applies, along with the following equations:

$$R_{n2} = R_{Ln} + 2r_F + R_{Pn2}; \quad (11)$$

$$L_{n2} = L_n + L_{Pn2}. \quad (12)$$

Based on the information provided above, a modified version of (10) can be derived:

$$nZi_n + 2U_{TO} + R_{n2} i_n + L_{n2} \frac{\mathrm{d}i_n}{\mathrm{d}t} = 0. \quad (13)$$

Solving the equation yields the time-dependent behavior of the desired current i_n, which is expressed by the following formula:

$$i_n = \frac{-2U_{TO}}{(R_{n2}+nZ)}\left(1-e^{-\frac{(R_{n2}+nZ)}{L_{n2}}t}\right) + I_2 e^{-\frac{(R_{n2}+nZ)}{L_{n2}}t}. \quad (14)$$

Substituting the value of time $t = t_{off} = (1–z)/f$ into the equation provides, as illustrated in Fig. 4, the expression for the current i_n with a magnitude of I_1:

$$I_1 = \frac{-2.U_{TO}}{(R_{n2}+nZ)}\left(1-e^{-\frac{(R_{n2}+nZ)}{L_{n2}}\cdot\frac{(1-z)}{f}}\right) + I_2 e^{-\frac{(R_{n2}+nZ)}{L_{n2}}\cdot\frac{(1-z)}{f}}. \quad (15)$$

Based on (9) and (15), it is possible to derive expressions for the initial values of currents I_1 and I_2 at the beginning of both intervals of the converter. These values are determined solely by the circuit parameters. The value of current I_2 from (9) is substituted into (15), resulting in the following expression:

$$I_1 = \frac{-2.U_{TO}}{(R_{n2}+nZ)}\left(1-e^{-\frac{(R_{n2}+nZ)}{L_{n2}}\cdot\frac{(1-z)}{f}}\right) + \left(\frac{U-U_{TO}}{(R_{n1}+nZ)}\left(1-e^{-\frac{(R_{n1}+nZ)}{L_{n1}}\cdot\frac{z}{f}}\right) + I_1 e^{-\frac{(R_{n1}+nZ)}{L_{n1}}\cdot\frac{z}{f}}\right) e^{-\frac{(R_{n2}+nZ)}{L_{n2}}\cdot\frac{(1-z)}{f}}. \quad (16)$$

The final expression for the current I_1 value is obtained after manipulating (16) in the following form:

$$I_1 = \frac{\left(\frac{-2U_{TO}}{(R_{n2}+nZ)}\left(1-e^{-\frac{(R_{n2}+nZ)}{L_{n2}}\cdot\frac{(1-z)}{f}}\right) + \left(\frac{U-U_{TO}}{(R_{n1}+nZ)}\left(1-e^{-\frac{(R_{n1}+nZ)}{L_{n1}}\cdot\frac{z}{f}}\right) e^{-\frac{(R_{n2}+nZ)}{L_{n2}}\cdot\frac{(1-z)}{f}}\right)\right)}{\left(1-e^{-\frac{(R_{n1}+nZ)}{L_{n1}}\cdot\frac{z}{f}} \cdot e^{-\frac{(R_{n2}+nZ)}{L_{n2}}\cdot\frac{(1-z)}{f}}\right)}. \quad (17)$$

The magnitude of the current I_2 is determined by substituting (17) into (9):

$$I_2 = \frac{U-U_{TO}}{(R_{n1}+nZ)}\left(1-e^{-\frac{(R_{n1}+n.Z)}{L_{n1}}\cdot\frac{z}{f}}\right) + \frac{\left(\frac{-2U_{TO}}{(R_{n2}+nZ)}\left(1-e^{-\frac{(R_{n2}+nZ)}{L_{n2}}\cdot\frac{(1-z)}{f}}\right) + \left(\frac{U-U_{TO}}{(R_{n1}+nZ)}\left(1-e^{-\frac{(R_{n1}+nZ)}{L_{n1}}\cdot\frac{z}{f}}\right) e^{-\frac{(R_{n2}+nZ)}{L_{n2}}\cdot\frac{(1-z)}{f}}\right)\right)}{\left(\frac{1}{e^{\frac{(R_{n1}+nZ)}{L_{n1}}\cdot\frac{z}{f}}} - e^{-\frac{(R_{n2}+nZ)}{L_{n2}}\cdot\frac{(1-z)}{f}}\right)}. \quad (18)$$

Based on (8), (14), (17), (18), the time-dependent current through any branch of a multi-phase buck-boost converter can be expressed.

However, determining the optimal number of branches for the converter also requires calculating the total losses in the system as a function of the number of branches. These losses are categorized into steady-state losses, occurring during both operating intervals, and dynamic losses, arising during transient processes. The composition and notation for these losses are as follows:

Steady-state losses:

P_{RPn1} – losses due to the resistance of the input conductor in the n^{th} branch.
P_{MF} – losses on the MOSFET transistor in the ON state.
P_{MR} – losses on the MOSFET transistor in the OFF state.
P_{RLn} – losses due to the resistance of the inductor in the n^{th} branch.
P_{DF} – losses on the diode in the ON state.
P_{DR} – losses on the diode in the OFF state.
P_{RPn2} – losses due to the resistance of the output conductor in the n^{th} branch.

Dynamic losses:

P_{Mon} – switching losses on the MOSFET transistor during turn-on.
P_{Moff} – switching losses on the MOSFET transistor during turn-off.
P_{DQR} – switching losses on the diode during turn-off.
P_{DQF} – switching losses on the diode during turn-on.

Considering standard waveforms for the switching processes and using (1), the total losses P_C of the converter can be expressed as:

$$P_C = P_{RPn1} + P_{MF} + P_{MR} + P_{RLn} + P_{DF} + P_{DR} + P_{RPn2} + P_{Mon} + P_{Moff} + P_{DQR} + P_{DQF}. \quad (19)$$

The average value of the current in a branch of the converter can be determined as:

$$I_{n(AV)} = (I_1 + I_2)/2 = I/n\,, \tag{20}$$

where I is the average current of the converter. Based on this, the total losses of the converter can be expressed as:

$$\begin{aligned} P_C = {} & nR_{Pn1}\left(I_{n(AV)}\right)^2 z + nr_{DS(on)}\left(I_{n(AV)}\right)^2 z + nUI_{DS}(1-z) + \\ & + nR_{Ln}\left(I_{n(AV)}\right)^2 + 2n\left(U_{TO} + r_F\left(I_{n(AV)}\right)\right)I_{n(AV)}(1-z) + \\ & + n\left(U_{TO} + r_F\left(I_{n(AV)}\right)\right)I_{n(AV)}z + nUI_R z + nR_{Pn2}\left(I_{n(AV)}\right)^2 + \\ & + 0{,}5nUI_1 t_{on} f + 0{,}5nUI_2 t_f f + 0{,}5nQ_{rr}Uf + 0{,}5nU_{FP}I_2 t_{fr} f, \end{aligned} \tag{21}$$

where $r_{DS(on)}$ is the on-state resistance of the transistor; $r_{DS(off)}$ is the off-state resistance of the transistor; I_R is the reverse current flowing through the diode; $I_{DS(off)}$ is the current flowing through the transistor during its off-state; t_{on} is the time required for the MOSFET transistor to transition from the off-state to the on-state; t_f is the time required for the MOSFET to transition from the on-state to the off-state; Q_{rr} is the reverse recovery charge of the diode; U_{FP} is the voltage across the diode during its transition from the off-state to the on-state, governed by the time constant t_{fr}.

By reformulating (21) and applying (20), a simplified final form of the expression is obtained, enabling the calculation of the total losses within the converter [20]:

$$\begin{aligned} P_C = {} & \left(\frac{I^2}{n}\right)\cdot\left(R_{Pn1}z + r_{DS(on)}z + R_{Ln} + 2r_F(1-z) + r_F z + R_{Pn2}\right) + \\ & + nUI_{DS}(1-z) + 2U_{TO}I(1-z) + U_{TO}Iz + nUI_R.z + \\ & + 0{,}5nUI_1 t_{on} f + 0{,}5nUI_2 t_f f + 0{,}5nQ_{rr}Uf + 0{,}5nU_{FP}I_2 t_{fr} f. \end{aligned} \tag{22}$$

The efficiency of the converter can then be expressed by the following equation:

$$\eta = \frac{P_{output}}{P_{input}} = \frac{P_{input} - P_C}{P_{input}} = 1 - \frac{P_C}{P_{input}} = 1 - \frac{P_C}{UI}\,. \tag{23}$$

From (23), it is evident that overall efficiency is primarily influenced by the total power losses. These losses can be minimized through the careful selection of individual circuit components. Additionally, the total losses can be further influenced by the number of parallel branches in the converter, as the input current is distributed linearly among the branches, while resistive losses decrease quadratically. As a result, converters with multiple branches may exhibit lower overall losses compared to a single-branch configuration. However, due to the additional losses introduced by the parallel branches, the assertion that increasing the number of branches always reduces losses does not hold true universally.

Consequently, determining the optimal number of branches for a given input power requirement becomes essential (assuming constant input voltage, desired input current, and a fixed duty cycle). The converter can be dynamically managed by adjusting its topology and duty cycle to achieve maximum efficiency for any given input power level. This optimization assumes fixed construction parameters and characteristics of the converter components.

To determine the optimal number of branches, equation (22) must be differentiated. By deriving this equation with respect to n, the number of branches, it is possible to identify the local extremum, which corresponds to the number of branches that minimizes the total power losses:

$$\begin{aligned} P'_C = {} & -\left(\frac{I^2}{n^2}\right)\cdot\left(R_{Pn1}z + r_{DS(on)}z + R_{Ln} + 2r_F(1-z) + r_F z + R_{Pn2}\right) + \\ & + UI_{DS}(1-z) + UI_R z + 0{,}5UI_1 t_{on} f + 0{,}5UI_2 t_f f + \\ & + 0{,}5Q_{rr}Uf + 0{,}5U_{FP}I_2 t_{fr} f. \end{aligned} \tag{24}$$

If the result of the differentiation is set equal to zero and solved for n, the equation takes the following form:

$$n = I\cdot\sqrt{\frac{\begin{pmatrix} R_{Pn1}z + r_{DS(on)}z + R_{Ln} + \\ + 2r_F(1-z) + r_F z + R_{Pn2} \end{pmatrix}}{\begin{pmatrix} UI_{DS}(1-z) + UI_R z + 0{,}5UI_1 t_{on} f + \\ + 0{,}5UI_2 t_f f + 0{,}5Q_{rr}Uf + 0{,}5U_{FP}I_2 t_{fr} f \end{pmatrix}}}\,. \tag{25}$$

The above discussion indicates that, based on (25), the optimal number of branches for a buck-boost converter operating in buck mode can be determined using its design and operational parameters. This ensures that the converter delivers maximum power to the load under all operating conditions.

Experimental results. To verify the derived results, a single-branch and a three-branch buck-boost converter with resistive load R were implemented. The circuit diagram of the single-branch buck converter is shown in Fig. 6.

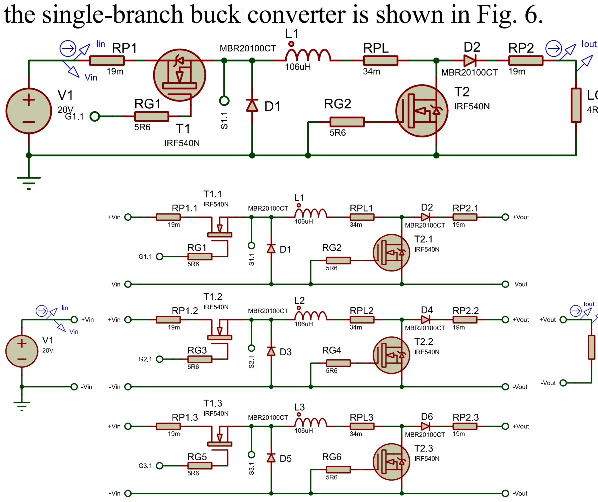

a)

b)

Fig. 6. Schematic of the implemented
a) 1-branch; *b*) 3-branches converter

The operational and design parameters of the converter are as follows: U=20 V, R_{pn1}=19 mΩ, L_{pn1}=1.5 μH, R_{Ln}=34 mΩ, L_n=106 μH, R_{pn2}=19 mΩ, L_{pn2}=0 H, $r_{DS(ON)}$=77 mΩ, I_{DS}=2.25 mA, t_{ON}=55 ns, t_f=96 ns, f=50 kHz, r_F=34 mΩ, U_{TO}=0.43 V, I_R=6 mA, Q_{rr}=0 C, U_{FP}=0 V, t_{fr}=2 ns, $Z = R$ = 4.5 Ω, The catalog data for the MOSFET IRF540N and the diode MBR20100CT were used in the implementation. The example of a practical implementation of the converter is shown in Fig. 7 [21].

a)

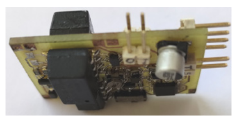

b)

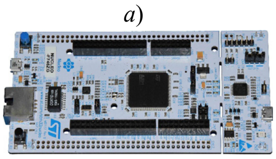

c)

Fig. 7 Practical realization:
a) 3 branch buck-boost converter;
b) galvanic separation;
c) control development board Nucleo-F746ZG

The waveforms of the measured main quantities for different input power levels (i.e., duty cycle values) and for different configurations of the number of phases are presented in Fig. 8 – 13. For all oscillograms, the following applies:
C1 – 900 mA/div: input current; C2 – 7 V/div: input voltage;
C3 – 900 mA/div: output current; C4 – 4 V/div: output voltage;
M1 – average input power; M2 – average output power;
M3 – average efficiency.

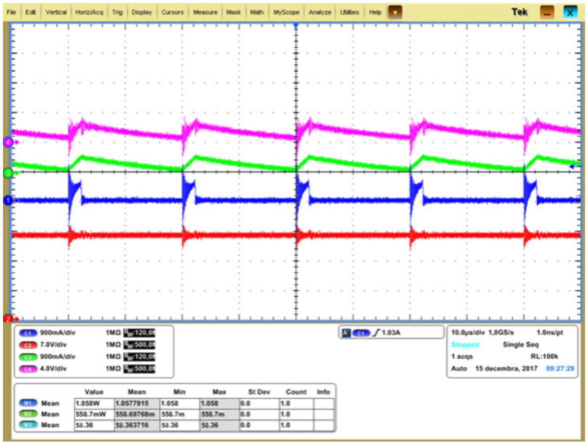

Fig. 8. Measured time waveforms of voltages and currents for the single-phase buck-boost converter in buck mode with 1 W input power

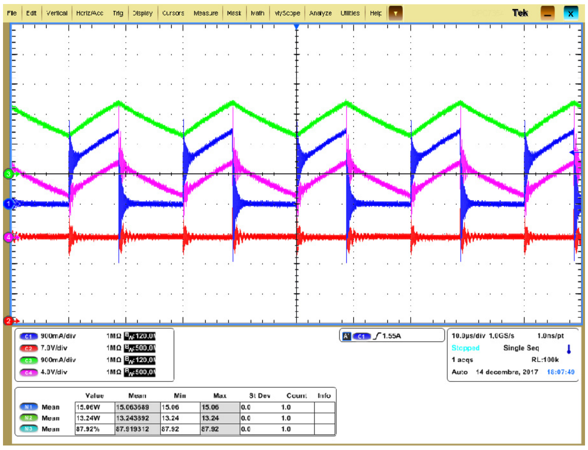

Fig. 9. Measured time waveforms of voltages and currents for the single-phase buck-boost converter in buck mode with 15 W input power

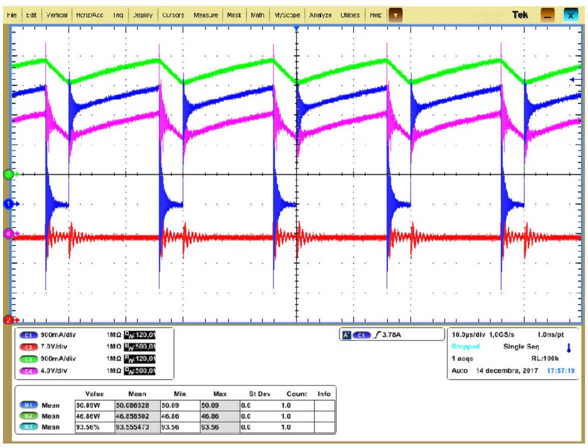

Fig. 10. Measured time waveforms of voltages and currents for the single-phase buck-boost converter in buck mode with 50 W input power

Based on the equations provided above and the parameters of the converter's equivalent circuit, the theoretical efficiency of the buck-boost converter in buck mode at a given power input can be calculated. The results obtained in this manner are presented in Table 1, where they are compared with the measurement results.

To provide a clearer understanding of the obtained results, graphs have been created (Fig. 14, 15).

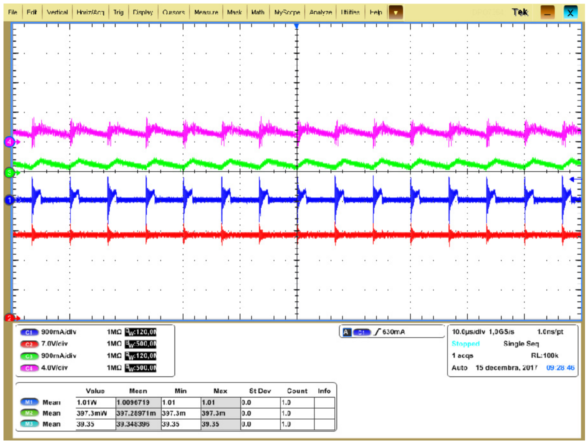

Fig. 11. Measured time waveforms of voltages and currents for the three-phase buck-boost converter in buck mode with 1 W input power

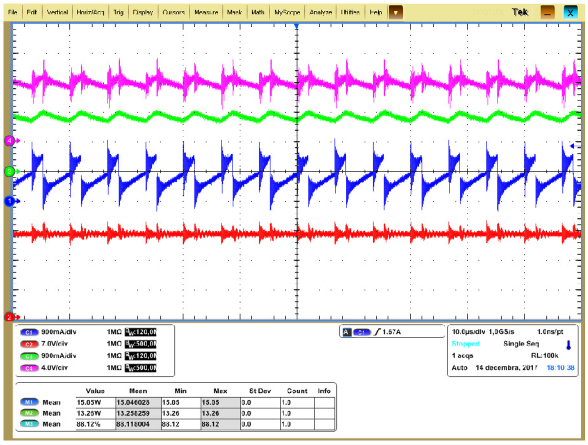

Fig. 12. Measured time waveforms of voltages and currents for the three-phase buck-boost converter in buck mode with 15 W input power

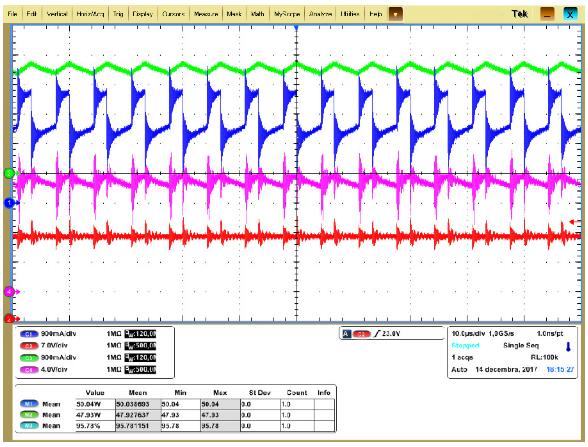

Fig. 13. Measured time waveforms of voltages and currents for the three-phase buck-boost converter in buck mode with 50 W input power

The comparison of results obtained through calculations, simulations, and measurements shows a sufficient agreement, indicating that the theoretically derived equations can be considered correct. The deviation between the calculated and measured efficiency values is less than 3 %. From this, it can be inferred that (22) is valid, and consequently, equation (25) for determining the optimal number of branches in a multi-branch buck-boost converter in the buck mode is also valid.

Table 1

Summary of results obtained from calculations and measurements

Single-phase converter in buck mode			
Calculated		Measured	
P_1, W	Efficiency, %	P_1, W	Efficiency, %
1,05	58,39	1,058	56,36
5,05	80,02	5,056	78,23
10,08	85,4	10,08	85,49
15,01	87,75	15,06	87,92
20	89,17	20,07	89,33
30	90,78	30,08	91,16
40	91,71	40,06	92,38
50,1	92,32	50,09	93,56
Three-phase converter in buck mode			
Calculated		Measured	
P_1, W	Efficiency, %	P_1, W	Efficiency, %
1,02	41,92	1,01	39,35
5	77,11	5	75,71
10,02	84,96	10,02	84,72
15,07	88,33	15,05	88,12
20,04	90,25	20,09	91,08
30,07	92,44	30,00	93,47
40,03	93,65	40,04	94,95
50	94,4	50,04	95,78

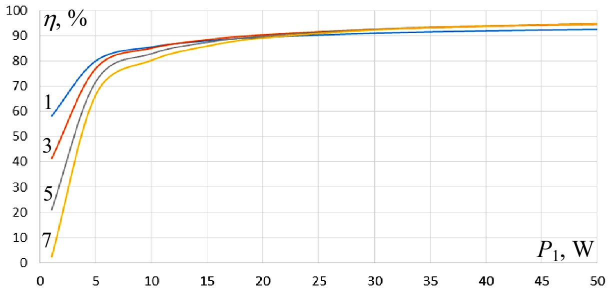

Fig. 14. Calculated efficiency of the converter as a function of input power and number of branches (1, 3, 5, 7)

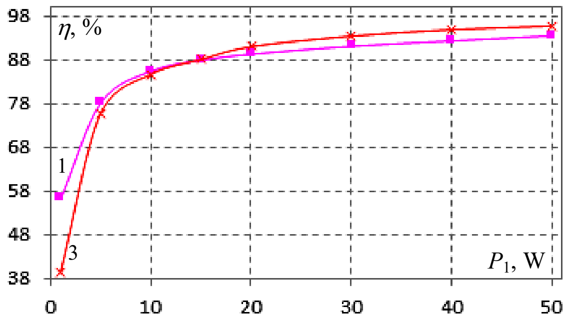

Fig. 15. Measured efficiency of the converter as a function of input power and number of branches (1, 3)

To illustrate the implications of the calculated results, Fig. 16 presents the computed dependence of the converter's efficiency on its output power for a higher-power converter. The implementation of this converter assumes the use of the following components: IRG4PH50S-EPbF and BYV29-500, alongside the circuit parameters: U=200 V, R_{pn1}=19 mΩ, L_{pn1}=1.5 μH, R_{Ln}=34 mΩ, L_n=330 μH, R_{pn2}=19 mΩ, L_{pn2}=1 μH, $r_{DS(ON)}$=47 mΩ, I_{DS}=1 mA, t_{ON}=61 ns, t_f=1270 ns, f=50 kHz, r_F=19 mΩ, U_{TO}=0.7 V, I_R=50 μA, Q_{rr}=40 nC, U_{FP}=2.5 V, t_{fr}=200 ns, $Z = R = 10$ Ω.

The figure illustrates that the efficiency difference between the single-branch and seven-branch configurations of the 3 kW converter can reach up to 5 % at an output power of 500 W.

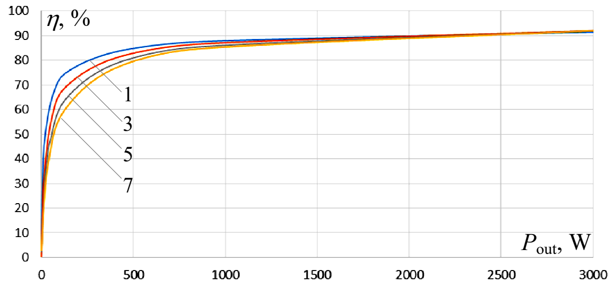

Fig. 16. Calculated efficiency of the higher power converter as a function of output power and number of branches (1, 3, 5, 7)

The next subsection presents the calculation of the optimal number of branches for the boost mode.

Analysis of the operation and losses in the boost mode of a buck-boost converter. The configuration of the analyzed multi-branch buck-boost converter in boost mode with n branches is shown in Fig. 1 [22]. Since the first transistor remains continuously open in this mode, its resistance in the closed state will be considered in the analysis of the converter.

All components in the circuit, indicated with the index p, represent parasitic elements. According to KCL, the equation (1) applies to the currents in the circuit.

Each branch of the converter operates similarly to the buck mode, where the control signals for the individual branches are time-shifted by T/n, with T being the switching period. The operation of each branch can be divided into two basic intervals.

1st Interval. During this operational interval, the transistor in the corresponding vertical branch is closed, causing energy to accumulate in the main inductance of the circuit, which is powered by the input voltage source with a value of U. This situation is depicted in Fig. 17.

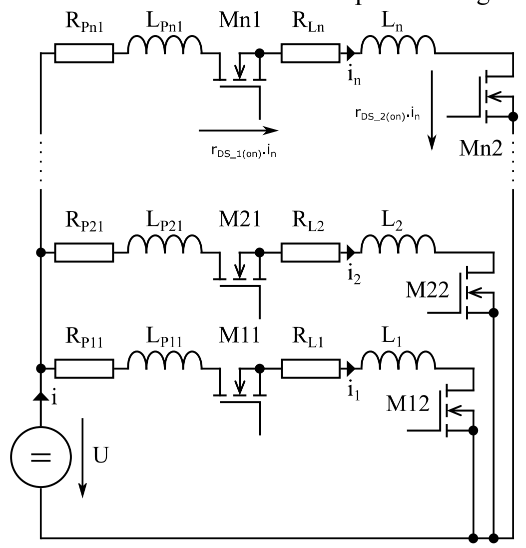

Fig. 17. Substitute diagram for the first operational interval of the converter in boost mode

For the n-th conductive loop of the converter, the equation can be formulated based on KVL as follows:

$$-U + R_{Pn1} \cdot i_n + L_{Pn1} \cdot \frac{\mathrm{d}i_n}{\mathrm{d}t} + r_{DS\_1(on)} \cdot i_n + R_{Ln} \cdot i_n + + L_n \cdot \frac{\mathrm{d}i_n}{\mathrm{d}t} + r_{DS\_2(on)} \cdot i_n = 0. \quad (26)$$

The current waveform follows the same pattern as depicted in Fig. 4. The loop of the n-th branch of the converter, as shown in Fig. 17, can be simplified using lumped parameter modeling.

$$R_{n1} = R_{Pn1} + r_{DS\_1(on)} + R_{Ln} + r_{DS\_2(on)}\,; \qquad (27)$$

$$L_{n1} = L_{Pn1} + L_n\,. \qquad (28)$$

Considering (27) and (28), the initial equation (26) takes the following form:

$$-U + R_{n1} \cdot i_n + L_{n1} \cdot \frac{\mathrm{d}i_n}{\mathrm{d}t} = 0\,. \qquad (29)$$

Its solution yields:

$$i_n = \frac{U}{R_{n1}} \cdot \left(1 - e^{-\frac{R_{n1}}{L_{n1}} \cdot t}\right) + I_1 \cdot e^{-\frac{R_{n1}}{L_{n1}} \cdot t}\,. \qquad (30)$$

If the time variable $t = t_{on} = z/f$ is substituted into this time-dependent expression for the current, the current i_n at the specified moment will, as shown in Fig. 4, attain the value I_2:

$$I_2 = \frac{U}{R_{n1}} \cdot \left(1 - e^{-\frac{R_{n1}}{L_{n1}} \cdot \frac{z}{f}}\right) + I_1 \cdot e^{-\frac{R_{n1}}{L_{n1}} \cdot \frac{z}{f}}\,. \qquad (31)$$

2[nd] Interval. In the 2[nd] operational interval of the buck-boost converter operation in boost mode, the transistor is switched off, and the energy stored in the inductance L_n is transferred to the load through the power supply and diode D_{n2}, as illustrated in Fig. 18.

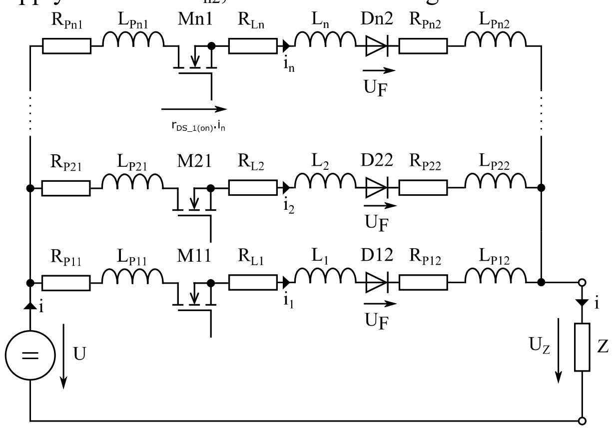

Fig. 18. Equivalent circuit for the second operational interval of the buck-boost converter in boost mode

For the n-th conductive loop of the converter, the equation can be written based on KVL as:

$$\begin{aligned} &-U + R_{Pn1} \cdot i_n + L_{Pn1} \cdot \frac{\mathrm{d}i_n}{\mathrm{d}t} + r_{DS\_1(on)} \cdot i_n + R_{Ln} \cdot i_n + \\ &+ L_n \cdot \frac{\mathrm{d}i_n}{\mathrm{d}t} + U_F + R_{Pn2} \cdot i_n + L_{Pn2} \cdot \frac{\mathrm{d}i_n}{\mathrm{d}t} + U_Z = 0, \end{aligned} \qquad (32)$$

where (3) and the following equations hold:

$$R_{n2} = R_{Pn1} + r_{DS\_1(on)} + R_{Ln} + r_F + R_{Pn2}\,; \qquad (33)$$

$$L_{n2} = L_{Pn1} + L_n + L_{Pn2}\,. \qquad (34)$$

Based on the above, the modified version of (32) can be derived.

$$-U + R_{n2} \cdot i_n + L_{n2} \cdot \frac{\mathrm{d}i_n}{\mathrm{d}t} + U_{TO} + Z \cdot n \cdot i_n = 0\,. \qquad (35)$$

The solution yields the time-dependent waveform of the desired current, expressed by the following equation:

$$i_n = \frac{U - U_{TO}}{R_{n2} + n \cdot Z}\left(1 - e^{-\frac{R_{n2} + n \cdot Z}{L_{n2}} \cdot t}\right) + I_2 e^{-\frac{R_{n2} + n \cdot Z}{L_{n2}} \cdot t}\,. \qquad (36)$$

By substituting the time variable $t = t_{off} = (1–z)/f$, the expression for the current i_n with a magnitude of I_1 is obtained, as shown in Fig. 18:

$$I_1 = \frac{U - U_{TO}}{R_{n2} + n \cdot Z}\left(1 - e^{-\frac{R_{n2} + n \cdot Z}{L_{n2}} \cdot \frac{1-z}{f}}\right) + I_2 e^{-\frac{R_{n2} + n \cdot Z}{L_{n2}} \cdot \frac{1-z}{f}}\,. \qquad (37)$$

Based on (31) and (37), expressions for the initial values of currents I_1 and I_2 at the beginning of both converter intervals can be derived, with these values determined solely by the circuit parameters. The current I_2 from (31) is substituted into (37):

$$\begin{aligned} I_1 = {} & \frac{U - U_{TO}}{R_{n2} + n \cdot Z} \cdot \left(1 - e^{-\frac{R_{n2} + n \cdot Z}{L_{n2}} \cdot \frac{1-z}{f}}\right) + \\ & + \left(\frac{U}{R_{n1}} \cdot \left(1 - e^{-\frac{R_{n1}}{L_{n1}} \cdot \frac{z}{f}}\right) + I_1 e^{-\frac{R_{n1}}{L_{n1}} \cdot \frac{z}{f}}\right) \cdot e^{-\frac{R_{n2} + n \cdot Z}{L_{n2}} \cdot \frac{1-z}{f}}\,. \end{aligned} \qquad (38)$$

The final expression for the current I_1 is obtained by rearranging (38) in the following form:

$$I_1 = \frac{\left(\begin{aligned} & \frac{U - U_{TO}}{R_{n2} + n \cdot Z} \cdot \left(1 - e^{-\frac{R_{n2} + n \cdot Z}{L_{n2}} \cdot \frac{1-z}{f}}\right) + \\ & + \frac{U}{R_{n1}} \cdot \left(1 - e^{-\frac{R_{n1}}{L_{n1}} \cdot \frac{z}{f}}\right) \cdot e^{-\frac{R_{n2} + n \cdot Z}{L_{n2}} \cdot \frac{1-z}{f}} \end{aligned}\right)}{\left(1 - e^{-\frac{R_{n1}}{L_{n1}} \cdot \frac{z}{f}} \cdot e^{-\frac{R_{n2} + n \cdot Z}{L_{n2}} \cdot \frac{1-z}{f}}\right)} \qquad (39)$$

The expression for the current I_2 is obtained by substituting (39) into (31).

Based on (30), (36), (39), (40), the time-dependent current waveform for any branch of a multi-branch buck-boost converter in boost mode can be expressed.

By considering the standard waveforms of the switching-on and switching-off processes, along with equation (1), the total losses P_C of the converter can be expressed similarly to the buck mode, as given in (19):

$$\begin{aligned} I_2 = {} & \frac{U}{R_{n1}} \cdot \left(1 - e^{-\frac{R_{n1}}{L_{n1}} \cdot \frac{z}{f}}\right) + \\ & + \frac{\left(\begin{aligned} & \frac{U - U_{TO}}{R_{n2} + n \cdot Z} \cdot \left(1 - e^{-\frac{R_{n2} + n \cdot Z}{L_{n2}} \cdot \frac{1-z}{f}}\right) + \\ & + \frac{U}{R_{n1}} \cdot \left(1 - e^{-\frac{R_{n1}}{L_{n1}} \cdot \frac{z}{f}}\right) \cdot e^{-\frac{R_{n2} + n \cdot Z}{L_{n2}} \cdot \frac{1-z}{f}} \end{aligned}\right)}{\left(1 - e^{-\frac{R_{n1}}{L_{n1}} \cdot \frac{z}{f}} \cdot e^{-\frac{R_{n2} + n \cdot Z}{L_{n2}} \cdot \frac{1-z}{f}}\right)} \cdot e^{-\frac{R_{n1}}{L_{n1}} \cdot \frac{z}{f}}\,. \end{aligned} \qquad (40)$$

The average current of a converter branch can be determined using (20). Using this, the total losses of the converter can be expressed as:

$$P_C = nR_{Pn1}\left(I_{n(AV)}\right)^2 + nr_{DS\_1(on)}\left(I_{n(AV)}\right)^2 + nR_{Ln}\left(I_{n(AV)}\right)^2 + nr_{DS\_2(on)}z\left(I_{n(AV)}\right)^2 + nr_{DS\_2(off)}I^2_{DS(off)}(1-z) + nR_{Pn2}\left(I_{n(AV)}\right)^2(1-z) + n\left(U_{TO} + r_F\left(I_{n(AV)}\right)\right)I_{n(AV)}(1-z) + nUI_R + 0{,}5nU_{DS(on)}I_1t_{on}f + 0{,}5nU_{DS(off)}I_2t_ff + 0{,}5nQ_{rr}U_{DS(on)}f + 0{,}5nU_{FP}I_2t_{fr}f, \quad (41)$$

where $U_{DS(on)}$ is the voltage across the transistor just before it turns on, which can be expressed using (42); $U_{DS(off)}$ is the voltage across the transistor that increases shortly after it turns off, which can be expressed using (43):

$$U_{DS(on)} = U_{TO} + I_1 \cdot (r_F + R_{Pn2} + Z)\,; \quad (42)$$

$$U_{DS(off)} = U_{TO} + I_2 \cdot (r_F + R_{Pn2} + Z)\,. \quad (43)$$

By manipulating (41) and applying (20), a simplified final form of the relationship is obtained, which can be used to calculate the total losses in the converter:

$$P_C = \left(\frac{I^2}{n}\right)\cdot\left(R_{Pn1} + r_{DS\_1(on)} + R_{Ln} + r_F(1-z) + r_{DS\_2(on)}z + R_{Pn2}(1-z)\right) + nr_{DS\_2(off)}I^2_{DS(off)}(1-z) + nUI_R + U_{TO}I(1-z) + 0{,}5nU_{DS(on)}I_1t_{on}f + 0{,}5nU_{DS(off)}I_2t_ff + 0{,}5nQ_{rr}U_{DS(on)}f + 0{,}5nU_{FP}I_2t_{fr}f. \quad (44)$$

The efficiency of the converter is given by (23). From (23), it is evident that the dominant factor affecting efficiency is the total loss power. The magnitude of these losses can be influenced by the appropriate selection of individual design components. Additionally, the total losses can be affected by the number of parallel branches in the converter, as the input current is linearly divided among the branches, while the losses in the branch resistors decrease quadratically. Therefore, the total losses may be smaller with multiple branches than with a single branch. However, due to additional losses in the parallel branches, it is not necessarily true that a greater number of branches will always result in lower losses. Given these considerations, it is possible to determine the optimal number of branches for the desired input power (under constant input voltage, for the desired input current, and thus for a specific duty cycle) in the boost mode. The converter can, therefore, be controlled by adjusting the topology and duty cycle to achieve the highest possible efficiency for any given input power. This is, of course, under the condition of fixed design components and their characteristics.

To determine the optimal number of branches, equation (44) must be differentiated. By differentiating it with respect to n, the result for the local extremum can be obtained, providing an expression for the number of branches corresponding to the minimum loss power:

$$P'_C = -\left(\frac{I^2}{n}\right)\cdot\left(R_{Pn1} + r_{DS\_1(on)} + R_{Ln} + r_F(1-z) + r_{DS\_2(on)}z + R_{Pn2}(1-z)\right) + zUI_R + r_{DS\_2(off)}I^2_{DS(off)}(1-z) + 0{,}5U_{DS(on)}I_1t_{on}f + 0{,}5U_{DS(off)}I_2t_ff + 0{,}5Q_{rr}U_{DS(on)}f + 0{,}5U_{FP}I_2t_{fr}f. \quad (45)$$

If the result of the differentiation is set equal to zero and solved for n, the equation takes the following form:

$$n = I\sqrt{\frac{\begin{pmatrix} R_{Pn1} + r_{DS\_1(on)} + R_{Ln} + r_F(1-z) + \\ + r_{DS\_2(on)}z + R_{Pn2}(1-z) \end{pmatrix}}{\begin{pmatrix} zUI_R + r_{DS\_2(off)}I^2_{DS(off)}(1-z) + 0{,}5U_{DS(on)}I_1t_{on}f + \\ + 0{,}5U_{DS(off)}I_2t_ff + 0{,}5Q_{rr}U_{DS(on)}f + 0{,}5U_{FP}I_2t_{fr}f \end{pmatrix}}}\,. \quad (46)$$

It follows from the above that, based on (46), the optimal number of branches can be determined using the design and operating parameters of the converter in boost mode, ensuring that the converter delivers the maximum power to the load under all operating conditions. The validity of the formula for the buck mode has also been experimentally confirmed. A comparison of the results obtained through calculation and measurement is presented in Table 2. For the boost mode, the same circuit parameters were used, except for the input power source and load. In this case, the calculation was performed with a 10 V power supply and a 20 Ω load.

Table 2

Efficiency results of the boost converter mode as a function of power and the number of branches

Single-phase converter in boost mode			
Calculated		Measured	
P_1, W	Efficiency, %	P_1, W	Efficiency, %
5,03	92,95	5,05	92,25
10,03	93,91	10,05	93,49
15,02	93,5	15,08	93,10
20,02	92,58	20,06	92,22
30,03	90,25	30,07	89,83
40,06	87,66	40,08	87,14
50,04	84,99	50,06	84,38
Three-phase converter in boost mode			
Calculated		Measured	
P_1, W	Efficiency, %	P_1, W	Efficiency, %
5,05	90,7	5,01	89,65
10,04	93,2	10,05	92,71
15,01	94,2	15,02	93,72
20,07	94,7	20,05	94,12
30,05	94,93	30,09	94,38
40,08	94,5	40,00	93,97
50,01	93,85	50,04	93,15

To provide a clearer understanding of the obtained results, a graph has been created (Fig. 19).

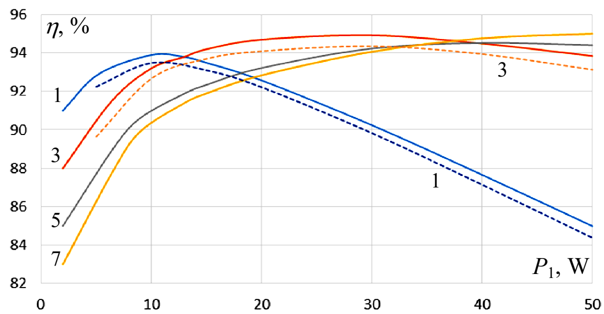

Fig. 19. Graphical representation of the efficiency results as a function of input power and the number of branches (1, 3, 5, 7), obtained through calculations (—) and measurement (- - -)

To further illustrate the implications of the calculations, Fig. 20 depicts the calculated dependence of the efficiency of a converter operating in boost mode on its output power.

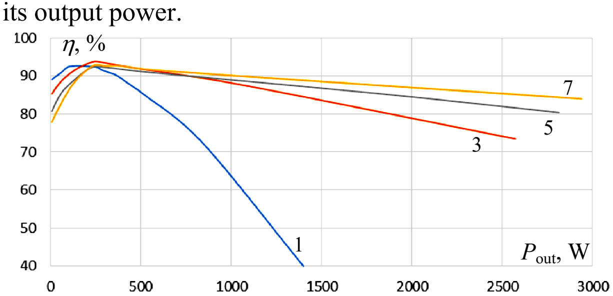

Fig. 20. Graphical representation of the efficiency results as a function of output power and the number of branches (1, 3, 5, 7), obtained through calculations for higher power converter

This analysis pertains to a higher-power converter implemented with the components and circuit parameters described in the preceding text.

Conclusions. Based on the obtained equations, as well as the presented waveforms, several critical factors influencing the optimal design and operation of multi-branch buck-boost converters can be identified. The analysis reveals that for operating points of a buck-boost converter functioning in buck mode with power input up to approximately 10 % of the installed power capacity (P_1), a single-branch configuration is more efficient than a seven-branch configuration. At 10 % of P_1, the efficiency difference between these configurations can reach up to 10 %. For a converter with an installed power capacity of, for instance, 3 kW, this efficiency gap could result in operational losses of up to 300 W. A similar situation arises for operating points of the buck-boost converter operating in boost mode. However, in this case, the single-branch configuration demonstrates a clear efficiency advantage only for power input levels up to approximately 6 % of the total installed capacity. Within this range, the single-branch configuration remains up to 10 % more efficient than the seven-branch configuration. It is important to note, however, that the absolute magnitude of the converter's losses is influenced not only by the number of branches but also by the parameters of the components used in the circuit.

Conflict of interest. The authors declare that they have no conflicts of interest.

REFERENCES

1. Alharbi M.A., Dahidah M.S.A., Ali S.A., Ethni S.A.E., Pickert V. Ripple-Free Multiphase Interleaved Stacked Converter for High-Power Applications. *IEEE Transactions on Power Electronics*, 2022, vol. 37, no. 12, pp. 14770-14780. doi: https://doi.org/10.1109/TPEL.2022.3194979.

2. Hafeez K.T., Dutta A., Singh S.G., Avalur K.K.G. A low-cost multi-phase 3A buck converter with improved ripple cancellation for wide supply range. *2016 IEEE International Symposium on Circuits and Systems (ISCAS)*, 2016, pp. 1618-1621. doi: https://doi.org/10.1109/ISCAS.2016.7538875.

3. Rahman A.U., Pellitteri F., Campagna N., Di Tommaso A.O., Miceli R. Current Sharing Control of Multiphase Interleaving Single Inductor Four Switch Buck-Boost Converter for Energy Storage System. *2024 IEEE 15th International Symposium on Power Electronics for Distributed Generation Systems (PEDG)*, 2024, pp. 1-6. doi: https://doi.org/10.1109/PEDG61800.2024.10667462.

4. Li J., Zhang L., Wu X., Zhou Z., Dai Y., Chen Q. Current Estimation and Optimal Control in Multiphase DC–DC Converters With Single Current Sensor. *IEEE Transactions on Instrumentation and Measurement*, 2024, vol. 73, pp. 1-14, art. no. 9003414. doi: https://doi.org/10.1109/TIM.2024.3396834.

5. Tang J., Guo T., Kim J.S., Roh J. A Current-Mode Four-Phase Synchronous Buck Converter With Dynamic Dead-Time Control. *IEEE Access*, 2021, vol. 9, pp. 81078-81088. doi: https://doi.org/10.1109/ACCESS.2021.3085826.

6. Golla T., Kapat S., Chittaragi N., Setty R.A., Sridharan S. Controller Design and Phase Current Balancing for Fast Dynamic Performance in Voltage Mode Controlled Multiphase Buck Converters. *2023 IEEE Applied Power Electronics Conference and Exposition (APEC)*, 2023, pp. 2163-2169. doi: https://doi.org/10.1109/APEC43580.2023.10131482.

7. Wang L., Zhang D., Duan J., Gu R. Research on High-Performance Multiphase DC–DC Converter Applied to Distributed Electric Propulsion Aircraft. *IEEE Transactions on Transportation Electrification*, 2023, vol. 9, no. 3, pp. 3545-3563. doi: https://doi.org/10.1109/TTE.2022.3207142.

8. Ayada A., Guiza D., Ounnas D., Tidjani N. Design and control of a DC-DC buck converter using discrete Takagi-Sugeno fuzzy models. *Electrical Engineering & Electromechanics*, 2025, no. 3, pp. 53-58. doi: https://doi.org/10.20998/2074-272X.2025.3.08.

9. Namoune A., Taleb R., Mansour N., Benzidane M.R., Boukortt A. Integrated through-silicon-via-based inductor design in buck converter for improved efficiency. *Electrical Engineering & Electromechanics*, 2023, no. 6, pp. 54-57. doi: https://doi.org/10.20998/2074-272X.2023.6.09.

10. Nguyen V.H., Do X.-D., Blaquiere Y., Cowan G. Multi-Phase Hybrid Boost Converter with High Conduction Loss Reduction and Fast Dynamic Response for Automotive Applications. *2022 20th IEEE Interregional NEWCAS Conference (NEWCAS)*, 2022, pp. 183-187. doi: https://doi.org/10.1109/NEWCAS52662.2022.9842223.

11. Deshmukh N., Prabhakar S., Anand S. Power Loss Reduction in Buck Converter Based Active Power Decoupling Circuit. *IEEE Transactions on Power Electronics*, 2021, vol. 36, no. 4, pp. 4316-4325. doi: https://doi.org/10.1109/TPEL.2020.3024721.

12. Kandeel Y., O'Driscoll S., O'Mathuna C., Duffy M. Optimum Phase Count in a 5.4-W Multiphase Buck Converter Based on Output Filter Component Energies. *IEEE Transactions on Power Electronics*, 2023, vol. 38, no. 4, pp. 4909-4920. doi: https://doi.org/10.1109/TPEL.2022.3226708.

13. Yama O., Khyzhniak T., Bondarenko O. Analysis of Modified Non-Isolated DC-DC Converters and Solutions to Improve their Characteristics. *2023 IEEE 4th KhPI Week on Advanced Technology (KhPIWeek)*, 2023, pp. 1-6. doi: https://doi.org/10.1109/KhPIWeek61412.2023.10312965.

14. Azer P., Emadi A. Generalized State Space Average Model for Multi-Phase Interleaved Buck, Boost and Buck-Boost DC-DC Converters: Transient, Steady-State and Switching Dynamics. *IEEE Access*, 2020, vol. 8, pp. 77735-77745. doi: https://doi.org/10.1109/ACCESS.2020.2987277.

15. Hinov N., Hranov T. Model-Based Optimisation of a Buck-Boost DC-DC Converter. *2020 21st International Symposium on Electrical Apparatus & Technologies (SIELA)*, 2020, pp. 1-5. doi: https://doi.org/10.1109/SIELA49118.2020.9167056.

16. Lyu Y., Sanusi B.N., Ouyang Z. Modeling and Analysis of Coupling Effect in Four Legged Core for Multi-phase Buck Converter. *2023 IEEE Applied Power Electronics Conference and Exposition (APEC)*, 2023, pp. 3307-3313. doi: https://doi.org/10.1109/APEC43580.2023.10131131.

17. Sridhar S., Li Q. Multiphase Constant On-Time Control With Phase Overlapping – Part I: Small-Signal Model. *IEEE Transactions on Power Electronics*, 2024, vol. 39, no. 6, pp. 6703-6720. doi: https://doi.org/10.1109/TPEL.2024.3368343.

18. Lu X., Yin X., Zhuo C. An Efficient Approach to Multiphase Constant On-Time Buck Converter Simulation. *2024 2nd International Symposium of Electronics Design Automation (ISEDA)*, 2024, pp. 143-148. doi: https://doi.org/10.1109/ISEDA62518.2024.10617689.

19. Hamdi R., Hadri Hamida A., Bennis O. On modeling and real-time simulation of a robust adaptive controller applied to a multicellular power converter. *Electrical Engineering & Electromechanics*, 2022, no. 6, pp. 48-52. doi: https://doi.org/10.20998/2074-272X.2022.6.08.

20. Zagirnyak M., Kalinov A., Maliakova M. Analysis of instantaneous power components of electric circuit with a semiconductor element. *Archives of Electrical Engineering*, 2013, vol. 62, no. 3, pp. 473-486. doi: https://doi.org/10.2478/aee-2013-0038.

21. Jacko P., Bereš M., Kováčová I., Molnár J., Vince T., Dziak J., Fecko B., Gans Š., Kováč D. Remote IoT Education Laboratory for Microcontrollers Based on the STM32 Chips. *Sensors*, 2022, vol. 22, no. 4, art. no. 1440. doi: https://doi.org/10.3390/s22041440.

22. Kulshreshtha A., Saxena A.R., Veerachary M. Non-Isolated Fourth-Order Boost DC-DC Converter for Power Management in Low Voltage Low Power DC Grids: Design and Interaction Analysis. *IEEE Access*, 2020, vol. 8, pp. 196500-196514. doi: https://doi.org/10.1109/ACCESS.2020.3034181.

Received 27.12.2024
Accepted 04.02.2025
Published 02.07.2025

I. Kovacova[1], *Professor,*
D. Kovac[1], *Professor,*
[1] Technical University of Kosice,
Department of Theoretical and Industrial Electrical Engineering,
Park Komenskeho 3, 042 00 Kosice, Slovakia,
e-mail: irena.kovacova@tuke.sk;
dobroslav.kovac@tuke.sk (Corresponding Author)

How to cite this article:
Kovacova I., Kovac D. Designing the optimal number of active branches in a multi-branch buck-boost converter. *Electrical Engineering & Electromechanics*, 2025, no. 4, pp. 44-52. doi: https://doi.org/10.20998/2074-272X.2025.4.06

UDC 621.3.014 https://doi.org/10.20998/2074-272X.2025.4.07

D.V. Martynov, Y.V. Rudenko, V.V. Martynov

Improving the operation of an asymmetric inverter with magnetically coupled inductors for energy storage systems

Introduction. *Bidirectional DC-DC converters are widely used in energy storage systems for efficient energy transfer. One of the effective converters for such systems is the asymmetric inverter with a magnetically coupled inductors. To enhance the efficiency of this converter for energy storage applications, it is necessary to optimize its parameters.* ***Objective***. *The objective is to develop a mathematical model of an asymmetric inverter with magnetically coupled inductors and based on this model, to establish the conditions for improving the energy efficiency of the inverter in energy storage systems.* ***Methods***. *The study uses the state-space averaging method and simulation modelling to analyse operational processes.* ***Results***. *Analytical expressions were derived for calculating current parameters of the magnetically coupled inductor within switching intervals. A correlation was identified between the inductor's inductance and power source parameters under conditions that eliminate circulating currents, thus reducing static energy losses in the inverter.* ***Novelty***. *Based on these expressions, new analytical and graphical dependencies were established, illustrating relationships between the inductor parameters and the magnetic coupling coefficient of its windings. These dependencies determine the boundaries of the discontinuous conduction mode for the asymmetric inverter with a magnetically coupled inductors within its switching range.* ***Practical value***. *The application of these dependencies during the design phase allows for a reduction in both static and dynamic energy losses in the inverter using discontinuous conduction mode. This will also improve the dynamics of transient processes during changes in the direction of energy flow, which is a significant advantage in the development of hybrid power systems for electric vehicles.* References 19, figures 9.

Key words: **energy storage systems, bidirectional DC-DC converter, asymmetric inverter, magnetic coupling inductors, circulating current.**

Вступ. *В системах накопичення енергії широко використовуються перетворювачі постійної напруги в режимах двонаправленої передачі енергії. Одним з ефективних перетворювальних пристроїв для застосування в таких системах є асиметричний інвертор з магнітозв'язаними індукторoми. Для використання вказаного перетворювача в системах енергонакопичення необхідним є удосконалення його параметрів для підвищення ефективності перетворювача.* ***Мета***. *Метою є розробка математичної моделі асиметричного інвертора з магнітозв'язаними індукторами та визначення на її основі умов підвищення енергетичної ефективності такого інвертора при застосуванні в системах накопичення енергії.* ***Методи***. *При дослідженні процесів в роботі використано метод усереднення в просторі станів та методи імітаційного моделювання.* ***Результати***. *Розроблено аналітичні вирази для розрахунків параметрів струмів магнітозв'язаних індукторів на інтервалах комутації, визначено взаємозв'язок між його індуктивністю та параметрами джерел електроживлення, при яких циркуляційні струми відсутні, що зменшує статичні втрати енергії інвертора.* ***Новизна***. *На основі розроблених виразів отримано нові аналітичні та графічні залежності між параметрами індуктора та коефіцієнтом магнітного зв'язку між їх обмотками, що визначають межі області переривчастої роботи асиметричного інвертора з магнітозв'язаними індукторами в діапазоні його комутації.* ***Практична значимість***. *Використання отриманих залежностей на етапі проектування дозволяє зменшити статичні та динамічні втрати енергії інвертора завдяки використанню режиму переривчастої провідності. Це також дозволить покращити динаміку перехідних процесів при зміні напрямку протікання електроенергії, що є суттєвою перевагою при створенні гібридних систем електроживлення електротранспортних засобів.* Бібл. 19, рис. 9.

Ключові слова: **системи накопичення електроенергії, двонаправлений перетворювач постійної напруги, асиметричний інвертор, магнітозв'язані індуктори, циркулюючий струм.**

Introduction. Batteries and supercapacitors are the most common and economical choices for energy storage today. This drives strong demand for bidirectional DC-DC converters, which facilitate energy transfer between storage units and power-consuming devices. These converters support bidirectional energy flow and flexible control across all modes of operation, making them integral to a range of energy systems, such as hybrid and fuel cell vehicles, renewable energy system, and beyond [1–3]. In renewable energy systems, a bidirectional DC-DC converter is used to combine different types of energy sources [4–14], with different voltage levels, providing a quick response when changing the direction of the electricity flow.

Currently, numerous circuit topologies for the potential implementation of bidirectional DC-DC converters are known [5–18]. These topologies are primarily classified into two types: non-isolated and isolated converters, each suited to specific applications.

A typical structure of a non-isolated bidirectional DC-DC converter combines a buck converter and a boost converter in a half-bridge configuration [4, 9, 13]. These converters can operate independently to create a bidirectional flow of electrical energy, although this leads to inefficient use of electromagnetic components and power switches. However, unidirectional DC-DC converters can be configured as bidirectional converters based on the half-bridge inverter topology by utilizing the built-in diodes within the switches and shared inductance. There are several disadvantages to the half-bridge inverter topology when used as a bidirectional converter. Firstly – excessive energy losses. Significant energy losses occur due to diode reverse recovery or faulty simultaneous conduction of both switches, which can lead to device failure. The conventional solution is to introduce dead time into the switching interval. However, this approach leads to duty cycle losses and limits the switching frequency. Secondly – poor transient response. The shared inductance used for current ripple smoothing negatively affects the dynamic response during changes in the direction of power flow, which is a major issue for hybrid power systems. This problem arises due to a reduction in stored energy, for example during the transition to regenerative breaking in electric vehicle power systems [4].

Many studies have been done to research bidirectional converters with efficient power flow management [7–15], as well as various control strategies to improve power quality. Recently, new converters based on an asymmetric inverter with magnetically coupled inductors have been introduced as an alternative to traditional bidirectional DC-DC converter topologies [4, 9, 15]. These structures have been applied in various applications due to their immunity to short-circuit issues and low losses during diode reverse recovery. This unique characteristic is achieved using magnetically coupled inductors and the structure of the asymmetric inverter, such as the dual buck inverter and the split-phase PWM inverter. The converter offers two key advantages: firstly, shoot-through currents are avoided because no active power switches are connected in series in each phase's arm; secondly, energy dissipation during the reverse recovery of the power switch is significantly reduced, as discrete diodes with superior dynamic characteristics compared to the internal diodes of power switches can be utilized.

The bidirectional converter using the topology of an asymmetric inverter with magnetically coupled inductors is shown in Fig. 1.

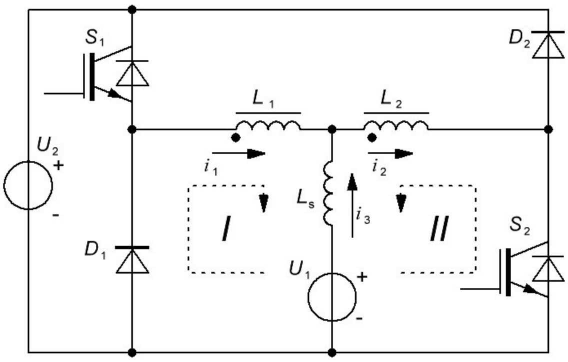

Fig. 1. Schematic of the bidirectional converter based on the topology of an asymmetric inverter with magnetically coupled inductors

The device consists of four switches, of which switches S_1 and S_2 are controllable. This converter topology allows operation in both buck and boost modes in both directions of power flow. When transferring energy from source U_2 to U_1, switch S_1 is activated while S_2 remains OFF; conversely, during energy transfer in the reverse direction from source U_1 to U_2, switch S_2 is activated.

The converter has some disadvantages when using a magnetically coupled inductor, especially when there is a significant voltage difference between the low-voltage and high-voltage sides. In this scenario, circulating currents may arise during certain operating modes of the converter [4], resulting in power loss.

Research has shown that the presence of circulating currents increases the static energy losses in the inverter. On the other hand, the efficiency of the inverter also depends on the dynamic energy losses. Dynamic power dissipation is reduced by operating in discontinuous conduction mode, which allows transistors to switch at zero current.

To date, research aimed at reducing circulating currents, improving transient response quality and increasing energy efficiency has mainly focused on modifying the structure of the asymmetric inverter or implementing new control methods [12, 13, 15, 17]. While structural modifications or the implementation of advanced control strategies can partially solve these issues, they also have certain disadvantages, such as an increased number of components, greater circuit complexity and higher energy losses. In addition, the implementation of new control methods increases the complexity of the control system. Analysis of the processes in inverters shows that the use of non-magnetically coupled inductors prevents the occurrence of circulating currents but also eliminates one of the main advantages of the asymmetric inverter, which is the fast transition dynamics between energy storage and discharge modes [15, 16]. Also, the use of counter-rotating inductor windings does not provide significant benefits due to the complexity of additional filtering systems [17]. It is known that in an asymmetric inverter with non-magnetically coupled inductors, circulating currents are absent; however, this leads to slow transient processes when changing the direction of power flow. Inverter structures with magnetically coupled inductors provide good speed during changes in power flow direction; nevertheless, under certain parameter ratios of the power sources on the low-voltage and high-voltage sides [4], circulating currents may arise [17]. Thus, it can be concluded that a strong magnetic coupling in the inductor leads to circulating currents, while the absence of magnetic coupling prevents them. These studies do not consider the relationship between an asymmetrical inverter's parameters, its magnetically coupled inductors, and the parameters of additional inductive filters (additional inductor) that can minimise circulating current.

In this work, we focus on the elimination of some disadvantages of the asymmetric inverter with magnetically coupled inductors and additional inductor (Fig. 1) by developing analytical expressions for the calculation and rational selection of effective parameters when used in a bidirectional DC-DC converter for energy storage systems. Solving these problems is expected to improve the overall energy efficiency of the asymmetric inverter. Furthermore, the use of analytical expressions will simplify the design and development of the asymmetric inverter for energy storage applications.

The **objective** of this work is to develop a mathematical model of an asymmetric inverter with magnetically coupled inductors, and based on this model, to determine the conditions for increasing the energy efficiency of such an inverter when used in energy storage systems.

Methods. To solve this problem, we need to optimise the parameters of magnetic coupling inductors, at which sufficient performance is kept, and the current circulation tends to zero. We will also find the ratio of the converter parameters at which it can operate in the intermittent conduction mode.

The study of the asymmetric inverter with magnetically coupled inductors was performed by analysing its operating modes using the PSIM circuit simulation software, based on the developed simulation model shown in Fig. 1. This model included magnetically coupled inductors with $L_1 = L_2 = 30$ μH and an additional inductor of $L_s = 6$ μH, designed to block unwanted circulating current. It was assumed that the switching elements of the converter operate instantaneously, the active resistance in the open state is zero, and the active resistance of the inductor winding is also zero. In the circuit illustrated in Fig. 1, the supply voltage $U_2 > 2U_1$.

In Fig. 2, the calculated results of the currents are presented: $i_1(t)$ is the current through inductor L_1, $i_2(t)$ is the current through inductor L_2, and $i_3(t)$ is the current through inductor L_s in the circuit shown in Fig. 1, during the operation of the bidirectional converter in the mode of discontinuous currents.

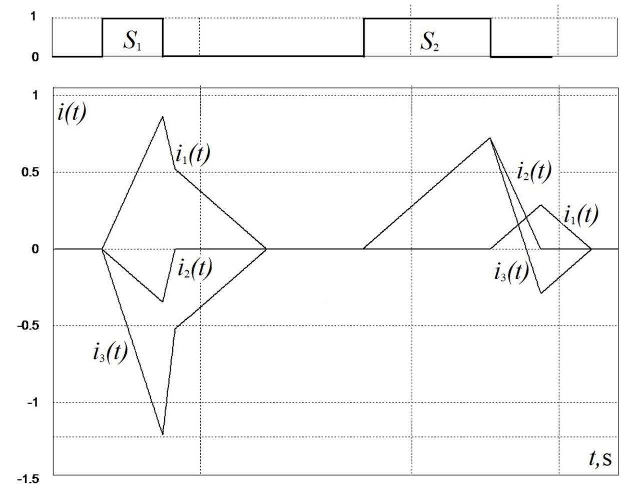

Fig. 2. Graph of the calculated current results during the operation of the bidirectional converter in the discontinuous mode

When transferring energy from source U_2 to U_1, the circuit operates as a buck regulator with the active transistor S_1. During the energy accumulation phase, with transistor S_1 in the ON state, voltage U_2 is applied to the inductors L_1=L_2. Due to the magnetic coupling of the inductors, the voltage at L_2 at the connection point of inductor L_s exceeds U_1, resulting in circulating current through the diode of transistor S_2 and inductor L_2. This increases static losses due to the current flowing through the antiparallel diode of transistor S_2. When the transistor is turned OFF, circulating current is absent, as shown in Fig. 2. This indicates that blocking the antiparallel diode in transistor S_2 prevents circulating current; however, it causes additional static losses in the converter. The path of the circulating current in the active mode of transistor S_1 is represented in Fig. 1 by the dashed contour *II*.

When transferring energy from source U_1 to source U_2, the circuit operates as a boost regulator with transistor S_2. During the activation of transistor S_2, voltage U_1 is applied to inductor L_2, and when the voltage U_1 is less than U_2, circulating current is absent. When transistor S_2 is turned OFF, as shown in Fig. 3, circulating current flows through diode D_1 and the inductor L_1, as the voltage $U_2/2>U_1$ is induced on the inductor L_1.

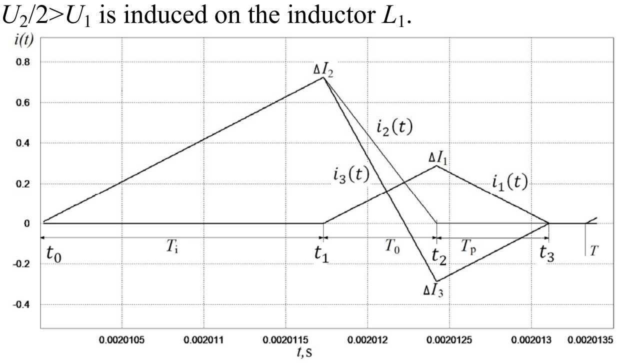

Fig. 3. Graphical representation of the currents in the inductors of the asymmetric inverter during the energy transfer period from the low-voltage source to the high-voltage source in the discontinuous mode

The appearance of the circulating current $i_1(t)$ in Fig. 2 leads to the fact that a part of the energy from the source U_1, accumulated in the inductor L_2 when the transistor S_2 is open, does not enter the source U_2. The path of the circulating current after transistor S2 is turned OFF is shown in Fig. 1 by the dashed contour *I*.

Let's analyze what occurs in the inverter when transistor S_2 operates in active mode. As shown by the calculations in Fig. 3, when the inverter is operating, for example in boost mode with discontinuous inductor currents, four continuous operating intervals of the circuit shown in Fig. 1 can be identified: the first interval, $T_i(t_0–t_1)$, occurs when the transistor S_2 is open while all other switches are OFF; the second interval $T_0(t_1–t_2)$ during the pause in the operation of transistor S_2; the third interval $T_p(t_2–t_3)$ during the time of reduction of inductor currents to zero; the fourth interval $(t_3–T)$ is the cutoff when all the switches of the converter are closed.

The presence of three intervals during pauses in transistor control is influenced by the coupling of the inductors and the voltage ratios of the power sources. An analysis of the time diagrams in Fig. 3 shows that the waveforms of the converter state variables – currents i_1, i_2, i_3 – exhibit a multistep character with several sequential stages of rise and fall, while the current i_2 demonstrates a varying sign.

The configurations of the equivalent circuits during the intervals of interest T_i, T_0 and T_p (Fig. 3), are shown in Fig. 4 – 6. Figure 4 shows the interval T_i, where the transistor S_2 is turned ON. Figure 5 shows the interval T_0, after the transistor S_2 has been switched OFF, during which the current $i_3(t)$ decreases to zero. Figure 6 shows the interval T_p the scenario in which the energy stored in the inductor by the circulating current is returned to the power source U_1.

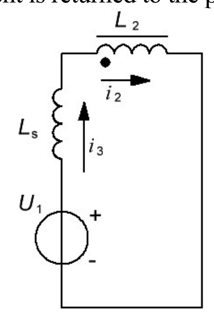

Fig. 4. Equivalent circuit during the time interval T_i

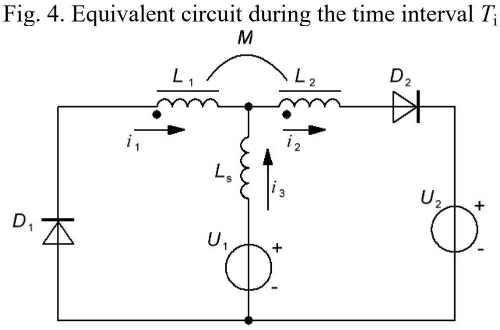

Fig. 5. Equivalent circuit during the time interval T_0

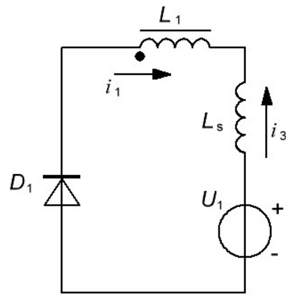

Fig. 6. Equivalent circuit during the time interval T_p

We will define the parameters of the equivalent circuits for which the circulating currents are negligible. To analyse the processes, we will use the converter model obtained by the averaging method developed in [19]. Accordingly, we will establish a system of differential equations for the three switching intervals:

$$\begin{cases} L_2 \dfrac{di_2}{dt} + L_s \dfrac{di_2}{dt} = U_1; \\ -L_2 \dfrac{di_1}{dt} + M \dfrac{di_2}{dt} - L_s \dfrac{di_3}{dt} = U_1; \\ U_1 + L_s \dfrac{di_3}{dt} + L_2 \dfrac{di_2}{dt} - M \dfrac{di_1}{dt} = U_2; \\ L_1 \dfrac{di_1}{dt} + L_s \dfrac{di_1}{dt} = U_1. \end{cases} \qquad (1)$$

We will move to a system of algebraic equations with averaged variables concerning the currents i_1, i_2 and i_3, taking into account the signs of the increments of the state variable functions during the switching intervals of the converter. Using the state-space averaging method based on Lagrange's theorems [19], we can express the system of algebraic equations as follows:

$$\begin{cases} L_2 \dfrac{\Delta I_2}{T_i} + L_s \dfrac{\Delta I_2}{T_i} = U_1; \\ -L_1 \dfrac{\Delta I_1}{T_0} + M \dfrac{\Delta I_2}{T_0} - L_s \dfrac{\Delta I_3}{T_0} = U_1; \\ U_1 + L_s \dfrac{\Delta I_3}{T_0} + L_2 \dfrac{\Delta I_2}{T_0} - M \dfrac{\Delta I_1}{T_0} = U_2; \\ L_1 \dfrac{\Delta I_1}{T_p} + L_s \dfrac{\Delta I_1}{T_p} = U_1; \\ \Delta I_1 + \Delta I_2 = \Delta I_3, \end{cases} \qquad (2)$$

where ΔI_1, ΔI_2, ΔI_3 are the increments of the corresponding state variable functions during the converter's switching intervals, equal to the ripple of these functions; $M = K_{cop}\sqrt{L_1 \cdot L_2}$ is the mutual inductance between the inductors; K_{cop} is the magnetic coupling coefficient between the inductors; T_i is the specified duration of the first interval; T_0 is the duration of the second interval; T_p is the duration of the third switching interval.

For further analysis of the processes in the converter, it is necessary to solve the obtained system of algebraic equations (2) with respect to the independent variables. The solution to this system is given by the following equations:

$$\Delta I_1 = T_i \frac{U_1}{(L_2 + L_s)} \cdot \frac{(M + L_2)U_1 + (L_s - M)U_2}{(M + L_1)U_1 - (L_s + L_1)U_2}; \qquad (3)$$

$$\Delta I_2 = T_i \frac{U_1}{L_2 + L_s}; \qquad (4)$$

$$\Delta I_3 = T_i \frac{U_1}{(L_2 + L_s)} \cdot \frac{(2M + L_1 + L_2)U_1 - (L_1 - M)U_2}{(M + L_1)U_1 - (L_s + L_1)U_2}; \qquad (5)$$

$$T_0 = T_i \frac{U_1}{(L_2 + L_s)} \cdot \frac{\left(L_2 L_1 + L_s L_2 + L_1 L_s + 2ML_s - M^2\right)}{(L_s + L_1)U_2 - (M + L_1)U_1}; \qquad (6)$$

$$T_p = T_i \frac{(L_1 + L_s)}{(L_2 + L_s)} \cdot \frac{(M + L_2)U_1 + (L_s - M)U_2}{(M + L_1)U_1 - (L_s + L_1)U_2}. \qquad (7)$$

Considering the case close to ideal magnetic coupling between the inductors $M \sim L_1 = L_2 = L$, we will find the relationship of parameters under which the current increase ΔI_1 in Fig. 3 approaches zero during the second interval. We express (3) in a simplified form as:

$$\Delta I_1 = T_i \frac{U_1}{(L + L_s)} \cdot \frac{2LU_1 + (L_s - L)U_2}{2LU_1 - (L_s + L)U_2}. \qquad (8)$$

Setting (8) equal to zero, we can determine the value of the additional inductor L_s at which the increase in circulating current approaches zero.

$$L_s = L \frac{U_2 - 2U_1}{U_2}. \qquad (9)$$

Using the notation $k = U_2/U_1$, we transform (9) to the following form:

$$\frac{L_s}{L} = 1 - \frac{2}{k}. \qquad (10)$$

According to (10), as the difference between the power sources $U_2 >> U_1$ increases, a larger additional inductance is required to prevent current circulation in the asymmetric inverter. Figure 7 shows the graphical solution of (10).

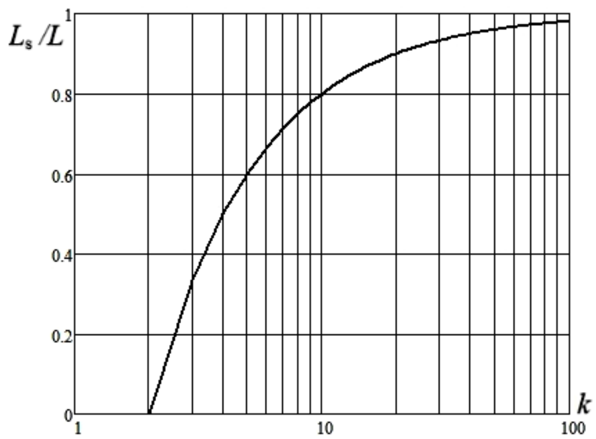

Fig. 7. Graphical interpretation of the dependence of additional inductance on the voltage ratio of power sources

From the analysis of the graph in Fig. 7, it follows that if the voltage of source U_2 is twice as large as the voltage of source U_1, then the additional inductor L_s, to reduce the current circulation in the asymmetric inverter, can be omitted. If the voltage source U_2 significantly exceeds the voltage source U_1, the value of the additional inductor tends to the value of the magnetically coupled inductors $L_s = L_1 = L_2 = L$.

To achieve high power density, bidirectional DC-DC converters often use the discontinuous mode, which allows the inductor to be minimised in size. The current ripple associated with this mode can be minimised either by employing multiphase configurations in power supply systems or by utilizing large energy storage devices. In particular, in hybrid electric vehicle power systems, energy storage is implemented using various batteries, supercapacitors, and generally large capacitive storage solutions. Another significant advantage of operating in discontinuous conduction mode is the zero losses during turn-on, resulting in low losses during the diode's reverse recovery.

The condition for the existence of discontinuous conduction mode in the converter is that the sum of the durations of its switching intervals must be less than the duration of the switching period. The limiting condition is when the sum of the durations of the intervals equals the duration of the switching period T, which leads to the following equation:

$$T_i + T_0 + T_p = T\,. \tag{11}$$

Using the parameter values from (3–7), we obtain the sum of the durations of the switching intervals:

$$T_i + T_0 + T_p = \frac{L_2 + M}{L_2 + L_s} T_i\,, \tag{12}$$

and the condition for the existence of the discontinuous conduction mode of the converter:

$$\frac{L_2 + M}{L_2 + L_s} T_i < T\,. \tag{13}$$

Let's consider the following relationship $\gamma = T_i/T$, $M = L_1 \cdot (K_{cop}/K_{tr})$, $L_2 = L_1/K_{tr}^2$, γ is the duty cycle of the converter's control pulses; K_{tr} is the transformation ratio between the coupled inductors. In this case, we can express the condition for the existence of discontinuous conduction mode as follows:

$$\frac{L_1\left(1 + K_{tr} K_{cop}\right)}{L_1 + K_{tr}^2 L_s} \gamma < 1\,. \tag{14}$$

Let's express the relationship between the inductors L_1 and L_2 using the parameter $\alpha = L_1/L_s$. From (14), we can derive the following formula in relative units concerning this parameter:

$$\alpha < \frac{K_{tr}^2}{\left(1 + K_{tr} K_{cop}\right)\gamma - 1}\,. \tag{15}$$

Equation (15) defines the relationships between the inductance values L_1 and L_s across the entire range of the converter's switching operation that ensures the operation in discontinuous conduction mode.

In the graphical representation, the condition derived in (15) corresponds to the range of values left and below the thresholds shown in Fig. 8.

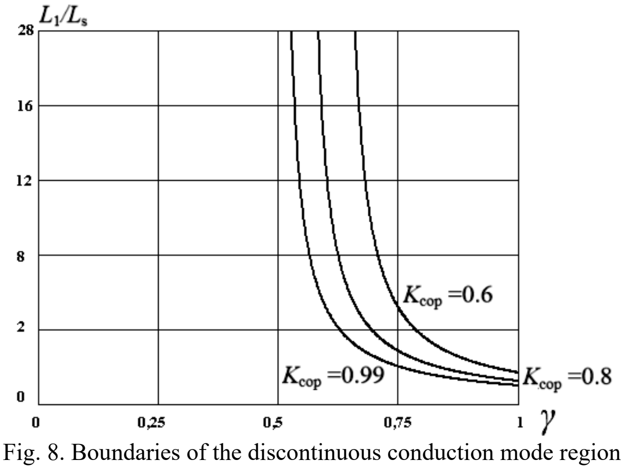

Fig. 8. Boundaries of the discontinuous conduction mode region as a function of the duty cycle of the control pulses of the converter for different values of the magnetic coupling coefficient between the inductors

In Fig. 8, the boundary values are depicted for $K_{tr}=1$, as well as for several values of the magnetic coupling coefficient between the inductors. From the analysis of (14) and the graphs in Fig. 8, in the switching modes when $\gamma<0.5$, the converter maintains the discontinuous conduction mode regardless of the magnetic coupling coefficient and the relationship between the inductors L_1 and L_s. Where $L_1=L$, L has been described above for use in the expression (8–10).

Figure 9 shows the simulation results of a bidirectional converter based on the asymmetric inverter circuit with the following parameters: $L_1=L_2=15$ μH, PWM modulation frequency is 300 kHz, power supplies $U_1=14$ V, $U_2=56$ V. According to (7), the additional inductance value is $L_s=8.57$ μH.

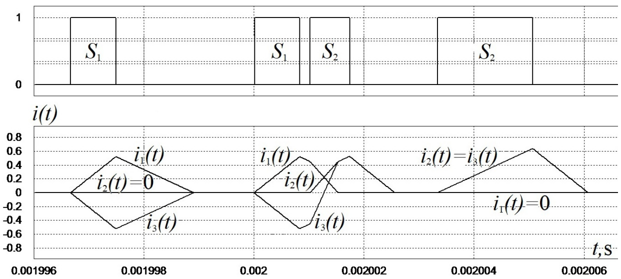

Fig. 9. The results of current calculations during the operation of a bidirectional converter with an additional inductor, whose parameters are determined by (7)

As can be seen from the simulation results, there are no circulating currents. Despite the presence of the additional inductor, the high-speed performance is maintained when the direction of energy transfer is changed. The work has therefore allowed the relationship to be established between the key parameters of the asymmetric converter with additional inductor to prevent circulating currents in an ideal magnetically coupled inductors.

Conclusions.

1. The new analytical model of an asymmetric inverter with magnetically coupled inductors for energy storage systems has been developed, along with a methodology for calculating its parameters. The derived analytical expressions allow the inverter parameters to be calculated at the design stage, ensuring improved efficiency.
2. The method for improving the structure of the asymmetric inverter with magnetically coupled inductors has been proposed, using an additional inductor to reduce undesirable circulating currents in the converter, that lead to power losses. The schematic implementation of the inductor connection has been determined, as well as the relationship between their inductance and the ratio of the power supply voltages, under which circulating currents are absent in the asymmetric inverter, reducing the static energy losses in the device. It was found that the higher the voltage of the high voltage power supply exceeds the low voltage power supply, the greater the additional inductance that needs to be added to prevent circulating currents in the asymmetric inverter with magnetically coupled inductors.
3. Analytical expressions and calculation methods for the converter parameters have been developed to ensure its ability to operate in discontinuous conduction modes. Such modes contribute to the reduction of dynamic losses in the converter, leading to an increase in the performance of the asymmetric converter by reducing switching losses.

It has been found that the asymmetric converter maintains the discontinuous conduction mode regardless of the magnetic coupling coefficient and the ratio between the inductance of the inductors and the additional inductance, provided that the relative duration of the control pulses is less than 0.5.

The simulation carried out confirms the reliability of the results obtained.

Acknowledgment. The work was carried out by the budget program on the topic «Source-4» state registration number 0124U000393 (KPKVK 6541030).

Conflict of interest. The authors declare that they have no conflicts of interest

REFERENCES

1. Zharkin A., Novsky V., Martynov V., Pazieiev A. Provision of high quality power supply in distribution networks with renewable energy sources. *Bulletin of NTU "KhPI". Series: Electric machines and electromechanical energy conversion*, 2019, no. 20 (1345), pp. 4-13. (Ukr). doi: https://doi.org/10.20998/2409-9295.2019.20.01.

2. Hein K., Xu Y., Wilson G., Gupta A. K. Coordinated Optimal Voyage Planning and Energy Management of All-Electric Ship With Hybrid Energy Storage System. *IEEE Transactions on Power Systems*, 2021, vol. 36, no. 3, pp. 2355-2365. doi: https://doi.org/10.1109/TPWRS.2020.3029331.

3. Fonseca de Freitas C. A., Bartholomeus P., Margueron X., Le Moigne P. Partial Power Converter for Electric Vehicle Hybrid Energy Storage System Using a Controlled Current Source Cascade Architecture. *IEEE Access*, 2024 vol. 12, pp. 150898-150913. doi: https://doi.org/10.1109/ACCESS.2024.3477935.

4. Yurchenko O.M., Martynov D.V., Martynov V.V. Research of a bidirectional voltage converter for application in energy storage system. *Proceedings of the Institute of Electrodynamics of the National Academy of Sciences of Ukraine*, 2023, no. 65, pp. 121-126. (Ukr). doi: https://doi.org/10.15407/publishing2023.65.121.

5. El Fadil H., Giri F. Sliding Mode Control of Fuel Cell and Supercapacitor Hybrid Energy Storage System. *IFAC Proceedings Volumes*, 2012, vol. 45, no. 21, pp. 669-674. doi: https://doi.org/10.3182/20120902-4-FR-2032.00117.

6. Cosso S., Benevieri A., Marchesoni M., Passalacqua M., Vaccaro L., Pozzobon P. A New Topology of Multi-Input Bidirectional DC-DC Converters for Hybrid Energy Storage Systems. *Energies*, 2024, vol. 17, no. 20, art. no. 5120. doi: https://doi.org/10.3390/en17205120.

7. Hosseinzadeh M.A., Sarebanzadeh M., Garcia C.F., Babaei E., Rodriguez J. An Asymmetric Switched-Capacitor Multicell Inverter With Low Number of DC Source and Voltage Stress for Renewable Energy Source. *IEEE Access*, 2022, vol. 10, pp. 30513-30525. doi: https://doi.org/10.1109/ACCESS.2022.3140786.

8. Passos Nascimento A.J., Ferro de Menezes B., Jo de Mesquita S., Rabelo Costa K., Lessa Tofoli F., Daher S., Marcelo Antunes F.L. Bidirectional Isolated Asymmetrical Multilevel Inverter. *IEEE Transactions on Circuits and Systems II: Express Briefs*, 2023, vol. 70, no. 1, pp. 151-155. doi: https://doi.org/10.1109/TCSII.2022.3201601.

9. Meng Z., Wang Y.-F., Yang L., Li W. High Frequency Dual-Buck Full-Bridge Inverter Utilizing a Dual-Core MCU and Parallel Algorithm for Renewable Energy Applications. *Energies*, 2017, vol. 10, no. 3, art. no. 402. doi: https://doi.org/10.3390/en10030402.

10. Akbar F., Khan U.A., Khan A.A., Ahmed H.F., Elkhateb A., Cha H., Park J.-W. Dual-Buck Three-Switch Leg Converters With Reduced Number of Passive Components. *IEEE Transactions on Power Electronics*, 2022, vol. 37, no. 11, pp. 13484-13498. doi: https://doi.org/10.1109/TPEL.2022.3183834.

11. Lyu D., Sun Y., Teixeira C.A., Ji Z., Zhao J., Wang Q. A Modular Multilevel Dual Buck Inverter With Adjustable Discontinuous Modulation, *IEEE Access*, 2020, vol. 8, pp. 31693-31709. doi: https://doi.org/10.1109/ACCESS.2020.2972906.

12. Bui D-V., Cha H. Nguyen V-C. Asymmetrical PWM Scheme Balancing Voltages Dual-outputs Interleaved Four-switch Buck-Boost DC-DC Converter. *2022 IEEE Ninth International Conference on Communications and Electronics (ICCE)*, 2022, pp. 482-487. doi: https://doi.org/10.1109/ICCE55644.2022.9852055.

13. Mirza A.B., Emon A.I., Vala S.S., Luo F.A Comprehensive Analysis of Current Spikes in a Split-Phase Inverter. *2022 IEEE Applied Power Electronics Conference and Exposition (APEC)*, 2022, pp. 1580-1585. doi: https://doi.org/10.1109/APEC43599.2022.9773407.

14. Yao Z. Review of Dual-Buck-Type Single-Phase Grid-Connected Inverters. *IEEE Journal of Emerging and Selected Topics in Power Electronics*, 2021, vol. 9, no. 4, pp. 4533-4545. doi: https://doi.org/10.1109/JESTPE.2020.3027770.

15. Patarroyo-Gutierrez L.D., Hernández Gómez O.M., Jiménez López F.R. El inversor dual buck de inductor simple: control de voltaje y procedimiento para obtener su modelo matemático. *Revista EIA*, 2024, vol. 21, no. 41, art. no. 4117, pp. 1-21. (Esp). doi. https://doi.org/10.24050/reia.v21i41.1692.

16. Bui V.-D., Cha H. Asymmetrical PWM split-phase boost PWM AC-AC converter with inherent output voltage balancing. *Journal of Power Electronics*, 2024, vol. 24, no. 1, pp. 20-31. doi: https://doi.org/10.1007/s43236-023-00717-w.

17. Guo S., Huang A.Q. Control and analysis of the high efficiency split phase PWM inverter. *2014 IEEE Applied Power Electronics Conference and Exposition - APEC 2014*, 2014, pp. 2415-2420. doi: https://doi.org/10.1109/APEC.2014.6803641.

18. Kumar R.S., Reddy C.S.R., Chandra B.M. Optimal performance assessment of intelligent controllers used in solar-powered electric vehicle. *Electrical Engineering & Electromechanics*, 2023, no. 2, pp. 20-26. doi: https://doi.org/10.20998/2074-272X.2023.2.04.

19. Rudenko Y. Analysis of DC-DC Converters by Averaging Method based on Lagrange Theorems. *2021 IEEE 2nd KhPI Week on Advanced Technology (KhPIWeek)*, 2021, pp. 367-370. doi: https://doi.org/10.1109/KhPIWeek53812.2021.9570089.

Received 30.10.2024
Accepted 20.02.2025
Published 02.07.2025

D.V. Martynov[1], *PhD Student,*
Y.V. Rudenko[1], *Doctor of Technical Science,*
V.V. Martynov[1], *Doctor of Technical Science,*
[1] Institute of Electrodynamics of the National Academy of Sciences of Ukraine,
56, Prospect Beresteiskyi, Kyiv, 03057, Ukraine,
e-mail: d.martynov@electrotechimpulse.com (Corresponding Author); mart_v@ied.org.ua; rudenko@ied.org.ua

How to cite this article:
Martynov D.V., Rudenko Y.V., Martynov V.V. Improving the operation of an asymmetric inverter with magnetically coupled inductors for energy storage systems. *Electrical Engineering & Electromechanics*, 2025, no. 4, pp. 53-58. doi: https://doi.org/10.20998/2074-272X.2025.4.07

UDC 621.3.022:621.396.6:533.93 https://doi.org/10.20998/2074-272X.2025.4.08

M.I. Baranov

The main characteristics of the leader channel during breakdown of a long air gap by high pulse voltage

Goal. *Calculation-experimental determination of basic descriptions of plasma channel of leader at an electrical breakdown of long air gap in the double-electrode discharge system (DEDS) «edge-plane» by artificial electricity of high pulse voltage of positive polarity.* ***Methodology.*** *Bases of the theoretical electrical engineering and electrophysics, electrophysics bases of technique of high and extra-high voltage, large pulse currents and high electromagnetic fields, basis of high-voltage pulse and measuring technique.* ***Results.*** *The simplified electrophysics model of origin and development of positive leader is offered in the long air gap of probed DEDS, which the followings descriptions of plasma channel of this positive leader were found on the basis of: a closeness of n_{eL} charge and electric potential U_{eL} in the head of leader; linear charge q_{Ll} of leader of plasma channel; closeness δ_{eL} of electron current i_{eL} and this current i_{eL} in the channel of leader; strength of high electric field outside E_{Le} and inwardly E_{Li} of the channel of leader; length l_s of streamer area before the head of leader; maximal electron temperature T_{mL} in plasma of channel of leader; linear active resistance R_{Ll} and active resistance R_{Lc} of channel of leader. Executed on a domestic powerful over-high voltage electrical equipment outdoors in the conditions of electrophysics laboratory high-voltage experiments with the use of standard interconnect aperiodic pulse of voltage $U_e(t)$ of temporal shape of $T_m/T_p\approx200$ μs/1990 μs of positive polarity for probed DEDS at a change in it of minimum length l_{min} of its discharge in air gap in the range of 1 m$\leq l_{min}\leq$4 m confirmed power and authenticity of row of the got calculation correlations for the indicated descriptions of plasma channel of positive leader which is formed and develops in this DEDS.* ***Originality.*** *In a complex kind calculation-experimental way the indicated basic descriptions of plasma channel of positive leader are certain in probed DEDS. By calculation way it is first rotined that on the stage of development of positive leader in atmospheric air of indicated DEDS high electric potential U_{eL} of his spherical head with the charge of $q_{eL}\approx58{,}7$ nC has a less value (for example, $U_{eL}\approx605$ kV for length of his channel of $l_L=0{,}395$ m at $l_{min}=1{,}5$ m) the radius of $R_{eL}\approx0{,}5$ mm, what high potential $U_e(t)\approx U_e(T_d)\approx611{,}6$ kV its active metallic electrode-edge. Obtained result for the maximal electron temperature $T_{mL}\approx1{,}639\cdot10^4$ K in plasma of the probed leader testifies that this plasma is thermo-ionized.* ***Practical value.*** *Practical application in area of industrial electrical power engineering, high-voltage pulse technique, techniques of high and extra-high voltage of the obtained new results in area of physics of gas discharge allows not only to deepen our electrophysics knowledges about a leader discharge in atmospheric air but also more grounded to choose the air insulation of power high and over-high voltage electrical power engineering and electrical engineering equipment, and also to develop different new electrical power engineering and electrophysics devices in area of industrial electrical power engineering and powerful pulse energy with enhanceable reliability and safety of their operation in the normal and emergency modes.* References 49, figures 7.

Key words: **long air gap, leader discharge, electrical breakdown of gap, plasma channel of positive leader, characteristics of positive leader.**

Надані результати розрахунково-експериментального визначення основних характеристик плазмового каналу позитивного лідера при електричному пробої довгого повітряного проміжку двоелектродної розрядної системи (ДЕРС) «вістря-площина» стандартним комутаційним аперіодичним імпульсом високої напруги часової форми $T_m/T_d\approx200$ мкс/1990 мкс позитивної полярності. Запропоновано спрощену електрофізичну модель виникнення і розвитку позитивного лідера в довгому розрядному повітряному проміжку досліджуваної ДЕРС, на основі якої у комплексному вигляді були знайдені наступні основні характеристики плазмового каналу даного позитивного лідера: густина n_{eL} електронів і електричний потенціал U_{eL} в головці лідера; погонний заряд q_{Ll} лідерного плазмового каналу; густина δ_{eL} електронного струму i_{eL} і цей струм i_{eL} в каналі лідера; напруженості сильного електричного поля всередині E_{Li} і зовні E_{Le} каналу лідера; довжина l_s стримерної зони перед головкою лідера; максимальна електронна температура T_{mL} в плазмі каналу лідера; погонний активний опір R_{Ll} і повний активний опір R_{Lc} каналу лідера. Виконані на вітчизняному потужному надвисоковольтному електрообладнанні на відкритому повітрі в умовах електрофізичної лабораторії високовольтні експерименти підтвердили працездатність і достовірність низки отриманих розрахункових співвідношень для вказаних характеристик плазмового каналу позитивного лідера електричного розряду, який формується і розвивається в цій високовольтній повітряній ДЕРС. Бібл. 49, рис. 7.

Ключові слова: **довгий повітряний проміжок, лідерний розряд, електричний пробій проміжку, плазмовий канал позитивного лідера, характеристики позитивного лідера.**

State and relevance of the problem. According to the provisions of modern gas discharge physics, the electrical breakdown of both long (length l_d of the order of 1–10^2 m, which corresponds to the gas insulation of extra- and high-voltage electrical equipment), and ultra-long (length l_d of the order of $(1–3)\cdot10^3$ m, which is characteristic of extra-high-voltage lightning discharges in the Earth's troposphere) air gaps occurs according to the leading electrophysical mechanism and ends with spark form of the discharge and their short-circuiting mode [1–4]. As a result of this breakdown, the gas medium of these gaps passes from a dielectric state in the zone of propagation of this discharge to an electrically conductive one by transforming it into plasma. At the same time, the leader discharge in atmospheric air has one characteristic property [1–3]: from a source of artificial (charged with high electric potential of the order of $\varphi_e\approx\pm1$ MV metal electrode of an electrical device [1, 3]) or natural (charged in the Earth's troposphere thundercloud with extra-high electric potential of the order of $\varphi_R\approx\pm(100–500)$ MV [2, 5]) electricity, a thin (radius of about $R_L\approx0{,}5\cdot10^{-3}$ m [1, 3]) plasma thermionic channel with main spherical part (head with radius $R_{eL}\approx R_L$ with excess charge q_{eL} of the corresponding polarity) that glows brightly, which in the electrophysics of high (extra-high) voltages is called a «leader». From the head of this leader towards the grounded metal electrode of the discharge electrical system or the surface of the earth with objects on it, when considering linear lightning, numerous streamers develop, which are capable of branching. After the head of the developed leader, which has an electric potential $\pm U_{eL}$, meets the grounded metal electrode (surface of the earth or ground technical object) to which it developed, the charge ±qeL of the leader head is neutralized and a stage of powerful reverse discharge occurs in the leader channel [1–3]. Further, with speed of about 10^7 m/s [1, 3] in the direction of the potential electrode of the specified systems, first a wave of potential removal in the leader channel with the disappearance of its charge $\pm q_L$ propagates, and then a wave of a large discharge pulse current, and finally, in place of a thin zigzag leader plasma channel with absolute temperature of the order of $T_{mL}\approx(5–10)\cdot10^3$ K [3] of its plasma, a strongly ionized spark plasma channel with absolute temperature of the order of $(20–40)\cdot10^3$ K and a maximum radius $r_{mk}>>R_L$, which is determined by the Braginsky formula [6, 7], with volumetric electron density n_{ei} in it of the order of $n_{ei}\approx(10^{21}–10^{23})$ m^{-3} [1, 3].

To date, from the published results of research on the leader and spark stages of electrical breakdown of long (ultra-long) air gaps in various discharge electrode systems (mainly in two-electrode extra- and high-voltage systems «tip-plane» and «thundercloud-ground»), high-current pulse discharges in gas and condensed media in the field of high-voltage technology (HVT), high-voltage pulse technology (HVPT) and atmospheric electricity with its huge reserves of electrical energy and powerful thunderstorm discharges according to [1–33], the questions that remain poorly studied are those related to the computational and experimental determination of the quantitative values of such basic characteristics of the leader plasma channel in atmospheric air as:

- electron density n_{eL} and electric potential U_{eL} in the leader head;
- linear electric charge q_{Ll} of the leader channel;
- density δ_{eL} of electron current i_{eL} and this current i_{eL} in the leader channel;
- high electric field strengths inside E_{Li} and outside E_{Le} of the leader channel;
- length l_s of the streamer zone in front of the leader head;
- maximum electron temperature T_{mL} in the plasma of the leader channel;
- linear active resistance R_{Ll} and total active resistance R_{Lc} of the leader channel.

Knowledge of the quantitative values of these characteristics of the zigzag plasma channel of the leader will contribute to the deepening of scientific knowledge about such a complex electrophysical phenomenon in nature as the electrical breakdown of long and ultra-long air gaps, which we need in practice for the well-founded design and engineering selection of high-voltage gas insulation of power electrical and electrical equipment for various ground and air technical facilities and their reliable protection against the striking action of linear lightning.

The **purpose** of the article is the computational and experimental determination of the main characteristics of the plasma channel of the leader during the electrical breakdown of a long air gap in a double-electrode discharge system (DEDS) «tip-plane» by artificial electricity of high pulse voltage of positive polarity.

1. Problem definition. Let us consider a high-voltage DEDS placed in the atmospheric air in the form of a «tip-plane» discharge system [3, 27]) with air gap of length l_d from the range 1 m$\leq l_d \leq$100 m, in which in the vertical direction from the potential metal electrode-rod of this DEDS with radius r_0 with pointed lower edge with the radius of its curvature $r_c<<r_0$ to its grounded metal electrode-plane, the development of the plasma channel of the positive leader with radius R_L is observed in time t (Fig. 1).

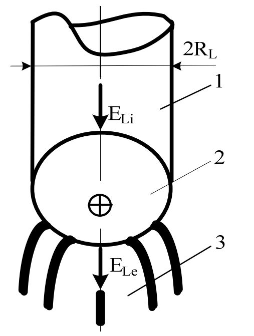

Fig. 1. Schematic representation of a positive leader during its development and movement in a long air gap of the tip-plane DEDS (1 − leader channel with radius R_L; 2 − leader head with radius $R_{eL}\approx R_L$; 3 − leader streamer zone)

Let the electric potentials of the specified electrodes of this DEDS, varying in time t, be equal to $\varphi_e(t)$ and $\varphi_0(t)\approx0$, respectively, and the air placed between them corresponds to the following normal atmospheric conditions [34]: the pressure of its gas molecules is $P_a\approx(1{,}013\pm0{,}03)\cdot10^5$ Pa; their absolute temperature is $T_a\approx(273{,}15\pm10)$ K; the relative humidity of these gases is $\gamma_a\approx(45\pm30)$ %. We assume that the density $\rho(h)$ of air in the DEDS under consideration, in the first approximation, can be, depending on the height $h\approx l_d$ of its upper electrode location relative to the Earth's surface with potential φ_e of the order of 1 MV, described by the relation of the form [4]: $\rho(h)\approx\rho(0)exp(-h/H)$, where $\rho(0)\approx1{,}293$ kg/m^3 is the air density at the Earth's surface [34], and $H\approx7{,}5\cdot10^3$ m is the height of the Earth's homogeneous troposphere [35]. Therefore, at $h\approx l_d\approx100$ m, the ratio $\rho(h)/\rho(0)$ takes a numerical value of about 0,98. In connection with this, the influence of the density $\rho(h)$ of the atmospheric air in the DEDS under study on the value of the radius R_L of the plasma channel of the positive leader in it can be neglected in the case under consideration [3, 7].

We assume that the radius R_L of the leader channel in the DEDS is quantitatively determined in the first approximation by the level $R_L\approx0{,}5$ mm [1]. This value for R_L corresponds to the known ratio for the maximum radius R_a of the electron avalanche head in air, which has the following form: $R_a\approx0{,}5\ \alpha_i^{-1}$, where $\alpha_i\approx10^3$ m^{-1} is the impact ionization coefficient of atmospheric air in the DEDS [1, 3]. It is known that the positive leader in the DEDS under study arises on the basis of a positive (cathode-directed) streamer developed in its air with significant heating of its channel by the current. This initial streamer with density of n_{es0} electrons in it originates in a spherical zone with radius of $r_i \approx x_i$ of active impact ionization by air electrons near the active electrode-tip of the DEDS, when the maximum electron temperature T_{ms} in its channel reaches a level near $T_{ms} \approx (5–10) \cdot 10^3$ K [3]. Therefore, this absolute temperature T_{ms} is also characteristic of the maximum electron temperature T_{mL} of the equilibrium plasma of the channel of the positive leader at the beginning of its emergence [3]. Let us consider the case of a multi-streamer-leader electric discharge in the air of a DEDS [1, 3], when near the electrode-tip of this DEDS, N_s of individual positive streamers with excess positive charge q_{es} in their heads simultaneously start from the spherical head with radius R_{eL} of the positive leader towards its grounded electrode-plane, the radius R_s of the plasma channel of which is much smaller than the radius R_L of the channel of the positive leader with excess positive charge q_{eL} of its head, which corresponds to the modulus of the electron density n_{eL} in it. We assume that at $q_{eL} \approx N_s q_{es}$ this density n_{eL} of electrons in the head with radius $R_{eL} \approx R_L \approx 0{,}5$ mm [1, 3] of the positive leader, which is formed in the spherical zone with radius $r_i \approx x_i$ of active impact ionization by air electrons near the electrode-tip of this DEDS, corresponds to the density n_{es} of electrons in the head of a separate positive streamer with radius $R_{es} << R_{eL}$ with the inequality $n_{es} << n_{eL}$ being fulfilled. According to [1, 3] the density n_{es0} of electrons in the initial developed positive streamer of the DEDS should be of the order $n_{es0} \approx 10^{19}$ m^{-3} and more. Under these physical conditions and the above-mentioned levels of temperature T_{ms} and electron density n_{es0} in the initial developed positive streamer in the spherical zone with radius $r_i \approx x_i$ near the potential electrode of the tip-plane DEDS, a positive leader can be formed, which will grow from this zone with velocity v_L into the long air gap of this DEDS with the help of individual positive streamers in their number N_s (see Fig. 1) and photoionization of atmospheric air molecules [1, 3, 15].

Let us limit ourselves to considering the electrophysical case when the rate of change in time t of the high voltage $U_e(t) \approx \varphi_e(t) - \varphi_0(t)) \approx \varphi_e(t)$ in the DEDS under study, during the electrical breakdown of its long air gap with length of 1 m $\leq l_d \leq$ 100 m, satisfies the inequalities of the form $\mathrm{d}U_e(t)/\mathrm{d}t \geq 5$ kV/μs [3] and the development of the positive leader in it occurs continuously, i.e. without the stepwise formation of the «tip-plane» of individual leader channels in the long discharge gap of this DEDS. This position regarding the specified electrophysical influence of the derivative $\mathrm{d}U_e(t)/\mathrm{d}t$ on the nature of the development of the positive leader in the atmospheric air of this DEDS for a separate case when the length l_d of this gap in the DEDS corresponded to the range 1 m $\leq l_d \leq$ 4 m, was confirmed by us experimentally using domestic ultrahigh-voltage equipment [4, 27].

It is necessary, taking into account the calculated and experimental data, to determine in an approximate form the main characteristics of the plasma channel of the positive leader in the DEDS under study, which include the values of the following physical indicators: electron density n_{eL} and electric potential U_{eL} in the head of the positive leader; linear charge q_{Ll} of the leader plasma channel; density δ_{eL} of electron current i_{eL} and this current i_{eL} in the leader channel; strong electric field strengths inside E_{Li} and outside E_{Le} of the leader channel with specific electrical conductivity E_{Le} of its plasma; length l_s of the streamer zone in front of the leader head; maximum electron temperature T_{mL} in the plasma of the leader channel; active resistance R_{Lc} of the leader channel.

2. Determination of the parameters of the zone of active impact ionization of air in the DEDS. As is known, diatomic oxygen molecules O_2 in the composition of the atmospheric air gases of the DEDS under study occupy up to 21 % of the working volume of its long discharge gap [34]. At the same time, according to the data of Table 1.6 from [3], the ionization energy $W_i \approx W_{i0}$ of oxygen molecules O_2 by electron impact is one of the smallest for the main atoms (molecules) of gases that make up the air of this DEDS, and is numerically about $W_{i0} \approx 12{,}5$ eV. For comparison, we note that for diatomic nitrogen molecules N_2, which occupy up to 78 % of the volume of the air gap of the DEDS «tip-plane» [34], the ionization energy of them by electron impact is about $W_i \approx W_{iN} \approx 15{,}6$ eV [3]. Therefore, the shortest duration of the process of ionization of air insulation gases in this DEDS by electron impacts will be determined by the ionization energy $W_i \approx W_{i0}$ of its diatomic oxygen molecules O_2. Taking this into account, in further calculations of the process of active impact ionization by electrons of atmospheric air in the studied DEDS, we will limit ourselves to using the ionization energy W_{i0}, which is characteristic of its oxygen molecules O_2.

Let us consider the case when the process of avalanche-like electron propagation in the atmospheric air of the DEDS under study is carried out due to the impact ionization of this air under the influence of one initial electron (N_0=1) for gas-discharge plasma formations, which are caused by the action of an ultra-strong electric field in a spherical zone with radius of $x_i \approx r_i$ of active air ionization by electron impacts near the DEDS electrode-tip. In this electrophysical process at the edge of this zone with radius of $x_i \approx r_i$ of active ionization by electrons of atmospheric air, located near the potential metal electrode of the DEDS, the number of electrons N_x in the head of the developed positive streamer, which is formed in this zone due to the specified process of their multiplication, in the first approximation will be described by the dependence [1, 3]: $N_x \approx N_0 exp(\alpha_i^* x_i)$, where $\alpha_i^* = (\alpha_i - \eta)$ is the effective coefficient of impact ionization of air in the DEDS, and η is the coefficient of electron adhesion in the air of this DEDS.

Electrons with their charge modulus e_0=1,602·10^{-19} C and rest mass m_e=9,109·10^{-31} kg [34] between their two successive collisions with effective frequency v_m with atoms or molecules of air (for example, oxygen O_2) in the DEDS under study, gain near the potential electrode-tip of this DEDS in its superstrong electric field with averaged strength E_x a drift velocity of approximately $v_{ed} \approx e_0 E_x / (m_e v_m)$ and, accordingly, an energy $W_e \approx e_0 E_x v_{ed} / v_m$ [1], which for the condition of the beginning of the process of active ionization of this air must be at least equal to the ionization energy $W_i \approx W_{i0}$ of its oxygen molecules O_2. Therefore, from the equality $W_e \approx W_{i0} \approx e_0^2 E_{xk}^2/(m_e \nu_m^2)$ one can obtain a calculated expression for the averaged value of the critical strength E_{xk} of the electric field at the edge of the ionization zone of the atmospheric air under consideration. This value turns out to be equal to $E_{xk} \approx e_0^{-1} \nu_m (m_e W_{i0})^{1/2}$. At $\nu_m \approx 2{,}96 \cdot 10^{12}$ s^{-1} [1] and $W_{i0} \approx 12{,}5$ eV [3] the critical electric field strength E_{xk} in the DEDS under study takes a quantitative value of about $E_{xk} \approx 24{,}9 \cdot 10^6$ V/m. In this case, the drift velocity $v_{ed} \approx e_0 E_{xk}/(m_e \nu_m)$ of electrons at this edge of the spherical zone with radius $x_i \approx r_i$ of active impact ionization of air near the potential electrode of the DEDS is equal to $v_{ed} \approx 1{,}48 \cdot 10^6$ m/s.

According to [1], the coefficient η of electron adhesion to molecules for the atmospheric air we have adopted in the DEDS under study, with the frequency of their adhesions $\nu_\eta \approx 10^8$ s^{-1} and the electron drift velocity $v_{ed} \approx 1{,}48 \cdot 10^6$ m/s in the plasma of the positive streamer discharge channel in the DEDS, takes a numerical value of about $\eta \approx \nu_\eta / v_{ed} \approx 67$ m^{-1}. Therefore, with $\alpha_i \approx 10^3$ m^{-1} [1, 3], the influence of electron adhesion on their propagation in the air of this DEDS can be neglected, and the parameter α_i^* depending on the number of electrons N_x in the head of the developed positive streamer in the specified zone of its ionization is taken equal to α_i.

Let us indicate that the radius $x_i \approx r_i$ of the zone of active impact ionization of atmospheric air molecules by electron impacts near the potential electrode-tip of the DEDS is determined by the following calculated expression: $x_i \approx r_i \approx U_{ed}/E_{xk} \approx U_{ed} e_0 \nu_m^{-1} (m_e W_{i0})^{-1/2}$, where U_{ed} is the voltage of the appearance of a continuous positive leader in the air DEDS [3]. According to formula (5.35) from [3], the voltage U_{ed} in the studied DEDS is determined by the approximate expression: $U_{ed} \approx E_{e0} l_{\min}/k_c$, where $E_{e0} \approx 23[1+1{,}22(r_{ec})^{-0{,}37}]$ with the dimension (kV/cm) is the initial electric field strength in the DEDS at the edge of its metal electrode-tip with the equivalent radius of its curvature $r_{ec} \approx r_c$, and $k_c \approx (14+1{,}5 l_{\min})$ with the dimension of the minimum length $l_{\min}$ of the DEDS air gap in (m) is the critical value of the dimensionless coefficient of electric field heterogeneity in the DEDS. We see that the electric voltage U_{ed} in the DEDS «tip-plane» depends both on the length of the air gap $l_d \approx l_{\min} \geq 1$ m in the DEDS, and on the geometry (curvature) of the edge of its potential electrode-tip. With the increase in the length $l_{\min}$ of the gap in the DEDS, its influence on the voltage U_{ed} decreases. We note that the reliability of this calculation expression for $x_i \approx r_i$ in the DEDS under consideration, at 1 m $\leq l_d \leq$ 4 m, was confirmed by us experimentally [4, 27].

For the electrophysical case, when in the high-voltage DEDS the «tip-plane» is investigated, at $r_{ec} \approx r_c \approx 3$ mm ($r_0 \approx 15$ mm) and the electrical breakdown of its air gap with minimum length $l_d = l_{\min} = 1{,}5$ m, which corresponds to the length of the straight line drawn from the tip of the potential electrode of the DEDS along the normal to the flat surface of its grounded plane, the calculation voltage U_{ed} according to the above-mentioned relations from [3] is numerically equal to about $U_{ed} \approx 616{,}6$ kV. Note that in this case, the experimental breakdown (discharge) voltage U_d for a switching aperiodic voltage pulse of the time shape $T_m/T_p \approx 200$ µs/1990 µs of positive polarity (T_m, T_p are, respectively, the time corresponding to the amplitude U_{em} and the duration of the voltage pulse $U_e(t)$ in the DEDS at the level of $0{,}5U_{em}$) took the quantitative value $U_d \approx 611{,}6$ kV [4, 27], which differs from the calculated value $U_{ed} \approx 616{,}6$ kV within 1 %. Therefore, at $\nu_m \approx 2{,}96 \cdot 10^{12}$ s^{-1} [1], $U_{ed} \approx 616{,}6$ kV and $W_{i0} \approx 12{,}5$ eV [3], which is characteristic of electron impact ionization of oxygen molecules O_2 in the atmospheric air of the studied DEDS ($\alpha_i \approx 10^3$ m^{-1} [1, 3]), the radius of the spherical zone of active ionization by electron impacts of air near its potential metal electrode-tip takes the numerical value $x_i \approx r_i \approx 24{,}7$ mm.

According to [1, 3], taking into account the above calculated relations, the density n_{es0} of electrons in the head of a developed positive streamer with radius $R_{es} \approx 0{,}5\alpha_i^{-1} \approx 0{,}5$ mm, which is formed in a spherical zone with radius $x_i \approx r_i \approx 24{,}7$ mm ($U_{ed} \approx 616{,}6$ kV) of active impact ionization of air by electrons near the electrode-tip of the DEDS, $N_0=1$ and $\alpha_i \approx 10^3$ m^{-1} is approximately equal to the numerical value $n_{es0} \approx 10{,}2 \cdot 10^{19}$ m^{-3}. We see that the obtained estimated quantitative value nes0 corresponds to the required level of electron concentration (of the order of $n_{es0} \approx 10^{19}$ m^{-3} [1, 3]) in the head of the initial developed positive streamer, on the basis of which a positive leader with radius of about $R_L \approx 0{,}5$ mm of its plasma channel can be formed in a spherical zone with radius of $r_i \approx x_i \approx 24{,}7$ mm near the potential electrode-tip of the studied DEDS «tip-plane».

3. Determination of the electron density n_{eL} in the head of the positive leader in the air DEDS. At the level of high electric voltage $U_e(t) \geq 1$ MV in the studied DEDS and the duration $t_L \approx T_d \approx 100$ µs of the main phase of electric discharge processes in its long air gap [3, 15, 24], where the parameter T_d corresponds to the time of its electrical breakdown (the time of cut-off T_c of high voltage $U_e(t)$ at this insulating gap), the positive leader in the considered high-voltage DEDS will correspond to the mode of its continuous development in its air with the fulfillment of the specified condition d$U_e(t)$/d$t \geq 5$ kV/µs. For an approximate calculation of the electron density neL in the head of the positive leader in a high-voltage air DEDS «tip-plane», we use the well-known generalized Saha formula for the electron density n_{eL} in the equilibrium plasma of this DEDS as a function of their temperature T_{mL} and the ionization energy W_i of neutral atoms (molecules) of atmospheric air gases in this plasma [1, 36]:

$$n_{eL} \approx (A g_+ / g_a)^{1/2} n_{nL}^{1/2} T_{mL}^{3/4} \exp(-0{,}5 W_i / T_{mL}), \quad (1)$$

where $A=6{,}06 \cdot 10^{21}$ cm$^{-3} \cdot$eV$^{-3/2}$; g_+, g_a are, respectively, the statistical weights of ions and neutral atoms (molecules) of air gases in the leader plasma; nnL is the density of neutral atoms (molecules) of atmospheric air in the leader plasma (cm^{-3}); T_{mL} is the maximum electron temperature in the leader plasma (eV); W_i is the ionization energy of neutral atoms (molecules) of air in the leader plasma (eV).

According to [1], the Saha equation (1) was obtained using statistical physics methods regardless of the mechanisms of electron generation in the equilibrium plasma under consideration. In the case of atmospheric air in the DEDS, which is a mixture of different gases, this Saha equation can be used for atoms (molecules) of each type that are part of it [1]. Therefore, during a single impact ionization by electrons of oxygen molecules O_2 (g_+=4, and g_a=3 [1]), which are present in the electroneutral air plasma of the long discharge gap of the studied DEDS, the specified Saha formula (1) takes the following simplified form:

$$n_{eL} \approx 0{,}9 \cdot 10^{11} n_{nL0}^{1/2} T_{mL}^{3/4} \exp(-0{,}5 W_{i0} / T_{mL}) \,, \quad (2)$$

where n_{nL0} is the density of neutral oxygen molecules O_2 of the atmospheric air DEDS in the leader plasma (cm^{-3}); W_{i0} is the impact ionization energy of neutral oxygen molecules O_2 of the atmospheric air DEDS in the leader plasma (eV).

For the case of using in the calculations of the electron density neL in the head of the positive leader the process of impact ionization of neutral oxygen molecules O_2 of atmospheric air in a high-voltage DEDS (n_{nL0}≈2,52·10^{11} cm^{-3} according to the data of Table 8.3 from [1]) at W_i≈W_{i0}≈12,5 eV [3] and T_{mL}≈1,639·10^4 K (see Section 8), which corresponds to T_{mL}≈1,413 eV [34, 37], by (2) the electron density n_{eL} in the head of the positive leader in the air DEDS under study is quantitatively equal to approximately n_{eL}≈0,7·10^{21} m^{-3}. Therefore, for this case, the degree of ionization χ≈n_{eL}/N_L, where N_L=2,687·10^{25} m^{-3} is the Loschmidt number [34, 38], the air in the tip-plane DEDS will be about χ≈0,26·10^{-4}. The numerical value of neL obtained by (2) differs from the density n_{eL}≈0,9·10^{21} m^{-3} adopted in Section 8 when determining the specified plasma temperature T_{mL} by (12) within 22 %. Let us point out that these quantitative values of the electron density neL in the positive leader are in good agreement with the known data for the concentration of free electrons in air plasma at its temperatures of the order of T_{ms}≈T_{mL}≈(5–10)·10^3 K [1, 3, 39, 40]. In addition, the result obtained for (2) for the density neL of electrons in the positive leader corresponds to the condition of the Loeb electrical breakdown for gas insulation, according to which the density n_e of electrons in their avalanche when a streamer appears on its base in short gas gaps (air of the DEDS) must be at least $n_e \geq 0{,}7 \cdot 10^{18}$ m^{-3} [1, 3].

4. Determination of the linear charge q_{Ll} of the positive leader channel in the air DEDS. When calculating the linear charge q_{Ll} of the leader plasma channel in the high-voltage DEDS under study, we will proceed from the physical position that this charge is formed by positively charged heads of positive electric streamers with charges q_{es}≈q_{eL}/N_s, which are formed by the positive leader growing in the air of this DEDS. During this leader germination in the air, the positive charge q_{eL} of its head and the electron density modulus n_{eL} in it according to (2) remain for this DEDS of artificial origin little changed until the moment of the through discharge phase in its long air gap. With similar approximate mechanism of the electrophysical development of this leader in a short time Δt_L≈R_L/v_L of its advancement in the air gap of the DEDS, the total positive charges q_{ess}≈$q_{es}N_s$≈q_{eL} of the heads of individual electric streamers starting from the leader head into the air will determine the charge q_{Ll} of the leader channel. Therefore, for the linear positive charge q_{Ll} of the leader plasma channel in an air high-voltage DEDS, in which the electron current i_{eL} and its density δ_{eL} are determined by the negatively charged sections of positive streamers with radius R_{es}≈0,1α_i^{-1}≈0,1·10^{-3} m [1, 3] moving towards the grounded electrode-plane of the DEDS in a total quantity of about N_s≈2(R_{eL}/R_{es})^2≈50 with density of electrons n_{es} in them, and the ion current i_{iL} and its density δ_{iL} are determined by the heads of these cathodically directed positive streamers with module of the density of electrons n_{es} in them (see Fig. 1), we have the following approximate calculation relationship:

$$q_{Ll} \approx 0{,}5 q_{es} N_s R_L^{-1} \approx 0{,}5 q_{eL} / R_L \approx 2\pi e_0 n_{eL} R_L^2 / 3 \,. \quad (3)$$

According to (3), the greater the value of the charge q_{eL} of the head of the positive leader, the greater the linear positive charge q_{Ll} of its plasma channel will be.

With n_{eL}≈0,7·10^{21} m^{-3} and R_L≈0,5α_i^{-1}≈0,5·10^{-3} m [1] according to (3), the linear charge q_{Ll} of the plasma channel of the positive leader in the air of the studied DEDS ($l_{\min}$≈1,5 m) has a value of about q_{Ll}≈58,7·10^{-6} C/m. To compare this result for q_{Ll} with known data, we indicate that with leader high-current extra-high-voltage discharge in this DEDS ($l_{\min}$≈100 m) with switching aperiodic pulse of extra-high electric voltage $U_e(t)$ with amplitude U_{em}≈3,2 MV of time shape T_m/T_p≈1,5 μs/3000 μs of positive polarity, the linear charge q_{Ll} of this leader was q_{Ll}≈100 μC/m [3].

With the germination of the DEDS channel of this leader with speed v_L in the air, its all new cylindrical sections will receive the indicated positive charges from the heads of positive streamers emerging from its spherical head. Taking into account such monotonic charging of the leader channel, its positive charge q_L will increase until it covers the air gap of this DEDS (within the limit of q_L≈q_{Ll}·$l_{\min}$). In this case, the total current $i_{L\Sigma}$ of the plasma channel of the positive leader in this DEDS is determined by the sum of its ionic current i_{iL}≈q_{Ll}·v_L and electron current i_{eL}, which is determined by the negatively charged areas of the specified positive streamers, caused by this positive leader, and directed towards the grounded electrode of the DEDS. According to (3), at q_{Ll}≈58,7·10^{-6} C/m and v_L≈10^5 m/s [1, 27], the ionic current i_{iL} in the channel of this leader takes the approximate value i_{iL}≈5,87 A, and its density δ_{iL}≈i_{iL}/(πR_L^2) is approximately δ_{iL}≈7,47·10^6 A/m^2.

5. Determination of the density δ_{eL} of the electron current i_{eL} and the current i_{eL} in the channel of the positive leader in the air DEDS. According to the proposed approximate model of the electrophysical development of the positive discharge leader with the actual use of charges from its streamer zone from the atmospheric air of the DEDS and the further advancement of this leader towards the grounded electrode of the DEDS «tip-plane» (see Fig. 1), for the velocity ved of the directed motion (drift) of electrons in the plasma channel of the leader towards the potential electrode-tip of this DEDS, caused, among other things, by positive streamers with density nes of electrons in their individual channels, one can use the well-known formula [38]: v_{ed}≈δ_{eL}/($e_0 n_{eL}$). On the other hand, for this electron velocity ved we have the following expression [1]: v_{ed}≈$e_0 E_{xk}$/($m_e \nu_m$), where

$E_{xk} \approx e_0^{-1} v_m (m_e W_i)^{1/2}$ is the critical strength of the extra-high electric field in the long air gap of the studied DEDS. As a result, for the density δ_{eL} of the electron current i_{eL} in the plasma channel with radius $R_L \approx 0{,}5\alpha_i^{-1} \approx 0{,}5$ mm [1, 3] of the studied positive leader in this DEDS, we can obtain an analytical relation of the form:

$$\delta_{eL} \approx e_0 n_{eL} m_e^{-1/2} W_i^{1/2} . \quad (4)$$

From (4) it follows that the density δ_{eL} of the electron current i_{eL} in the channel of the positive leader is determined by the density n_{eL} of electrons in its spherical head with radius $R_{eL} \approx R_L \approx 0{,}5\alpha_i^{-1} \approx 0{,}5 \cdot 10^{-3}$ m [1, 3]. The greater the value of this density n_{eL} of electrons in its head, the greater the density δ_{eL} of the electron current i_{eL} in the leader channel.

At $n_{eL} \approx 0{,}7 \cdot 10^{21}$ m^{-3} and $W_i \approx W_{i0} \approx 12{,}5$ eV [3] (in the case of impact ionization by electrons of oxygen molecules O_2 in the atmospheric air of the DEDS), the density δ_{eL} of the electron current i_{eL} in the plasma channel of the positive leader in this air DEDS «tip-plane» by (4) takes a quantitative value of about $\delta_{eL} \approx 1{,}66 \cdot 10^8$ A/m^2. This value of δ_{eL} corresponds numerically to the current density in the positive leader, which is given in [1, 3, 40].

As for the electron current ieL in the channel of the positive leader under study, it is calculated by the approximate formula of the form: $i_{eL} \approx \pi R_L^2 \delta_{eL}$. At $\delta_{eL} \approx 1{,}66 \cdot 10^8$ A/m^2 and $R_L \approx R_{eL} \approx 0{,}5\alpha_i^{-1} \approx 0{,}5$ mm [1, 3] this electron current i_{eL} in the cylindrical plasma channel of the positive leader for the specified applied electrophysical case during the electrical breakdown of a long air gap in the studied high-voltage air-based DEDS «tip-plane» ($l_{\min}$=1,5 m; $U_d \approx 611{,}6$ kV [4, 27]; $\alpha_i \approx 10^3$ m^{-1} [1, 3]; $v_m \approx 2{,}96 \cdot 10^{12}$ s^{-1} [1]; $N_s \approx 50$; $W_i \approx W_{i0} \approx 12{,}5$ eV [3]; $x_i \approx 24{,}6 \cdot 10^{-3}$ m) is quantitatively approximately $i_{eL} \approx 130{,}5$ A. The obtained calculated numerical result for the electron current ieL in the positive leader channel corresponds to the empirical data that were previously provided in a number of literature sources in the field of HVT and HVPT [1, 3, 40]. We note that in the plasma channel of the positive leader in this DEDS, the obtained electron current $i_{eL} \approx 130{,}5$ A significantly exceeds the above-mentioned ion current $i_{iL} \approx 5{,}87$ A, which is provided by the motion with speed of about $v_L \approx 10^5$ m/s [1, 27] of this channel. Physically, this difference can be explained by the corresponding speeds of directed motion of these electricity carriers (these drift speeds in the leader channel are about 10^6 m/s for electrons, and 10^3 m/s for ions [1, 3, 15]).

6. Determination of the electric field strengths inside E_{Li} and outside E_{Le} of the positive leader channel in the air DEDS. For an approximate calculation of the longitudinal electric field strength E_{Li} inside a thin zigzag cylindrical channel ($R_L \approx 0{,}5 \cdot 10^{-3}$ m [1]) of the positive leader in the air DEDS under study, we will use the classical electrodynamic relation of the form: $E_{Li} \approx \delta_{eL}/\gamma_{Le}$ [41–43]. Then, for the length-averaged longitudinal electric field strength E_{Li} inside the plasma channel of the positive leader in this DEDS, taking into account (4), we use the expression:

$$E_{Li} \approx i_{eL} / (\pi \gamma_{Le} R_L^2) \approx e_0 n_{eL} \gamma_{Le}^{-1} m_e^{-1/2} W_i^{1/2} , \quad (5)$$

where $\gamma_{Le} \approx 10^4$ $(\Omega \cdot \text{m})^{-1}$ is the specific electrical conductivity of the plasma of the positive leader channel in the DEDS [1], which takes into account the change in the degree of ionization $\chi \approx n_{eL}/N_L$ of its air with increase in the maximum electron temperature T_{mL} of the plasma of the positive leader channel in this DEDS.

According to (5), the length-averaged longitudinal electric field strength E_{Li} inside the plasma cylindrical channel of the positive leader in the air DEDS «tip-plane» is determined both by the value of the electron density n_{eL} in its head with radius $R_{eL} \approx R_L \approx 0{,}5\alpha_i^{-1} \approx 0{,}5$ mm [1, 3], and by the specific electrical conductivity γ_{Le} of the discharge leader plasma. At $n_{eL} \approx 0{,}7 \cdot 10^{21}$ m^{-3}, $W_i \approx W_{i0} \approx 12{,}5$ eV [3], $R_L \approx 0{,}5$ mm [1, 3] and $\gamma_{Le} \approx 10^4$ $(\Omega \cdot \text{m})^{-1}$ [1] according to (5) the calculated length-averaged electric field strength E_{Li} in the case of using the specified standard switching aperiodic voltage pulse $U_e(t)$ during electrical breakdown of a long air gap ($l_{\min}$=1,5 m) takes a quantitative value of about $E_{Li} \approx 16{,}6$ kV/m. This value of E_{Li} corresponds to the accepted in HVT and HVPT levels of length-averaged longitudinal strong electric field strength inside the channel of the positive leader, which develops in the microsecond time range in the high-voltage air DEDS «tip-plane» for its gaps from the range 1 m $\leq l_{\min} \leq$ 5 m [3, 39, 40]. According to [40], at values of the minimum length $l_{\min}$ in this DEDS of the order of $l_{\min} \approx 100$ m, the level of electric field strength E_{Li} in the channel of the positive leader approaches its minimum numerical value of the order of $E_{Li} \approx 10$ kV/m [1], which is observed in the channel of an open stationary electric arc at currents of the order of 1 A.

When determining the length-averaged values of the electric field strengths outside (in the streamer zone of the leader according to Fig. 1) E_{Le} and inside E_{Li} of the plasma channel of the positive leader in the air DEDS «tip-plane», as well as the averaged length ls of the streamer zone in this DEDS when the condition $dU_e(t)/dt < 10^3$ kV/μs is met, we will use the balance equation for the electric voltage on the discharge long air gap of this DEDS, which corresponds to the moment of the onset of the through phase of the discharge in this air gap of the high-voltage DEDS [3, 40]:

$$U_e(t) \approx U_d \approx E_{Li}(l_d - l_s) + E_{Le} l_s , \quad (6)$$

where $l_d \approx 1{,}13 l_{\min}$ is the length of the zigzag path of the leader-streamer discharge in the air of the DEDS [4, 27].

We note that when the through phase of the leader-streamer discharge occurs in the DEDS under study, the following geometric equality is satisfied: $(l_L + l_s) = l_d$, where l_L is the length of the positive leader channel in the DEDS.

According to [40], under normal atmospheric conditions in the DEDS, which correspond to the conditions we have adopted for its air, the value of the length-averaged electric field strength E_{Le} in the streamer zone of the positive leader is quantitatively equal to about $E_{Le} \approx 465$ kV/m. We see that this numerical level of the averaged longitudinal electric field strength E_{Le} outside the cylindrical plasma channel of the positive leader in its air streamer zone corresponds to the range of strong pulsed electric fields [37]. The reliability of this value given above for the level of averaged electric field strength E_{Le}≈465 kV/m outside the plasma channel of the positive leader (in its air streamer zone) in the DEDS under study may be indicated by the experimental data obtained by us when determining the maximum breakdown strength $E_{d\max}$≈$U_{em}/l_{\min}$≈462,6 kV/m of the electric field for this high-voltage air DEDS «tip-plane» ($l_{\min}$=1,5 m), which, during its electric spark breakdown, experienced the direct action of a standard switching aperiodic voltage pulse $U_e(t)$ with amplitude U_{em} of the time shape T_m/T_p ≈ 200 μs/1990 μs of positive polarity [4, 27].

From (6) for the averaged length l_s of the streamer zone in the DEDS «tip-plane» we have the following expression:

$$l_s \approx (U_d - E_{Li} l_d)/(E_{Le} - E_{Li})\,. \quad (7)$$

For the electrophysical case of the action in the air DEDS «tip-plane» ($l_{\min}$=1,5 m; l_d≈1,13$l_{\min}$≈1,695 m) of the above-mentioned aperiodic voltage pulse $U_e(t)$ of positive polarity with breakdown voltage U_d≈611,6 kV [4, 27], using (7) at E_{Li}≈16,6 kV/m and E_{Le}≈465 kV/m, we obtain a quantitative value for the average length l_s of the streamer zone in the DEDS, which will be about l_s≈1,3 m. Let us indicate that according to [1] in this air DEDS at 1,5 m ≤ $l_{\min}$ ≤ 10 m the streamer zone extends in front of the head of the positive leader to a distance of the order of l_s≈1 m. The numerical result obtained by calculation and experimental methods for the averaged length l_s≈1,3 m of the streamer zone in the «tip-plane» DEDS may indicate the validity of the data we used for the averaged length-wise electric field strengths inside E_{Li}≈16,6 kV/m and outside E_{Le} ≈ 465 kV/m of the positive leader channel in this DEDS.

For a rough numerical estimate of the maximum value E_{Lem} of the electric field strength in the air streamer zone with the radial coordinate x_s>>R_{eL} of the positive leader of the studied DEDS with sharply inhomogeneous electromagnetic field, the following approximate relationship can be written using the theory of the electrostatic field [41]:

$$E_{Lem} \approx q_{eL}/(4\pi\varepsilon_0 x_s^2) \approx e_0 n_{eL} R_{eL}^3 (3\varepsilon_0 x_s^2)^{-1}\,, \quad (8)$$

where x_s is the distance along the radius from the center of the spherical head of the leader in the air towards the grounded electrode-plane of the DEDS; q_{eL}≈4π$e_0 n_{eL} R_{eL}^3$/3 is the electric charge of the head of the positive leader in the air gap of the DEDS, which at n_{eL}≈0,7·10^{21} m^{-3} and R_{eL}≈R_L≈0,5α_i^{-1}≈0,5 mm [1, 3] is approximately q_{eL}≈58,7 nC; ε_0=8,854·10^{-12} F/m is the electric constant [34].

We see that according to (8) this maximum strength E_{Lem} in the streamer zone of the positive leader with the radius R_L of its thin plasma channel is directly proportional to the value of the electron density n_{eL} in the spherical head with the radius R_{eL}≈R_L of this leader. At n_{eL}≈0,7·10^{21} m^{-3}, R_{eL}≈R_L≈0,5α_i^{-1}≈0,5·10^{-3} m [1, 3] and x_s≈10R_{eL}≈5 mm according to (8) the maximum strength E_{Lem} of the electric field in the vicinity of the head of the positive leader in the studied DEDS takes the quantitative value E_{Lem}≈21,1 MV/m. This level of the electric field strength E_{Lem} outside the head of the positive leader corresponds to the range of ultra-strong pulsed electric fields [40]. It was shown above that the critical electric field strength E_{xk} near the metal electrode-tip of the studied DEDS, which causes active impact ionization by electrons of its atmospheric air, should have a value of the order of E_{xk}≈24,9 MV/m. Therefore, in the atmospheric air of this DEDS near the spherical head with radius R_{eL} ≈ R_L ≈ 0,5 mm [1, 3] of the positive leader (x_s ≈ 10R_{eL} ≈ 5 mm) at the level of the maximum electric field strength near E_{Lem}≈21,1 MV/m, physical conditions will be created for the active development in its given local air zone (see Fig. 1) of electron avalanches and, accordingly, positive streamers, which will supply to this spherical head of the positive leader the electric charges necessary for its development and advancement in the atmospheric air of this DEDS.

7. Determination of the electric potential U_{eL} of the head of the positive leader in the air DEDS. According to (6), when the «tip-plane» through-phase of the leader-streamer discharge occurs in a high-voltage DEDS, when the equality (l_L+l_s)=l_d is satisfied, for the electric potential U_{eL} of the spherical head with radius R_{eL}≈R_L≈0,5 mm [1, 3] of the positive leader in the air DEDS studied by us, the following approximate calculation relation can be obtained:

$$U_{eL} \approx U_d - E_{Li}(1{,}13 l_{\min} - l_s)\,. \quad (9)$$

Taking into account the results of our quantitative determination of the average length l_s≈1,3 m of the streamer zone in this DEDS ($l_{\min}$=1,5 m; U_d≈611,6 kV [4, 27]) according to (9) at E_{Li}≈16,6 kV/m for the potential U_{eL} of the head of the positive leader (l_L≈1,13$l_{\min}$–l_s≈0,395 m) we obtain a value that is numerically about U_{eL}≈605 kV. We see that in this case the voltage drop U_L on the channel of the positive leader takes a numerical value that is approximately equal to U_L≈$E_{Li} l_L$≈6,6 kV. Thus, the main part of the voltage during the leader-streamer through-phase discharge (U_d≈611,6 kV [4, 27]) by an aperiodic voltage pulse $U_e(t)$ of the time shape T_m/T_p≈200 μs/1990 μs of positive polarity of a long air gap with minimum length $l_{\min}$=1,5 m falls on the positive streamers (voltage about U_s≈605 kV), which develop from the leader head towards the grounded electrode-plane of the DEDS. When the head of the positive leader touches the grounded electrode-plane of the DEDS, its electric potential takes on a zero value (U_{eL}≈0), and the entire breakdown voltage U_d is added to the leader channel.

8. Determination of the maximum electron temperature T_{mL} in the plasma of the positive leader channel in the air DEDS. When determining the temperature level in the plasma of the positive leader, which propagates in the long air gap of the high-voltage DEDS under study, we will proceed from the position that in the adiabatic regime, due to the rapid in time t flow of thermal processes in the plasma channel of this leader (with its change of the order of 10^6 K/s [4, 9, 15]), it corresponds to the maximum temperature T_{mL} of its electrons, which have a speed of movement (drift) in it of the order of 10^6 m/s [3]. We will indicate that in this case the maximum temperature T_{mi} of ions for the equilibrium plasma of the leader at their drift speed in it of the order of 10^3 m/s [3] is equal to the specified temperature T_{mL} of electrons. To find the maximum electron temperature T_{mL} in the plasma of the positive leader channel in the DEDS, we will use the relation known from thermal physics for the maximum heat flux density q_{mL} in the leader channel [38]:

$$q_{mL} \approx \pi^{-1}\sigma_c T_{mL}^4 , \qquad (10)$$

where σ_c=5,67·10^{-8} W(m^{2}K^4)$^{-1}$ is the fundamental Stefan-Boltzmann constant [34].

Due to the fact that the primary source of energy input into the leader plasma channel is the electrical energy stored in the studied DEDS, the following approximate electrophysical expression can be used for the heat flux density q_{mL} [44]:

$$q_{mL} \approx \delta_{eL} U_{e0} , \qquad (11)$$

where δ_{eL} is the electron current density in the plasma channel of the leader; U_{e0} is the electrode voltage drop in the plasma channel of the positive leader at the moment of its genesis near the potential metal electrode-tip of the DEDS (this constant electric voltage U_{e0} varies in the numerical range U_{e0}≈(5–10) V for various metal electrodes of this DEDS, which are used in the field of HVT and HVPT [3, 4, 45]).

Then, taking into account (4), (10) and (11), to calculate the maximum electron temperature T_{mL} in the plasma channel of the positive leader, which is formed in the zone with radius r_i≈x_i of impact ionization by air electrons near the potential metal electrode-tip of the studied DEDS, we have the relation:

$$T_{mL} \approx \sqrt[4]{\pi e_0 n_{eL} U_{e0} m_e^{-1/2} W_i^{1/2} \sigma_c^{-1}} . \qquad (12)$$

We see that according to (12) the electron temperature T_{mL} in the equilibrium plasma of a positive leader, which is born and develops in a long air gap of the DEDS «tip-plane», is mainly determined by the level of electron density n_{eL} in the head with radius R_{eL}≈R_L≈0,5α_i^{-1}≈0,5 mm [1, 3] of this leader. For example, at n_{eL}≈0,9·10^{21} m^{-3} [4], W_i≈W_{i0}≈12,5 eV [3] and U_{e0}≈6,1 V (for a DEDS steel electrode-tip) [44] according to (12) the maximum electron temperature T_{mL} in the plasma of the positive leader takes a numerical value of approximately T_{mL}≈1,639·10^4 K. At n_{eL}≈0,7·10^{21} m^{-3} according to (12) this maximum temperature T_{mL} is equal to about T_{mL}≈1,539·10^4 K. These approximate temperature levels T_{mL} obtained by (12), which differ within 6 %, correspond both to the characteristic range of its change in the positive leader channel at the beginning of its occurrence in atmospheric air of the «tip-plane» DEDS during the electrical breakdown of its long gap, indicated in [3], and to the value of this temperature given in [1] of the order T_{mL}≈(2–4)·10^4 K in the air equilibrium plasma of the positive leader. In addition, these quantitative values of the temperature T_{mL} in the plasma channel of the positive leader obtained by (12) correspond to the threshold temperature level T_{mL}≈(1–2)10^4 K [1, 39], upon transition of which the value of the degree of ionization χ≈n_{eL}/N_L of its plasma increases significantly. Let us point out that, for example, the temperature value T_{mL}≈1,639·10^4 K corresponds to the beginning of active thermal ionization of atmospheric air in the studied DEDS, for which the temperature in this channel is not less than 8·10^3 K [1]. By the way, the generalized Saha formula according to (1) takes into account the influence of the plasma temperature T_{mL} in the positive leader channel on the process of thermal ionization of atmospheric air gases in the DEDS. Now the physical reasons for the bright glow of the positive leader head in this DEDS, which is a harbinger of an electrical breakdown of a long air gap in the DEDS, become clearer to us.

9. Determination of the active resistance R_{Lc} of the positive leader channel in the air DEDS. For the linear active resistance R_{Ll} of the positive leader channel in the high-voltage air DEDS «tip-plane», we have the classical approximate relationship [38, 43]:

$$R_{Ll} \approx (\pi \gamma_{Le} R_L^2)^{-1} . \qquad (13)$$

At R_L≈0,5α_i^{-1}≈0,5 mm [1, 3] and γ_{Le}≈10^4 (Ω·m)$^{-1}$ [1] by (13) we find that the linear active resistance R_{Ll} of the plasma channel of the positive leader in the air DEDS under consideration, the emergence and development of which in its long discharge interval is due to the action of the standard switching aperiodic high voltage pulse $U_e(t)$ of the above-mentioned time shape [4, 27] used in it, has a quantitative value of about R_{Ll}≈127,3 Ω/m. Then, for an air gap of length $l_{\min}$=1,5 m in this DEDS, the total active resistance R_{Lc} of the plasma channel of the positive leader will take at l_d≈1,13$l_{\min}$≈1,695 m [4, 27] a value that will be numerically equal to about R_{Lc}≈R_{Ll}·l_d≈215,8 Ω. At this value of the resistance R_{Lc}, taking into account the influence of the resistance R_{Lc}≈4,59 kΩ of the current-limiting resistor, the discharge in the electric circuit of the powerful ultrahigh-voltage generator of test switching aperiodic high-voltage pulses $U_e(t)$ used by us [46–48], the electrical circuit and general view of which are shown in Fig. 2, 3 with the studied DEDS «tip-plane»according to Fig. 4, at the stage of development in its long air gap of the leader channel, which at time t≈T_d≈T_c≈95 µs together with positive streamers covers (galvanically short-circuits) this gap, will be aperiodic in nature.

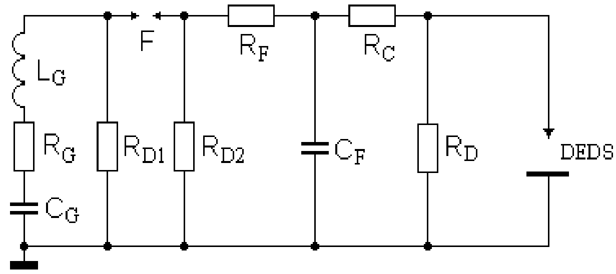

Fig. 2. Electrical substitution circuit of the discharge circuit of the generator of standard switching voltage pulses of the time shape T_m/T_p≈200 µs/1990 µs of positive (negative) polarity with amplitude of up to U_{em}≈±2 MV (R_G≈4,5 Ω, L_G≈80 µH, C_G≈0,125 µF – the intrinsic electrical parameters of the pulse voltage generator of the GIN-4 type; R_{D1}≈440 kΩ – the discharge resistance of the GIN-4 generator with switch F; R_{D2}≈32,7 kΩ – the additional discharge resistance; R_F≈4,28 kΩ – the resistance of the shaping resistor; C_F≈13,3 nF – the shaping capacitance for voltage of ±2,5 MV; R_C≈4,59 kΩ – the resistance of the current-limiting resistor; R_D≈107,3 kΩ – the resistance of the high-voltage ohmic arm voltage divider type OPN-2,5 for nominal impulse voltage of ±2,5 MV with division factor K_d≈53650) [46]

Fig. 3. General view of a powerful extra-high-voltage generator of standard switching aperiodic voltage pulses of the time shape T_m/T_p≈200 μs/1990 μs of positive (negative) polarity with amplitude of up to U_{em}≈±2 MV (on the left, on an insulating support 12 m high, a forming capacitance C_F≈13,3 nF is installed, to the upper potential electrode of which forming R_F≈4,28 kΩ and current-limiting R_C≈4,59 kΩ high-voltage resistors are connected) [46]

Fig. 4. General view of the high-voltage aerial DEDS «tip-plane» ($l_{\min}$=1,5 m), in which an ohmic voltage divider of the OPN-2.5 type for a nominal pulse voltage of ±2,5 MV with division factor equal to K_d≈53650 is connected to the potential upper steel rod electrode pointed at the lower edge (r_c≈3 mm) with radius r_0≈15 mm, located in the center of its grounded lower flat electrode made of galvanized steel with dimensions of 5 m × 5 m

This discharge mode in the generator circuit is confirmed by the data of the oscillograms in Fig. 5, 6. Therefore, with this discharge mode, the amplitude I_{me} of the current $i_e(t)$ in its electrical circuit can be calculated by the following expression [43]: $I_{me}≈U_e(T_d)/(R_{Lc}+R_C)$. As a result, this amplitude I_{me} of the discharge current at $U_e(T_d)≈U_d$≈611,6 kV, R_{Lc}≈215,8 Ω and R_C≈4,59 kΩ can take the numerical value I_{me}≈127,3 A. We see that this value of the discharge electric current I_{me} ≈ 127,3 A practically corresponds (within an error of 3 %) to the previously obtained electron current i_{eL}≈130,5 A in the positive leader channel.

10. Results of some experimental studies of breakdown of long air gaps in DEDS.

Figure 4 shows a general view of a high-voltage air DEDS «tip-plane», which tested the direct action of a standard switching aperiodic voltage pulse $U_e(t)$ of the time shape T_m/T_p≈200 μs/1990 μs of positive polarity from a powerful ultra-high-voltage generator of the corresponding voltage pulses $U_e(t)$, the general view, electrical diagram and parameters of the discharge circuit of which were given in [46–48] and additionally presented in Fig. 2, 3.

Figure 5 shows the oscillogram of the full standard switching aperiodic high-voltage pulse $U_e(t)$ with amplitude of U_{em}≈622,3 kV of the time shape T_m/T_d≈200 μs/1990 μs of positive polarity, which acts in the discharge circuit of the powerful ultra-high-voltage test generator of the corresponding voltage pulses [46] used by us on the tip-plane DEDS without electrical breakdown of its long air gap of length $l_{\min}$=3 m.

Figure 6 shows an oscillogram of a standard switching aperiodic high-voltage pulse T_m/T_d≈200 μs/1990 μs cut off on the rising part with electrical breakdown of a long air discharge gap in a test DEDS «tip-plane» with minimum length $l_{\min}$=1,5 m.

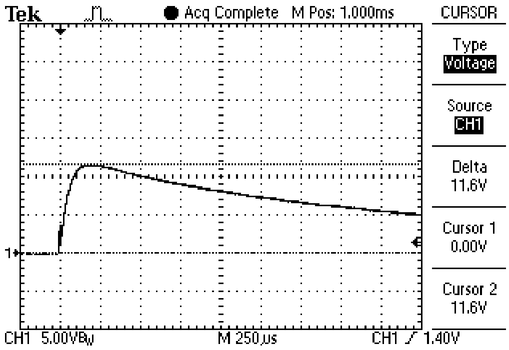

Fig. 5. Oscillogram of a full switching aperiodic high-voltage pulse $U_e(t)$ of the time shape T_m/T_p≈200 μs/1990 μs of positive polarity without electrical breakdown of a long air gap in the «tip-plane» DEDS ($l_{\min}$=3 m; U_{em}≈11,6 V × 53650≈622,3 kV – amplitude of the high-voltage test pulse; T_m≈200 μs – rise time (rise) of the high-voltage pulse to its amplitude U_{em}; T_p≈1990 μs – duration of the voltage pulse at the level of 0,5 U_{em}; vertical scale – 268,2 kV/div; horizontal scale – 250 μs/div) [27]

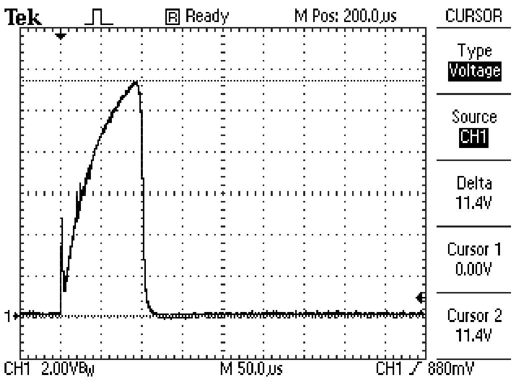

Fig. 6. Oscillogram of a truncated standard switching aperiodic high-voltage pulse $U_e(t)$ of the time shape T_m/T_p≈200 μs/1990 μs of positive polarity during an electrical breakdown of a long air gap in the «tip-plane» DEDS ($l_{\min}$=1,5 m; U_d≈11,4 V × 53650≈611,6 kV – voltage pulse cut-off level; $T_c≈T_d$≈95 μs − voltage pulse cut-off time (breakdown); T_{dc}≈17 μs – voltage pulse cut-off (switching) duration; vertical scale – 107,3 kV/div; horizontal scale – 50 μs/div) [27]

We would like to point out that when obtaining the experimental data according to Fig. 5, 6, the following were used: a domestic powerful generator of standard switching aperiodic pulses of ultra-high voltage $U_e(t)$ of the time shape T_m/T_p≈200 μs/1990 μs of positive (negative) polarity for a nominal electrical voltage of ±2 MV [46, 48]; an ohmic voltage divider of the OPN-2.5 type (K_d≈53650) for a nominal pulse voltage of ±2,5 MV [47]; a digital oscilloscope Tektronix TDS 1012B certified by the State Metrological Service, which stores measured electrical signals (calibration certificate UA01№1312 dated 29.06.2023). We would like to note that the amplitude-time parameters of high-voltage pulses $U_e(t)$ according to the data in Fig. 5, 6 were determined according to the requirements of the Standard [49].

Figure 7 shows a general view of the spark discharge channel and the spherical zone of active impact ionization of air near the potential electrode in the tip-plane DEDS ($l_{\min}$=1,5 m; U_d≈611,6 kV).

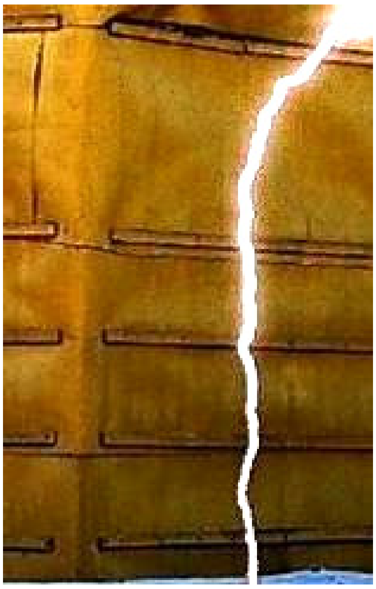

Fig. 7. General view of a zigzag cylindrical plasma channel of a spark discharge with almost spherical zone of radius r_i≈x_i of active impact ionization of air, which glows brightly at the top near the potential electrode of the DEDS «tip-plane», during the electrical breakdown of its air gap by a switching aperiodic high-voltage pulse of the time shape T_m/T_p≈200 μs/1990 μs of positive polarity ($l_{\min}$=1,5 m; $U_e(T_d)$≈U_d≈611,6 kV [27])

Let us point out that according to the approximate experimental data obtained by us, the diameter $2x_i$ of the spherical zone of active impact ionization of atmospheric air near the edge of a potential steel rod-tip with diameter of $2r_0$≈30 mm in the DEDS, in terms of its bright luminosity, was approximately twice as large as the diameter $2r_0$ of the electrode-tip and four times as large as the diameter $2r_{mk}$ of the plasma channel of the spark discharge (see Fig. 7) [4, 27].

Experimental studies of the electrical breakdown in the tip-plane DEDS (see Fig. 4) of long air gaps with length of 1 m ≤ $l_{\min}$ ≤ 4 m, carried out in the conditions of the high-voltage electrophysical laboratory of the Research and Design Institute «Molniya» of NTU «KhPI» using the above-mentioned test equipment, allowed us to confirm [4, 27] the following for the case of using in the experiments a standard switching aperiodic high-voltage pulse $U_e(t)$ of the time shape T_m/T_p≈200 μs/1990 μs of positive polarity: first, the emergence near the potential metal electrode-tip of the DEDS under study of an almost spherical zone with radius of about x_i≈r_i≈(25–30) mm of active impact ionization by electrons of atmospheric air; secondly, the emergence and further development in the long air gap of the DEDS under study of the positive leader channel always occurs from this local zone with radius of x_i≈r_i of active air ionization; thirdly, the level of the breakdown pulse voltage U_d in this DEDS, which at $l_{\min}$=1,5 m was about U_d≈611,6 kV (T_d≈95 μs), and at $l_{\min}$ =3 m – U_d ≈1062,3 kV (T_d ≈104 μs); fourthly, the fulfillment of the approximate relationship l_d≈1,13$l_{\min}$ for the length of the zigzag path of channel development in the long air gap of the DEDS; fifthly, the physical position that the electrical breakdown of air gaps with the specified length lmin in the studied DEDS always occurs on the increasing frontal part of the high-voltage switching pulse $U_e(t)$ used in the experiments.

Conclusions.

1. A simplified electrophysical model of the emergence and development of a positive leader in a long discharge air gap of a tip-plane DEDS is proposed, which tests the action of a standard switching aperiodic high-voltage pulse $U_e(t)$ of the time shape T_m/T_p≈200 μs/1990 μs of positive polarity. This approximate electrophysical model allows us to find in a complex form a number of basic characteristics of the plasma channel of this discharge leader during electrical breakdown of a long air gap in the DEDS under study by a high pulse voltage of positive polarity.

2. Approximate calculated relations are obtained for determining the following basic characteristics of the plasma channel of a positive leader in a tip-plane DEDS with atmospheric air: electron density n_{eL} and electric potential U_{eL} in the head of this leader; linear charge q_{Ll} of the leader plasma channel; density δ_{eL} of the electron current i_{eL} and this current i_{eL} in the leader channel; ion current i_{iL} and its density δ_{iL} in the leader channel; strong electric field strengths inside E_{Li} and outside E_{Le} of the leader channel; length ls of the streamer zone in front of the leader head; maximum electron temperature T_{mL} in the plasma of the leader channel; linear active resistance R_{Ll} and total active resistance R_{Lc} of the leader channel. Data are provided that confirm the reliability of a number of these approximate calculated relations for the plasma channel of a positive leader in air DEDS.

3. It is shown by calculation that the maximum electron temperature T_{mL} in the equilibrium plasma of the positive leader in the air DEDS «tip-plane» at a density n_{eL}≈$0,7\cdot10^{21}$ m^{-3} of electrons in the plasma of the leader of this DEDS takes the numerical value T_{mL}≈$1,539\cdot10^4$ K, which corresponds to the characteristic range of its change in a similar leader adopted in the field of HVT and HVPT for a long discharge gap of DEDS with atmospheric air and approaches the level T_{mL}≈$(2–4)\cdot10^4$ K, characteristic of a developed positive leader and obtained using known spectroscopic measurements. This obtained temperature level T_{mL} indicates that the plasma in the channel of the positive leader in this DEDS becomes thermoionized.

4. Based on the Saha equation known in plasma physics, in the case of ionization by electron impacts of neutral oxygen molecules O_2 of atmospheric air of the high-voltage «tip-plane» DEDS studied by us, it is shown that the density neL of electrons in the air equilibrium plasma of the positive leader channel of this DEDS at T_{mL}≈1,639·10^4 K takes a quantitative value of about n_{eL}≈0,7·10^{21} m^{-3}, which corresponds to its known numerical values in the field of physics and technology of high-voltage gas discharges of atmospheric pressure.

5. It is shown by calculation and experimental methods that for the electrophysical case considered in the air DEDS «tip-plane» ($l_{\min}$=1,5 m), at the stage of emergence, development and advancement of a positive leader in the atmospheric air of the studied DEDS at the electron density neL in the spherical head of this leader with radius R_{eL}≈0,5·10^{-3} m near n_{eL}≈0,7·10^{21} m^{-3} its electric potential U_{eL} changes from the level $U_e(T_d)$≈U_d≈611,6 kV (the beginning of the leader development) to approximately zero (the completion of the leader development and the onset of the through-discharge phase at the length of its plasma channel l_L≈1,13$l_{\min}$ in the air gap of the DEDS). For the intermediate state of development in the long air gap of this DEDS of the leader channel (l_L≈0,395 m), the electric potential U_{eL} of the head of the positive leader in its atmospheric air will be quantitatively U_{eL}≈605 kV with voltage drop on the leader channel U_L≈6,6 kV.

6. It has been established that in the streamer zone of the air gap near the head of the positive leader (at a distance x_s≈10R_{eL}≈5 mm from it) of the studied DEDS ($l_{\min}$=1,5 m) an extremely strong electric field is formed with maximum strength E_{Lem}≈21,1 MV/m (with averaged over the length of this gap strength E_{Le}≈465 kV/m, which is characteristic of the streamer zone in front of the leader), which is comparable to the critical strength E_{xk}≈24,9 MV/m of the electric field, which causes active impact ionization by electrons of its atmospheric air. In this regard, outside the head of this leader, physical conditions will be created for the active development of electron avalanches and positive streamers in the amount of N_s, which start from the head of the leader with its excess positive charge q_{eL}≈58,7 nC towards the grounded electrode-plane of this DEDS.

7. It is shown that the strength E_{Li} of the longitudinal electric field inside its plasma channel with radius of about R_L≈0,5·10^{-3} m in a high-voltage air DEDS «tip-plane» for the case when $l_{\min}$=1,5 m and $U_e(T_d)$≈U_d≈611,6 kV, with specific electrical conductivity γ_{Le}≈10^4 (Ω·m)$^{-1}$ of the equilibrium plasma of the channel of this leader, numerically amounts to approximately E_{Li}≈16,6 kV/m.

8. The value of the average length ls of the streamer zone in front of the head of the positive leader was obtained by calculation and experiment, which for the case of using in the air DEDS «tip-plane» ($l_{\min}$=1,5 m) a standard switching aperiodic high-voltage pulse $U_e(t)$ of the time shape T_m/T_p≈200 μs/1990 μs of positive polarity with breakdown voltage U_d≈611,6 kV is l_s≈1,3 m.

9. It was established that the density δ_{eL} of the electron current i_{eL} in the plasma channel of the positive leader for a high-voltage air-based DEDS «tip-plane» ($l_{\min}$=1,5 m) takes the quantitative value δ_{eL}≈1,66·10^8 A/m^2, and the electron current i_{eL} towards its grounded metal electrode-plane is i_{eL}≈130,5 A.

10. It is shown that the linear charge q_{Ll} of the thin plasma channel of the positive leader, which moves in the atmospheric air of the tip-plane DEDS, has a quantitative value of q_{Ll}≈58,7·10^{-6} C/m. This electric charge determines the ion current iiL in the plasma channel of this leader, which is numerically approximately equal to i_{iL}≈5,87 A at its density of about δ_{iL}≈7,47·10^6 A/m^2.

11. It is established that with the specific electrical conductivity γ_{Le}≈10^4 (Ω·m)$^{-1}$ of the thermoionized plasma of the positive leader channel in the high-voltage air tip-plane DEDS, the linear active resistance R_{Ll} of the plasma channel of this leader is quantitatively about R_{Ll}≈127,3 Ω/m. In this case, the total active resistance R_{Lc} of the zigzag plasma channel of the positive leader in this DEDS ($l_{\min}$=1,5 m) will take a value that will be numerically equal to R_{Lc}≈1,13R_{Ll}·$l_{\min}$≈215,8 Ω.

12. The corresponding experimental studies of electric discharge processes in the DEDS «tip-plane» with lengths of 1 m ≤ $l_{\min}$ ≤ 4 m of its long air gap, carried out on domestic powerful ultrahigh-voltage equipment in the open air under the conditions of an electrophysical laboratory, indicate the validity of the simplified model proposed by us of the formation near the potential electrode-tip of this DEDS and the further development in its atmospheric air of a thin plasma channel of the positive leader with its main characteristics indicated above.

Acknowledgment. The work was carried out with the support of the Ministry of Education and Science of Ukraine (project DB No. 0123U101704).

Conflict of interest. The author declares no conflict of interest.

REFERENCES

1. Rayzer Yu.P. *Physics of gas discharge*. Moscow, Nauka Publ., 1987. 592 p. (Rus).

2. Brzhezitsky V.O., Biliy I.V., Boiko M.I., Gul' V.I., Gurin A.G., Il'enko O.S., Isakova A.V., Kondra B.M., Kopshin V.O., Kravchenko V.I., Naboka B.G., Protsenko O.R., Rudakov V.V., Khymenko L.T., Khominich V.I., Shostak V.O., Yanishevsky V.I. *Technique and Electrophysics of High Voltages*. Kharkiv, NTU «KhPI», Tornado Publ., 2005. 930 p. (Ukr).

3. Bortnik I.M., Beloglovskiy A.A., Vereshchagin I.P., Vershinin Yu.N., Kalinin A.V., Kuchinskiy G.S., Larionov V.P., Monastyrskiy A.E., Orlov A.V., Temnikov A.G., Pintal' Yu.S., Sergeev Yu.G., Sokolova M.V. *Electrophysics bases of HV technique*. Moscow, Publ. House of MEI, 2010. 704 p. (Rus).

4. Baranov M.I. *Selected topics of Electrophysics. Monograph in 4 Vols. Vol. 4. Effects of interaction of physical bodies with fields and currents*. Kharkiv, FOP Panov A.N. Publ., 2023. 552 p. (Ukr).

5. Baranov M.I. Basic Electrophysical Characteristics of Natural Three-Phase Dispersed System «A Storm Cloud−Earth». *Elektronnaya Obrabotka Materialov*, 2023, vol. 59, no. 6, pp. 50-57. (Rus). doi: https://doi.org/10.52577/eom.2023.59.6.50.

6. Braginskiy S.I. To the theory of development of channel of spark. *Journal of Experimental and Theoretical Physics*, 1958, vol. 34, no. 6, pp. 1548-1556. (Rus).

7. Lozanskyi E.D., Firsov O.B. *Theory of spark*. Moscow, Atomizdat Publ., 1975. 272 p. (Rus).

8. Braginskiy S.I. To the theory of development of channel of spark. *Journal of Experimental and Theoretical Physics*, 1957, vol. 33, no. 3(9), pp. 645-654. (Rus).
9. Bobrov Yu.K., Vikhrov V.V., Fedotov I.P. Dynamics of high-current pulse discharge in air. *Physics of Plasma*, 1988, vol. 14, no. 9, pp. 1222-1227. (Rus).
10. Gulyy G.A. *Scientific basis of the discharge-pulse technologies*. Kyiv, Naukova Dumka Publ., 1990. 208 p. (Rus).
11. Dubovenko K.V. Interaction of shock waves with plasma of a high-current discharge channel in a high-pressure chamber. *Journal of Technical Physics*, 1992, vol. 62, no. 6, pp. 83-93. (Rus).
12. Vovchenko A.I., Bohuslavsky L.Z., Myroshnychenko L.N. Trends in development of high-powered high-voltage pulse current generators in the Institute of Pulse Processes and Technology of Ukraine (review). *Technical Electrodynamics*, 2010, no. 5, pp. 69-74. (Rus).
13. Niemeyer L., Pietronero L., Wiesmann H.J. Fractal Dimension of Dielectric Breakdown. *Physical Review Letters*, 1984, vol. 52, no. 12, pp. 1033-1036. doi: https://doi.org/10.1103/PhysRevLett.52.1033.
14. Wiesmann H.J., Zeller H.R. A fractal model of dielectric breakdown and prebreakdown in solid dielectrics. *Journal of Applied Physics*, 1986, vol. 60, no. 5, pp. 1770-1773. doi: https://doi.org/10.1063/1.337219.
15. Kuffel E., Zaengl W.S., Kuffel J. *High Voltage Engineering Fundamentals*. Oxford, Newnes Publ., 2000. 552 p.
16. Nijdam S., Teunissen J., Ebert U. The physics of streamer discharge phenomena. *Plasma Sources Science and Technology*, 2020, vol. 29, no. 10, art. no. 103001. doi: https://doi.org/10.1088/1361-6595/abaa05.
17. Charalambakos V.P., Agoris D.P., Kupershtokh A.L., Karpov D.I. Modelling of prebreakdown phenomena using cellular automata. *Proceedings of the IASTED International Conference on Modelling, Identification and Control (MIC2001)*, 2001, vol. 1, pp. 143-147.
18. Kupershtokh A.L., Charalambakos V., Agoris D., Karpov D.I. Simulation of breakdown in air using cellular automata with streamer to leader transition. *Journal of Physics D: Applied Physics*, 2001, vol. 34, no. 6, pp. 936-946. doi: https://doi.org/10.1088/0022-3727/34/6/315.
19. Petrov N.I., Petrova G.N., D'Alessandro F. Quantification of the probability of lightning strikes to structures using a fractal approach. *IEEE Transactions on Dielectrics and Electrical Insulation*, 2003, vol. 10, no. 4, pp. 641-654. doi: https://doi.org/10.1109/TDEI.2003.1219649.
20. Kebbabi L., Beroual A. Fractal analysis of creeping discharge patterns propagating at solid/liquid interfaces: influence of the nature and geometry of solid insulators. *Journal of Physics D: Applied Physics*, 2006, vol. 39, no. 1, pp. 177-183. doi: https://doi.org/10.1088/0022-3727/39/1/026.
21. Xiong Z., Robert E., Sarron V., Pouvesle J.-M., Kushner M.J. Dynamics of ionization wave splitting and merging of atmospheric-pressure plasmas in branched dielectric tubes and channels. *Journal of Physics D: Applied Physics*, 2012, vol. 45, no. 27, art. no. 275201. doi: https://doi.org/10.1088/0022-3727/45/27/275201.
22. Hu H.M., Yang Y., Lu W., Zhao G.P. Electrical Tree Simulation Based on the Self-Organization Criticality. *Energy and Power Engineering*, 2013, vol. 5, no. 4, pp. 1273-1276. doi: https://doi.org/10.4236/epe.2013.54B241.
23. Xia Y., Liu D., Wang W., Bi Z., Wang X., Niu J., Ji L., Song Y., Qi Z. Effects of previous ionization and excitation on the ionization wave propagation along the dielectric tube. *Journal of Physics D: Applied Physics*, 2016, vol. 49, no. 16, art. no. 165202 doi: https://doi.org/10.1088/0022-3727/49/16/165202.
24. Diaz O., Hettiarachchi P., Rahman M., Cooray V., Vayanganie S.P.A. Experimental study of leader tortuosity and velocity in long rod-plane air discharges. *IEEE Transactions on Dielectrics and Electrical Insulation*, 2016, vol. 23, no. 2, pp. 806-812. doi: https://doi.org/10.1109/TDEI.2015.005421.
25. Aziz N.H., Catterson V.M., Rowland S.M., Bahadoorsingh S. Analysis of partial discharge features as prognostic indicators of electrical treeing. *IEEE Transactions on Dielectrics and Electrical Insulation*, 2017, vol. 24, no. 1, pp. 129-136. doi: https://doi.org/10.1109/TDEI.2016.005957.
26. Baranov M.I. A generalized physical principle of development of plasma channel of a high-voltage pulse spark discharge in a dielectric. *Electrical Engineering & Electromechanics*, 2024, no. 1, pp. 34-42. doi: https://doi.org/10.20998/2074-272X.2024.1.05.
27. Baranov M.I. Calculation and experimental determination of the speed of advancement of the plasma leader channel of a pulse spark discharge in atmospheric air. *Electrical Engineering & Electromechanics*, 2024, no. 2, pp. 48-54. doi: https://doi.org/10.20998/2074-272X.2024.2.07
28. Hussein A.M., Janischewskyj W., Chang J.-S., Shostak V., Chisholm W.A., Dzurevych P., Kawasaki Z.-I. Simultaneous measurement of lightning parameters for strokes to the Toronto Canadian National Tower. *Journal of Geophysical Research: Atmospheres*, 1995, vol. 100, no. D5, pp. 8853-8861. doi: https://doi.org/10.1029/95JD00543.
29. Guerrieri S., Nucci C.A., Rachidi F., Rubinstein M. On the influence of elevated strike objects on directly measured and indirectly estimated lightning currents. *IEEE Transactions on Power Delivery*, 1998, vol. 13, no. 4, pp. 1543-1555. doi: https://doi.org/10.1109/61.714865.
30. Karpov D.I., Kupershtokh A.L. Models of streamers growth with «physical» time and fractal characteristics of streamer structures. *Conference Record of the 1998 IEEE International Symposium on Electrical Insulation*, 1998, vol. 2, pp. 607-610. doi: https://doi.org/10.1109/ELINSL.1998.694866.
31. Uman M.A., Rakov V.A. A critical review of nonconventional approaches to lightning protection. Bulletin *of the American Meteorological Society*, 2002, vol. 83, no. 12, pp. 1809-1820. doi: https://doi.org/10.1175/BAMS-83-12-1809.
32. Baranov M.I., Buriakovskyi S.G., Hrytsenko A.S., Kostiuk V.A. Results of investigations of thermal resistibility of prototypes of aluminum alloy panels of fuel tank of airplane to direct action of normalized components of artificial lightning current. *Electrical Engineering & Electromechanics*, 2019, no. 6, pp. 29-38. doi: https://doi.org/10.20998/2074-272X.2019.6.04.
33. Betz H.D., Schumann U., Laroche P. *Lightning: Principles, Instruments and Applications. Review of Modern Lightning Research*. Springer Dordrecht Publ., 2009. 641 p. doi: https://doi.org/10.1007/978-1-4020-9079-0.
34. Kuhling H. *Handbook of Physics*. Moscow, Mir Publ., 1982. 520 p. (Rus).
35. Chernogor L.F. Physical effects from the Yushu meteoroid. 1. *Kinematics and Physics of Celestial Bodies*, 2022, vol. 38, no. 3, pp. 20-46. doi: https://doi.org/10.15407/kfnt2022.03.020.
36. Golant V.E., Zhilinskiy A.P., Sakharov I.E. *Fundamentals of Plasma Physics*. Moscow, Atomizdat Publ., 1977. 384 p. (Rus).
37. Knopfel' G. *Ultra strong pulsed magnetic fields*. Moscow, Mir Publ., 1972. 391 p. (Rus).
38. Kuz'michev V.E. *Laws and formulas of physics*. Kyiv, Naukova Dumka Publ., 1989. 864 p. (Rus).
39. Bogatenkov I.M., Imanov G.M., Kizevetter V.E., Kostenko M.V., Kuchinskiy G.S., Mikhaylov Yu.A., Tadzhibaev A.I., Tikhodeev N.N., Khalilov F.Kh., Shkuropat P.I., Shneerson G.A., Yanchus E.I. *High Voltage Engineering. A Textbook for Universities*. SPb., PEIPK Publ., 1998. 700 p. (Rus).

40. Bazelyan E.M., Razhanskiy I.M. *Spark discharge in the air*. Novosibirsk, Nauka Publ., 1988. 165 p. (Rus).
41. Yavorskiy B.M., Detlaf A.A. *Physics Handbook*. Moscow, Nauka Publ., 1990. 624 p. (Rus).
42. Nikol'skiy V.V., Nikol'skaya T.I. *Electrodynamics and Propagation of Radio Waves: A Textbook for Universities*. Moscow, Nauka Publ., 1989. 544 p. (Rus).
43. Neyman L.R., Demirchyan K.S. *Theoretical foundations of electrical engineering: Textbook for universities in 2 vols. Vol. 2*. Leningrad, Energoizdat Publ., 1981. 416 p. (Rus).
44. Abramov N.R., Kuzhekin I.P., Larionov V.P. Descriptions of melting of walls of metallic objects at action on them of lightning. *Electricity*, 1986, no. 11, pp. 22-27. (Rus).
45. Baranov M.I. Approximate calculation of electrical erosion of metal electrodes of high-voltage high-current spark switches. *Technical Electrodynamics*, 2004, no. 5, pp. 11-14. (Rus).
46. Baranov M.I., Koliushko G.M., Kravchenko V.I. A switching aperiodic superhigh-voltage pulse generator for testing the electric strength of insulation of technical objects. *Instruments and Experimental Techniques*, 2013, vol. 56, no. 6, pp. 653-658. doi: https://doi.org/10.1134/S0020441213050126.
47. Baranov M.I., Koliushko G.M., Kravchenko V.I. Generation of standard switching aperiodic impulses of high and superhigh voltage for full-scale tests of electrical power objects. *Electrical Engineering & Electromechanics*, 2013, no. 2, pp. 52-56. (Rus).
48. Baranov M.I. *Selected topics of Electrophysics. Monograph in 4 Vols. Vol. 3. Theory and practice of electrophysics tasks*. Kharkiv, Tochka Publ., 2014. 400 p. (Rus).
49. *Standard GOST 1516.2-97. Electrical equipment and installations for a.c. voltages 3 kV and higher. General methods of dielectric tests*. Minsk, Intergovernmental Council of Standardization, Measuring and Certification Publ., 1997. 31 p. (Rus).

Received 23.09.2024
Accepted 28.01.2025
Published 02.07.2025

M.I. Baranov[1], *Doctor of Technical Science, Senior Researcher,*
[1] Research and Design Institute «Molniya»
of National Technical University «Kharkiv Polytechnic Institute»,
47, Shevchenko Str., Kharkiv, 61013, Ukraine,
e-mail: baranovmi49@gmail.com (Corresponding Author)

How to cite this article:
Baranov M.I. The main characteristics of the leader channel during breakdown of a long air gap by high pulse voltage. *Electrical Engineering & Electromechanics*, 2025, no. 4, pp. 59-71. doi: https://doi.org/10.20998/2074-272X.2025.4.08

UDC 621.3.015.52: 621.3.022: 621.319.53 https://doi.org/10.20998/2074-272X.2025.4.09

V.F. Bolyukh, G.M. Suchkov, R.P. Mygushchenko, M.E. Kalnytskyi

Determination of parameters of an autonomous source of a constant magnetic field for a portable electromagnetic-acoustic transducer

Purpose. *Determination of rational parameters of an autonomous source of constant magnetic field, ensuring the efficiency of using portable electromagnetic-acoustic transducers (EMAT) for diagnostics of remote ferromagnetic objects.* ***Methodology.*** *An analysis of the parameters of an autonomous magnetic field source consisting of a permanent magnet and a ferromagnetic screen magnetizing a ferromagnetic object with a flat surface, providing a central magnetic field along the magnet axis above 0.3 T, was carried out.* ***Results.*** *The results of experimental studies on a sample of an autonomous source, which contained 6 sections of a permanent magnet made of NeFeB ceramics with dimensions of 50×50×10 mm^3, correspond to the results of calculating the magnetic field on the surface of a ferromagnetic sample with an error of up to 9 %. Experimental studies were carried out for EMAT with two magnetic field sources containing rectangular permanent magnets of the same height but different widths.* ***Novelty.*** *It has been established that in order to select rational parameters of an autonomous source of magnetic field, it is necessary to use an integral criterion that takes into account the magnetic field in the surface layer of a ferromagnetic object, the magnetic scattering field, the volume of a permanent magnet, which determines the mass and size indicators and cost of the source, and the force of attraction to the ferromagnetic object.* ***Practical value.*** *For portable EMAT, increasing the magnetic field in a remote ferromagnetic object either by increasing the volume of a permanent magnet or by decreasing the air gap between the magnetic field source and the ferromagnetic object provides increased EMAT efficiency by increasing the ratio of the amplitude of the received ultrasonic bottom pulses to the noise amplitude.* References 27, figures 14.

Key words: **autonomous magnetic field source, permanent magnet parameters, magnetic field, remote ferromagnetic object, integral criterion, electromagnetic-acoustic transducer, signal amplitude, noise.**

Мета. *Визначення раціональних параметрів автономного джерела постійного магнітного поля, які забезпечують ефективність використання портативних електромагнітно-акустичних перетворювачів (ЕМАП) для діагностики віддалених феромагнітних об'єктів.* ***Методологія***. *Проведено аналіз параметрів автономного джерела магнітного поля, що складається з постійного магніту та феромагнітного екрана, що намагнічує феромагнітний об'єкт з плоскою поверхнею, забезпечуючи центральне магнітне поле вздовж осі магніту понад 0,3 Тл.* ***Результати*** *експериментальних досліджень на зразку автономного джерела, який містив 6 секцій постійного магніту з кераміки NeFeB розмірами 50×50×10 мм^3, відповідають результатам розрахунку магнітного поля на поверхні феромагнітного зразка з похибкою до 9 %. Експериментальні дослідження були проведені для ЕМАП з двома джерелами магнітного поля, що містять прямокутні постійні магніти однакової висоти, але різної ширини.* ***Новизна***. *Встановлено, що для вибору раціональних параметрів автономного джерела магнітного поля необхідно використовувати інтегральний критерій, який враховує магнітне поле в поверхневому шарі феромагнітного об'єкта, магнітне поле розсіювання, об'єм постійного магніту, який визначає масогабаритні показники та вартість джерела, силу притягання до феромагнітного об'єкта.* ***Практична значимість***. *Портативний ЕМАП забезпечує збільшення відношення амплітуд інформаційних донних імпульсів до шуму шляхом нарощування об'єму його постійного магніту та зменшення повітряного зазору між джерелом магнітного поля і феромагнітним об'єктом.* Бібл. 27, рис. 14.

Ключові слова: **автономне джерело магнітного поля, параметри постійного магніту, магнітне поле, віддалений феромагнітний об'єкт, інтегральний критерій, електромагнітно-акустичний перетворювач, амплітуда сигналу, шум.**

Introduction. Sources of constant magnetic field (SMF) intended for magnetization of ferromagnetic objects (FO) located at a considerable distance (up to 20–50 mm) are used in various fields of science and technology. Thus, electromagnetic-acoustic transducers (EMAT) are used for monitoring and diagnostics of ferromagnetic products with dielectric coatings or deposits on the surfaces. The coating thickness of the products being monitored can reach up to 5 mm, and deposits, for example, on the internal surfaces of pipelines, up to 20 mm or more. The efficiency of these transducers depends on the degree of magnetization of the FO surface layer, remote from the SMF [1].

The problem of creating a compact and powerful SMF for magnetizing a FO located at a considerable distance from it is relevant for various scientific and technical tasks. Such sources of constant magnetic field are necessary for magnetic separation, nanotechnology, materials science, biomedical diagnostics, etc. [2–7]. At the same time, in many practical applications they must operate autonomously, without using an external power source as part of a portable device performing various tasks, for example, non-destructive testing of ferromagnetic products.

Features of SMF for EMAT. In non-destructive testing of ferromagnetic products, EMATs with SMF are used, which magnetize the product, providing generation of ultrasonic waves using a high-frequency coil [8].

In principle, the EMAT includes a SMF 1 and a flat high-frequency inductance coil 2, which affect the FO 3 (Fig. 1).

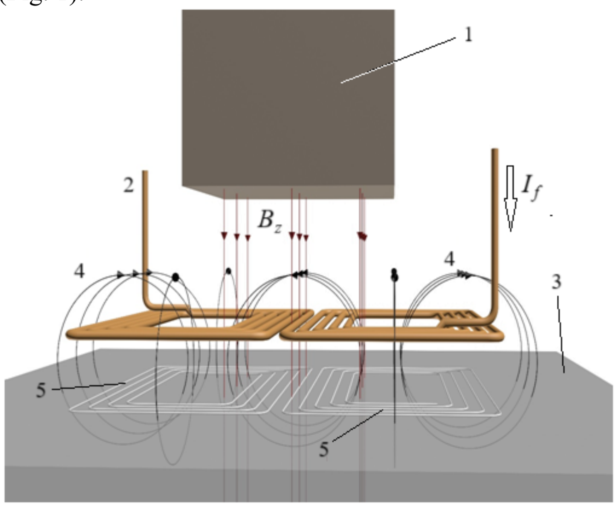

Fig. 1. Scheme of a portable EMAT: 1 – SMF; 2 – inductance coil; 3 – FO; 4 – electromagnetic field; 5 – eddy currents in FO

The SMF forms the normal component of the induction of the constant magnetic field B_z, which acts on the FO. A high-frequency current I_f flows in the inductance coil, which, due to the high-frequency electromagnetic field 4, induces eddy currents 5 in the surface layer of the FO. When the eddy current I_f interacts with the magnetic field B_z, an alternating elastic Lorentz force acts on the conduction electrons, which is transmitted to the crystal lattice of the FO. As a result, ultrasonic pulses with a frequency f are excited. Eddy currents in the FO, due to elastic oscillations of the crystal lattice, induce an alternating current with a frequency f in the inductance coil 2, which acts as a receiver of ultrasonic pulses.

Thus, for diagnostics of a steel pipe, an EMAT is used, containing an SMF of four permanent magnets (PM), the same poles of which are separated by an angle in the range from 30° to 60° [9]. This SMF provides better homogeneity of the magnetic field in the surface layer of the FO compared to configurations of two poles facing each other or quadrupole geometry.

To generate ultrasonic waves in the FO, SMFs with a periodic PM configuration are used in EMAT [10]. Compared to a single PM, a periodic configuration of magnets increases the maximum induction, providing the required value and distribution pattern on the FO surface, especially under the coil generating high-frequency signals [11]. To increase the magnetic field in the FO, both various magnetic concentrators [12] and several PMs, such as Halbach magnet configurations [13], are proposed.

A mobile robotic system designed to create internal maps of the investigated FO and its structural elements uses a movable EMAT. One of the main tasks of such a system was the selection of PM parameters that take into account the required magnetization of the FO and the mass and dimensional parameters of the converter [14].

Problems arise during operation of PM due to elevated temperatures and irreversible demagnetization [15]. The degree of recovery of irreversible demagnetization of PM depends on the choice of magnetic material and the configuration of the system, including the geometry of the magnet, its interaction with other ferromagnetic materials and magnetic fields [16]. As an alternative to PM, long-acting electromagnets or pulsed electromagnets are used, but their operation requires external power sources [17, 18].

When magnetizing the FO from an autonomous SMF, an attractive force arises between them, which must be taken into account, especially when the source is used in portable devices. Between cylindrical PM and FO, this force is directly proportional to the residual magnetic field of magnetization, the cross-sectional area of the PM, the saturation magnetic field and the cross-sectional area of the FO, and inversely proportional to the square of the distance between them [19].

When testing a FO using an EMAT that uses overhead SMFs, it is necessary to know the distribution of the magnetic flux in the surface and internal layers of the object being tested [20]. The gap between the SMF and the FO changes the spatial distribution of the field inside the tested object. Changing the gap under one of the magnets affects the distribution of the magnetic field in the entire volume of the tested FO, and not only in the area located with a gap under this magnet.

By increasing the size of the autonomous SMF to a certain level, a significant increase in the EMAT performance is ensured. However, with an excessive increase in the size of the source, the efficiency of the converter increases insignificantly, and the weight and size parameters become too large, which is unacceptable for a portable device [21].

As is known, the efficiency of EMAT, diagnosing a remote FO, is estimated by the conversion coefficient [22]:

$$\eta = k \cdot I_f \cdot B_z^2 \cdot \exp(-h/R),$$

where k is a coefficient depending on the electrical, magnetic and elastic characteristics of the FO material; I_f is the high-frequency current in the induction coil with an average radius R; B_z is the value of the normal component of the induction of the constant magnetic field in the surface layer of the FO; h is the distance from the SMF to the FO.

The efficiency of EMAT can be increased by both increasing the current I_f in the high-frequency coil and increasing the magnetic field induction B_z in the surface layer of the FO. Since the efficiency of EMAT depends to a greater extent on the value of B_z than on I_f, this necessitates an increase in the induction of the constant magnetic field in the surface layer of the FO to increase the efficiency of EMAT [1].

Thus, the autonomous SMF of a portable EMAT should maximally magnetize the FO located at a significant distance from it (up to 50 mm).

Despite the significant amount of research on the development of EMAT, the problem of choosing rational parameters of an autonomous SMF, taking into account the main indicators, remains unresolved. These are the magnetization level of the remote FO, the dimensions of the PM, which affect the weight and size indicators and the cost of the device, the force of attraction to the FO and the scattering field, which is important when operating the converter [23].

The **purpose** of the article is to determine the rational parameters of an autonomous source of a constant magnetic field, ensuring the efficiency of using portable EMATs for diagnostics of remote ferromagnetic objects with a flat surface.

Research object. Let us consider an autonomous SMF as part of a portable EMAT. The SMF consists of a PM 1 and a ferromagnetic screen (FS) 2, coaxially installed on the upper end of the PM (Fig. 2). The lower end of the PM faces the flat outer surface of the FO 3, which is of considerable length and thickness. The autonomous SMF is located at a considerable distance from the FO, so that between the lower end of the PM and the outer surface of the FO there is an air gap of height Z_1, in which a high-frequency inductance coil 4 is installed. Figure 2 shows the boundary for calculating the average value of the magnetic leakage field B_{ex} 5 and the central axis of the magnetic system 6, coinciding with the z axis of the Cartesian coordinate system.

PM based on NeFeB ceramics with a coercive force of 1114 kA/m [24] is made in the form of a square with a side a and a height H_1 with axial magnetization. FS is made of St10 steel in the form of a disk with a square cross-section and a height h_e.

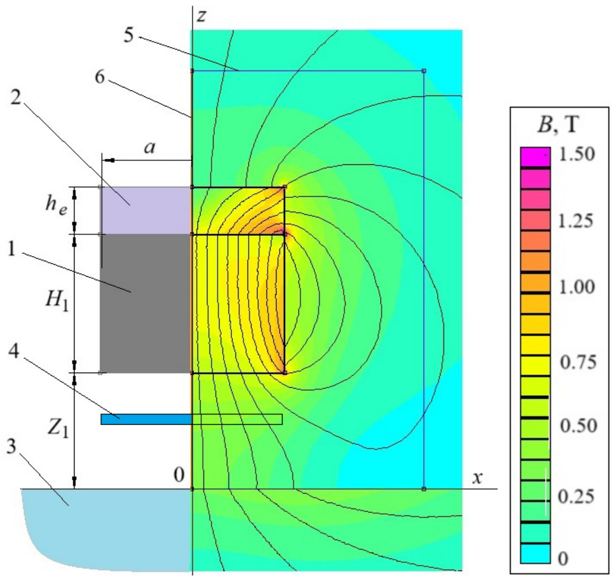

Fig. 2. Schematic diagram of an autonomous SMF as part of a portable EMAT (to the left of the 0*z* axis) and the distribution of the magnetic field it creates (to the right of the 0*z* axis):
1 – PM; 2 – FS; 3 – FO; 4 – inductance coil;
5 – calculation limit B_{ex}; 6 – central axis of the magnetic system

Influence of geometric parameters on SMF indicators. Let us consider an autonomous SMF with a permanent magnet intended for EMAT. The magnetic field analysis will be performed in the plane ($z0x$) passing through the central axis of the magnetic system. The magnetic system is calculated using known mathematical expressions using the FEMM program [25]. This program solves a large system of algebraic equations, which are formed based on the finite element method and a differential equation describing the magnetic field in the cross section of a magnetic system.

Autonomous SMF should magnetize FO so that the central magnetic field B_0 – magnetic field along the axis of magnetic system 6 in its surface layer (Fig. 2) was above B_{min}=0.3 T. Such a field is necessary for portable ultrasonic EMAT devices when performing thickness measurement and diagnostics of ferromagnetic products. PM is located at a distance of Z_1=25 mm from FO and its width *a* should not exceed 80 mm, which is important for portable EMAT. FS has the same cross-section as PM, and its height h_e=10 mm.

We will calculate the average value of the magnetic stray field B_{ex} at boundary 5, located at a distance of 25 mm from the outer boundary of the autonomous SMF.

Based on previous studies [1], we select the basic version of an autonomous source with the PM parameters: the square side *a*=30 mm, the height H_1=40 mm. This SMF at Z_1=25 mm magnetizes the FO to the minimum required value B_0=B_{min} (more precisely B_0=0.299 T). In this case, the magnetic stray field B_{ex}=0.106 T, and the source is acted upon by an axial attractive force F_z =37.44 N from the FO side. Figure 2 shows the lines of force and the induction of the magnetic field created by the basic version of the SMF during magnetization of the remote FO.

Let us consider the influence of the parameters of the autonomous SMF on the magnetic field in the surface layer of the FO (along the 0*x* axis). With an increase in the height of the PM H_1 and an unchanged cross-section with a side of *a*=50 mm, the maximum magnetic field in it increases (Fig. 3). The greatest value of the field occurs inside the PM. However, in the FO, the magnetic field also increases both in magnitude and in the area of influence.

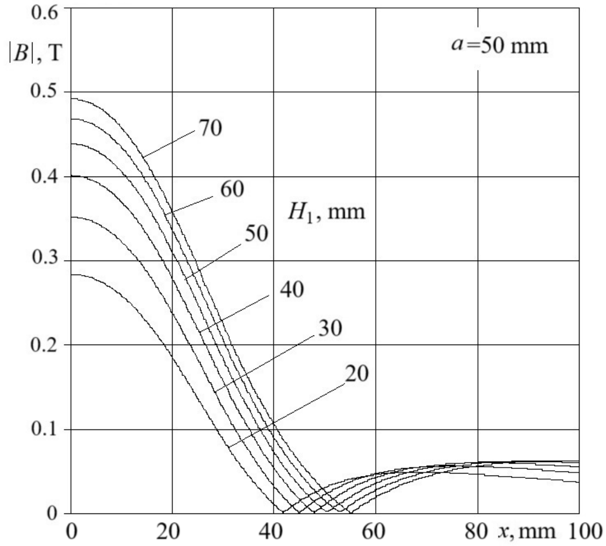

Fig. 3. Distribution of the magnetic field induction modulus in the surface layer of the FO at different PM heights

If the PM is made of a small height (H_1=20 mm), then the required value of the central field B_{min} on the surface of the FO is not ensured. With a linear increase in the height of the PM, the magnetic field in the FO increases nonlinearly with a decrease. This shows the inexpediency of increasing the height of the PM above a certain value.

A more appropriate way to increase the magnetic field in the FO is to increase the PM width (Fig. 4). In this case, both the central field B_0 and the width of the magnetization region increase in the surface layer of the FO. When the PM width is increased by 2 times from 30 to 60 mm, the central field increases by 1.33 times, and the magnetization area of the FO by a field higher than B_{min} increases by more than 10 times.

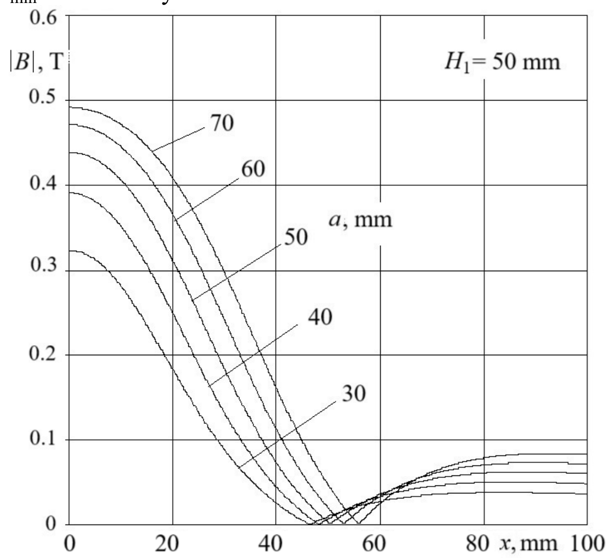

Fig. 4. Distribution of the magnetic field induction modulus in the surface layer of the FO at different PM widths

Figure 5 shows the dependence of the relative values of the central magnetic field B_0^* in the FO (relative to the basic version of the SMF) on the geometric parameters of the PM. With an increase in the volume of the PM, this field also increases, but with a nonlinear decrease in growth. Even with a significant increase in the dimensions of the PM, the central magnetic field increases no more than 2 times relative to the basic version of the SMF. In this case, it is possible to determine the geometric parameters of the PM that provide a magnetic field higher than B_{min} and the magnetization area of the FO by such a field.

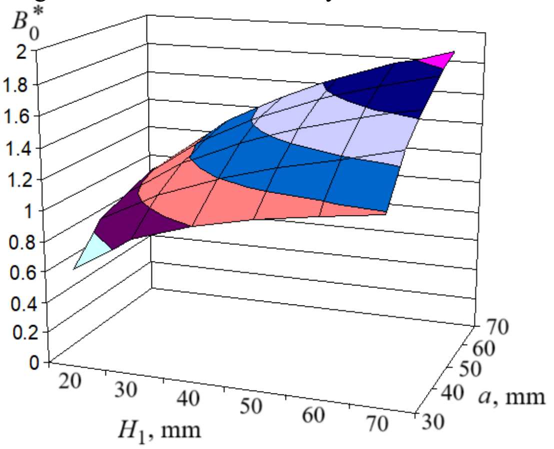

Fig. 5. Dependence of the relative value of the central magnetic field in the FO on the geometric parameters of the PM

However, for a portable EMAT, when selecting the geometric parameters of the PM, in addition to the magnetization field FO, it is necessary to take into account other indicators. These are the magnetic scattering field B_{ex}, the volume of the autonomous source V and the force of attraction of the autonomous source to the FO F_z. The magnetic scattering field B_{ex} has a negative effect on both the nearby electronic system of the device and on the service personnel [26].

The volume V determines the mass, dimensions and cost of the autonomous SMF. The cost is mainly determined by the high-coercivity PM. The attractive force to the FO F_z determines the operating conditions of the portable EMAT. This force is calculated using the well-known formula:

$$F_z = \frac{1}{\mu_0} \oint_S 2\pi r (B_r \cdot B_z) \mathrm{d}S ,$$

where B_r, B_z are the radial and axial components of the magnetic field induction in the volume of the SMF covered by the surface S.

Figure 6 shows the force of attraction of the SMF to the FO F_z^* in relative form.

As follows from the presented graph, with an increase in the volume of the PM V (height H_1 or width a), the attractive force increases. If the width of the PM is insignificant (a=30 mm), then the force from the height of the PM increases insignificantly. With the maximum parameters of the PM from the considered range (H_1=a=70 mm), this force increases almost 14 times compared to the basic version of the SMF.

As calculations show, the nature of the change in the magnetic field scattering B_{ex} into the surrounding space depending on the geometric parameters of the PM largely corresponds to the nature of the change in the central magnetic field B_0 in the FO.

Since with the increase in the volume of PM V all the indicators of SMF increase, the question arises about the nature of these indicators with the same volume, but a different combination of height H_1 and width a.

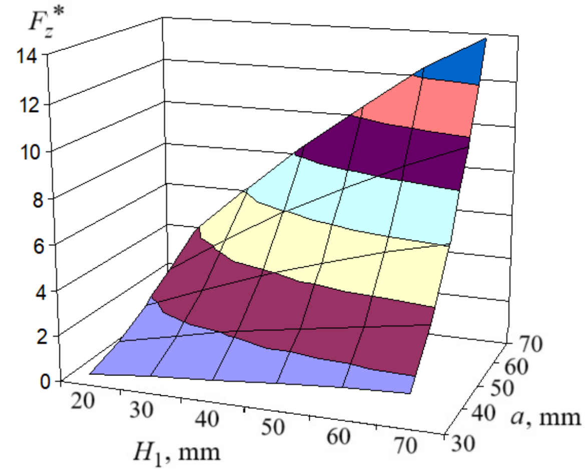

Fig. 6. Dependence of the relative values of the force of attraction of the SMF to the FO on the geometric parameters of the PM

Figure 7 shows the dependence of the relative SMF indicators on the width a for a small (V=125·10^3 mm^3) and large (V=216·10^3 mm^3) volume of the PM. The small value of V is due to the choice of the basic version of the PM with parameters H_1=a=50 mm, and the large value of V is due to the choice of the basic version of the PM with parameters H_1=a=60 mm.

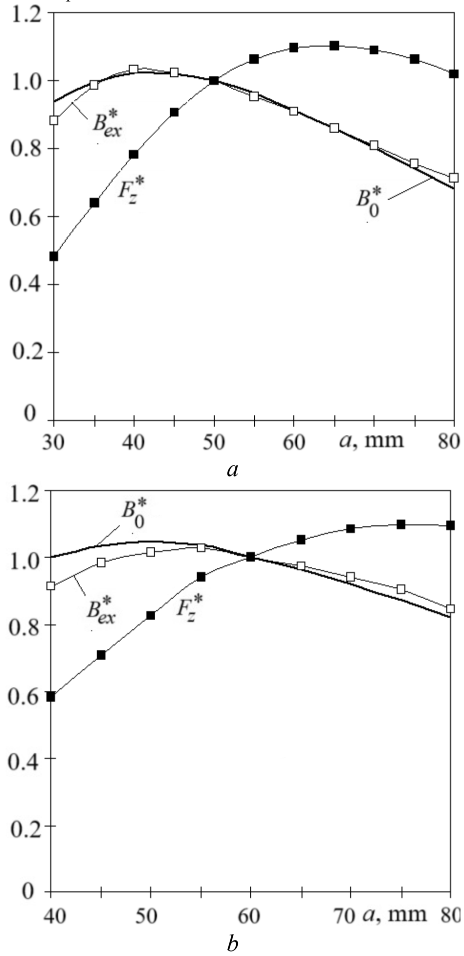

Fig. 7. Dependence of relative SMF indicators on the width of the PM for a small (a) and large (b) volume V

With a constant PM volume, the maximum value of the central field B_0 in the FO occurs at a certain width. For a PM with a small volume, this is approximately a=40 mm, and for a PM with a large volume, this is approximately a=50 mm. Note that these dimensions are smaller than the width of the base PM. The nature of the scattering field B_{ex} largely corresponds to the central field B_0.

The nature of the force of attraction of F_z SMF to FO is different. The maximum force occurs when the width of the magnet is greater than the base one. For PM with a small volume, this is approximately a=65 mm, and for PM with a large volume, a=75 mm.

Let us consider the influence of the height FS he on the SMF indices (Fig. 8). This screen slightly (up to 4 %) increases the central magnetic field in the FO B_0. As a result, the force of attraction of the SMF to the FO F_z increases to a greater extent (up to 8 %). At the same time, the magnetic field of scattering into the surrounding space B_{ex} decreases, but slightly (up to 3 %).

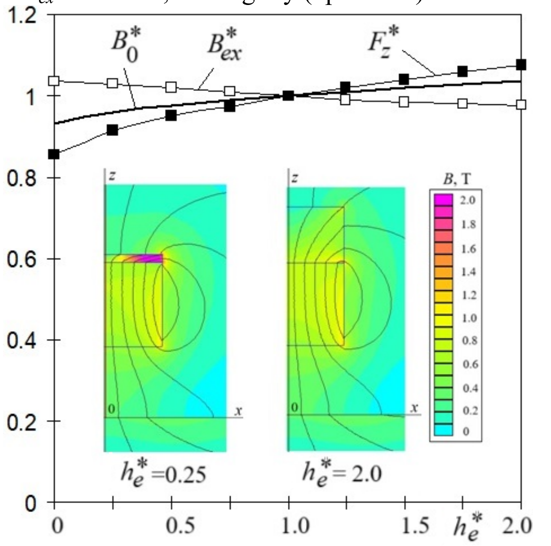

Fig. 8. Dependence of relative SMF indicators on the height of the ferromagnetic shield

The highest value of the scattering field B_{ex} occurs in the absence of FS, and the highest central field B_0 occurs at its maximum height. Note that the location of FS on the lateral sides of the PM is inappropriate, since such a design reduces the central magnetic field in the FO with a large air gap Z_1 [1].

Considering that increasing the height of the FS leads to an increase in the height and weight of the autonomous SMF, it can be assumed that the SMF variant with h_e=10 mm, like the basic variant, is acceptable.

Thus, with an increase in the height H_1 and the width a PM, all SMF indicators increase, although to varying degrees. However, an increase in the central magnetic field B_0 in the FO is a positive indicator of an autonomous source, reflecting its main purpose, and an increase in the remaining indicators are negative factors.

Based on the above, the parameters of the autonomous SMF, namely the geometric dimensions of the PM, must be selected taking into account both the positive indicator (the central magnetic field B_0 in the FO) and the negative indicators (the scattering magnetic field B_{ex}, the volume of the SMF V and the force of its attraction to the FO F_z).

The task of selecting the geometric parameters of the PM can be considered as multicriterial. For this purpose, we will reduce the above SMF indicators to one integral criterion using the scalarization function – the canonical additive-multiplicative objective function:

$$K^* = \beta\left(\alpha_1 B_0^* + \frac{\alpha_2}{V^*} + \frac{\alpha_3}{F_z^*} + \frac{\alpha_4}{B_{ex}^*}\right) + (1-\beta)\times$$
$$\times \left(B_0^*\right)^{\alpha_1}\left(\frac{1}{V^*}\right)^{\alpha_2}\left(\frac{1}{F_z^*}\right)^{\alpha_3}\left(\frac{1}{B_{ex}^*}\right)^{\alpha_4}, \quad \sum_{i=1}^{4}\alpha_i = 1,$$

where α_i are the weight coefficients of the objective function; β is the empirical coefficient.

Based on expert assessments, we set the coefficients α_1=0.5; α_2=0.2; α_3=0.2; α_4=0,1; β=0.75. The integral efficiency criterion from the geometric parameters of the PM of an autonomous SMF is presented in Fig. 9.

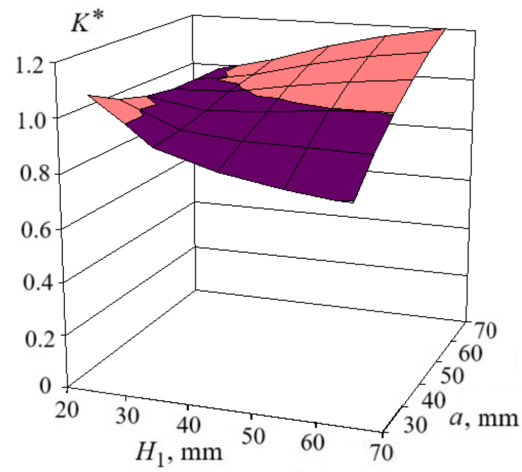

Fig. 9. Dependence of the integral criterion of SMF efficiency on the geometric parameters of the PM

Based on the obtained dependencies, it can be concluded that the most effective are SMFs, in which the PM have the largest width and height from the considered range. This is due to the fact that such magnets magnetize the FO more strongly. However, PMs with a small width and height can also be quite effective, provided that their central field value B_0>B_{min}. Such SMFs have small mass-dimensional parameters and a relatively low cost.

Experimental studies. For experimental verification of the magnetic field modeling results, a sample of an autonomous SMF was manufactured, providing magnetization of a remote FO (Fig. 10). This sample contained 6 flat PM sections with dimensions of 50×50×10 mm^3 each made of NeFeB ceramics. The sections were arranged in a column so that the PM height was 60 mm. On top of the PM there was an FS with dimensions of 50×50×10 mm^3, made of St10 steel.

An experimental sample made of St45 steel with dimensions of 180×65×30 mm^3 was used as the FO, on the surface of which measuring paper with divisions of 1 mm was applied (to control the movement step of the Hall sensor, which provided measurement of the axial component of the magnetic field induction B_z at a height of 0.5 mm above the surface of the FO). The measurement of the magnetic field induction value was performed using a pre-calibrated F4354/1 teslameter.

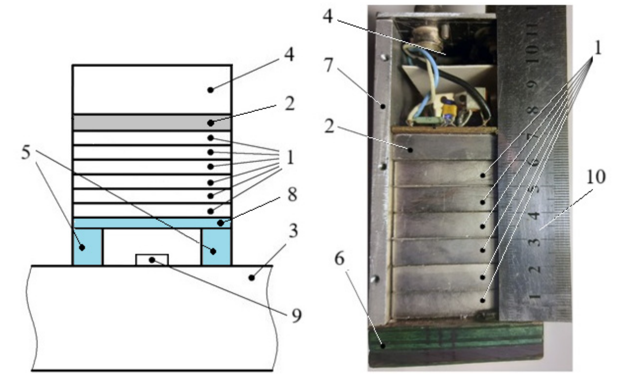

a *b*

Fig. 10. Scheme (a) and experimental sample (b) of an autonomous SMF that provides magnetization of a remote FO: 1 – PM sections; 2 – FS; 3 – FO; 4 – electronic unit; 5 – insulating supports of variable height; 6 – dielectric pads; 7 – housing; 8 – insulating protector; 9 – Hall sensor; 10 – measuring ruler

A sample of an autonomous small-sized SMF was installed on the FO with a non-magnetic gap Z_1=25 mm (the total height of the insulating supports 5 and the protector 8). The axial component of the magnetic field induction B_z was measured by a Hall sensor on the FO surface every 5 mm from the center at a distance of up to 40 mm along the long side of the experimental steel sample. The measurement results are shown in Fig. 11. In the presented distribution of the magnetic field, the FO is outlined by a contour below the 0*x* axis.

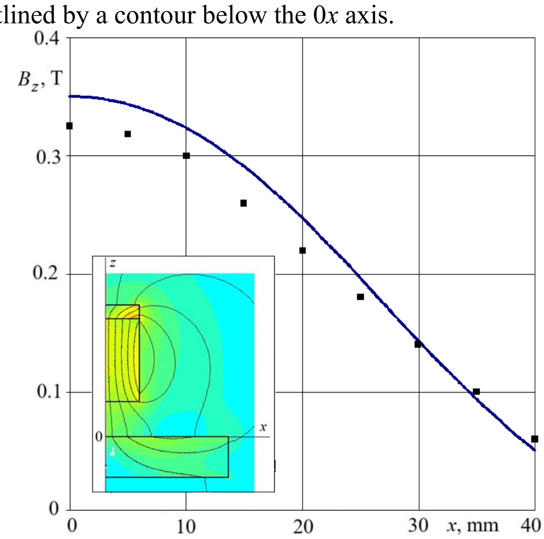

Fig. 11. Results of experimental (points) and calculated (line) values of the axial component of the magnetic field induction B_z and the distribution of the magnetic field for the experimental sample

The experimental data correspond to the simulation results with an error of up to 9 %, which indicates the reliability of the results obtained. The difference between the experimental results and the calculated ones is due to the spread of the parameters of the PM sections due to the manufacturing technology, as well as errors in the location of the Hall sensor relative to the FO.

Practical implementation. Let us consider the use of an autonomous SMF for a portable EMAT, providing excitation and reception of ultrasonic pulses in the FO. Figure 12 shows the diagram and layout of the converter of electromagnetic energy into ultrasonic energy [27] with an autonomous SMF and a system for measuring the distribution of the magnetic field on the surface of the FO.

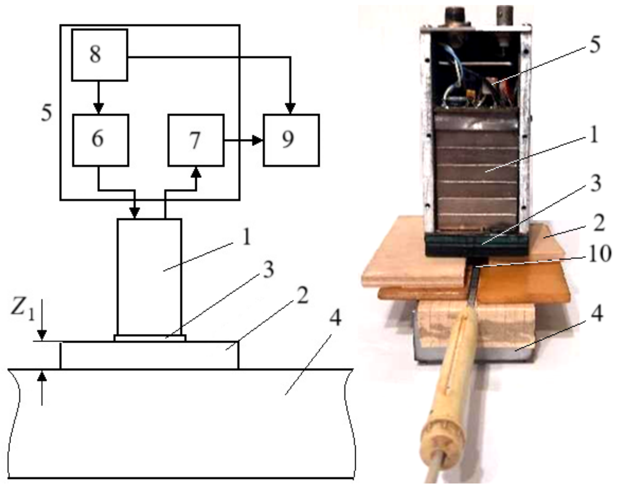

a *b*

Fig. 12. Scheme (a) and layout (b) of EMAP: 1 – SMF; 2 – gaskets; 3 – plate 3 with an inductance coil; 4 – FO; 5 – electronic unit; 6 – pulse generator; 7 – amplifier; 8 – synchronizer; 9 – oscilloscope; 10 – Hall sensor

The converter includes a DPMP 1, dielectric spacers 2 of adjustable height, a dielectric plate 3 with a built-in high-frequency inductance coil, a FO 4, an electronic unit 5 with a high-frequency current pulse generator 6, an amplifier of received ultrasonic pulses 7 and a synchronizer 8. A digital oscilloscope 9 records ultrasonic pulse signals in the FO, and a Hall sensor 10 measures the axial component of the magnetic field on the FO surface.

The converter was installed on the surface of the FO through dielectric spacers of different thicknesses. The efficiency of the SMF was estimated by the amplitude of the received ultrasonic pulses using a SmartDS7202 oscilloscope [8].

Studies were conducted for EMAT with two magnetic field sources: SMF-1 contained 6 PM sections with dimensions of 50×50×10 mm^3, SMF-2 contained 4 PM sections with dimensions of 30×30×15 mm^3. Both sources contained FS with a height of 10 mm. These sources have the same axial height H_1=60 mm, but different PM volumes. SMF-1 has V=150·10^3 mm^3, and SMF-2 has V=54·10^3 mm^3.

Figure 13 shows the time sweeps of the ultrasonic pulses reflected in the FO volume, obtained at different gaps between SMF-1 and the FO surface.

The oscillograms show the probing 1 and the sequence of short bottom 2 ultrasonic pulses reflected in the FO volume.

With a non-magnetic gap between SMF-1 and FO Z_1=25 mm, when the value of the central magnetic field in FO B_0=0.44 T, the amplitudes of the bottom pulses in relation to the noise are at least 10/1, which is sufficient for thickness measurement of ferromagnetic products. With a two-fold decrease in the gap Z_1=12.5 mm, and therefore an increase in the central field to B_0=0.85 T, the amplitudes of the bottom pulses in relation to the noise increase to 30/1, which is applicable for monitoring and diagnostics of ferromagnetic products.

Thus, due to the increase in the magnetic field in the FO, the ratio of the amplitude of the first reflected ultrasonic pulse to the noise amplitude increases by 3 times, which makes it possible to increase the efficiency of EMAT.

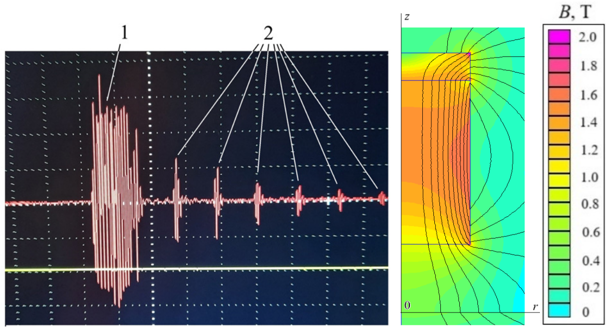

a

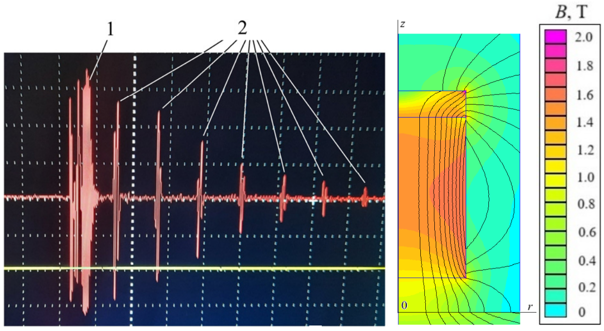

b

Fig. 13. Oscillograms of the sequence of bottom ultrasonic pulses reflected in the FO volume (left) and magnetic field induction (right) at Z_1: 25 mm (*a*) and 12.5 mm (*b*), obtained using SMF-1: 1 – probing pulse; 2 – bottom pulses.

Figure 14 shows the time sweeps of the ultrasonic pulses reflected in the volume of the FO, obtained with similar gaps between SMF-2 and the surface of the FO and the same magnitude of the probing ultrasonic pulse, as when using SMF-1. These oscillograms, as in Fig. 13, show the probing pulse and a sequence of short bottom pulses.

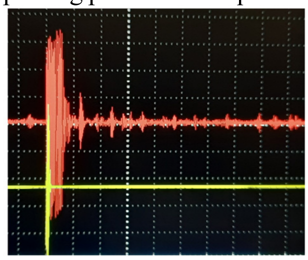

a

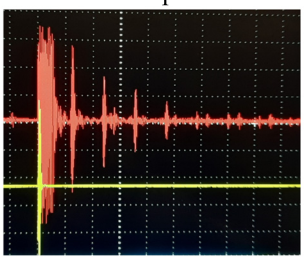

b

Fig. 14. Oscillograms of the sequence of bottom ultrasonic pulses reflected in the FO volume at Z_1: 25 mm (*a*) and 12.5 mm (*b*), obtained using SMF-2

With a non-magnetic gap between SMF-2 and FO Z_1=25 mm (B_0=0.34 T), the amplitudes of the bottom pulses in relation to the noise are 5/1, and when the gap Z_1 is reduced by half, the central magnetic field increases to B_0=0.61 T, which increases the ratio of the amplitude of the bottom pulses to the noise to 13.5/1.

When using SMF-2, which has a PM volume that is almost 3 times smaller than SMF-1, the EMAT efficiency decreases (Fig. 13). This is due to the fact that the amplitudes of short bottom pulses reflected in the FO volume decrease, and their sequence attenuates faster. This indicates the influence of the SMF magnetic field on the EMAT efficiency.

Thus, it has been experimentally confirmed that increasing the magnetic field in the FO by a source with permanent magnets with rational parameters increases the efficiency of EMAT.

In the future, it is advisable to consider the use of either a pulsed electromagnet or the joint use of a pulsed electromagnet and a permanent magnet to amplify and regulate the magnitude of the magnetic field in the surface layer of the FO.

Conclusions.

1. As a result of the analysis of literary sources, the need to select rational parameters for a source of a constant magnetic field that magnetizes a ferromagnetic object when converting electromagnetic energy into ultrasonic energy was established.

2. An analysis was carried out of the parameters of an autonomous source of magnetic field, consisting of a PM and a ferromagnetic screen, which acts on the flat surface of a remote ferromagnetic object, magnetizing it to a given level.

3. It has been established that in order to select rational parameters of an autonomous SMF, it is necessary to use an integral criterion that takes into account the magnetic field in the surface layer of the FO, the magnetic scattering field, the volume of the PM, which determines the mass-dimensional indicators and cost of the SMF, and the force of attraction to the FO.

4. The results of experimental studies on a sample of an autonomous source, which contained 6 sections of PM made of NeFeB ceramics with dimensions of 50×50×10 mm^3, correspond with an error of up to 9 % to the results of calculating the magnetic field on the surface of a ferromagnetic sample made of St45 steel with a thickness of 40 mm.

5. For a portable electromagnetic-acoustic transducer, increasing the magnetic field in the FO either due to the dimensions of the PM or due to a decrease in the air gap between the SMF and the FO provides an increase in the efficiency of the EMAP, increasing the ratio of the amplitude of the bottom pulses to the amplitude of the noise.

Conflict of interest. The authors declare that they have no conflicts of interest

REFERENCES

1. Suchkov G.M., Bolyukh V.F., Kocherga A.I., Mygushchenko R.P., Kropachek O.Y. Increasing the efficiency of the surface-mounted ultrasonic electromagnetic-acoustic transducer on account of the magnetic field source. *Tekhnichna Elektrodynamika*, 2023, no. 2, pp. 3-8. doi: https://doi.org/10.15407/techned2023.02.003.

2. Khalil Baqer Z., Hliyil Hafiz M., Sayyid F.F. Processing of Hematite Ore by using Magnetizing Reduction Roasting and Magnetic Separation. *Salud, Ciencia y Tecnología – Serie de Conferencias*, 2024, vol. 3, art. no. 832. doi: https://doi.org/10.56294/sctconf2024832.

3. Tan Y.W., Leong S.S., Lim J., Yeoh W.M., Toh P.Y. Low-gradient magnetic separation of magnetic nanoparticles under continuous flow: Experimental study, transport mechanism and mathematical modelling. *Electrophoresis*, 2022, vol. 43, no. 21-22, pp. 2234-2249. doi: https://doi.org/10.1002/elps.202200078.

4. Ciannella S., Wu X., González-Fernández C., Rezaei B., Strayer J., Choe H., Wu K., Chalmers J., Gomez-Pastora J. Kinetic and Parametric Analysis of the Separation of Ultra-Small, Aqueous Superparamagnetic Iron Oxide Nanoparticle Suspensions under Quadrupole Magnetic Fields. *Micromachines*, 2023, vol. 14, no. 11, art. no. 2107. doi: https://doi.org/10.3390/mi14112107.

5. Riaz W., Liu Z., Wang X., Shen Y., Farooq O., He C., Shen G. Comparative analysis of electromagnet and coil-based

magneto-acoustic emission detection in pre-stressed Q235 steel. *NDT & E International*, 2025, vol. 155, art. no. 103414. doi: https://doi.org/10.1016/j.ndteint.2025.103414.
6. Wang F., Tang D., Gao L., Dai H., Wang P., Gong Z. Magnetic entrainment mechanism of multi-type intergrowth particles for Low-Intensity magnetic separation based on a multiphysics model. *Minerals Engineering*, 2020, vol. 149, art. no. 106264. doi: https://doi.org/10.1016/j.mineng.2020.106264.
7. Kosse J.J., Wessel W.A.J., Zhou C., Dhallé M., Tomás G., Krooshoop H.J.G., Ter Brake H.J.M., Ten Kate H.H.J. Mechanical design of a superconducting demonstrator for magnetic density separation. *Superconductor Science and Technology*, 2021, vol. 34, no. 11, art. no. 115019. doi: https://doi.org/10.1088/1361-6668/ac2c0f.
8. Migushchenko R.P., Suchkov G.M., Petrishchev O.N., Bolyukh V.F., Plesnetsov S.Y., Kocherga A.I. Information-measuring electromechanical transducers for assessing the quality of the surface of ferromagnetic metal items by ultrasonic waves Rayleigh. *Technical Electrodynamics*, 2017, no. 2, pp. 70-76. doi: https://doi.org/10.15407/techned2017.02.070.
9. Pham H.Q., Le V.S., Vu M.H., Doan D.T., Tran Q.H. Design of a lightweight magnetizer to enable a portable circumferential magnetic flux leakage detection system. *Review of Scientific Instruments*, 2019, vol. 90, no. 7, art. no. 074705. doi: https://doi.org/10.1063/1.5090938.
10. Huang X., Xie Y., Liu F., Li J., Jiang W., Huang P., Sun H., Liang H., He S., Hao W., Xu L. A Hybrid Denoising Method for Electromagnetic Acoustic Detection. *IEEE Sensors Journal*, 2024, vol. 24, no. 16, pp. 25523-25530. doi: https://doi.org/10.1109/JSEN.2024.3416161.
11. Gautam A.K., Yin C.-C., Bhattacharya B. A new chevron electromagnetic acoustic transducer design for generating shear horizontal guided wave. *Ultrasonics*, 2023, vol. 135, art. no. 107137. doi: https://doi.org/10.1016/j.ultras.2023.107137.
12. Liu Z., Deng L., Zhang Y., Li A., Wu B., He C. Development of a mode-tuning magnetic-concentrator-type electromagnetic acoustic transducer. *Ultrasonics*, 2020, vol. 103, art. no. 106094. doi: https://doi.org/10.1016/j.ultras.2020.106094.
13. Zhang T., Yang X., Li M., Peng H., Peng W. Enhancing unilateral EMAT performance through topological optimization of Halbach permanent Magnet arrays. *NDT & E International*, 2024, vol. 146, art. no. 103172. doi: https://doi.org/10.1016/j.ndteint.2024.103172.
14. McMillan R., Hampson R., Tabatabaeipour M., Jackson W., Zhang D., Tzaferis K., Dobie G. Design and Manufacture of an Optimised Side-Shifted PPM EMAT Array for Use in Mobile Robotic Localisation. *Sensors*, 2023, vol. 23, no. 4, art. no. 2012. doi: https://doi.org/10.3390/s23042012.
15. Mudapaka V., Garewal P., Gantala T., Balasubramanian K. Design of a Permanent Magnet Electromagnetic Acoustic Transducer (EMAT) for In-Situ Inspection of Metals at high Temperatures. *Proceedings of the 11th European Workshop on Structural Health Monitoring (EWSHM 2024), e-Journal of Nondestructive Testing*, 2024, vol. 29, no. 7. doi: https://doi.org/10.58286/29803.
16. Suresh N., Elliott P., Radu C., Corcoran J. The design of high temperature EMATs to avoid irreversible magnetic losses. *NDT & E International*, 2025, vol. 150, art. no. 103279. doi: https://doi.org/10.1016/j.ndteint.2024.103279.
17. Huo Z., Cai D., Liu D., Duan Y., Meng H., Liu S., Liu X. Development of an electromagnetic bulk wave EMAT. *Journal of Physics: Conference Series*, 2023, vol. 2674, no. 1, art. no. 012012. doi: https://doi.org/10.1088/1742-6596/2674/1/012012.
18. Bolyukh V.F., Katkov I.I. Influence of the Form of Pulse of Excitation on the Speed and Power Parameters of the Linear Pulse Electromechanical Converter of the Induction Type. *Proceedings of the ASME 2019 International Mechanical Engineering Congress and Exposition. Volume 2B: Advanced Manufacturing*, 2019, V02BT02A047. doi: https://doi.org/10.1115/IMECE2019-10388.
19. Hyun D., Shin A. Quantitative Approach to the Magnetic Force of a Cylindrical Permanent Magnet Acting on a Ferromagnetic Object. *New Physics: Sae Mulli*, 2018, vol. 68, no. 11, pp. 1249-1261. doi: https://doi.org/10.3938/NPSM.68.1249.
20. Liu Z., Riaz W., Shen Y., Wang X., He C., Shen G. Magneto acoustic emission technique: A review of methodology, applications, and future prospects in non-destructive testing. *NDT & E International*, 2024, vol. 146, art. no. 103171. doi: https://doi.org/10.1016/j.ndteint.2024.103171.
21. Mirkhani K., Chaggares C., Masterson C., Jastrzebski M., Dusatko T., Sinclair A., Shapoorabadi R.J., Konrad A., Papini M. Optimal design of EMAT transmitters. *NDT & E International*, 2004, vol. 37, no. 3, pp. 181-193. doi: https://doi.org/10.1016/j.ndteint.2003.09.005.
22. Liu C., Li Q., Liu J., Guo A. Influence of coil structure on the distribution of transmitting magnetic field in downhole electromagnetic detection. *2024 6th International Conference on Intelligent Control, Measurement and Signal Processing (ICMSP)*, 2024, pp. 417-420. doi: https://doi.org/10.1109/ICMSP64464.2024.10866240.
23. Rozov V.Y., Reutskiy S.Y., Pelevin D.Y., Kundius K.D. Magnetic field of electrical heating cable systems of the floors for residential premises. *Electrical Engineering & Electromechanics*, 2024, no. 5, pp. 48-57. doi: https://doi.org/10.20998/2074-272X.2024.5.07.
24. Permanent neodymium magnets. Available at: http://www.polus-n.com/post_magn_eng.html (Accessed: 22 July 2024).
25. Finite Element Method Magnetics: Download – Stable Distribution (21Apr2019) – 64-bit Executable. Available at: https://www.femm.info/wiki/Download (Accessed: 22 July 2024).
26. Rozov V.Y., Pelevin D.Y., Kundius K.D. Simulation of the magnetic field in residential buildings with built-in substations based on a two-phase multi-dipole model of a three-phase current conductor. *Electrical Engineering & Electromechanics*, 2023, no. 5, pp. 87-93. doi: https://doi.org/10.20998/2074-272X.2023.5.13.
27. Plesnetsov S.Y., Petrishchev O.N., Mygushchenko R.P., Suchkov G.M., Sotnik S.V., Kropachek O.Y. Powerful sources of pulse high-frequency electromechanical transducers for measurement, testing and diagnostics. *Electrical Engineering & Electromechanics*, 2018, no. 2, pp. 31-35. doi: https://doi.org/10.20998/2074-272X.2018.2.05.

Received 29.12.2024
Accepted 14.02.2025
Published 02.07.2025

V.F. Bolyukh[1]*, Doctor of Technical Science, Professor,*
G.M. Suchkov[1]*, Doctor of Technical Science, Professor,*
R.P. Mygushchenko[1]*, Doctor of Technical Science, Professor,*
M.E. Kalnytskyi[1]*, Postgraduate Student,*
[1] National Technical University «Kharkiv Polytechnic Institute»,
2, Kyrpychova Str., Kharkiv, 61002, Ukraine,
e-mail: vfbolyukh@gmail.com (Corresponding Author)

How to cite this article:
Bolyukh V.F., Suchkov G.M., Mygushchenko R.P., Kalnytskyi M.E. Determination of parameters of an autonomous source of a constant magnetic field for a portable electromagnetic-acoustic transducer. *Electrical Engineering & Electromechanics*, 2025, no. 4, pp. 72-79. doi: https://doi.org/10.20998/2074-272X.2025.4.09

UDC 621.319 https://doi.org/10.20998/2074-272X.2025.4.10

D.G. Koliushko, S.S. Rudenko, V.O. Vevenko

Application of the multilayer soil equivalence method in determining the normalized parameters of the grounding system

Introduction. *Normalized parameters of the grounding system, such as touch voltage and resistance, are critically important for ensuring electrical safety and reliability of power plants and substations. The complexity of the multi-layered soil structure makes it difficult to determine mentioned parameters. This is due to the fact that real soils on the territory of energy facilities of Ukraine have three or more layers, and the specified parameters are determined by software with two-layer calculation models. Therefore, the need to provide multilayer geoelectric structures into equivalence two-layer models for practical application is an urgent task.* ***Goal.*** *Determination of the application limits of the multilayer soils equivalence method based on the calculating results analysis of the grounding system normalized parameters.* ***Methodology.*** *The study considered a three-layer model for four soil types (A, H, Q, K) common in Ukraine. The calculations were performed using the LiGro software package, which is based on the method of integro-differential equations, applied to the analytical solution of the problem of the electric field potential of a point current source in a three-layer conducting half-space. As a criterion for the possibility of applying the equivalence method, a relative error value of 10 % was chosen when determining the normalized parameters of a grounding system of the given topology and soil type. When determining the error, the calculation results in the original three-layer soil structure for the given topology of the grounding system were taken as the true value.* ***The results*** *show that the effectiveness of equivalent technique significantly depends on the type of soil and the area of the grounding system. In particular, for soil type A, replacing the upper and middle layers with the equivalent first layer (the lower layer with the second) provides a smaller error in the calculations of the grounding resistance than representing the upper layer as the first, and the middle and lower layers as the second equivalent layer. At the same time, there is a tendency for the error to decrease with increasing area of the object: from 225 m^2 to 14400 m^2, for the first case, the error decreased from –14.6 % to –2.6 %, and for the second case, it changed from –9.3 % to 14.6 %, respectively.* ***Originality.*** *For the first time, the results of the methodical error evaluation of the equivalence techniques of multilayered soils of different types when calculating the normalized parameters of grounding system are presented.* ***Practical value.*** *Determination of the conditions and limits of the use of the equivalence method when calculating the normalized parameters of grounding system by software complexes can be used in the design of new or reconstruction of existing energy facilities of Ukraine.* References 20, tables 5, figures 4.

Key words: **grounding system, touch voltage, resistance of grounding, method of equivalence, multi-layered soil.**

Вступ. *Нормовані параметри заземлювального пристрою, такі як напруга дотику та опір, є критично важливими для забезпечення електричної безпеки та надійності роботи електростанцій та підстанцій. Складність багатошарової структури ґрунту створює проблеми для визначення вказаних параметрів. Це обумовлено тим, що реальні ґрунти на території енергооб'єктів України мають три і більше шарів, а нормовані параметри визначаються програмними засобами з двошаровими розрахунковими моделями. Тому необхідність еквівалентування багатошарових геоелектричних структур у двошарові моделі для практичного застосування є актуальною задачею.* ***Мета.*** *Визначення меж застосування методу еквівалентування багатошарових ґрунтів на основі аналізу результатів розрахунку нормованих параметрів заземлювального пристрою.* ***Методологія.*** *У дослідженні розглянуто тришарову модель для чотирьох типів ґрунту (A, H, Q, K), поширених в Україні. Розрахунки виконано за допомогою програмного комплексу LiGro, який базується на методі інтегро-диференційних рівнянь, застосованому для аналітичного вирішення задачі про потенціал електричного поля точкового джерела струму в тришаровому провідному напівпросторі. В якості критерію можливості застосування методу еквівалентування обрано величину відносної похибки в 10 % при визначенні нормованих параметрів заземлювального пристрою заданої топології та типу ґрунту. При визначенні похибки за істинне значення приймались результати розрахунку у вихідній тришаровій структурі ґрунту для заданої топології заземлювального пристрою.* ***Результати*** *демонструють, що ефективність методу еквівалентування суттєво залежить від типу ґрунту та площі системи заземлення. Зокрема, для ґрунту типу A заміна верхнього та середнього шару еквівалентним першим шаром (нижнього – другим), забезпечує меншу похибку розрахунків опору заземлення, ніж представлення верхнього шару в якості першого, а середнього та нижнього – другого. При цьому спостерігається тенденція до зменшення похибки від –14,6 % до –2,6 % зі зростанням площі об'єкту від 225 м^2 до 14400 м^2.* ***Оригінальність.*** *Вперше представлено результати оцінки похибки методу еквівалентування багатошарових ґрунтів різних типів при розрахунку нормованих параметрів заземлювальних пристроїв.* ***Практична цінність.*** *Визначення умов та меж застосування методу еквівалентування при розрахунку нормованих параметрів заземлювальних пристроїв програмними комплексами може бути використано при проєктуванні нових або реконструкції існуючих енергооб'єктів України.* Бібл. 20, табл. 5, рис. 4.

Ключові слова: **заземлювальний пристрій, напруга дотику, опір заземлювального пристрою, метод еквівалентування, багатошаровий ґрунт.**

Introduction. Calculation of the normalized parameters of grounding devices (GDs) of power plants and substations, namely GD resistance, GD voltage and touch voltage, is an important scientific and practical task both from the point of view of designing new energy facilities [1–3] and operating existing ones [4]. The initial data for performing such calculations are the single-phase ground fault current, the operating time of the main and backup protection, GD topology [5], the material and cross-section of the grounding conductors, the resistance of the base [6] and the electrophysical characteristics of the soil [7]. The latter factor is practically independent of human influence and cannot be changed during operation.

In common software packages for modelling electromagnetic processes in GDs [8–13], a two-layer soil model with a separation boundary parallel to the ground surface is used. Based on the fact that, according to the results of the analysis of 612 soundings, more than 80 % of soils in the locations of energy facilities in Ukraine have three or more layers [7], there is a need to reduce the existing structure to a two-layer one. Usually, the equivalence method is used for this [12–18]. Its idea is that a model with such characteristics of the geoelectric structure of the earth is considered equivalent, under which the grounding conductor will have the same values of electrical parameters as in the original multilayer structure.

To reduce the multilayer geoelectric structure to equivalent, the total transverse (normal) and longitudinal (tangential) conductivities are determined when currents flow in the corresponding directions in a rectangular soil column of height h_Σ, with a base in the form of a square with a side of a known size (for example, a = 1 m). The expressions for determining the equivalent resistivity ρ_e (1) and the equivalent layer thickness h_e (2) have the form [7, 14, 15]:

$$\rho_e = \sqrt{\sum_{i=1}^{m}(h_i \cdot \rho_i) \times \left(\sum_{i=1}^{m}\frac{h_i}{\rho_i}\right)^{-1}}; \qquad (1)$$

$$h_e = \sqrt{\sum_{i=1}^{m}(h_i \cdot \rho_i) \times \sum_{i=1}^{m}\frac{h_i}{\rho_i}}, \qquad (2)$$

where ρ_i and h_i are the resistivity and thickness of the i-th layer, m is the number of equivalent layers.

In general, three methods (see section 2.3.2 [3]) of applying the equivalence method [7] have become widespread in practice:

1. Method No. 1 – the upper layer of a real geoelectric structure is considered as the first layer of an equivalent two-layer one, and the following layers are equivalent to the second (it is believed that this method allows to determine the potential distribution on the soil surface and the touch voltage with the smallest errors).

2. Method No. 2 – all upper layers of the real structure are represented as the first layer of an equivalent geoelectric structure, and the lower one is the second layer (this method is usually used when calculating the resistance and potential on the ground).

3. Method No. 3 – all upper layers of the real structure before the grounding conductor and additional 0.1–0.2 m are represented as the first layer of the equivalent geoelectric structure, and the lower ones (or those that are lower relative to the grounding conductor elements, other layers) are represented as the second layer.

The first and second methods are obtained on the basis of the physical meaning of the normalized parameters: the ratio of the specific electrical resistance ρ of the upper layers has the greatest influence on the value of the potential on the soil surface, and therefore on the touch (step) voltage, and the resistance and potential on the grounding conductor are more influenced by ρ of the layer in which the grounding conductor is located (see section 2.3.2 [3]). The third method has been practically applied in the Research and Design Institute «Molniya» of NTU «KhPI» on the basis of numerical calculations and comparison of experimental and calculated values.

However, in [9–15] there are no visual information and analytical and statistical data that would allow assessing the general impact of the equivalence of different types of soil (A, H, Q, K) on the results of calculating the normalized parameters. The results obtained in [4] can be considered only a preliminary analysis for a GD 5×5 m^2 area and insufficient for practical use.

Considering that the specified parameters affect the electrical safety of station and substation service personnel, as well as the reliability of equipment operation, relay protection systems and telemechanics, the study of such an impact to increase the accuracy of their determination is a relevant task.

The goal of the work is to determine the limits of application of the method of equivalence of multilayer soils based on the analysis of the results of calculating the normalized parameters of the grounding device.

Research materials. Considering that in Ukraine, in the locations of energy facilities, the vast majority of soils are three-layered, it is advisable to consider this particular geoelectric structure and the method of its equivalence. It is generally known that three-layer soils are divided into four types based on the ratio of the electrical resistivity of the layers:

- Q – ($\rho_1 > \rho_2 > \rho_3$);
- A – ($\rho_1 < \rho_2 < \rho_3$);
- H – ($\rho_1 > \rho_2 < \rho_3$);
- K – ($\rho_1 < \rho_2 > \rho_3$).

The analysis of the percentage distribution of the results of experimental soil sounding studies on the territory of energy facilities of Ukraine, carried out in [4], showed that the soil type Q is 44.43 %; A – 0.84 %; H – 31.42 %; K – 23.31 %.

To achieve the goal, as a criterion for the limits of application of the equivalence method, it is proposed to choose a value of relative error of 10 % (acceptable for solving practical problems on calculating the soil surface [6, 8, 11]) when determining the normalized parameters of the GD of a given topology and soil type. To carry out the study of the above soil types, the LiGro software package was used [17], which allows determining the normalized parameters of the GD of arbitrary complexity, located in a three-layer soil. The specified complex was created on the basis of the method of integro-differential equations, applied for analytical solution of the problem of electric field potential of a point current source in a three-layer conductive half-space, with subsequent integration of a set of point current sources in the form of an arbitrarily oriented grounding conductor.

To perform the calculations, three variants of the GD with the size of 15×15 m^2, 45×45 m^2 and 120×120 m^2 were used. The cell size in all cases is 3×3 m^2 (see Tables 1 – 4). A rod made of hot-rolled steel BSt3SP (Fe37-3FN) with diameter of 14 mm with the corresponding electromagnetic characteristics was chosen as the grounding conductor. The grounding conductor is located at a depth of 0.5 m, which meets the requirements of the regulatory document [19].

According to [7], it is advisable to consider the values at the ratio $\rho^* = \rho_i/\rho_{i+1}$ in the range [0.01; 10], which allows to cover 99.9 % of three-layer soils of Ukraine in the locations of operating energy facilities [4]. According to [4], the thickness of the layers is within $h_1 \in$ [0.02; 10] m for the first layer and $h_2 \in$ [0.01; 35] m for the second one. To perform a qualitative analysis, the average value of h_1 and h_2 was chosen [7]. The parameters of the considered initial three-layer and equivalent two-layer soil models are given in Table 1 – 4.

In this case, the average statistical values obtained in [7] are taken as the initial soil model. The equivalent two-layer ones are obtained using (1) and (2).

When performing calculations, it is assumed that the resistance of the base is 100 Ω [3], and the current of a single-phase fault to the ground is 10 kA. The calculation of the touch voltage was performed at the center (U_{tc}) and at the edge (U_{tk}) of the grounding conductor (see Tables 1 – 4). The resistance of the GD (R_G) and the voltage on the GD (U_G) were also determined. The calculation results (values of U_{tc}, U_{tk}, R_G and U_G) for a given grounding system located in soil type A are given in Table 1.

Table 1

Results of calculation of the parameters of the GD for soil type A

Parameter	Original model	Equivalent model by method:		
		No. 1	No. 2	No. 3
ρ_1, Ω·m	10	10	64,3	10
h_1, m	0,79	0,8	8,7	0,6
ρ_2, Ω·m	100	570,3	1000	510
h_2, m	5,46			
ρ_3, Ω·m	1000			
GD 15×15 m^2				
U_{tc}, V	91,81	73,43	848,60	92,82
R_G, Ω	3,61	3,94	4,13	4,40
U_G, V	36050,0	39420,0	41310,0	43990,0
U_{tk}, V	512,80	548,70	2183,00	635,60
GD 45×45 m^2				
U_{tc}, V	34,77	39,26	111,20	38,41
R_G, Ω	2,36	2,29	2,49	2,15
U_G, V	23550,0	22940,0	24940,0	21540,0
U_{tk}, V	243,50	237,60	974,10	234,30
GD 120×120 m^2				
U_{tc}, V	30,16	31,15	40,16	32,11
R_G, Ω	1,45	1,24	1,49	1,24
U_G, V	14530,0	12410,0	14910,0	12400,0
U_{tk}, V	127,70	116,20	436,30	121,60

Tables 2–4 show the results of a similar calculation for other soil types.

Table 2

Results of calculation of the parameters of the GD for soil type H

Parameter	Original model	Equivalent model by method:		
		No. 1	No. 2	No. 3
ρ_1, Ω·m	1000	1000	39,4	1000
h_1, m	0,8	0,8	21,7	0,6
ρ_2, Ω·m	10	211,5	1000	212,3
h_2, m	6,3			
ρ_3, Ω·m	1000			
GD15×15 m^2				
U_{tc}, V	24770	21300	736,10	15860
R_G, Ω	4,60	9,08	1,84	8,06
U_G, V	46000	90820	18410	80580
U_{tk}, V	25740	28340	1270	22710
GD 45×45 m^2				
U_{tc}, V	5126	4340,00	133,60	3225
R_G, Ω	1,68	2,75	1,08	2,55
U_G, V	16810	27450	10810	25470
U_{tk}, V	6270	7909	477,10	6577
GD 120×120 m^2				
U_{tc}, V	467,2	594,30	36,92	446,2
R_G, Ω	0,84	0,89	0,72	0,86
U_G, V	8290	8920	7180	8644
U_{tk}, V	1466	1958	217,30	1704

Table 3

Results of calculation of the parameters of the GD for soil type Q

Parameter	Original model	Equivalent model by method:		
		No. 1	No. 2	No. 3
ρ_1, Ω·m	1000	1000	155,54	1000
h_1, m	0,8	0,8	8,7	0,6
ρ_2, Ω·m	100	17,5	10	19,6
h_2, m	6,3			
ρ_3, Ω·m	10			
GD 15×15 m^2				
U_{tc}, V	23800	24810	2953	16380
R_G, Ω	4,81	3,77	2,89	2,53
U_G, V	48120	37660	28920	25330
U_{tk}, V	26810	25850	4793	17570
GD 45×45 m^2				
U_{tc}, V	5494	5437	812,8	530,6
R_G, Ω	1,01	0,87	0,62	0,27
U_G, V	10040	8657	6203	2680
U_{tk}, V	6127	5926	1250	935
GD 120×120 m^2				
U_{tc}, V	861,5	815	159,8	497,7
R_G, Ω	0,19	0,18	0,13	0,16
U_G, V	1852	1772	1320	1587
U_{tk}, V	1082	1095	274,1	874,2

Table 4

Results of calculation of the parameters of the GD for soil type K

Parameter	Original model	Equivalent model by method:		
		No. 1	No. 2	No. 3
ρ_1, Ω·m	10	10	253,8	10
h_1, m	0,8	0,8	21,7	0,6
ρ_2, Ω·m	1000	47,3	10	47,1
h_2, m	6,3			
ρ_3, Ω·m	10			
GD 15×15 m^2				
U_{tc}, V	84,22	159,20	4412,00	193,50
R_G, Ω	2,29	0,95	6,00	1,01
U_G, V	22890,0	9500,0	59960,0	10090,0
U_{tk}, V	538,70	432,90	7935,00	478,90
GD 45×45 m^2				
U_{tc}, V	51,27	56,47	1056,00	63,57
R_G, Ω	0,85	0,39	1,54	0,40
U_G, V	8542,0	3888,0	15350,0	4012,0
U_{tk}, V	200,80	165,50	2372,00	179,00
GD 120×120 m^2				
U_{tc}, V	34,37	33,79	220,10	34,80
R_G, Ω	0,25	0,16	0,34	0,16
U_G, V	2479,0	1626,0	3364,0	1649,0
U_{tk}, V	78,17	76,61	536,10	80,03

To analyze the data of the calculation experiments, the error in determining the normalized parameters δ using the equivalence method was considered. The true values were those obtained when calculating using the model of the GD placed in a three-layer soil. For each of the normalized parameters and the corresponding soil type, the dependence of the relative error δ on the GD area S was constructed.

Figure 1 shows the specified dependence for soil type A. Here, in Fig. 1,*a*, the dotted line indicates the family of curves for the touch voltage at the edge of the GD (U_{tk}), and the solid line indicates the touch voltage in the center of the GD (U_{tc}). The designations No. 1 – No. 3 correspond to the methods of equivalence. In Fig. 1,*b*, the solid curves correspond to the dependence $\delta(S)$ for the

GD resistance (R_G), and the dotted lines indicate the voltage on the GD (U_G).

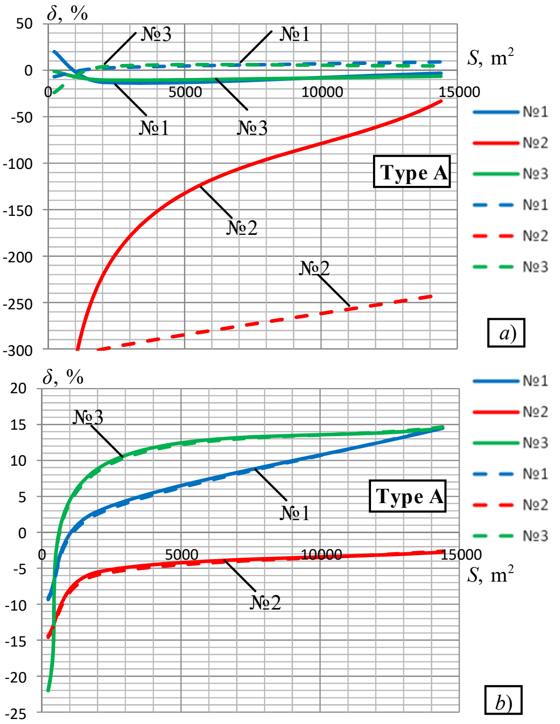

Fig. 1. Error in determining normalized parameters depending on the area of the GD and the method of equivalence of soil type A:
a – solid curve – U_{tc}; dotted curve – U_{tk};
b – solid curve – R_G; dotted curve – U_G

It should be noted that the error of more than 300 % is not shown in the graph. According to the results of modeling for soil type A, we see confirmation of the initial hypothesis – method No. 2 is quite effective for calculating the voltage on the GD and the GD resistance (the error decreases with increasing area), and methods No. 1 and No. 3 show a sufficiently high accuracy in determining the touch voltage. At the same time, in the center of the GD, method No. 3 shows the best results (error up to –10.5 %), and at the edge of the GD – method No. 1 (error up to 9 %).

Figure 2 shows similar calculation results for soil type H.

According to the results of modeling for soil type H, we see that the error in calculating the touch voltage in the center and at the edge of the GD lies in the range from –27 % to 15 % (equivalence methods No. 1 and No. 3). However, it is practically impossible to identify a specific range of application for them. For the specified type of soil, the use of the equivalence method for calculating the voltage on the GD and the GD resistance is not recommended, although the tendency for the error to decrease with increasing area remains. At the same time, contrary to the established opinion, methods No. 1 and No. 3 have the smallest error (for them, the absolute value of the error decreases from –97 % to –6 % and from –75 % to –4 %, respectively). However, in the future, it is necessary to additionally investigate their behavior with an increase in the RP area.

Figure 3 shows similar calculation results for soil type Q. The symbols are similar to Fig. 1.

According to the modeling results for soil type Q, we see that only method No. 1 can be used to calculate the touch voltage in the center and at the edge of the GD (the error lies in the range from –4.2 % to 5.6 %), the voltage on the GD and the GD resistance (the error is from 22 % to 4.3 %).

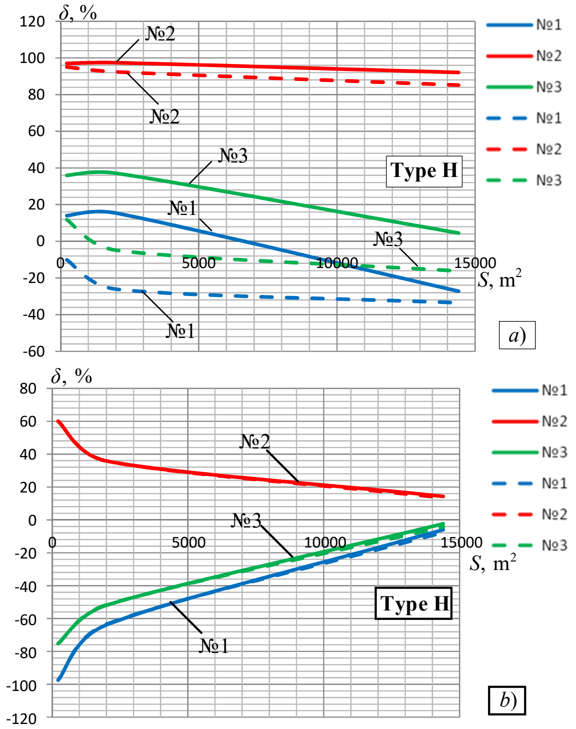

Fig. 2. Error in determining normalized parameters depending on the area of the GD and the method of equivalence of soil type H:
a – solid curve – U_{tc}; dotted curve – U_{tk};
b – solid curve – R_G; dotted curve – U_G

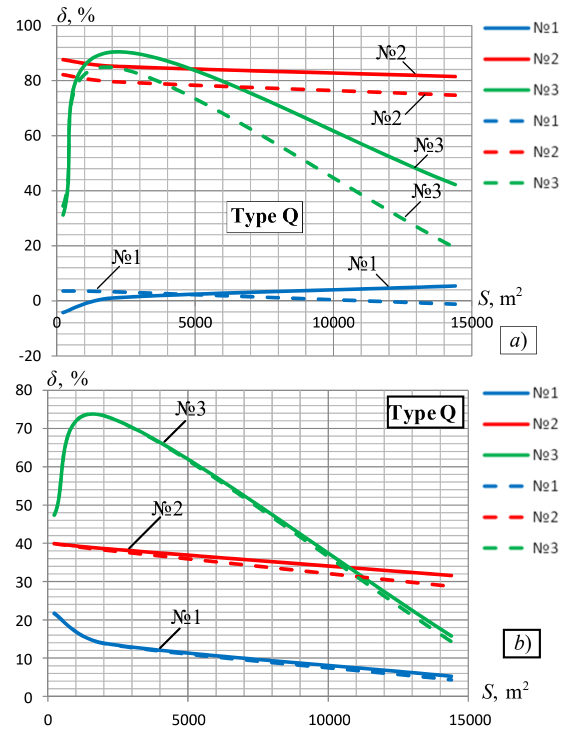

Fig. 3. Error in determining normalized parameters depending on the area of the GD and the method of equivalence of soil type Q:
a – solid curve – U_{tc}; dotted curve – U_{tk};
b – solid curve – R_G; dotted curve – U_G

Figure 4 shows similar calculation results for soil type K. The symbols are similar to Fig. 1. In Fig. 4,*a*, method No. 2 is not shown, since it gives an error of more than –500 %.

According to the simulation results for soil type K, we see that the equivalence methods No. 1 and No. 3 can be used to calculate the touch voltage in the center and at the edge of the foundation, respectively, with area of less than 2000 m^2 (the error lies in the range from –10 % to 15 %). The use of the equivalence method for calculating the voltage on the foundation and the foundation resistance is not recommended, although the tendency for the error to decrease with increasing area is also preserved.

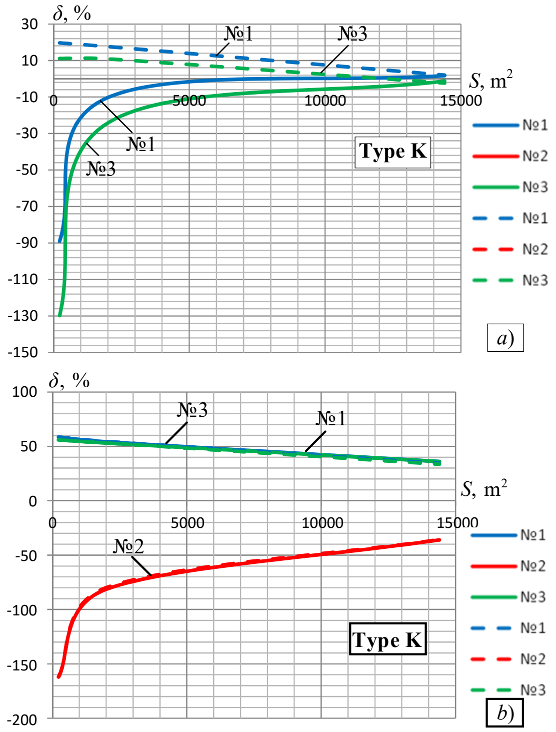

Fig. 4. Error in determining normalized parameters depending on the area of the GD and the method of equivalence of soil type K:
a – solid curve – U_{tc}; dotted curve – U_{tk};
b – solid curve – R_G; dotted curve – U_G

According to the results of the analysis of Fig. 1 – 4, we can form the following algorithm for choosing an equivalence method for calculating a certain normalized parameter of the GD depending on the type of soil (see Table 5). The principle of forming Table 5 was as follows: if for a certain type of soil when calculating one of the normalized parameters the condition

$$|\delta| \leq 10\ \% \qquad (3)$$

is achieved, then the number of the corresponding equivalence method is indicated and it is recognized as acceptable for use.

If there are certain restrictions on the area of the GD for which condition (3) is achieved, then the method is accepted as conditionally acceptable, and the restrictions are given in the note. If condition (3) is not met, then the method is considered unacceptable, and Table 5 indicates «–».

The application of the proposed algorithm for selecting the equivalence method is considered on the example in Appendix 1.

Table 5

Recommendations for the algorithm for choosing the equivalence method

Soil type / GD parameter	U_{tc}	U_{tk}	R_G	U_G
Type A ($\rho_1 < \rho_2 < \rho_3$)	3	1	2*	2*
Type H ($\rho_1 > \rho_2 < \rho_3$)	–	–	–	–
Type Q ($\rho_1 > \rho_2 > \rho_3$)	1	1	–	–
Type K ($\rho_1 < \rho_2 > \rho_3$)	1**	3**	–	–

Note: * – permissible at S > 1000 m^2;
** – permissible at S > 2000 m^2.

Conclusions.

1. Based on a series of calculation experiments and analysis of the obtained values of the normalized parameters of the grounding device, it was established:

– for soil type A, methods No. 1 (the upper layer of the real geoelectric structure – the first layer of the equivalent two-layer, and the following layers are equivalent to the second) and No. 3 (all the upper layers of the real structure to the GD and an additional 0.1–0.2 m – the first layer of the equivalent structure, and the following ones – the second layer) can be used to determine the touch voltage, where method No. 3 is better for the center of the GD (error up to –10.5 %), and method No. 1 is better for the edge of the GD (error up to 9 %). Method No. 2 (the upper layers of the real structure – the first layer of the equivalent structure, and the lower one – the second layer) for calculating the voltage and resistance of the GD is allowed to be used for areas over 1000 m^2;

– for soil type H, none of the equivalence methods allows for a calculation with error of less than 10 %;

– for soil types Q and K, the equivalence method can be used only for calculating the touch voltage. In this case, for Q, the equivalence method No. 1 should be used (error from –4.2 % to 5.6 %). For type K, method No. 1 is better for the center of the GD, and method No. 3 is better for the edge of the GD with area of over 2000 m².

2. Regardless of the soil type, when determining the GD resistance and the GD voltage, in all cases there is a decrease in the error with increase in the GD area, which indicates the possibility of improving the accuracy of calculations for objects with area of over 10,000 m^2.

3. Based on the analysis of the modelling results, an algorithm for selecting the equivalence method for calculating a certain normalized GD parameter depending on the soil type was formed. The relative error within ±10 % was chosen as the acceptance criterion. At the same time, depending on the soil type and the GD parameter being determined, the methods are divided into acceptable, unacceptable and conditionally acceptable (taking into account the limitation on the GD area).

4. Considering that a full calculation of all normalized parameters using the equivalence method can be performed only for soil type A, it is most advisable to use software packages that allow taking into account the three-layer structure of the soil in the process of determining the normalized GD parameters.

APPENDIX 1

An example of applying the proposed algorithm for selecting the equivalence method. The initial object has a size of 120×65 m^2 with depth of the soil location of 0,6 m. Soil parameters: ρ_1 = 53,9 Ω·m; ρ_2 = 117 Ω·m; ρ_3 = 12,3 Ω·m;

h_1 = 1,2 m; h_2 = 12,3 m. Accordingly, the soil is located in the first layer.

The given soil parameters correspond to soil type K, and the area of the soil is 7800 m^2 and meets the condition S > 2000 m^2. Therefore, to determine the touch voltage in the center of the GD (U_{tc}), one should use the equivalence method No. 1 according to expressions (1) and (2), according to the results of which the parameters of the equivalent model will be: ρ_{1e} = 53,9 Ω·m; ρ_{2e} =32,18 Ω·m; h_{1e} = 1,2 m. To determine the touch voltage at the edge of the GD (U_{tk}) using the equivalence method No. 3: ρ_{1e} = 53,9 Ω·m; ρ_{2e} = 32,32 Ω·m; h_{1e} = 0,8 m. In case of need to determine the voltage on the GD and the GD resistance, one should use a three-layer soil model.

Conflict of interest. The authors declare no conflict of interest.

REFERENCES

1. Wang Y., Jiang J., Huang Y., Wang J. Design of substation grounding grid in CFETR. *Scientific Reports*, 2024, vol. 14, no. 1, art. no. 25009. doi: https://doi.org/10.1038/s41598-024-76764-5.

2. Chiliquinga W., Robles P. Considerations in the design of electrical substations, including the effect of potential gradient on surrounding metallic structures. *Ingenius*, 2022, no. 28, pp. 9-24. doi: https://doi.org/10.17163/ings.n28.2022.01. (Esp).

3. Volkov V.P., Bondarenko V.E. *Calculation and design of grounding devices for high-voltage electrical installations: Textbook.* Kyiv, UMK VO, 1990. 116 p. (Rus).

4. Koliushko D.G., Rudenko S.S. Analysis of methods for monitoring of existing energy objects grounding devices state at the present stage. *Electrical Engineering & Electromechanics*, 2019, no. 1, pp. 67-72. doi: https://doi.org/10.20998/2074-272X.2019.1.11.

5. Koliushko D.G., Rudenko S.S. The factors of the influence on the touch voltage from the review of the development of recommendations for the reconstruction of the grounding device. *Technical Electrodynamics*, 2019, no. 3, pp. 29-36. doi: https://doi.org/10.15407/techned2019.03.029.

6. Nahman J., Paunovic I. Effects of the Local Soil Nonuniformity Upon Performances of Ground Grids. *IEEE Transactions on Power Delivery*, 2007, vol. 22, no. 4, pp. 2180-2184. doi: https://doi.org/10.1109/TPWRD.2007.905284.

7. Koliushko D.G., Rudenko S.S. Analysis of electrophysical characteristics of grounds in the vicinity electrical substation of Ukraine. *Electrical Engineering & Electromechanics,* 2015, no. 3, pp. 67-72. doi: https://doi.org/10.20998/2074-272X.2015.3.10.

8. Turri R., Andolfato R., Cuccarollo D. A numerical simulation tool for cathodic protection and electromagnetic interference analysis. *NACE Milano Italia Section – Conference & Expo 2016 «A European event for the Corrosion Prevention of Oil&Gas industry».* 17 p. Available at: https://www.researchgate.net/publication/303685228_A_NUME (accessed 10 April 2022).

9. Hossain M.S., Ahmed R., Hossain S. Design and Optimization of Substation Grounding Grid for Ensuring the Safety of Personnel and Equipment. *Journal of Electrical Power & Energy Systems*, 2021, vol. 5, no. 1, pp. 71-80. doi: https://doi.org/10.26855/jepes.2021.08.001.

10. Pereira Sodre R., Lopes Pereira B., Leite Sidrim L., Almeida J.F., Souza Sobrinho C.L.S. Optimization of Grounding Grids Design for a Square-Shaped Mesh. *IEEE Latin America Transactions*, 2018, vol. 16, no. 1, pp. 135-139. doi: https://doi.org/10.1109/TLA.2018.8291465.

11. Cardoso C., Rocha L., Leiria A., Teixeira P. Validation of an integrated methodology for design of grounding systems through field measurements*. CIRED - Open Access Proceedings Journal,* 2017, vol. 2017, no. 1, pp. 897-901. doi: https://doi.org/10.1049/oap-cired.2017.0452.

12. *IEEE Std 80-2013 Guide for Safety in AC Substation Grounding*. New York, IEEE, 2013. 226 p. doi: https://doi.org/10.1109/IEEESTD.2015.7109078.

13. *IEEE Std 81-2012 Guide for Measuring Earth Resistivity, Ground Impedance, and Earth Surface Potentials of a Grounding System.* New York, IEEE, 2012. 74 p. doi: https://doi.org/10.1109/IEEESTD.2012.6392181.

14. Permal N., Osman M., Ariffin A.M., Abidin Ab Kadir M.Z. Effect of Non-Homogeneous Soil Characteristics on Substation Grounding-Grid Performances: A Review. *Applied Sciences*, 2021, vol. 11, no. 16, art. no. 7468. doi: https://doi.org/10.3390/app11167468.

15. Nikolovski S., Knežević G., Baus Z. Assessment of Step and Touch Voltages for Different Multilayer Soil Models of Complex Grounding Grid. *International Journal of Electrical and Computer Engineering (IJECE)*, 2016, vol. 6, no. 4, pp. 1441-1455. doi: http://doi.org/10.11591/ijece.v6i4.pp1441-1455.

16. Malanda S.C., Davidson I.E., Singh E., Buraimoh E. Analysis of Soil Resistivity and its Impact on Grounding Systems Design. *2018 IEEE PES/IAS PowerAfrica*, 2018, pp. 324-329. doi: https://doi.org/10.1109/PowerAfrica.2018.8520960.

17. Dilushani P.D.R., Nawodani W.R.N., Bambaravanage T., Udayakumar K.A.C. Soil Resistivity Analysis and Earth Electrode Resistance Determination. *IOSR Journal of Electrical and Electronics Engineering (IOSR-JEEE)*, 2020, vol. 15, no. 2, pp. 26-35. doi: https://doi.org/10.9790/1676-1502012635.

18. Alotto P., Torchio R., Andolfato R., Cuccarollo D. Identification of Multilayer Soil Models for Grounding Systems from Surface Measurements. *Technical Report*, 2018. doi: https://doi.org/10.13140/RG.2.2.35135.15526.

19. *Rules for installing electrical installations.* Kyiv, Ministry of Energy and Coal Industry of Ukraine, 2017. 760 p. (Ukr).

20. Koliushko D.G., Rudenko S.S., Istomin O.Ye., Saliba A.N. Simulation of electromagnetic processes in the grounding system with a short circuit in the operating high-voltage substation. *Electrical Engineering & Electromechanics*, 2022, no. 4, pp. 75-80. doi: https://doi.org/10.20998/2074-272X.2022.4.11.

Received 25.09.2024
Accepted 16.01.2025
Published 02.07.2025

D.G. Koliushko[1]*, PhD, Senior Researcher,*
S.S. Rudenko[1]*, PhD, Senior Researcher,*
V.O. Vevenko[1]*, Postgraduate Student,*
[1] National Technical University «Kharkiv Polytechnic Institute», 2, Kyrpychova Str., Kharkiv, Ukraine, 61002,
e-mail: serhij_rudenko@ukr.net (Corresponding Author)

How to cite this article:
Koliushko D.G., Rudenko S.S., Vevenko V.O. Application of the multilayer soil equivalence method in determining the normalized parameters of the grounding system. *Electrical Engineering & Electromechanics*, 2025, no. 4, pp. 80-85. doi: https://doi.org/10.20998/2074-272X.2025.4.10

Матеріали приймаються за адресою:
Кафедра "Електричні апарати", НТУ "ХПІ", вул. Кирпичева, 2, м. Харків, 61002, Україна
Електронні варіанти матеріалів по e-mail: a.m.grechko@gmail.com

Довідки за телефонами: +38 067 359 46 96 Гречко Олександр Михайлович

Передплатний індекс: 01216